Development of a Welding Process to Improve Welded Microalloyed Steel Characteristics

by

Mohsen Mohammadijoo

A thesis submitted in partial fulfillment of the requirements for the degree of

Doctor of Philosophy

in
Materials Engineering

Department of Chemical and Materials Engineering

University of Alberta

Abstract

During the past several decades, the relationship between microstructure and mechanical properties of high strength microalloyed steels has been extensively studied in an effort to improve the fracture toughness and strength of these types of steels, without appreciably increasing steel manufacturing and pipeline fabrication (welding) costs. Fueled by the demand for developing pipeline steels with high strength, toughness and low cost by the construction, energy and transportation industries, it has always been essential to improve the properties of microalloyed steels and their weld and heat affected zone (HAZ).

High strength, low-carbon microalloyed steels possess an excellent combination of strength and toughness obtained by appropriate alloying design and thermo-mechanical controlled processing (TMCP). However, this strength and toughness combination can be deteriorated by the high heat input and the thermal cycles that the steel experiences during welding. Since welding is an unavoidable stage in pipe manufacturing, it is essential to produce welded sections with as low a heat input as possible, while retaining adequate joint geometry and properties. From a metallurgical point of view, the property deterioration associated with welded microalloyed steels has always been a main challenge for manufacturing, specifically for pipeline manufacturers. The HAZ, particularly the coarse grain heat affected zone (CGHAZ), i.e., the region adjacent to the fusion line, typically has lower fracture toughness compared with the rest of the steel. The deterioration in toughness of the CGHAZ is attributed to the formation of martensite-austenite (M-A) constituents, local brittle zones (LBZ) and large prior austenite grains (PAG). Submerged arc welding (SAW) with more than one electrode, i.e., tandem submerged arc welding (TSAW), has been preferred over other welding process in the pipeline industry due to its inherent properties, such as deep penetration, high deposition rate and capability of welding thick sections. Nevertheless, the heat input in the TSAW process may be increased due to the increase in the overall welding current and voltage needed for a higher deposition rate, resulting in some adverse effects on the microstructure and toughness of the weld joint. In the present research, a welding process, tandem submerged arc welding with an additional cold wire (CWTSAW), has been developed for pipeline manufacturing to improve the weld and HAZ geometry, mechanical properties, particularly fracture toughness, and microstructure in the HAZ.

Since an appropriate understanding of the welding conditions to guarantee requisite weld geometry, appearance and mechanical properties is always essential in the development of a welding process, the CWTSAW process was initially optimized and the effect of cold wire addition parameters on dilution, geometry and properties of the weld metal (WM) and the HAZ was investigated. As such, heat input, voltage and travel speed of both electrodes, along with three main cold wire parameters, were correlated with the geometry of the weld and HAZ, i.e., aspect ratio (AR), semi-penetration ratio (SPR), reinforcement area (RA) and CGHAZ area, dilution and the microhardness of the WM and CGHAZ. The results showed that the addition of a cold wire at a lagging position close to the trail electrode at 63° resulted in an overall improvement in the weld geometry, dilution and microhardness.

Macrostructural analysis showed a decrease in the CGHAZ size by addition of a cold wire. Microstructural evaluation, using both tint etching optical microscopy (TEOM) and scanning electron microscopy (SEM), indicated the formation of finer PAGs and less fraction of M-A constituents with refined morphology within the CGHAZ when the cold wire was fed in TSAW. The low-temperature fracture toughness of the HAZ was improved by 38% when a cold wire was fed at 25.4 cm/min with a heat input of 22.2 kJ/cm. The improvements are attributed to lower actual heat introduced to the weldment and consequently faster cooling rate in the CGHAZ by cold wire addition. Incorporating a cold wire in TSAW essentially moderates the heat input by consuming the heat of molten pool and/or the energy of the trail electrode as the wire melts into the weld puddle. Analysis of the effective heat input of the CWTSAW process has indicated that the trail electrode heat input was reduced by 13% when cold wire was fed at 25.4 cm/min.

In addition, the influence of cold wire addition in the conventional TSAW on welding productivity in terms of deposition rate and travel speed of welding has been studied. From a welding point of view, it is essential to weld and join the sections more quickly and at a lower cost with as a low heat input as possible, since high welding heat input is detrimental to the properties of the weld and HAZ. The cold wire provides a higher deposition rate and better productivity for the welding process, without increasing heat input compared with the TSAW process. Accordingly, better quality welds are achieved with deep penetration at lower heat inputs per mass of deposited material, and with a substantial reduction in arcing time causing the formation of a smaller weld pool (compared with TSAW without a cold wire). Cold wire addition at 58 cm/min in the TSAW process with a heat input of 23.2 kJ/cm resulted in a maximum 26% increase and 12% increase in the welding travel speed and deposition rate, respectively.

Since the CGHAZ typically exhibits lower fracture toughness compared with the rest of the steel in single pass welding, the single-edge notch tension (SENT) testing method has been utilized to evaluate the fracture toughness in the CGHAZ. In fact, it is generally accepted that actual cracks in pipelines and pressure vessels are more often shallow and dominated by tensile loads, which results in a less severe crack-tip constraint condition compared with a deep crack under bending test conditions. As such, the J-R curve (resistance curve) increases due to a shallower crack and tensile loading conditions. Accordingly, many experimental and analytical endeavors have been accomplished in recent decades to determine more reasonable fracture toughness for ductile cracks in low-constraint conditions. In this research, SENT testing has been conducted (according to the method developed by Canmet Materials) on two types of weld specimens manufactured by both conventional TSAW and CWTSAW processes, and then the weld specimens were exposed to the tensile loading during SENT testing. The J-integral results showed overall improvement in the fracture toughness of the CGHAZ at different temperatures by cold wire addition, which is in agreement with Charpy impact testing results and microstructural analysis performed on the CGHAZ.

Preface

The materials presented in the current thesis are parts of the research project under the supervision of Dr. Douglas G. Ivey and Dr. Hani Henein, which has been financially supported by the Natural Sciences and Engineering Research Council (NSERC) of Canada, Evraz Inc. NA, TransCanada PipeLines Ltd., Enbridge Pipeline Inc., UT quality Inc. and Alliance Pipeline Ltd. The research was conducted in the Advanced Materials and Processing Laboratory (AMPL) at the University of Alberta and the R&D Division of Evraz Inc. NA.

Chapter 3 of this thesis is published as **M. Mohammadijoo, S. Kenny, L. Collins, H. Henein, D.G. Ivey, 2016,** "**Influence of cold wire tandem submerged arc welding parameters on weld geometry and microhardness of microalloyed pipeline steels**", *International Journal of Advanced Manufacturing Technology*, doi: 10.1007/s00170-016-8910-z. Some parts of Chapter 3 are published as **M. Mohammadijoo, S. Kenny, J.B. Wiskel, D.G. Ivey, H. Henein, 2015,** "**Cold wire tandem submerged arc welding: a novel technique for pipeline manufacturing**" in *Proceedings of 54th Conference of Metallurgists,* Toronto, ON, Canada.

Chapter 4 of this thesis is accepted for publication as **M. Mohammadijoo, S. Kenny, L. Collins, H. Henein, D.G. Ivey, 2017,** "**Characterization of HAZ of API X70 microalloyed steel welded by cold wire tandem submerged arc welding**", *Metallurgical and Materials Transactions A*. Some parts of Chapter 4 are published as **M. Mohammadijoo, S. Kenny, L. Collins, H. Henein, D.G. Ivey, 2016** "**Effect of cold wire addition in the TSAW process on microstructure and mechanical properties of the HAZ of X70 microalloyed pipeline steel**", *American Society of Mechanical Engineers-Digital Library*, doi: 10.1115/IPC2016-64549 (presented at *11th International Pipeline Conference,* Calgary, AB, Canada).

Chapter 5 of this thesis has been submitted for publication as **M. Mohammadijoo, L. Collins, H. Henein, D.G. Ivey,** "**Evaluation of cold wire addition effect on heat input and productivity of tandem submerged arc welding for low-carbon microalloyed steels**", *International Journal of Advanced Manufacturing Technology*. Also, some parts of Chapter 5 are published as **M. Mohammadijoo, S. Kenny, H. Henein, D.G. Ivey, 2016** "**Application of cold wire tandem submerged arc welding for low-carbon microalloyed linepipe steels**" in *Proceedings of 10th*

International Conference on Trends in Welding Research, American Welding Society and Japanese Welding Society in Tokyo, Japan.

Chapter 6 of this thesis is being prepared for publication as **M. Mohammadijoo, H. Henein, D.G. Ivey,** "**Correlation between M-A constituents and toughness in the HAZ of the welded X70 microalloyed steel using single-edge notch tension (SENT) testing**", *Materials Science and Engineering: A*.

Appendix C of this thesis is published as **M. Mohammadijoo, H. Henein, D.G. Ivey, 2016,** "**Microstructural characterization of the HAZ in welded microalloyed steel**" in *Proceedings of 43rd Annual Meeting of Microscopy Society of Canada,* Edmonton, AB, Canada.

In all the research papers, I was responsible for the data collection and analysis as well as the manuscript composition. The experimental design and mathematical data analysis were carried out using Minitab software 17.0, a commercial statistical package. In all the aforementioned publications, Dr. Douglas G. Ivey and Dr. Hani Henein contributed to the manuscript composition and edits.

It should be mentioned that the format of this thesis is paper-based and there may be some repetition, especially in the "Experimental" section of each chapter.

Acknowledgments

Words cannot describe my gratitude towards my supervisors, Dr. Douglas G. Ivey and Dr. Hani Henein, for their appreciable inspiration, guidance and patience throughout my whole PhD experience. Their invaluable kindness, support and advice helped me to develop my knowledge and personality. It was a great pleasure to have the opportunity to work under their supervision. I am truly inspired by their scientific knowledge, insight, energy and passion. Dr. Henein, the AMPL bi-weekly group meetings provided a fruitful and friendly environment for me to develop my knowledge. Dr. Ivey, your fundamental and technical guidance in our weekly meetings made my PhD research quite exciting for me. My sincerest appreciation also goes to Dr. Laurie Collins for his technical assistance and support conducting some part of the research at the R&D division of Evraz Inc. NA.

I would especially like to acknowledge and thank Dr. Leijun Li, Robert Lazor (TransCanada PipeLine Ltd.), Dr. Barry J. Wiskel, David Hoffman (Enbridge Inc.), Stephen Kenny (Evraz Inc. NA), Dr. Kioumars Poorhaydari, Dr. Aziz Bogno and Dr. Jonas Valloton for their kind guidance and helpful suggestions. The assistance of Victoria Chum from SGS Ludwig, Jason Szarkowicz and Jon Jackson from Evraz Inc. NA for conducting the single-edge notch tension tests, welding trials and Charpy tests, respectively, is greatly appreciated. I would like to express special gratitude to all my friends and colleagues at the Advanced Materials and Processing Laboratory (AMPL) for all their continuous support and encouragement throughout my program. Special gratitude is given to my friends Saoussen Ouhiba, Dr. Meisam Nouri, Jacobs Kenny, Mirjavad Geramian, Jun Ma, Pusong Wang, Taghi Amiri, Shengze Yin, Justin Forth and Kartik Vasudev for being there for me when I needed good advice.

I would like to acknowledge the Natural Sciences and Engineering Research Counsil (NSERC) of Canada, Evraz Inc. NA, TransCanada PipeLines Ltd., Enbridge Pipeline Inc., UT quality Inc. and Alliance Pipeline Ltd. for financial support.

I would like to gratefully express my gratitude to my parents and my siblings, without whom I could never have reached this stage in my life. My last, but not least, appreciation goes to my lovely wife, Zeinab, whose love, patience and support was always with me. You have always been my muse; a source of unwavering passion and encouragement in my life.

Contents

List of Figures

List of Tables

Acronyms

AC	alternating current
ACSQ	square-wave alternating current
ANOVA	analysis of variance
API	American petroleum institute
AR	aspect ratio
ASME	American society of mechanical engineers
AWS	American welding society
BCC	body-centered cubic
BCT	body-centered tetragonal
BF	bainitic ferrite
BM	base metal
CC	constant current
CE	carbon equivalent
CGHAZ	coarse grain heat affected zone
CMOD	crack-mouth opening displacement
CR	cooling rate
CT	compact tension
CTOD	crack tip opening displacement
CV	constant voltage
CVN	Charpy V-notch
CWA	cold wire angle
CWFS	cold wire feed speed
CWP	cold wire position
CWTSAW	cold wire tandem submerged arc welding
DBTT	ductile-to-brittle transition temperature
DC	direct current
DCEN	direct current electrode negative
DCEP	direct current electrode positive
DCT	disc-shaped compact tension
EBSD	electron backscattered diffraction
ECA	engineering critical assessment
ERW	electric resistance welding
F_{arc}	arc force
FCC	face-centered cubic
FGHAZ	fine grain heat affected zone
FL	fusion line

GB	granular bainite
GBF	grain boundary ferrite
GMAW	gas metal arc welding
GTAW	gas tungsten arc welding
HAZ	heat affected zone
HI	heat input
HIC	hydrogen induced cracking
HI-L	heat input-lead electrode
HI-T	heat input-trail electrode
HR-ERW	high-frequency electric resistance welding
HRR	Hutchinson-Rice-Rosengren
HSLA	high strength low-alloy
HV	hardness Vickers
ICHAZ	inter-critical heat affected zone
ICRCGHAZ	inter-critically reheated coarse grain heat affected zone
ID	inner-diameter
LBZ	local brittle zone
M-A	martensite-austenite
Ms	martensite start temperature
MVC	microvoid coalescence
NEB	national energy board of Canada
OD	outer-diameter
PAG	prior austenite grain
PF	polygonal ferrite
RA	reinforcement area
RC-ERW	rotary contact wheel electric resistance welding
SAW	submerged arc welding
SBD	strain-based design
SCC	stress corrosion cracking
SCHAZ	sub-critical heat affected zone
SE	secondary electron
SEM	scanning electron microscopy
SENB	single-edge notch bend
SENT	single-edge notch tension
SIA	structural integrity assessment
SMAW	shielded metal arc welding
S/N	signal-to-noise ratio
SPR	semi-penetration ratio
SS	sum of squares
SS-FCAW	self-shielded flux cored arc welding
TEM	transmission electron microscopy
TEOM	tint etching optical microscopy

TMCP	thermo-mechanical controlled processed
TOMRA	three-order multiple regression analysis
TS	travel speed
TSAW	tandem submerged arc welding
UOE	a method of pipe manufacturing (U-press, O-press, Expansion)
V-L	voltage-lead electrode
V-T	voltage-trail electrode
WF	Widmanstatten ferrite
WFS	wire feed speed
WM	weld metal
X42	a grade of pipeline steel, with a specified minimum yield strength of 289.6 MPa (42 ksi)
X52	a grade of pipeline steel, with a specified minimum yield strength of 358.5 MPa (52 ksi)
X56	a grade of pipeline steel, with a specified minimum yield strength of 386.1 MPa (56 ksi)
X60	a grade of pipeline steel, with a specified minimum yield strength of 413.6 MPa (60 ksi)
X65	a grade of pipeline steel, with a specified minimum yield strength of 448.2 MPa (65 ksi)
X70	a grade of pipeline steel, with a specified minimum yield strength of 482.6 MPa (70 ksi)
X80	a grade of pipeline steel, with a specified minimum yield strength of 551.5 MPa (80 ksi)
X100	a grade of pipeline steel, with a specified minimum yield strength of 689.4 MPa (100 ksi)
X120	a grade of pipeline steel, with a specified minimum yield strength of 827.3 MPa (120 ksi)

Symbols

a	crack (flaw) depth (mm)
a_0	initial crack depth (mm)
A_{pl}	plastic area under the load-LLD curve (kN mm)
Ar	bead reinforcement area (mm^2)
α	thermal diffusivity ($m^2\ s^{-1}$)
B_N	thickness of side grooved specimen (mm)
C_i	concentration of solute I (wt.%)
d_p	mean particle size (μm)
d_{M-A}	size of martensite-austenite constituents (μm)
f_p	volume fraction
f_{M-A}	volume fraction of martensite-austenite constituents
I	current (amperes)
J	energy (joules)
J_{el}	elastic component of elastic-plastic plane strain fracture mechanics (J/m^2)
J_{Ic}	elastic-plastic plane strain fracture mechanics (J/mm^2)
J_{el}	plastic component of elastic-plastic plane strain fracture mechanics (J/m^2)
k	heat transfer coefficient ($W\ m^{-2}\ K^{-1}$)
K	stress intensity factor ($MPa/m^{-1/2}$)
K_{Ic}	elastic plane strain fracture mechanics ($MPa/m^{-1/2}$)
k_y	strengthening coefficient ($MPa\ mm^{1/2}$)
λ	thermal conductivity ($J\ s^{-1}\ m^{-1}\ °C^{-1}$)
$λ_p$	inter-particle spacing (μm)
Pcm	welding crack susceptibility index (wt.%)
ρc	specific heat capacity ($J\ m^{-3}\ °C^{-1}$)
q	heat energy (joules)
$σ_B$	brittle fracture stress (MPa)
$σ_i$	friction stress of iron (MPa)
$σ_Y$	yield stress (MPa)
$σ_{UTS}$	ultimate tensile stress (MPa)
T	temperature (°C)
t	time (s)
$Δt_{8-5}$	weld time constant (sec)
ν	velocity (m/s)
V	voltage (volts)
w	specimen width (mm)

Chapter 1

1. Introduction

1.1. Motivation

High-strength low-alloy (HSLA) microalloyed steel has been adopted for oil and gas transportation line pipes to improve transport efficiency through high pressure operation of long distance pipelines and reduction of pipe laying costs [1–4]. Microalloyed steels possess exceptional properties, such as high strength and toughness, and excellent weldability. However, any imperfection in the steel, manufacturing process and joining of pipelines may result in deterioration in the properties and eventually a severe failure at an unexpected time. History has shown many examples of pipeline failure and oil spills all around the world (Figure 1-1[1]). The oil pipeline spills in North Battleford (Saskatchewan) in 2016, the Red Deer River in 2012, Rainbow Lake (Alberta) in 2012, Slave Lake (Alberta) in 2006, Glennifer Lake in 2008 and the Gulf of Mexico in 2010 are some of the recent pipeline failures resulting in contamination of the environment. In addition, pipeline failures cost the transmission pipeline industry 5.4 to 8.6 billion dollars annually (extracted from "activehistory.ca/2012/oil-pipeline-spills"). Although preventative actions have been taken during manufacturing of pipelines, pipeline failure still occurs. According to the National Energy Board (NEB) of Canada (extracted from "https://www.neb-one.gc.ca/sftnvrnmnt/sft/pplnrptr/index-eng.html"), the failure of Canadian pipelines during the years of 1992 to 2014, has been mainly due to the cracking and materials/manufacturing causes (more than 45%), geotechnical failure (~8%), metal loss (~29%) and other causes (18%). As such, from the view point of pipeline joining and welding, besides reducing manufacturing cost, a major concern is to improve the mechanical properties of pipelines, particularly fracture toughness. Figure 1-2[2] shows some examples of on-shore and off-shore oil pipeline spills and the impact on the environment.

[1] Extracted from: http://activehistory.ca/2012/06/the-history-of-oil-pipeline-spills-in-alberta-2006-2012/
[2] Extracted from:
http://www.ctvnews.ca/world/arkansas-cleanup-underway-after-millions-of-litres-of-canadian-oil-spills-from-pipeline
http://www.vice.com/en_ca/read/the-canadian-government-wants-to-sell-the-northern-gateway-pipeline to-voters-283
http://www.seankheraj.com/alberta-oil-spill-history-uncovered-1975-2013/

Besides many achievements in the development of steels and their processing methods, such as microalloyed steels and thermo-mechanical controlled processing (TMCP), there have been profound endeavors over the past decades in the area of steel pipeline welding to improve the quality of the weld and heat affected zone (HAZ) in terms of the geometry, microstructure, properties and weld defects. However, in addition to weld quality, productivity related to welding speed and deposition rate for economics of construction is a major concern.

Submerged arc welding (SAW) has been preferred over other welding processes for steel pipe production, due to its inherent properties, such as high deposition rate, deep penetration and capability of welding thick sections [1]. Recently, there have been some modifications to the SAW process to provide a welding process with improved productivity. The commonly used techniques to improve welding deposition rate are increasing electrode stick-out [5], twin-wire SAW [6], tandem SAW (TSAW) [7,8], applying a metal-cored wire [9,10], varying electrode polarity [11] and addition of a cold wire to a single electrode SAW [12] or in twin-wire SAW [13]. TSAW, which is SAW with two to five electrodes, is a common process employed by industries to improve welding productivity in a global economy to manufacture pipelines, pressure vessels and construction equipment [7,8,13]. Nevertheless, in the TSAW process, heat input is increased as the number of electrodes increases, because of the increase in the overall welding current and voltage for a higher deposition rate. Although TSAW provides higher productivity due to the high heat input, some adverse effects can be produced in terms of the microstructure, properties and geometry of the weld joint. The weld metal (WM) and particularly the HAZ are affected, since the weldment experiences higher peak temperatures and cools down more slowly after welding [8,14–16].

In the current research, TSAW with an additional cold wire (CWTSAW) has been developed to improve the macrostructure, mechanical properties and microstructure of the HAZ. Cold wire addition also improves welding productivity in terms of deposition rate and travel speed, while retaining adequate weld geometry and properties without increasing heat input compared with the TSAW process. These improvements, as a result of cold wire addition, are attributed to changes in the actual heat introduced to the weldment and the cooling rate in the HAZ. In CWTSAW, the additional wire, which is electrically cold with no arc, can be fed into the tandem weld pool. The cold wire provides a higher deposition rate and productivity to the welding process without increasing heat input [17–19]. In addition to the specified advantages of applying cold wire in TSAW, better quality welds can be produced with lower heat inputs per gram of deposited material and with a substantial reduction in arcing time causing the formation of smaller weld pools (compared with TSAW without adding a cold wire). From the welding process point of view, it is

believed that any change in the welding process parameters, such as an additional electrode and wire, current, voltage, travel speed, electrode stick-out and so forth, can cause considerable changes in the weld and HAZ shape and geometry [20–23], as well as the microstructure and mechanical properties of the HAZ [24–26]. Accordingly, in this work, the CWTSAW process parameters, particularly cold wire parameters, are correlated with the weld and HAZ geometry, microstructure and properties.

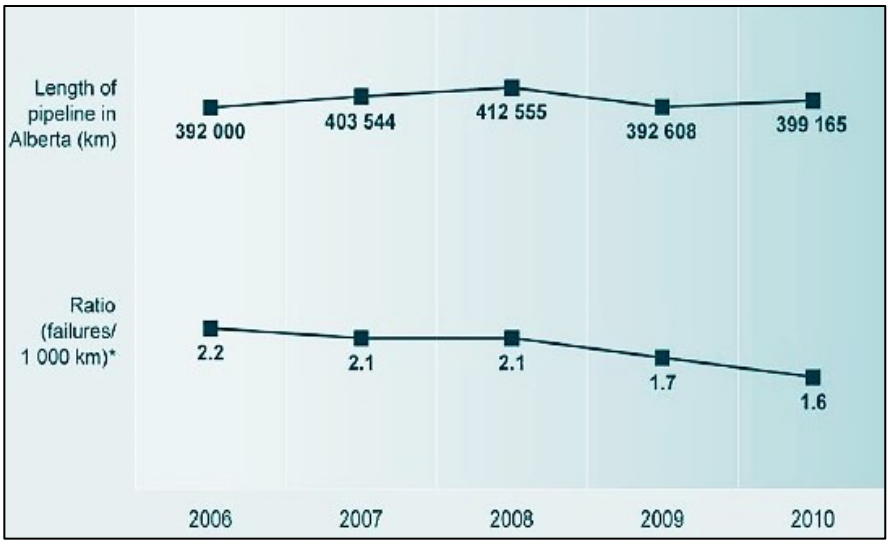

Figure 1-1 The history of oil pipeline spills in Alberta (2006-2010).

1.2. Objectives of the Research Project

Since increased productivity has been the sole purpose of adding a cold wire to the SAW process, which has been previously studied, the aim of this research is to investigate, in addition to improving welding productivity, the microstructural and mechanical property changes in the HAZ of a typical microalloyed steel when a cold wire is added to the TSAW process. Of particular interest is to optimize and control CWTSAW process parameters and to correlate CWTSAW process parameters with weld and HAZ geometry and mechanical properties of the weld while maximizing productivity. A designed research sequence has been developed to achieve these objectives, which are summarized as follows:

- **Development of the CWTSAW process**
  - Correlation of the CWTSAW process parameters with weld and HAZ geometry and mechanical properties.
  - Parametric optimization of CWTSAW to predict the weld and HAZ characteristics under different welding conditions.

- **Microstructure and mechanical property alterations in the HAZ by cold wire addition**
  - Comparison of the CWTSAW process with TSAW in terms of microstructure, mechanical properties, productivity and geometry.
  - Characterization of the microstructural alterations in the coarse grain heat affected zone (CGHAZ).
- **Correlation between heat input, productivity and properties of welded microalloyed steel**
  - Thermodynamic analysis of the welding heat input and its correlation with the properties.
  - Assessment of the extreme rate of deposition and speed of welding (productivity) achieved by additional cold wire to augment the pipeline manufacturing.
- **Fracture toughness analysis in the HAZ**
  - Single-edge notched tension (SENT) testing
  - Application of the SENT testing to investigate the CGHAZ fracture toughness

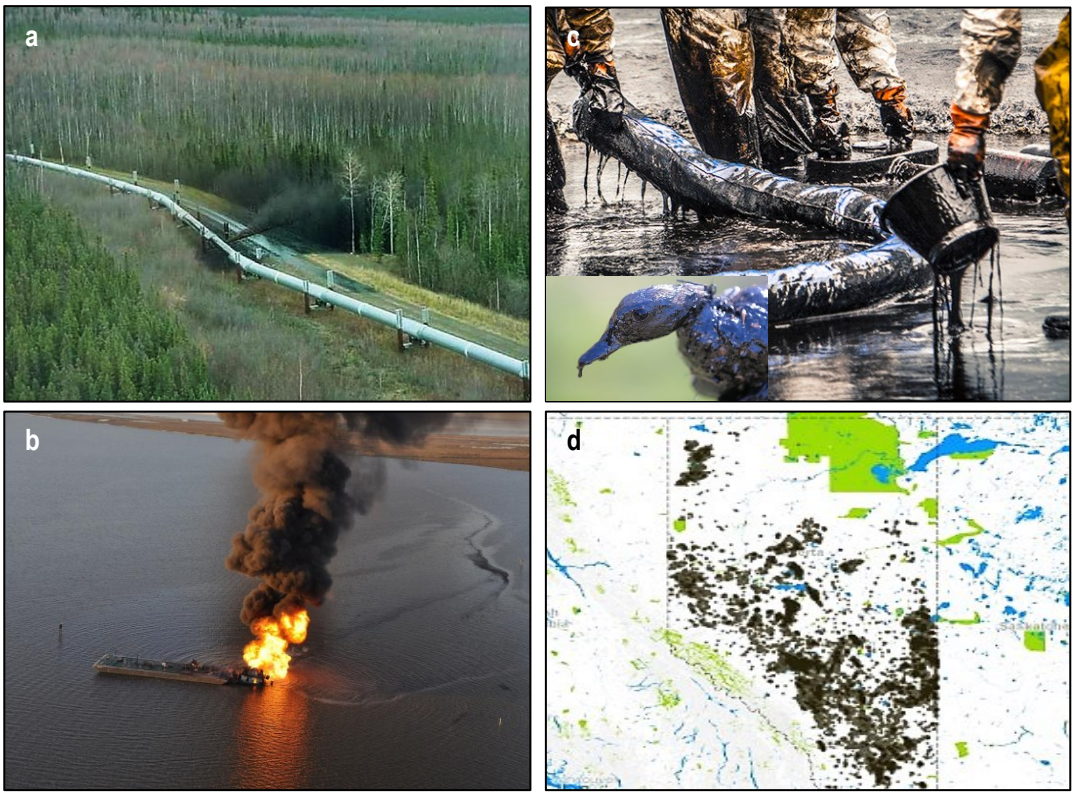

Figure 1-2 Examples of (a) On-shore and (b) off-shore oil pipeline failure and its impact on environment (c). (d) The map of oil spills in Alberta from 1975 to 2013.

1.3. Application of the Knowledge

A comprehensive literature review carried out at the preliminary stage of the research indicated many unclear points regarding the CWTSAW process, which needed to be addressed in the process development. The main questions that arose through this research project, such as "what are the optimized process parameters to produce a quality weld?", "from a metallurgical point of view, how are the microstructure and mechanical properties, particularly fracture toughness, altered in the HAZ when a cold wire is added to the conventional TSAW process?" and "from a welding technological point of view, to what extent is it possible to improve the welding productivity by cold wire addition without detrimental effect on the properties?". The aim has been to answer these questions through appropriately designed research. In addition, a recently developed test method, SENT, has been employed to assess the fracture toughness of the HAZ, particularly the CGHAZ, of microalloyed steel welded by both the developed CWTSAW and conventional TSAW process. The application of knowledge can be described in four main ways:

- Development of a welding process which fosters pipeline manufacturing by increasing the welding travel speed, enabling the manufacturer to fabricate microalloyed steel pipelines faster and at a lower cost without degrading the properties.
- Structure-property correlation in the HAZ of high strength microalloyed pipeline steels.
- Improvement of the mechanical properties, microstructure and macrostructure of the HAZ by modifying the conventional welding process.
- Application of the SENT testing methodology to characterize the fracture toughness in the HAZ of welded microalloyed steel.

Chapter 2

2. Background

2.1. Microalloyed Steels

The strength of steel can be increased by increasing the amount of alloying elements, such as carbon, manganese, molybdenum, nickel, chromium and copper [27]. However, these elements significantly enhance the formation of low-temperature phase transformation products (hardenability) in steel, which results in some difficulties introduced to manufacturing processes. In addition, the higher hardenability of steel may cause cracking in the HAZ [28]. Microalloyed steels are a class of high strength, low-carbon steels containing 0.05 to 0.2 wt.% carbon and small additions (in amounts less than 0.1 wt.% of each element) of niobium, titanium and vanadium. The steels may contain other alloying elements, such as molybdenum, in amounts exceeding 0.1 wt.% [29]. Microalloyed steels have high strength and excellent toughness, which are attributed in part to grain refinement and/or the presence of precipitates, especially nano-size precipitates. The precipitates can affect the recrystallization behavior and subsequent grain growth of the austenite, and induce precipitation hardening in the final matrix. The advantageous properties of microalloyed steels are not only due to their chemistries, but also to the thermo-mechanical treatments they undergo throughout processing.

Thermo-mechanical controlled processing (TMCP) is a microstructural control technique combining both controlled rolling and cooling. A typical TMCP process is shown in Figure 2-1. The post heat treatment (off-line heat treatment) at about 900°C is followed by cooling to ambient temperature. Normalizing (Figure 2-1a) is used to toughen the steel by generating a refined transformed structure from refined austenite. TMCP comprises thermo-mechanical rolling and accelerated cooling to strengthen and toughen steel plates, essentially by refining the transformed microstructure [30]. The microstructure is refined by a suitable combination of controlled rolling and accelerated cooling (Figure 2-1b). The nucleation sites for ferrite are increased during cooling by refining the grains and straining austenite. Afterwards, the transformed structure is further refined by accelerated cooling after the controlled rolling step, which involves cooling to a reduced

transformation temperature where the diffusion of the atoms is limited while a large driving force for the transformation is provided. The fine microstructure obtained from TMCP generates excellent mechanical properties such as high strength and toughness [31]. Phase transformation through a typical TMCP is shown in Figure 2-2.

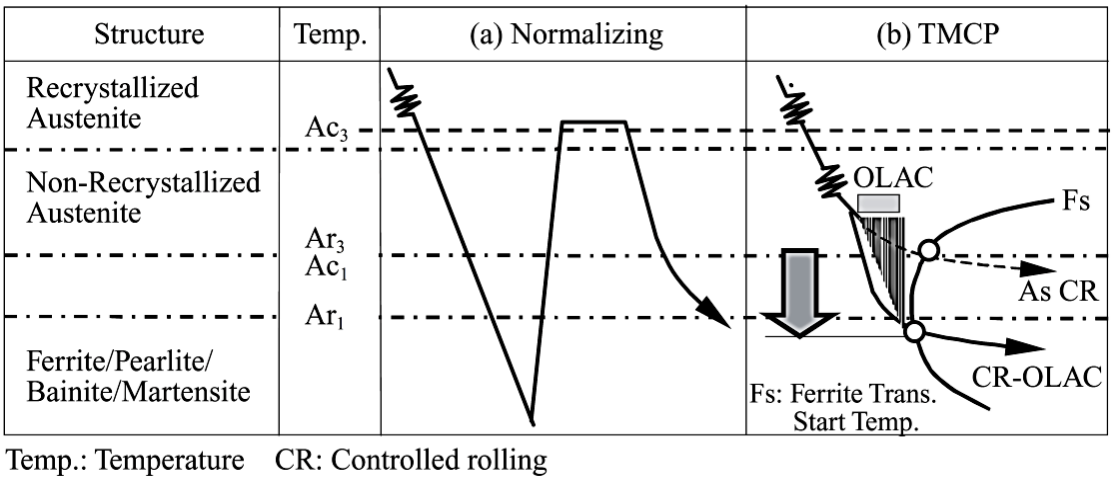

Figure 2-1 Schematic diagram of (a) normalizing and (b) TMCP processes [30] (OLAC: on-line accelerated cooling).

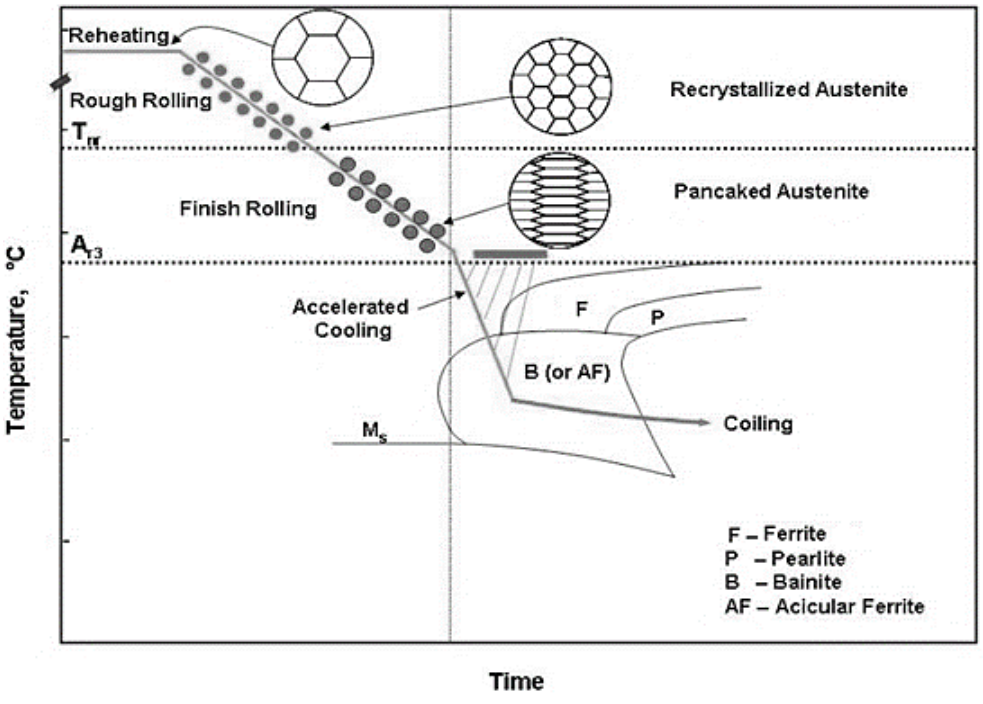

Figure 2-2 Schematic diagram of a thermo-mechanical controlled processing (TMCP) schedule indicating some part of the phase transformation through processing [32].

Due to the beneficial properties of microalloyed steels, such as high strength, excellent toughness and excellent weldability and, above all, relatively low cost, microalloyed steels are preferred over other high strength advanced steels and broadly used for transport pipelines and pressure vessels. Figure 2-3 compares high strength low-alloy (HSLA) steels (i.e., microalloyed steels) with all other types of steels. During the past several decades, many endeavors have been devoted to improving the properties and safety of pipelines and in decreasing the manufacturing cost. Therefore, pipeline steel plate has progressively been developed towards higher strength grades of API X60, X70, X80 and X100. The designation X corresponds to a pipeline grade and the digits correspond to the minimum specified yield strength in ksi. With higher strength, the pipe thickness can be decreased and the operating pressure can be increased. The X70 microalloyed steel used in this research project is produced by Evraz, Inc. NA and has a yield stress of ~480 MPa.

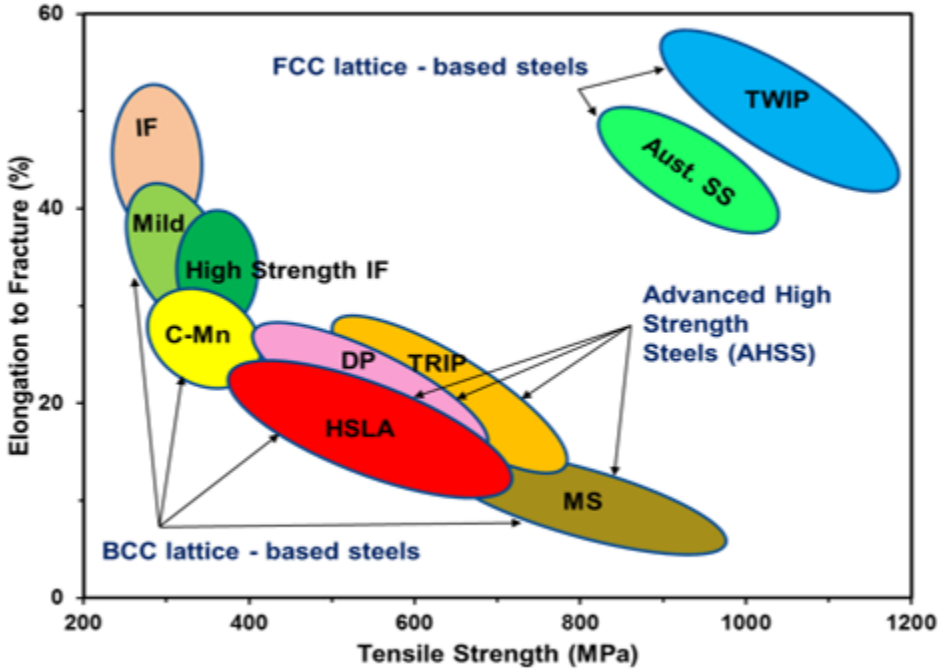

Figure 2-3 Schematic graph comparing HSLA steels with different types of steels [33]. IF: interstitial free steel; DP: dual phase steel; TRIP: transformation-induced plasticity steel; MS: martensitic steel, TWIP: twin-induced plasticity steel; Aust. SS: austenitic.

2.1.1. Development of pipeline steels

During the past several decades, high strength microalloyed steels have been used increasingly for pipeline and pressure vessel applications. It is not possible to fabricate a material completely resistant to crack formation; however, pipelines are required to have low susceptibility to crack initiation and propagation in order to prevent fracture, which typically occurs in the WM and/or

the HAZ rather than in the base material [34]. In addition, the susceptibility of pipeline steels to stress corrosion cracking (SCC) and hydrogen induced cracking (HIC) needs to be taken into account, especially in sour gas circumstances where H_2S is present. HIC occurs by a mechanism in which hydrogen concentrates by diffusion in the biaxial stress field at the tip of a crack [35]. Hydrogen is generated in the arc during fusion welding from moisture, and dissolves in the weld metal. Hydrogen then diffuses towards the HAZ after solidification, so that cracking can happen either in the WM or HAZ after decomposition of austenite [35,36].

The resistance of a steel to HIC can be improved by controlling the amount of alloying elements, which are added to prevent the formation of elongated non-metallic inclusions [28]. The good weldability of microalloyed steels, which is related to the beneficial microstructure of the WM and the HAZ [27] is due to the low carbon equivalent as a result of lower carbon and alloying element content [29].

Although the formation of a fine grained ferrite microstructure, obtained by the addition of microalloying elements and the use of TMCP, is expected to improve resistance to SCC, HIC and brittle fracture initiation in the HAZ [37], the reduction in the number of sulfides in microalloyed steels, due to the reduction in the sulfur levels, is believed to make the steel more susceptible to hydrogen cracking. In fact, the formation of MnS inclusions provides a sink for hydrogen and reduces the risk of HIC. In addition, they act as the nucleation sites for acicular ferrite formation; as such, the absence of MnS leads to the formation of low-temperature transformation products and higher hardness values in the HAZ [38]. As the strength and amount of the hard microstructural constituents increases, the susceptibility of steel to HIC increases [39,40]. The most susceptible phases (in order of decreasing susceptibility) are twinned martensite, bainite (upper or lower), granular bainite and lath martensite (the least susceptible) [41]. Accordingly, electrodes with lower hydrogen content are a requirement for low-sulfur, clean steels [29,42]. Careful storage and electrode baking procedures, or wire cleanliness and control of flux type, coupled with a reduction in carbon and carbon equivalent and preheat (needed for steels with 700 MPa yield strengths and higher) are the only means to reduce the risk of hydrogen cracking [43]. Taira et al. [44] and Sampatha [45] believe that the susceptibility to HIC in as-rolled X70 pipeline steel is due to the segregation of Mn to the centerline (segregation band), which promotes the formation of a “hard band” (i.e., low-temperature transformation products) in this zone. They have observed that the HIC susceptibility is high in the steels containing 0.05-0.15 wt.% C, when the manganese level is above 1%.

Since the mid-1960's, several classes of HSLA steels have been developed and utilized for oil and gas transportation. API[3] X42 and X52 pipeline steels with a ferrite-pearlite microstructure were some of the earliest classes of pipeline steels. In the early 1970's, API X70[4] microalloyed steel, produced through the TMCP process, was proposed to accommodate higher strength and toughness requirements. Some milestones in the development history of pipelines are listed in Table 2-1. Also, the required yield strength for pipeline development since the 1950s is historically shown in Figure 2-4. The strengthening mechanisms are mainly precipitation hardening and grain refinement, while the ferrite and pearlite still remained as the dominant microstructures [29,46]. However, in recent years, newer generations of high strength microalloyed steels are characterized as bainitic-ferritic microstructures with martensite-austenite (M-A) constituents [47]. X70 steel is a low-carbon microalloyed steel (≤ 0.05wt.%) with Ti, Nb and V as primary microalloying elements. Recently, new grades of HSLA steels, such as X100 and X120 have been proposed; however, they are still mainly at the laboratory research scale. In the case of X100, the microstructure is composed of bainite, with lath and granular morphology, and M-A constituents. A thorough study conducted by Hudson [48] assessed the process parameters of various techniques for girth welding of X100 steels.

Table 2-1 Some milestones during the development history of pipeline steels [49]

Milestone	Pipelines	Year
First X65 pipelines	Iran to Azerbaijan	1967
X70 steel (natural gas)	North America	1970s
First X80 (GRS 550)	Ruhrgas Werne to Schluchtern	1992

[3] Refers to the standard of the American Petroleum Institute (API).

[4] X70 indicates the specific minimum yield strength for high strength microalloyes steels in 'ksi'. Accordingly, an X70 microalloyed steel can yield at approximately 482 MPa prior to the plastic deformation.

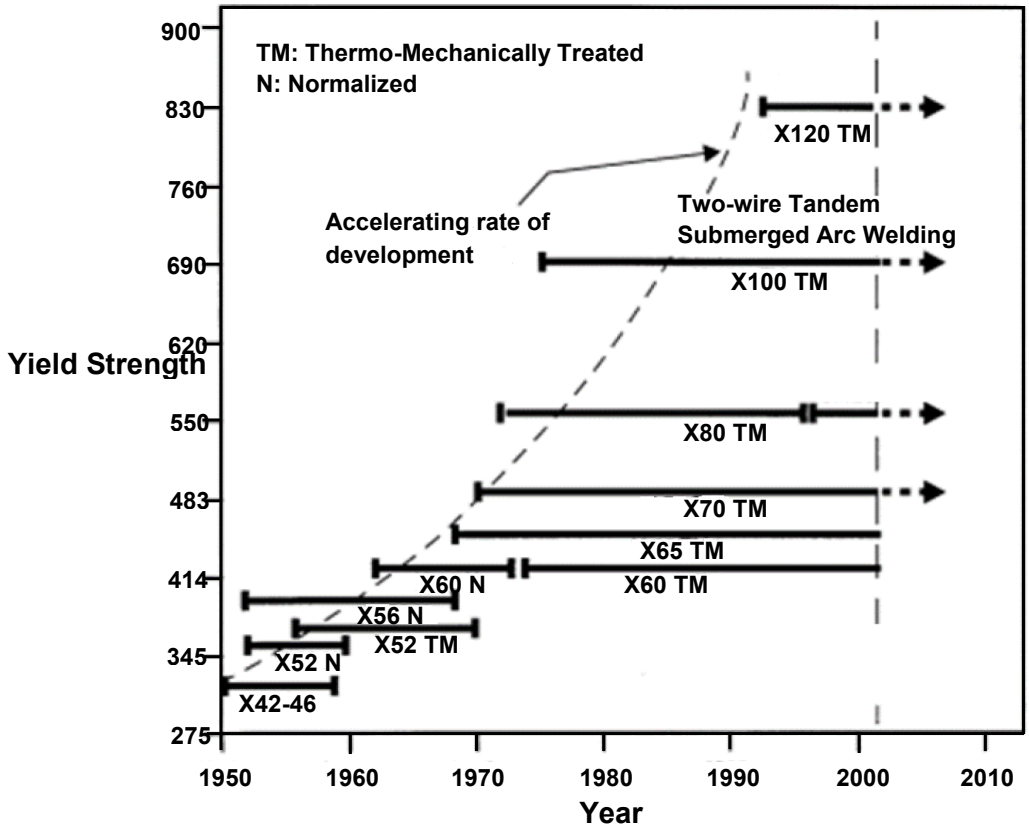

Figure 2-4 Required yield strength of pipelines during their years of development.

Ferrite-pearlite steels are considered as the first generation of pipeline steels manufactured by hot rolling and normalized conditions. As stated earlier, API 5L X52 steel is comprised of ferrite and pearlite. Gladman and Pickering [50,51] have reported that the strength and ductile to brittle transition temperature of the steel increase as the pearlite volume fraction increases. Moreover, due to the relatively high carbon content of 0.12-0.2 wt.%, the steel has poor weldability. To improve the properties, the fundamental approach was to reduce the level of carbon and, consequently, minimize the fraction of pearlite and to add some alloying elements, to provide grain refinement and precipitation hardening. In addition to alloying elements, TMCP can improve the toughness of the steel. Acicular ferrite microalloyed steels were the next generation of pipeline steels. Intragranular nucleation of the ferrite phase, with non-equiaxed characteristics, occurred on non-metallic inclusions. The term was initially introduced by Smith et al. [52] in the 1970s. Acicular ferrite is also known as bainitic ferrite [53,54]. Due to the fine grain structure and high angle grain boundaries, acicular ferrite steels offer a good combination of strength and toughness. In addition, a uniform distribution of fine precipitates and a high density dislocations provide more benefits to the mechanical properties of the acicular ferrite microalloyed steels. To develop higher grades of

high strength microalloyed steels, it was believed that an alternative microstructure of shear transformation products was necessary to achieve high strength and toughness. Accordingly, martensite-bainite microstructure containing lath martensite and lower bainite, with high dislocation densities were developed to obtain both strength and toughness. Two examples of these types of steels are X100 and X120 microalloyed steels with minimum yield strengths of 690 and 820 MPa, respectively. To achieve the desired microstructure, a microalloying design including low amounts of boron (B) was developed as B suppresses the transformation of ferrite and promotes lower bainite transformation [55].

2.1.2. Influence of alloying elements

Generally speaking, the alloying elements can be classified into three main categories: i. ferrite stabilizers, ii. austenite stabilizers and iii. carbide formers. Ferrite stabilizers are essentially those elements which enlarge the ferrite phase field, such as molybdenum (Mo), aluminum (Al), silicon (Si), chromium (Cr), niobium (Nb), titanium (Ti) and vanadium (V). Austenite stabilizers are, in contrast, the alloying elements that enlarge the austenite phase field; e.g., carbon, nitrogen (N), nickel (Ni), copper (Cu) and manganese (Mn). Carbide formers such as Ti, Nb, V, Cr and Mo form stable carbides [56].

2.1.2.1. Carbon

Steel is generally considered to be an alloy of iron (Fe) and carbon. However, in modern steels, there are a number of other alloying elements, in addition to carbon, to improve the steel properties. Accordingly, carbon is the most common and important alloying element in steel. A small addition of carbon in pure iron can increase the strength from 28 MPa to ~190 MPa. Carbon occupies the interstitial sites in the BCC and FCC crystal structures of iron. However, carbon has limited solubility in BCC iron (maximum 0.02 wt.%). Excessive carbon in steel will form iron carbide, cementite (Fe_3C), rather than remain in solid-solution. Carbon in low alloy steels, containing V, Nb and Ti, forms carbides which contribute to precipitation strengthening in the steel. With respect to weldability, it is essential to keep the carbon level in steel as low as possible to reduce the hardenability.

2.1.2.2. Niobium (Nb)

Niobium, formerly known as columbium (Cb), is a key element in the development of microalloyed steels. It plays a significant role in grain refinement and precipitation strengthening of steel. Nb is a strong carbide former, which improves strength, hardness, ductility, wear and corrosion resistance of steel. At elevated temperatures, Nb is dissolved in austenite in solid solution. During cooling, Nb

can partially precipitate in austenite in the form of carbides, nitrides and carbonitrides. Accordingly, Nb atoms slow down the kinetics of the austenite to ferrite transformation and retard the austenite recrystallization during hot rolling. After rolling, the remaining Nb in solution forms carbonitrides in ferrite, which overall contribute to precipitation strengthening of steel. However, high Nb contents have been reported to reduce the volume fraction of acicular ferrite in the weld during welding, resulting in lower weld metal toughness [57].

2.1.2.3. Titanium (Ti)

Titanium is known as a deoxidizer in both steelmaking and welding. Ti reacts with oxygen during welding to form inclusions, which promote nucleation of acicular ferrite in the weld [58]. However, similar to Nb, the major effect of Ti in microalloyed steels is in forming carbide, nitride and carbonitride precipitates. In addition to precipitation strengthening, these precipitates suppress grain boundary movement in austenite resulting in grain refinement strengthening. The work done by Evans [59] has indicated that Ti enhances the formation of acicular ferrite in the weld metal.

2.1.2.4. Vanadium (V)

Vanadium is widely used in high strength low alloy steels. It has relatively higher solubility in austenite compared with Nb and Ti. V contributes to precipitation strengthening and grain refinement strengthening due to the formation of vanadium carbides (VC) and vanadium nitrides (VN). Similar to Ti and Nb, V delays austenite recrystallization and affects the austenite to ferrite transformation temperature [60]. However, the solubility of its carbonitrides is much larger and the solubility of its nitrides and carbides are lower (nitride solubility is two orders of magnitude smaller than the carbide), which is contrary to Nb but similar to Ti [61]. The relatively high solubility of V(C,N) and the much lower solubility of VC and VN have led to V being a prime choice for strong and controllable precipitation strengthening. Nitrogen is an essential alloying element in V-microalloyed steels as it strongly determines the level of the V(C,N) precipitation and thereby the degree of precipitation strengthening. In addition, due to the higher solubility of nitrogen in ferrite than carbon, the total content of nitrogen is normally dissolved in ferrite before precipitation of V(C,N), while only a fraction of carbon is dissolved in ferrite. Accordingly, a controlled addition of nitrogen in V-microalloyed steels can facilitate V(C,N) precipitation hardening [61].

2.1.2.5. Nitrogen (N)

Similar to carbon, nitrogen is as an essential alloying element in the fabrication of microalloyed steels, as it contributes to precipitation and grain refinement strengthening by forming nitride and carbonitrides with Nb, Ti and V. Although nitrogen is an essential element in V-microalloyed steels,

it is detrimental to Nb as Nb(C,N) precipitates are less soluble and have a tendency to precipitate in austenite. As such, N has a lower strengthening effect in ferrite [62]. It has been reported that free nitrogen and nitride precipitates have a detrimental effect on the HAZ toughness; however, there is some research where high toughness in the HAZ was achieved even at high nitrogen content by selective choice of welding parameters [61]. Moreover, it has been shown that even when a reduction in the HAZ toughness is observed at high nitrogen levels and high heat input, it cannot be solely accounted for by the solute nitrogen but rather by changes in the HAZ microstructure and the amount of other alloying elements in the steel.

2.1.2.6. Manganese (Mn)

After carbon, manganese may be the second most important alloying element in steel. It is an essential element for hot rolled steels and combines with oxygen and sulfur. The hardenability and strength of steel is increased, whereas ductility decreases by Mn addition. As such, the weldability of steel is reduced. From a welding point of view, the Mn to S ratio has to be at least 10. A low amount of Mn (less than 0.3 wt.%) may result in internal porosity and cracking in the weld metal; however, too high a Mn content (>0.8 wt.%) may also promote cracking. Steels containing a low Mn to S ratio may form FeS, which is brittle with a low melting point. As such, “hot shortness”, the brittleness at high temperature caused by sulfur, happens. Since Mn is an austenite stabilizer, it reduces the austenite to ferrite transformation temperature, resulting in finer ferrite grains [63]. Although Mn has a moderate solid solution strengthening effect on steel, it improves strength by grain refinement. Ricks et al. [64] and Farrar et al. [65] have reported that the addition of Mn in steel increases the nucleation of acicular ferrite by retarding the growth of grain boundary ferrite. In addition to acicular ferrite formation, grain refinement with increasing Mn levels from 0.6 to 1.8 wt.% has been reported to improve the steel toughness [66].

2.1.2.7. Molybdenum (Mo)

Molybdenum is a ferrite stabilizer and a strong carbide former and is usually present in alloy steels in amounts less than 1 wt.%. Mo significantly increases the hardenability of steel by promoting the formation of low temperature transformation products, such as acicular ferrite, bainite and M-A constitudents. As such, the weldability of the steel is lowered; however, elevated temperature strength, corrosion resistance and creep resistance of steel are increased. In microalloyed steels, Mo addition results in strengthening of steel by increasing the volume fraction of acicular ferrite and M-A constituents, refining the grain structure and precipitation strengthening [67,68]. Lee et al. [69] studied the effect of Mo on the precipitation hardening of HSLA steels. In addition to precipitate hardening, Uemori et al. [70] suggested that Mo addition in microalloyed steels

containing Nb and Ti has a two-fold effect. All Mo atoms are in solution in the ferrite matrix, which results in solid solution strengthening. In addition, Mo atoms strongly segregate to the interface between Nb(C,N) and the ferrite matrix. This suppresses the diffusion of Nb atoms into Nb(C,N) from the ferrite matrix, resulting in the formation of fine precipitates in Ti-Nb-Mo steel [70,71]. Mo atoms partially replace some of the Nb atoms, forming Nb(Mo)C.

2.1.2.8. Nickel (Ni)

Since nickel is an austenite stabilizer, similar to Mn, it reduces the transformation temperature of austenite to ferrite, which hinders formation of granular bainite and promotes acicular ferrite formation. Accordingly, it improves the toughness of steel. The addition of Ni up to 3.5 wt.% into the weld metal has been reported to improve the weld toughness by forming acicular ferrite [72]. Ni has a solid solution strengthening effect on the steel and is not a carbide former [73].

2.1.2.9. Silicon (Si)

Silicon has a similar effect to Ni in terms of promoting acicular ferrite formation. It has been reported [59] that a high level of silicon up to 0.94 wt.% resulted in increasing acicular ferrite fraction in the microstructure. However, the effect of Si on the weld properties is not well understood. Farrar et al. [65] have reported that Si content beyond 0.5 wt.% results in a detrimental effect on weld toughness, whereas the work done by Crockett et al. [74] showed that addition of Si up to 0.8 wt.% did not cause any significant effect on the weld microstructure and toughness.

2.1.2.10. Chromium (Cr)

Although chromium is a ferrite stabilizer, it reduces the kinetics of the austenite to ferrite transformation. Cr is present in all stainless steel in solid solution. The addition of Cr increases the hardenability, but it reduces the weldability of steel. In low Mn steels, the addition of Cr in the weld during welding results in a refined microstructure; however, it has been reported [75,76] that increasing the Cr content in high strength low alloy steels results in detrimental effect on the weld properties. As stated earlier, Cr is a carbide former; as such it is found mostly in tool steels to increase the wear resistance [73].

As stated earlier, alloying element additions in microalloyed steels not only influence precipitation strengthening, but also affect the kinetics of phase transformations (austenite decomposition). In addition, precipitates pin austenite grain boundaries, which consequently reduces the austenite grain growth rate. A reduction in the carbon content results in a reduction in the martensite start temperature. As such, the volume fraction and size of the M-A constituent

decrease and its shape is refined in a microalloyed steel and its HAZ, which leads to improvement in the fracture toughness. However, it is essential to compensate the reduction in carbon content by alloying elements to obtain desirable microstructures and mechanical properties [58,77]. Figure 2-5a depicts the effect of alloying elements on the continuous cooling transformation (CCT) diagram of a typical steel. Moreover, the influence of prior austenite grain (PAG) size is also shown. As the PAG size decreases, the martensite start temperature decreases, resulting in improvement in toughness due to refinement of the M-A constituent. The reason the martensite start temperature decreases as the PAG size decreases is still unclear; however, it may be related to the increase in the number of ferrite nucleation sites with smaller PAG size (more austenite grain boundaries) which would suppress martensite formation. In addition to alloying elements and the PAG size, the heat input of welding plays a significant role on the final microstructure of the weld and HAZ (Figure 2-5b). As the heat input increases, the cooling rate decreases which results in the formation of high temperature transformation products, such as polygonal ferrite and pearlite.

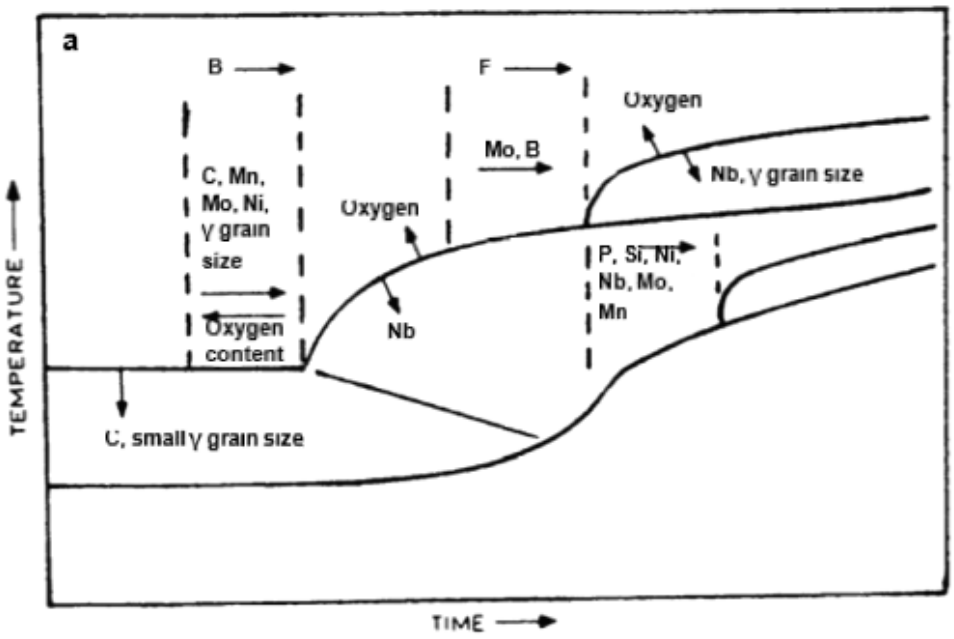

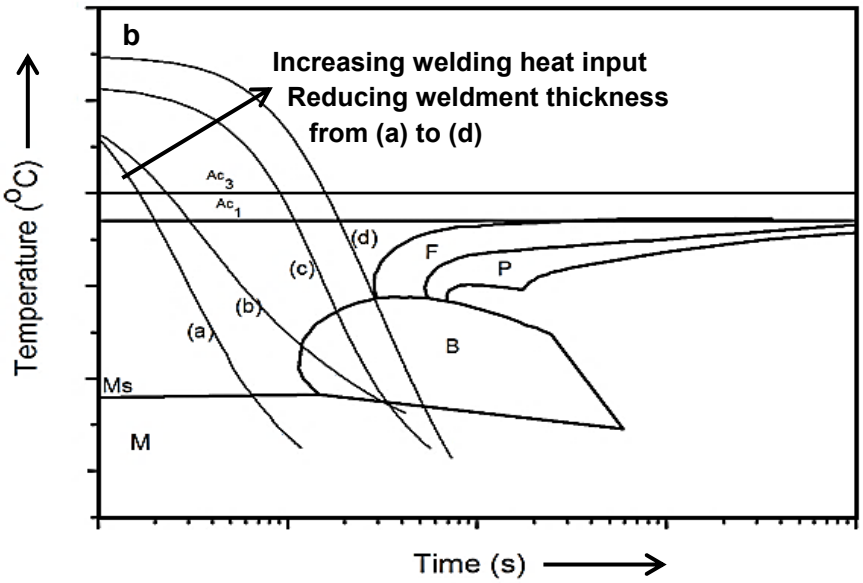

Figure 2-5 Effect of (a) alloying elements and PAG size and (b) welding heat input and weldment thickness on the CCT diagram of a typical steel [317].

2.1.3. Microalloyed steel weldability

Weldability literally means the ability of a material to be welded. The HAZ, the region adjacent to the fusion line, heats up above the A_3 temperature during welding, which results in austenite formation. During cooling, austenite in the HAZ transforms into new microstructural constituents, which are basically dependent on the peak temperature and cooling rate. If martensite becomes the dominant product of the austenite transformation, the HAZ becomes brittle and susceptible to crack initiation and propagation. "Weldability of a material is a measure of its resistance to cracking during and after welding and in service performance, i.e., adequate strength and resistance against brittle and ductile fracture propagation" [78]. If it is easy to avoid cracking, the material is deemed weldable [79].

The carbon equivalent carbon (CE) value as a function of carbon and other alloying elements was initially proposed by Easterling [80]. It determines how much the steel is susceptible to the formation of low-temperature transformation products, i.e., its hardenability, during welding. The CE value is directly related to hydrogen-induced cold cracking, which is a common weld defect [77]. A high concentration of carbon and other alloying elements, such as Mo, Cr, Mn, Si and V, increase the hardenability of the steel and consequently decrease the weldability [29,77]. Due to low carbon contents and small amounts of other alloying elements (maximum of 3-4 wt.%), high strength microalloyed steels generally possess good weldability. According to Easterling [80], the welding

crack susceptibility of steels is usually expressed in terms of a carbon equivalent that shows composition allowances to avoid cold cracking or hydrogen cracking. There are a number of different equations proposed to calculate CE. However, for low-carbon microalloyed steels, the welding crack susceptibility index, P_{cm}, is calculated according to the Ito-Bessyo equation [81].

$$\boldsymbol{P_{cm}} = \%C + \frac{\%Si}{30} + \frac{\%Mn + \%Cu + \%Cr}{20} + \frac{\%Mo}{15} + \frac{\%V}{10} + \frac{\%Ni}{60} + 5\%B \qquad [2.1]$$

where P_{cm} is in wt.% and is ~0.175 wt.% for X70 microalloyed steel.

2.2. Pipeline Manufacturing

Except for seamless pipe manufacturing, after production steel plates are essentially welded and joined to manufacture a pipe. Welding processes are categorized into two main groups, fusion welding and pressure welding. In fusion welding, binding between two sections is made by melting part of both pieces. The welding processes used in pipeline industries generally fall under the fusion welding category. Submerged arc welding (SAW) is commonly used to produce pipes by either spiral welding or UOE techniques.

The UOE technique essentially includes four steps (Figure 2-6a). Firstly, the plate edges are crimped together, followed by forming of the plate into a U-shape in the "U-press". The third step is pressing into a circular shape in the "O-press" and finally the steel is mechanically expanded to finalize the size to improve the circularity and welding [82–84]. To manufacture spiral-welded pipes (as used by Evraz Inc. NA), steel is rolled into sheets with prepared edges that are formed into a spiral shape, which is then welded to produce an individual pipe (Figure 2-6b).

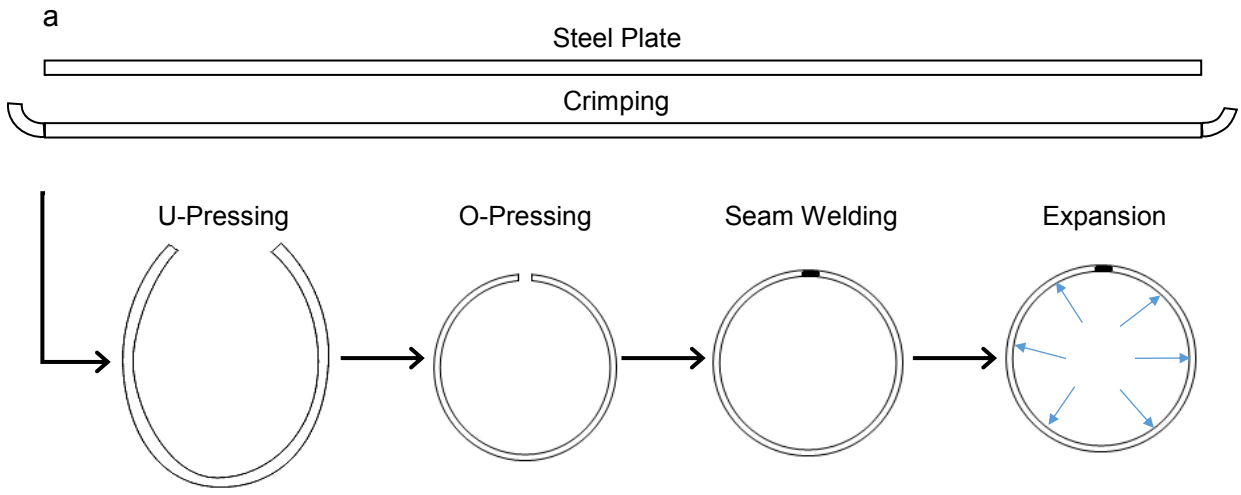

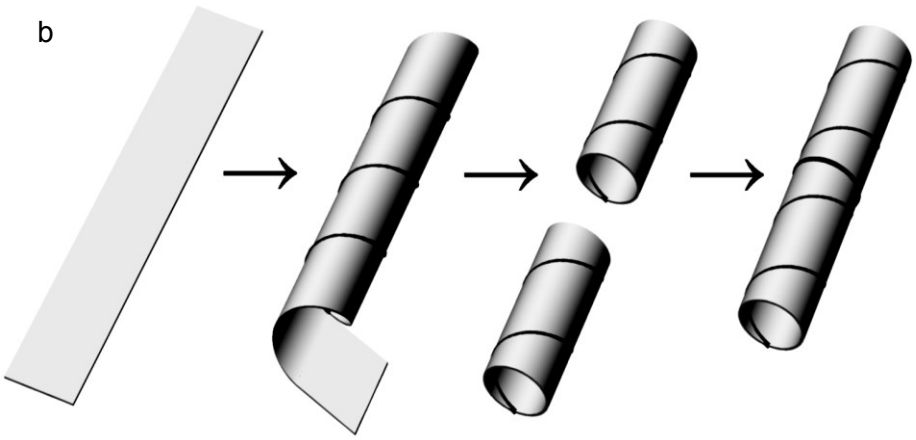

Figure 2-6 Schematic diagrams of (a) UOE and (b) spiral-welded pipeline manufacturing steps [30].

2.3. Welding Process

To manufacture a microalloyed steel pipe, the steel plates can be joined using any of the common arc welding processes [29,42]. The most common welding processes employed by manufacturers are gas metal arc welding (GMAW), gas tungsten arc welding (GTAW), self-shielded flux cored arc welding (SS-FCAW), shielded metal arc welding (SMAW), electric resistance welding (ERW) and submerged arc welding (SAW). However, SAW has been widely used for pipeline manufacturing due to its inherent properties, e.g., high deposition rate, deep penetration and capability of welding thick sections. Spiral welding is typically performed via SAW or tandem SAW (TSAW) or SAW with more than one electrode, with one pass initially from the inside followed by one pass from the outside [85]. When two short pipe lengths are girth-welded at the mill, a "double jointer" weld is performed using the SAW process. This is done either by using multi-passes around the outer-diameter (OD), or by using a single pass from the inner-diameter (ID) and one from the OD (similar to the process used for the spiral weld). The GMAW process with relatively low heat input is used for the girth welds performed in the field (during pipeline assembly) using multi-passes around the OD [85]. According to the AWS welding handbook [86], a brief introduction to the common arc welding processes is presented below.

2.3.1. Gas metal arc welding (GMAW)

Gas metal arc welding (GMAW) is a welding process in which an arc is generated between the workpiece and a continuously consumed metal electrode. An inert and/or slightly oxidizing gas (e.g., argon and CO_2, respectively) are usually used to shield the arc from the atmosphere. An arc is

generated by applying current passed through the shielding gas, leading to the simultaneous melting of the electrode and base metal. A typical GMAW set up is shown in Figure 2-7.

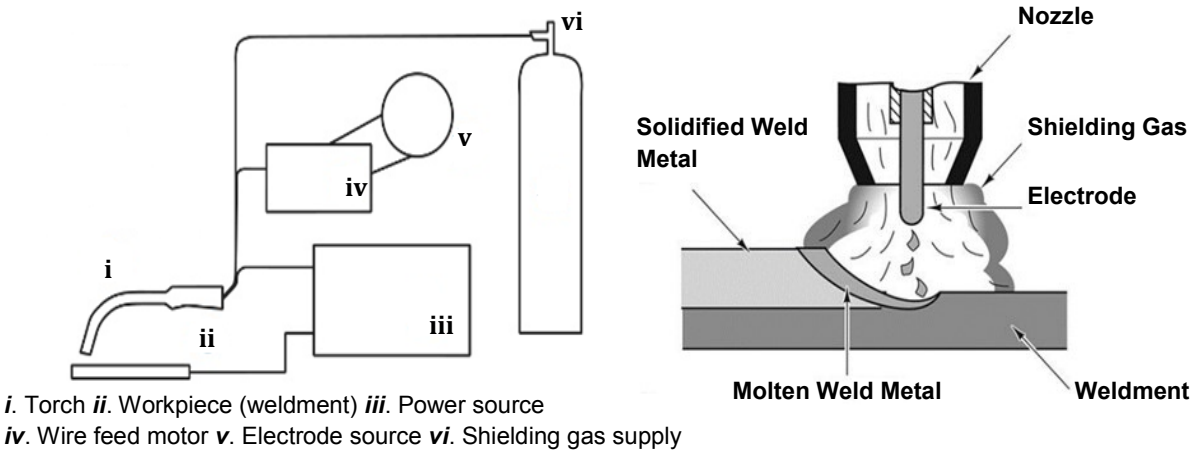

Figure 2-7 Schematic view indicating (a) setup of GMAW process and (b) arc configuration [86,203].

The GMAW process has a number of advantages over other welding processes. This is the only process that can be used to weld all commercial metals. The process also enables a large degree of automation, which helps to ensure a high level of quality control. However, there are still some limitations associated with the process. Due to the size and cost of the equipment required, it is not feasible for all welding jobs. Also, care must be taken to ensure that the shielding is protected from drafts.

2.3.2. Gas tungsten arc welding (GTAW)

Unlike GMAW, gas tungsten arc welding (GTAW) uses a nonconsumable tungsten electrode to create an arc between a torch and the base material (weldment). Similar to GMAW, an inert or reducing shielding gas is passed through the torch to shield the arc, electrode and weldment against atmosphere contamination. When a sufficient size of weld pool is created, the arc is moved along the joint. The welding setup is similar to that of the GMAW, other than for GTAW a filler metal wire is fed into the arc for joining. There is precise control over the welding variables and independent control over the heat source and filler metal additions. Direct current electrode positive (DCEP) is the most common polarity as it allows for deep penetration and fast welding speeds. Direct current electrode negative (DCEN) polarity is not commonly used as it leads to overheating of the electrode. The use of alternating current (AC) is generally restricted to aluminum and magnesium as it provides a cathode cleaning effect that removes oxides from the surface.

2.3.3. Shielded metal arc welding (SMAW)

Shielded metal arc welding (SMAW) is the most commonly used welding process, in which an arc is struck between the electrode and the workpiece by bringing the electrode in close enough proximity to overcome the potential threshold. The heat of the generated arc is used to simultaneously melt both the base material and the tip of the electrode. A simple electrical circuit is created via an electrical connection between a power source, weldment and an electrode. SMAW is typically performed using a constant current power source in either direct current (DC) or AC polarity. Enough current needs to be provided to melt the electrode and an appropriate amount of weldment. Accordingly, a typical welding current ranges from 50 to 550 amps. The gap between the electrode and the weldment, which is controlled manually by the welder, determines the circuit voltage.

2.3.4. Self-shielded flux cored arc welding (SS-FCAW)

Self-shielded flux cored arc welding (SS-FCAW) is a process in which a continuous consumable electrode is fed through the welding gun into the weld joint. The SS-FCAW process differs from GMAW as it does not require an external shielding gas, such as CO_2 or argon, in order to protect the weld pool from atmospheric contamination. As shown in Figure 2-8, a flux compound contained within the hollow wire reacts with the welding arc to form a gas that protects the weld pool. In semi-automatic welding, the electrode is fed by a wire feeder and the power source maintains the arc length. The welding gun and the parameters are manipulated by the welder. Flux cored arc welding is also used in machine welding where, in addition to feeding the wire and maintaining the arc length, the machinery also provides travel of the joint. The welding operator continuously monitors the welding and makes adjustments in the welding parameters. Automatic welding is used in high production applications. Some SS-FCAW processes are used with DCEP while others are developed for use with DCEN. Electrode positive current gives better penetration into the weld joint, whereas electrode negative current gives lighter penetration. Accordingly, DCEN polarity is usually used for welding thinner metals or metals where there is poor fit-up. The weld created by DCEN is wider and shallower than the weld produced by DCEP.

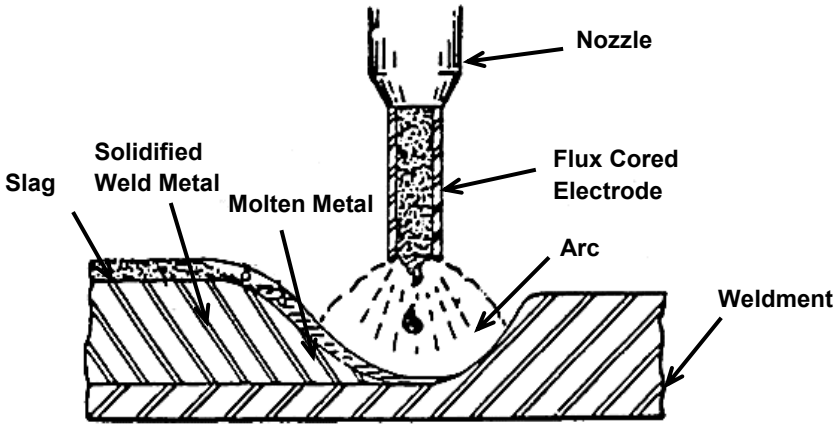

Figure 2-8 Schematic view of SS-FCAW process [86].

2.3.5. Electric resistance welding (ERW)

Electric resistance welding refers to a specific type of welding process which is associated with both spot and seam welding. There are generally two different types of ERW: i. Rotary contact wheel ERW (RC-ERW) and ii. High frequency ERW (HF-ERW). RC-ERW, known as low frequency ERW, is the common type of the ERW process in which the current is transferred through a contact wheel at the point where joining is taking place (Figure 2-9). Moreover, the contact wheel provides some forge pressure needed for the ERW process. Although the current could be any type of alternating current (AC), direct current (DC) or square wave alternating current (ACSQ), AC with frequencies from 50 to 400 Hz is usually used. A greater variety of shapes and sizes can now be produced by ERW than what was possible in the past. RC-ERW has the capability of fabricating sections in round, square, rectangular and hexagonal shapes.

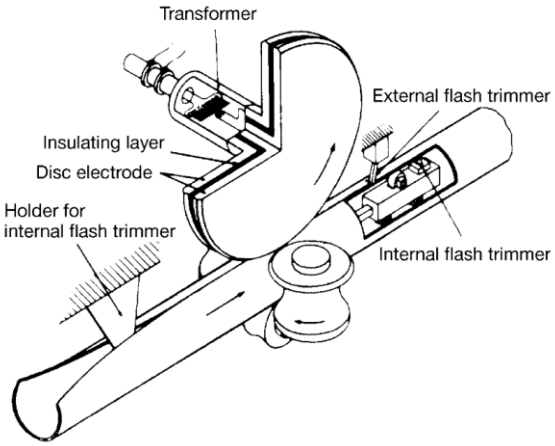

Figure 2-9 Schematic setup of RC-ERW [87].

HF-ERW, is basically categorized into two classes, i.e., contact HF-ERW and induction HF-ERW. In both classes, the equipment that generates the forging force is independent from the equipment that supplies the electrical current. As shown in Figure 2-10a, the current in contact HF-ERW is transmitted to the weldment through a contact that rides on the strip. Since the power is directly transferred to the pipe, this is more electrically efficient than induction HF-ERW and, therefore, more suited to produce heavy-wall and large diameter pipes. In contrast to contact HF-ERW, current in induction HF-ERW is induced to the weldment through a coil in front of the weld point (Figure 2-10b). No contact between coil and the workpiece is made and the material is melted by the heat generated by the magnetic fields surrounding the pipe. Although the electrical efficiency of induction HF-ERW is less than that for contact HF-ERW, it has less challenges in processing as contact setups are eliminated and fast changes between pipes can be done during manufacturing.

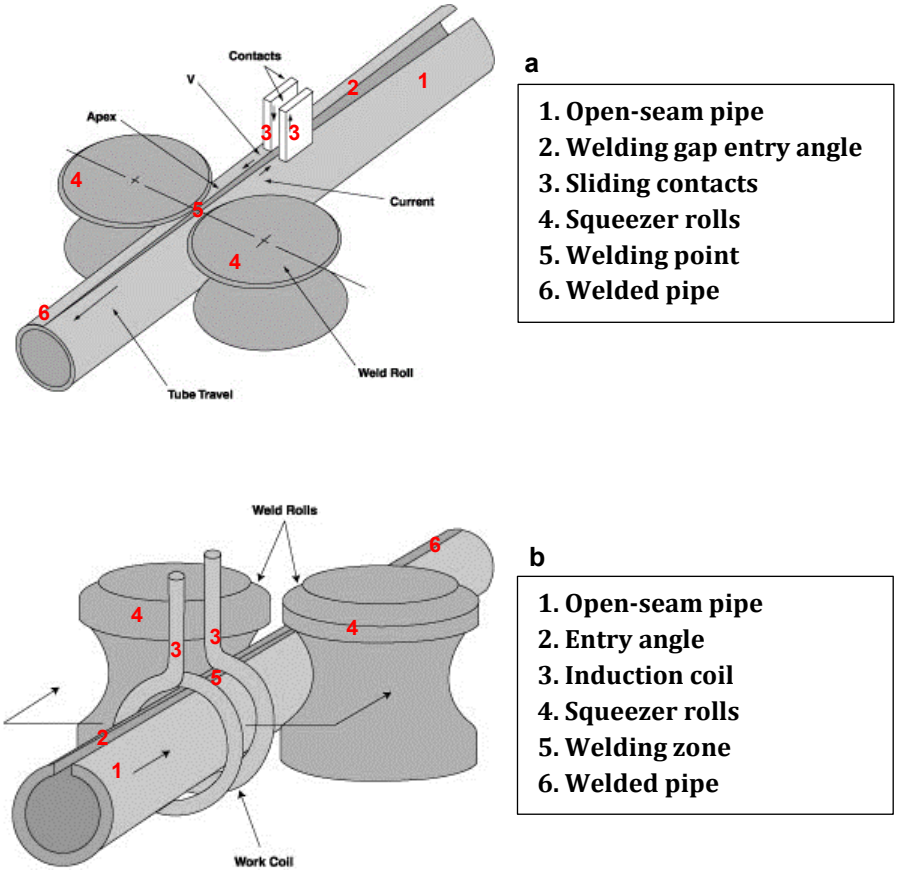

Figure 2-10 Schematic setup for (a) contact HF-ERW and (b) induction HF-ERW processes [318].

2.3.6. Submerged arc welding (SAW)

Submerged arc welding (SAW) is principally similar to GMAW, in which an arc is generated between a consumable electrode and weldment. However, as depicted in Figure 2-11, in contrast to the GMAW, a solid granular flux is used to shield the arc and weld pool from atmospheric contamination. Large diameter wires with high current are typically used in the process, which results in a fast continuous welding process. High deposition rates, deep penetration and the capability of welding thick sections have made the SAW process an appropriate candidate for pipeline manufacturing [88]. It is believed that, regardless of the welding process, electrode(s) current, voltage, polarity, welding travel speed, electrode(s) diameter and electrode stick-out significantly influence the electrode and flux melting rate, the final weld and HAZ geometry and properties. The work done by Chandel et al. [89] and Kiran et al. [90] has indicated that the melting rate of the electrode and flux increases by increasing the welding current. Moreover, the electrode melting rate is the highest in DCEN, followed by AC and DCEP for a given welding current. However, the flux melting rate is the highest in AC polarity followed by DCEN and DCEP at higher levels of welding current. The authors argued that the greater electrode tip surface temperature resulted in larger droplets followed by higher melting rates of electrode and flux in DCEN in comparison to DCEP. A decrease in arc voltage resulted in an increase in the electrode melting rate and decrease in the flux melting rate. The arc length was reduced by decreasing arc voltage and, as such, the electrode stick-out was increased causing an increase in electrode resistive heating, resulting in greater rate of electrode melting.

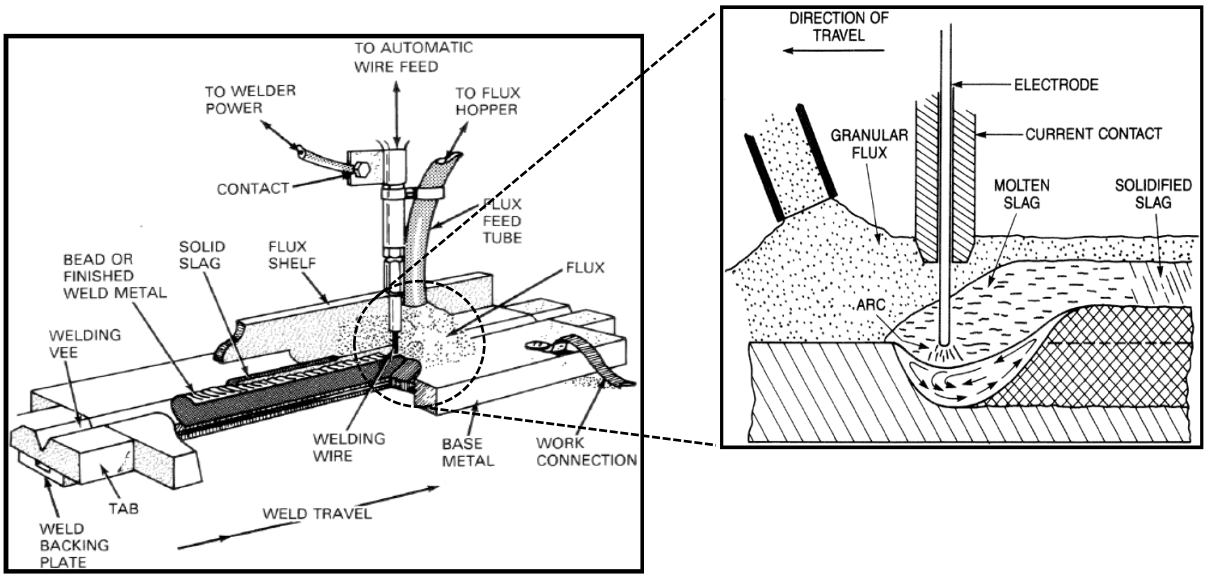

Figure 2-11 Schematic view of SAW process setup [86,93].

Renwick et al. [91] reported that the weld penetration depth and reinforcement height increased with an increase in electrode current and decrease in electrode diameter. Murugan et al. [16] evaluated the effect of electrode stick-out, voltage, travel speed and wire feed speed on the weld geometry of 20 mm thick IS 2062 steel plate welded by SAW. The bead width, penetration depth and reinforcement height were inversely dependent on the welding speed. Also, an increase in welding voltage resulted in a decrease in the reinforcement height and an increase in the bead width, whereas no effect was observed on the weld penetration. A detailed study on the influence of the welding variables on the weld and HAZ properties and geometry is discussed in Chapter 3.

Table 2-2 indicates an overview of the main generic welding processes. Accordingly, the main welding processes used for pipe production are HF-ERW, GMAW and SAW. The latter is widely used for pipeline manufacturing.

Table 2-2 Typical welded pipe manufacturing processes [87]

Welding Process	**Nomenclature**	**Weld Type**	**Pipe Size (OD)**
Hot Pressure Welding	Fretz-Moon	Longitudinal	13-114 mm
ERW	DC	Longitudinal	10-20 (30) mm
	Low-frequency		10-114 mm
	High-frequency		20-600 mm
Arc Welding (Fusion Welding)	SAW	Spiral, UOE	168-2500 mm
	GMAW	Spiral/longitudinal	406-2032 mm
	GTAW	Longitudinal	30-500 mm

2.3.6.1. SAW consumables

As stated earlier, in SAW the electrical current is conducted by the electrode which supplies the materials required to fill the workpiece and fuse the weld joint. The electrode is usually coated with copper for a higher electrical conductivity and corrosion resistance [92,93]. To weld a typical X70 microalloyed steel, electrodes containing low carbon content of ~0.10 wt.% and low levels of residual and impurity elements, especially N, S and P, are used.

The solid granular flux used to shield the arc and weld joint from atmospheric contamination is believed to play a significant role in achieving a good quality weld. The flux usually contains oxide and fluoride refractories to withstand high temperature welding without significant melting. The basicity index has been used to characterize the type of the flux, which is a measure of the ability of oxygen to transfer to the weld during welding. According to Tuliani et al. [66], the basicity index is defined as follows with the compositions in wt.%:

$$\textbf{\textit{Basicity Index}} = \frac{\%CaO + \%CaF + \%MgO + \%K_2O + \%Na_2O + 0.5(\%MnO + \%FeO)}{\%SiO_2 + 0.5(\%Al_2O_3 + \%TiO_2 + \%ZrO_2)} \quad [2.2]$$

The basicity index is classified as follows: basic >2.5, semi-basic = 1.5-2.5, neutral = 1-1.5 and acidic <1. Since the amount of oxygen plays a significant role in formation of inclusions in the weld metal and the formation of inclusions increases the nucleation of acicular ferrite, flux basicity is of fundamental importance to the final microstructure in the weld metal. The weld metal oxygen content decreases as the flux basicity increases. However, high basicity flux produces a clean weld metal with regard to oxide inclusions.

2.3.6.2. SAW productivity

To increase the productivity of welding, a SAW process associated with more than one electrode and up to five electrodes (TSAW) has been developed to increase the speed of welding. TSAW uses separate large-diameter electrodes, power sources and wire feeders. The arcs are shielded by a blanket of granular flux on the workpiece. However, in today's manufacturing reality, six common approaches have been considered by related industries to improve the productivity of the SAW process. Figure 2-12 compares different SAW processes according to their welding duration to make a weld sample (productivity).

i. Metal-cored wire was introduced in 1957 for gas metal arc welding (GMAW) to increase the productivity of the welding process. The welding equipment typically does not need any modification when compared with the solid-wire equipment setup. The outer metallic sheath of a cored wire conducts the electrical current for welding, which leads to a higher current density and improved deposition rate [6].

ii. Increased stick-out welding operates on the principle that an increased amount of welding current will be used to preheat the welding wire due to an increase in electrical resistance created by using a long stick-out. The rate of preheating behaves according to the $R.I^2$ relationship, where I and R are the welding current and the resistance of the wire from the contact point to the arc, respectively. The benefit achieved by taking advantage of this electrical behavior is an increase in wire feed speed for a given current level, which translates to higher deposition rates [94].

iii. Twin-wire SAW provides increased deposition rates by feeding two electrodes into the same weld pool. Two electrodes are fed to the weldment with the same current, voltage,

polarity and feed speed by a single wire feeder. Although twin-wire SAW provides high productivity, it is not possible to profit from the advantages of welding with different variations in current, voltage and polarity for both electrodes [95].

iv. Tandem SAW operates with multiple independent arcs oriented in-line with the direction of travel. The advantage of TSAW over twin-wire SAW is the ability to control all the arcs independently. Each arc can operate under different welding conditions and even different polarity [24].

v. The application of electrodes with different polarity in the TSAW process has been developed based on providing a deep enough penetration depth by the lead electrode and increased deposition rate by the trail electrode(s). TSAW is considered as the leading welding technology to increase the productivity of pipeline production [11].

vi. Hot-wire SAW was initially developed by Tsuyama et al. [96] with the intent of increasing the deposition rate. The process involves a single wire with high current and voltage to fulfill the required bead width and penetration depth along with an electrically heated wire (hot wire) positioned at the rear part of the weld pool. Although this method results in an increase in the deposition rate, the welding heat input increases, depending on the current and voltage used for the hot wire.

vii. SAW with additional cold wire has recently been developed to increase the productivity of the conventional SAW process by adding a cold wire to the weld pool. The addition of a cold wire to the one electrode SAW process was initially proposed by Mruczek et al. in 2005 [17]. Different techniques used to increase the productivity of SAW are indicated in Figure 2-13.

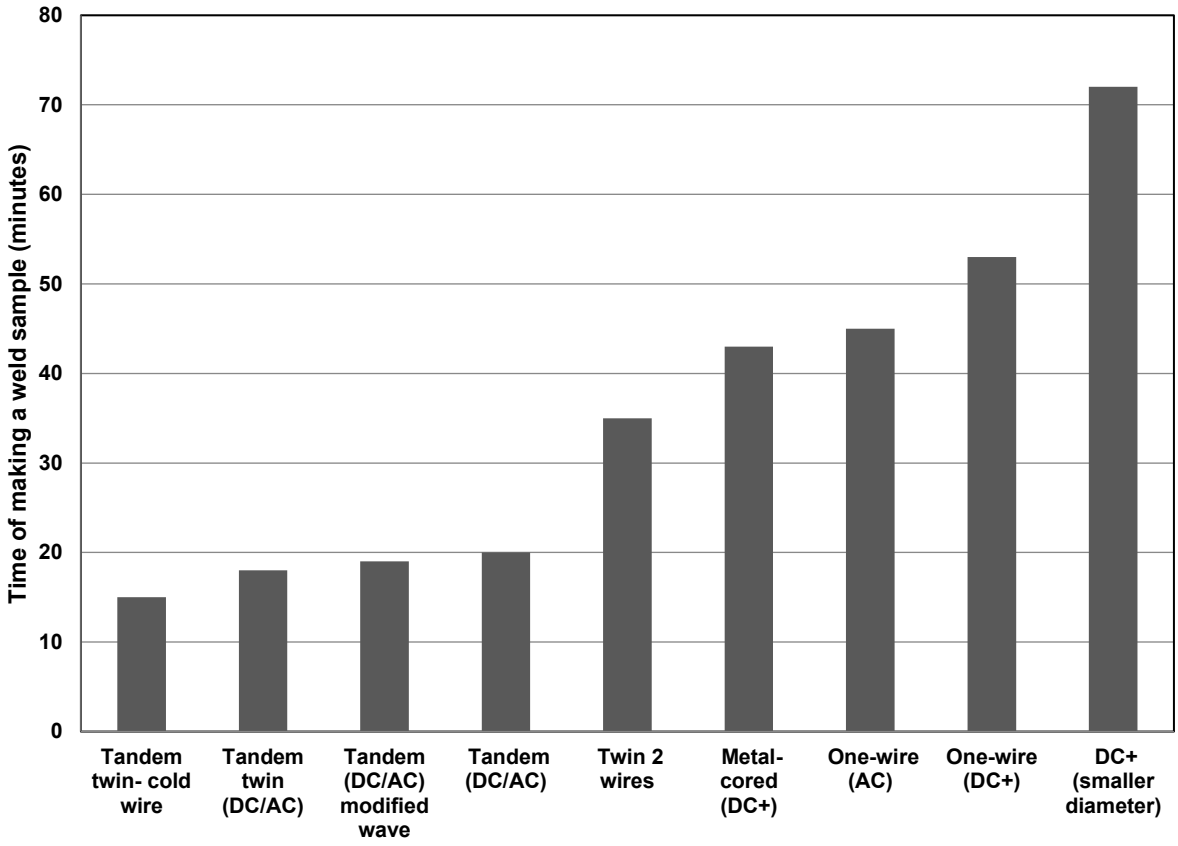

Figure 2-12 Welding time for different types of submerged arc welding process [10].

In the two-wire TSAW process, the lead arc is essentially used to provide deep penetration, whereas the trail electrode is employed to increase the deposition rate and fill the weld joint. Accordingly, the lead and trail electrodes are typically fed into the molten pool with DCEP and AC, respectively. It is worth noting that the most important aspect of the AC trail arc is that it does not cause significant interference with the lead arc. It would not be practical to run two DC arcs in close proximity to one another as the electrodes would deflect each other and cause highly unstable arcs.

Increasing the number of electrodes in TSAW introduces a higher heat input to the pipe resulting in a larger weld pool in all three dimensions. The length of the weld pool has been a main concern for TSAW of pipes by spiral welding; therefore, there is a restriction to the number of electrodes used in TSAW for spiral-welded pipes. The recent research work on three-electrode TSAW done in the Advanced Materials and Processing Laboratory (AMPL) at the University of Alberta confirms the formation of a long molten pool because of the high heat input introduced to the weldment [97]. Thus, it is essential to develop a welding method for pipeline production, in particular spiral-welded pipe production, to increase the productivity of welding without increasing heat input and, consequently, without a longer molten pool. In addition, regardless of the

welding technique, since any heat treatment carried out on a microalloyed steel can change the microstructure, e.g., generate grain growth, and subsequently the mechanical properties (in particular toughness and hardness), it is of particular interest to not increase the heat introduced to the weldment to increase productivity. The thermal cycle during welding of microalloyed steels is a prominent parameter affecting the microstructure and properties of the WM and HAZ of the welded microalloyed steel.

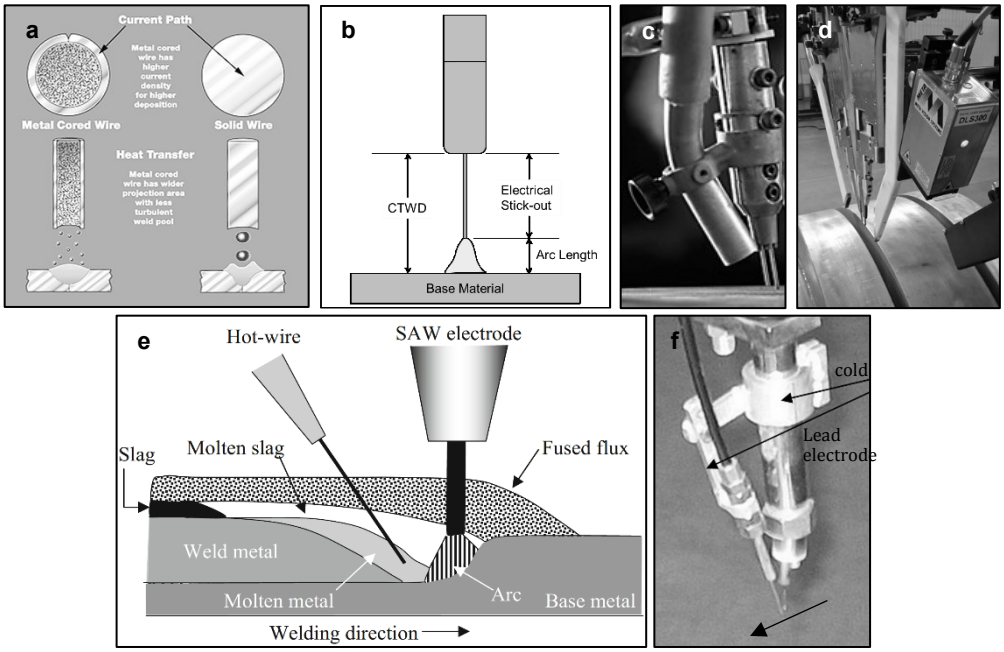

Figure 2-13 Schematics and pictures of different techniques to improve SAW productivity. (a) Metal-cored wire, (b) increased stick-out, (c) twin-wire SAW, (d) TSAW, (e) hot-wire SAW and (f) cold wire SAW.

2.4. Welding Thermal Cycle

General speaking, the heat introduced to the material of interest during welding, along with the pre-heat treatment temperature and weldment thickness, determine the thermal cycle that the material is exposed to and the final microstructure of the WM and the HAZ. The heat input is usually expressed in terms of the heat energy introduced to the material per unit length, which is calculated according to the equation defined in Chapter 3. Heat input is not only responsible for the microstructural alterations and mechanical property changes during welding, but also influences the geometry of the WM and the HAZ. Nand and Singh [98] found that increasing the welding parameters, particularly current and voltage, leads to a higher welding deposition rate, more penetration and a larger bead width; however, the HAZ toughness decreases as a result of grain coarsening due to the increased welding heat input. Moreover, high heat input results in increasing

weld dilution. There is a general agreement [99–102] that although increasing heat input increases welding productivity, fracture toughness deteriorates in the HAZ. This deterioration in the properties is attributed to higher peak temperatures and relatively slower cooling rates, which result in the formation of large prior austenite grains (PAGs) along with a higher fraction of large M-A constituents in the HAZ. The work done by Dallam et al. [103] has indicated that the weld microstructure of low heat input welding is predominantly a fine distribution of acicular ferrite, whereas, the results of the work performed by Randhawa et al. [104] showed a reduction in the properties by increasing welding heat input. The influence of welding heat input as a function of cold wire addition in the conventional TSAW process is studied in Chapter 4.

2.4.1. Rosenthal's theory

According to Rosenthal's theory, in a welding process, it is assumed that a point source (welding torch) with heat energy of q moves along the weldment with thickness of t at a velocity of ν. Figure 2-14 illustrates a schematic of the point heat source in a weld. The differential equation for the heat flow in welding is defined as follows [80]:

$$\frac{\partial^2 T}{\partial x^2}+\frac{\partial^2 T}{\partial y^2}+\frac{\partial^2 T}{\partial z^2}=\frac{\rho c}{k}\times\frac{\partial T}{\partial t} \qquad [2.3]$$

where T is the temperature distribution as a function of time (t) and position (x,y,z). ρc and k are the specific heat capacity (J m^{-3} $°C^{-1}$) and heat transfer coefficient (W m^{-2} K^{-1}), respectively. For the regions outside the weld, there are two general solutions to the Rosenthal equation for a moving point heat source, i.e., thick plate and thin plate. For the thick plate, a three-dimensional heat flow condition, the peak temperature, T_P, as a function of distance, the temperature variation during welding as a function of time at a given location, the weld time constant, $\Delta t_{8\text{-}5}$, and the cooling rate, CR, are expressed as follows:

$$T-T_0=\frac{q}{2\pi\lambda\nu t}\exp\left(-\frac{r^2}{4\alpha t}\right) \qquad [2.4]$$

$$T_p-T_0=\frac{2q}{\pi e\rho c\nu}\times\frac{1}{r^2} \qquad [2.5]$$

$$\Delta t_{8-5}=\frac{q}{2\pi\lambda\nu}\left[\frac{300}{(800-T_0)(500-T_0)}\right] \qquad [2.6]$$

$$CR=\frac{2\pi\lambda\nu}{q}(800-T_0)(500-T_0) \qquad [2.7]$$

where, T_0, λ and α are the initial temperature (25°C), thermal conductivity (41 J s^{-1} m^{-1} $°C^{-1}$) and thermal diffusivity (9.1 x 10^{-6} m^2 s^{-1}), respectively. ρc is the specific heat capacity per unit volume (4.5 x 10^6 J m^{-3} $°C^{-1}$). Another form of the Rosenthal's equations is discussed in Chapter 5. As stated earlier, the heat introduced to the weldment governs the cooling rate in the WM and the HAZ, which is responsible for the microstructure and mechanical properties.

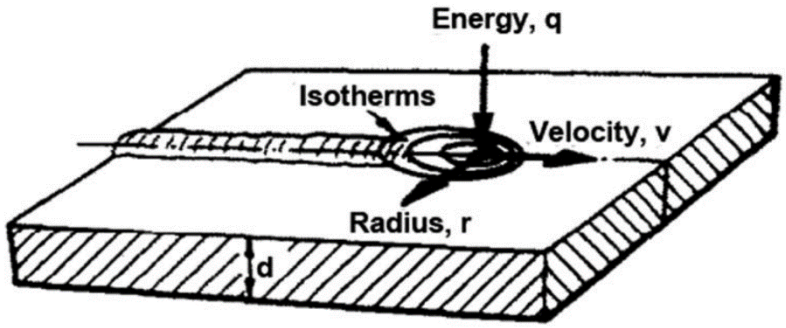

Figure 2-14 Schematic of a point heat source. Temperature profile is calculated for a point at distance r [105].

2.5. Weld Zones

During arc welding, a portion of the base metal, which is directly in contact with the arc reaches to a temperature above the melting point to provide the weld joint, known as the WM. However, the region adjacent to the fusion line, the HAZ, experiences different welding thermal cycles depending on the distance from the fusion line. As such, the microstructure and mechanical properties change relative to the original microstructure of the base metal. Due to the heat dissipation from the weld puddle, a microstructure gradient forms along the HAZ, which makes the study of the HAZ more complex. Due to the temperature gradient in the HAZ, this zone is divided into four main regions with different microstructure and properties.

2.5.1. Weld metal (WM)

As stated earlier, the weld metal is a mixture of the filler metal and base metal, which has melted during the welding process. Similar to an as-cast structure, the WM is comprised of a columnar solidification structure [106]. Easterling [80] has expressed the evolution of the columnar microstructure as epitaxial growth, since the solidifying grain is a continuation of the base metal grain at the fusion boundary. The work done by Grong et al. [107] and Abson et al. [108] has indicated that the columnar grain size and shape, in addition to the WM chemical composition, can be altered by the weld pool shape. The inoculation of the weld pool by inclusions and oscillation of the welding arc, current, voltage and welding travel speed influence the solidified weld microstructure [42,80]. The WM microstructure consists mainly of allotriomorphic ferrite (grain

boundary ferrite), idiomorphic ferrite, Widmanstatten ferrite and intergranularly nucleated acicular ferrite [108]. In addition, a small quantity of other microstructural constituents, including a mixture of carbides, sulfides and M-A constituents (martensite and retained austenite), are formed during cooling [109,110].

With reference to high strength microalloyed steels, it is generally accepted that a WM containing a relatively high fraction of acicular ferrite has optimum mechanical properties in terms of strength and toughness [108,111]. This is because of the basket-weave-type morphology, 1-3 μm in size, which makes acicular ferrite resistant to crack propagation [108]. The formation of other structures, such as grain boundary ferrite (GBF) and Widmanstatten ferrite (WF), decrease the weld toughness because they provide preferential paths for crack propagation [112–115].

Single-pass Welding

In single pass welding, the base material only experiences one welding pass which results in the formation of a single HAZ with different regions. In general, the region of the HAZ adjacent to the fusion line, the coarse grain HAZ (CGHAZ), has the poorest toughness relative to the rest of welded steel. This deterioration in the toughness is essentially due to the thermal cycle and consequent microstructural alterations taking place in the CGHAZ during welding. The different regions formed during welding are depicted in Figure 2-15 and discussed in the following.

2.5.2. Coarse grain heat affected zone (CGHAZ)

The CGHAZ shows poor mechanical properties, particularly toughness, relative to the rest of the steel [116–118]. The peak temperature in the CGHAZ reaches 1100-1450°C, which results in austenite grain growth and precipitate dissolution. These phenomena lead to an increase in the hardenability, due to the formation of the low temperature transformation products, such as martensite, M-A constituents and bainite in some regions depending on the carbon level in the base metal [38]. However, the deterioration in the CGHAZ fracture toughness of welded microalloyed steels is fundamentally due to the formation of large prior austenite grains (PAGs) and large elongated M-A constituents and bainite formed partially along the PAG boundaries.

2.5.3. Fine grain heat affected zone (FGHAZ)

The FGHAZ is characterized by a fine grained ferritic microstructure. The peak temperature varies between A_{C3} and ~1100 °C (the recrystallization temperature range). Accordingly, new grains of prior austenite nucleate in the FGHAZ, which results in the formation of a fine grained microstructure. Since the temperature is not too high compared with the CGHAZ, a sufficient amount of precipitates (e.g., Ti-rich nitrides and carbonitrides) remains, which also prevents

austenite growth. As such, a large area of PAG boundaries promotes the formation of fine ferrite and the remaining austenite may transform to bainite and small regions of M-A constituents [119].

2.5.4. Inter-critical heat affected zone (ICHAZ)

The ICHAZ experiences a peak temperature between A_{C1} and A_{C3}. As such, the initial microstructure of the base metal is partially transformed in this region. Depending on the welding heat input and cooling rate, the austenite may transform to pearlite, upper bainite and small amounts of martensite. In addition, reduction in dislocation density and coarsening of precipitates (e.g., Nb-rich carbonitrides) may occur in this region.

2.5.5. Sub-critical heat affected zone (SCHAZ)

In this region no transformation takes place; however, due to the peak temperature reaching AC_1, the base metal microstructure experiences tempering. Due to the low concentration of C and N in microalloyed steels, no significant strain hardening is observed.

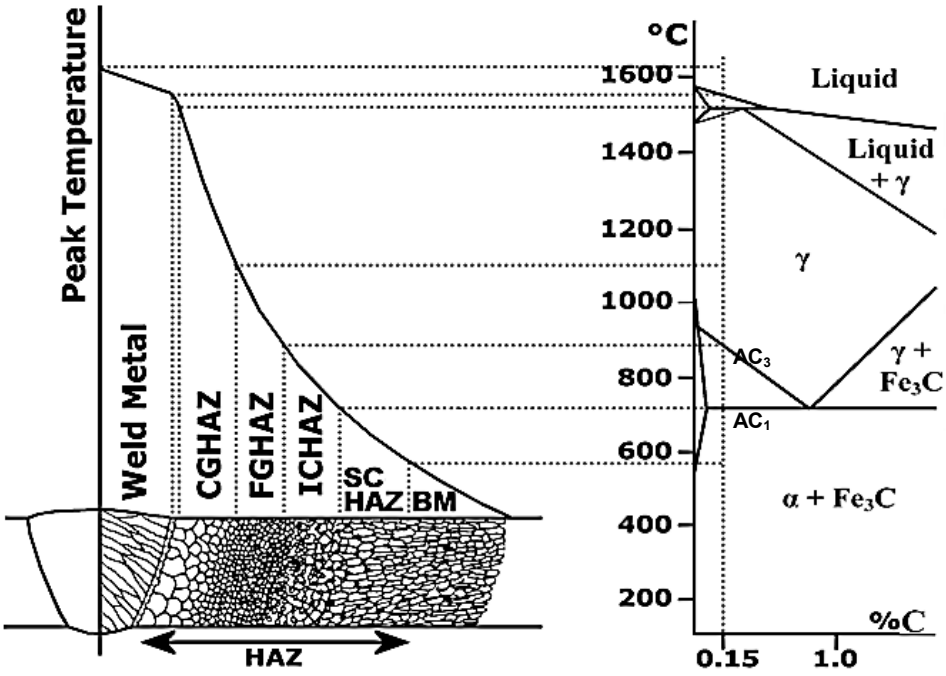

Figure 2-15 Schematic diagram of different regions of the heat affected zone of a 0.15 wt.% C steel formed during single pass welding. The temperature range in each region is correlated to the Fe-Fe3C phase diagram [80].

Multi-pass Welding

Unlike single-pass welding, in multipass welding the HAZ of the first pass is influenced by the thermal cycle of the second pass. In spiral-welded pipeline manufacturing, usually an inner-diameter (ID) welding pass is conducted followed by an outer-diameter (OD) welding pass. This results in overlap of the HAZs formed by the different welding passes. Figure 2-16 depicts the different regions formed during ID and OD welding due to the overlap of the HAZs.

2.5.6. Inter-critically reheated coarse grain heat affected zone (ICRCGHAZ)

The inter-critically reheated coarse grain heat affected zone (ICRCGHAZ) is a region where the CGHAZ formed during the first pass (ID pass) is reheated to the inter-critical temperature range (between Ac_1 and Ac_3) by the subsequent second welding pass (OD pass). As shown in Figure 2-15, the ICRCGHAZ is a small, narrow region which exhibits the most deteriorated toughness of all the HAZ sub-regions [120–122]. Crack tip opening displacement (CTOD) tests have demonstrated the low fracture toughness of the ICRCGHAZ, which is confirmed by the occurrence of the so-called pop-in phenomenon [123]. This deterioration in the fracture toughness is attributed to the formation of M-A constituents in the partially transformed carbon enriched regions of the CGHAZ of the ID weld [124,125]. The work done by Silwal et al. [126] on Grade 91 steel has shown that post-weld heat treatment of the CGHAZ formed during the first welding pass (ID pass) at a temperature greater than Ac_1 results in formation of fresh martensite and a reduction in the toughness. In addition, many other studies have shown that the ICCGHAZ formed in multipass welding exhibits deteriorated toughness, even lower than that in the CGHAZ [121,127–129].

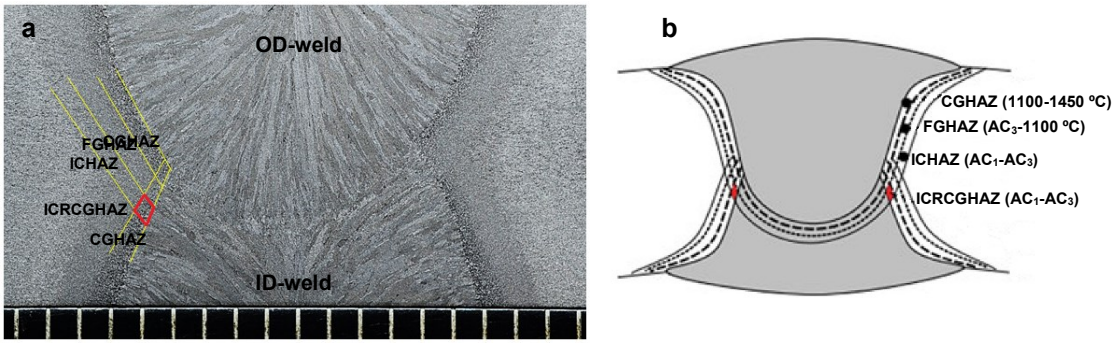

Figure 2-16 (a) Macrograph of ID and OD weld passes and (b) schematic illustration [121] of ICRCGHAZ formed during two-pass TSAW.

2.6. Phase Transformation in the HAZ of Microalloyed Steels

2.6.1. Precipitation

Precipitation is a fundamental mechanism for strengthening and toughening of microalloyed steels. In the presence of carbon, nitrogen and other alloying elements, particularly Ti, Nb and V, three types of precipitates, i.e., carbides, nitrides and carbonitrides, are generally formed during TMCP. Some precipitates are undissolved in the austenite temperature range, which pins the austenite grain boundaries, resulting in the formation of fine austenite grains and finer ferrite grains after transformation. On the other hand, some precipitates which have relatively lower dissolution temperatures form during the austenite to ferrite transformation (interphase precipitates) or after transformation in ferrite. Some NbC precipitates formed in ferrite in the range of 400-600°C are less than 5 nm in size and are effective in strengthening the matrix by precipitation hardening. Since the precipitation phenomenon leads to the desired mechanical properties in the microalloyed steel, any conditions that affect re-precipitation and/or partial dissolution of these precipitates are of concern. During welding, depending on the thermal cycle and peak temperature, precipitate dissolution, re-precipitation and coarsening may take place, which affect the final phase transformation products in the HAZ [130]. Since different parts of the HAZ (e.g., the CGHAZ and FGHAZ) are exposed to different temperature profiles (different peak temperature and cooling rate) throughout welding, precipitate fraction and size are not the same throughout the HAZ.

Due to the high cooling rate of the weld in most cases, the time for re-precipitation is limited. As such, re-precipitation does not usually occur. In the FGHAZ, the thermal cycle and peak temperature are too low for intermediate-size (<500 nm for Ti-rich and and <150 nm for Nb-rich carbonitrides) and small-size (<20-30 nm) precipitates to dissolve, which is also in agreement with the theoretical analysis performed by Poorhaydari et al. [119]. With reference to the CGHAZ, transmission electron microscopy (TEM) analysis [131] showed that intermediate-size and small-size NbC precipitates dissolved at a low heat input of 0.5 kJ/mm. At higher heat inputs, the precipitates became coarser than those in the BM and FGHAZ. Precipitates agglomerated at the grain boundaries of the martensitic structure for a heat input of 0.5 kJ/mm and within the bainitic structure of the matrix at heat inputs of 1.5 and 2.5 kJ/mm. A higher heat input leads to a higher fraction of precipitates that dissolve. Due to the high cooling rate at low heat inputs, re-precipitation is typically suppressed. However, re-precipitation occurs in high heat input welds due to the lower cooling rate and higher transformation temperature for austenite. Dissolution of precipitates (which enriches the matrix with microalloying elements) and re-precipitation (which pins the PAGs and restricts growth) of Nb-rich precipitates in the CGHAZ influence austenite grain growth, phase transformation and,

consequently, the mechanical properties of the weld. However, coarsening of Ti-rich precipitates, which takes place in the CGHAZ, diminishes the influence of these precipitates on PAG growth.

2.6.2. Phase transformation

The goal of TMCP is to develop a fine microstructure comprised of finely distributed acicular ferrite and fine precipitates. However, other microstructural constituents may form during processing, such as polygonal ferrite, pearlite, granular bainite and martensite associated with retained austenite. Polygonal ferrite forms at high temperatures when the austenite is cooled at sufficiently low cooling rates. Ferrite nucleates below the A_{e3} temperature at austenite grain boundaries and grows along austenite grain boundaries resulting in grain boundary allotriomorphs, followed by growth into equiaxed grains [134]. The type, grain size and properties of ferrite are greatly dependent on the prior austenite grain size and the cooling rate, since these factors influence the nucleation sites and kinetics of transformation. As the cooling rate increases, the undercooling of austenite increases, leading to a decrease in the transformation start temperature. This results in an increase in the nucleation rate, but the growth rate decreases, which results in finer ferrite. Carbon is rejected during ferrite formation into the surrounding austenite as the maximum solubility in ferrite is significantly lower at 0.02 wt.%. Accordingly, austenite is enriched with carbon and different constituents form. At relatively low cooling rates, ferrite formation is often accompanied by pearlite formation, which is a colony of alternating lamella of ferrite and cementite. However, at faster cooling rates, the formation of pearlite is restricted and low temperature transformation products form. Bainite (upper and lower) forms at lower temperatures, where ferrite forms in laths or plates and contains an intra-ferritic distribution of cementite (Fe_3C) due to the low carbon diffusivity at lower temperatures [135]. Upper bainite forms at a higher temperature relative to lower bainite. Carbides form outside the ferrite laths at the ferrite-austenite phase boundaries in upper bainite, whereas carbides form inside ferrite plates in lower bainite.

As stated earlier, acicular ferrite is a common phase formed in microalloyed steels during TMCP. After its initial identification by Smith et al. [52] in 1972, the term “acicular ferrite” was denoted for non-equiaxed ferrite formed during continuous cooling with a mixed mechanism of diffusion and shear transformation. Acicular ferrite, also known as bainitic ferrite, is generally formed on inclusions, which results in high strength and toughness due to the fine grain structure and high angle grain boundaries. Acicular ferrite formation is a key technique to improve the toughness in microalloyed steel welds.

Due to the low carbon content of microalloyed steels, upper and lower bainite formation is usually restricted; however, a microstructural constituent called “granular bainite” forms, which is

essentially a ferritic matrix containing islands of M-A constituents. Carbon can rapidly diffuse out from the ferrite-austenite interface, which prevents the precipitation of inter- or intra-lath carbides. Due to carbon enrichment, austenite becomes stabilized and transformation of remaining austenite is prohibited. Accordingly, granular bainite consisting of a ferrite matrix with dispersed M-A islands forms.

Another microstructural constituent is martensite with a body-centered tetragonal (BCT) crystal structure that forms at very high undercoolings, where bainite ceases to form. Martensite is formed by a shear (diffusionless), displacive transformation, which involves the cooperative movement of individual atoms. In low-carbon steels, lath martensite is commonly formed, which consists of highly dislocated parallel lath-shaped needles with retained austenite located within the laths. Plate martensite, in turn, occurs in high carbon steels, where a large amount of retained austenite with fine martensite plates containing transformation twins are formed. Martensite forms at the speed of sound; as such, detailed kinetics studies of its formation are difficult to perform [136]. Martensite starts to form at a distinct temperature, termed the martensite start temperature (M_s), which is greatly dependent on steel composition and the PAG size. The effect of PAG size on the M_s is studied in this thesis. The following empirical equation proposed by Andrews [137,138] expresses the dependency of M_s on steel composition for Mn-C low-alloy steels.

$$\boldsymbol{M_s}\ (°C) = 539 - 423C - 30.4Mn - 12.1Cr - 17.7Ni - 7.5Mo + 10Co - 7.5Si \quad [2.8]$$

The element concentrations are in wt.%. As indicated in the equation, elements such as Mn, Cr, Ni and Mo enhance the ability of steel to form martensite (hardenability) and, consequently, reduce weldability. Equation [2.8] is valid over a wide range of compositions, including the steel composition studied in this thesis.

M-A constituents usually form in low-carbon microalloyed steels, where carbon diffuses out of ferrite into the surrounding austenite, resulting in the formation of martensite along with retained austenite. It is generally believed that the M-A constituent is associated with a loss in toughness as it is a very hard and brittle constituent. However, Bhadeshia [139] reported that the fraction, shape, size, distribution and morphology of M-A constituents play a significant role in toughness and, as such, they may be beneficial to the toughness. Granular M-A islands do not participate in crack initiation and brittle fracture, whereas elongated M-A regions are detrimental to fracture toughness. The M-A constituent is the dominant microstructural feature influencing the mechanical properties, particularly fracture toughness, in the HAZ of welded microalloyed steels. Due to its importance, it is essential to reveal M-A constituents and distinguish them from the other microstructural features. Revealing M-A regions in microalloyed steels and their welds is

challenging, as it highly depends on the etchant type, composition and temperature. Tint etching is a powerful method enabling analysis of M-A characteristics [140,141].

2.6.3. Overall alteration of HAZ characteristics

The main drawback of the welding process is that the microstructure and mechanical properties alter due to the thermal cycle that the material experiences during welding. However, in TSAW, the high heat introduced to the material, because of an overall increase in the deposition rate, results in a higher peak temperature through the HAZ regions and a slower cooling rate. The thermal cycle during welding of microalloyed steels is a prominent parameter in terms of microstructure and properties of the WM and the HAZ of welded microalloyed steel [142]. In other words, the heat input introduced to the weld directly affects the microstructure and mechanical properties of the weld and the HAZ. Moeinifar et al. [7,143] showed that by increasing the heat input in a four-wire TSAW process, the peak temperature in the coarse-grain heat affected zone (CGHAZ) is increased in magnitude by 100°C and the weld and HAZ are cooled at a lower rate resulting in significant alterations in the microstructure of the HAZ. In the CGHAZ, with a higher peak temperature, the soaking time increases resulting in large austenite grains. Chandel et al. [144] have stated that as heat input increases, the time required to cool the weld increases, especially between 800 and 500°C. Also, they showed that increasing the heat input from 3.15 to 4.72 kJ/mm leads to larger WM and HAZ areas from 118.4 to 174.8 mm^2 and 66.6 to 121.2 mm^2, respectively. Das [145] and Xiao et al. [146] have recently reported that the most effective parameter in improving toughness of the HAZ of microalloyed steels is the refinement of microstructure in the HAZ, in particular the CGHAZ, through retardation of austenite grain growth and acicular ferrite transformation by precipitates or inclusions inside the austenite grains. It has been reported that toughness is expected to be low in the CGHAZ for single pass welding [147]. Also, TSAW with high heat input causes significant changes, particularly the formation of larger prior austenite grain sizes in the CGHAZ [143,148]. Since grain growth is a diffusion based phenomenon and is temperature dependent, austenite grains within the HAZ are significantly coarser than those of the base metal. Shen et al. [149] have studied the effect of heat input on weld geometry of SAW ASTM A709 Grade 50 steel joints. Their results showed that the cooling time from 800°C to 500°C in the weld region is increased by increasing the heat input, and it affects various weld bead characteristics, such as bead width and bead width-to-depth ratio. Therefore, it is not always accepted that increasing the number of arcs and, consequently, the heat input is the way to increase productivity, since properties of the weld and the HAZ are directly affected by the heat input. One potential way to increase productivity without increasing heat input is adding a wire, which is electrically cold

relative to the arc(s). Besides increasing productivity, incorporating a cold wire in the TSAW process moderates the heat input by consuming the energy introduced to the weld puddle. The CWTSAW process is discussed in detail through Chapter 3 and 4.

2.7. Weld and HAZ Defects

Defects may occur in the WM and HAZ due to several reasons, such as lack of fusion, penetration of diffusible gas atoms (e.g., oxygen, nitrogen and hydrogen), slag entrapment, insufficient current and voltage, fast travel speed, diffusible hydrogen in HAZ and so on. The presence of defects in the weld and HAZ may result in catastrophic failures; however, the weld can tolerate the defects if they fall within acceptable limits [150]. Depending of the service condition, the acceptance criteria vary. Defects are essentially formed due to two main reasons; i. welding technical issues and ii. metallurgical aspects. Herein, a list of the common defects is presented. Defects can be generally divided in two types, surface defects and internal defects.

2.7.1. Surface defects

Typical surface defects that form in weld joints are surface porosity, misalignment, undercutting, excessive reinforcement and solidification cracks. Figure 2-17 depicts the different types of surface defects formed during welding.

When the weldment surface is contaminated by dampness or atmospheric entrainment and excessive grease, surface porosity may form during welding. Unsuitable selection of welding parameters also causes surface defects. When the gap between two pieces of weldment is too large, misalignment or distortion occurs due to the excessive solidification force of the weld metal. Undercutting is an irregular groove located at the weld toe adjacent to the HAZ. This the most common defect formed during welding. Improper selection of welding parameters, particularly welding travel speed and voltage, is the main reason for undercut formation. When the travel speed is fast, the deposition rate and reinforcement area are reduced and a steeper weld bead is formed. This will create surface tension forces on the molten metal along the edges of the weld bead. As such, the molten metal will pile up along the center of the weld bead from the edges, which results in undercutting occurring at the edges of the weld bead during solidification of the WM. The high heat input of welding will cause excessive reinforcement of the weld bead. Solidification cracking is a local discontinuity, which is formed during the last stage of solidification due to insufficient strength of the weld bead to endure the stress concentration generated as the weld solidifies. As shown in Figure 2-17e, the solidification crack is usually formed as a straight line along the weld

centerline. Avoiding improper weld bead geometry and using high purity weld material with low inclusion content may reduce the chance of solidification crack formation.

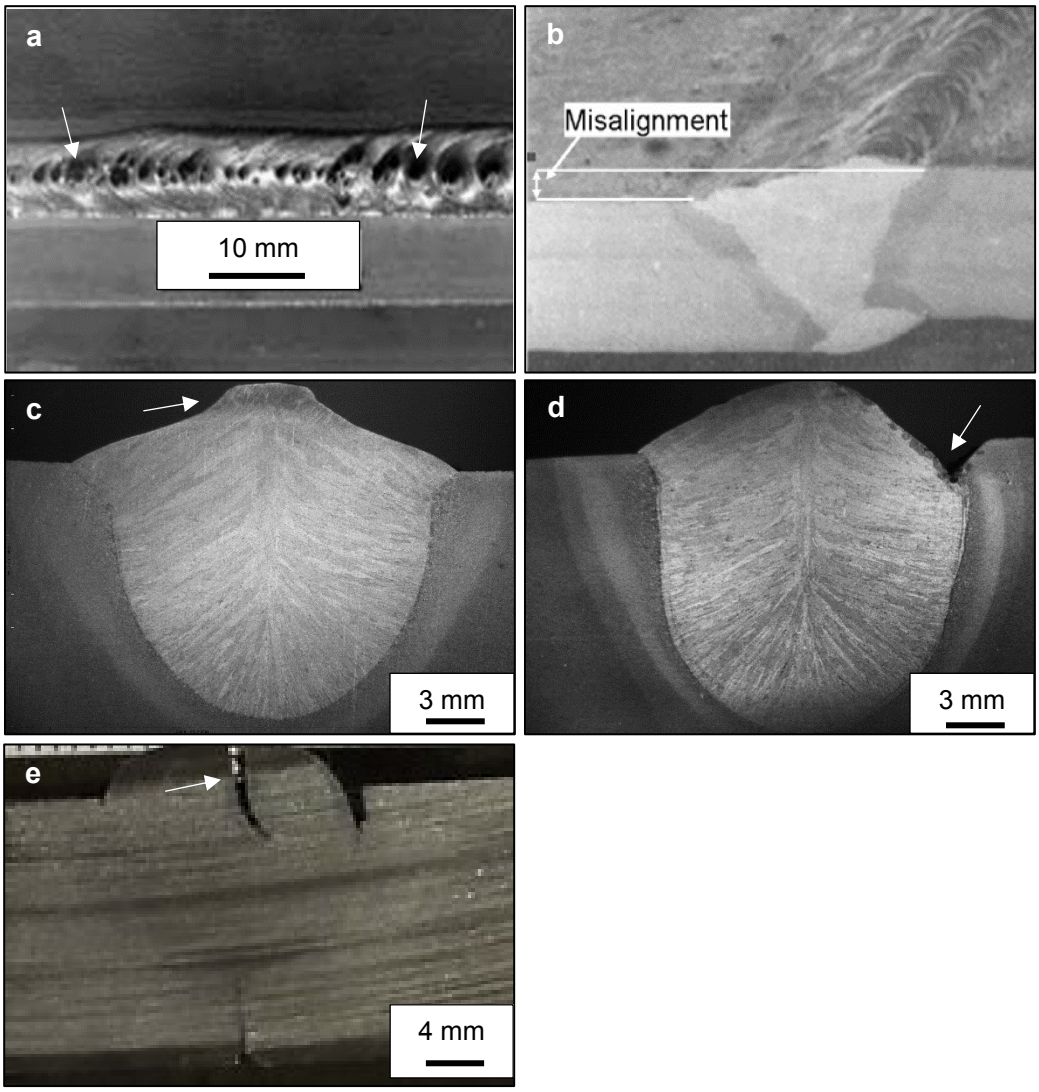

Figure 2-17 Macrographs of typical surface defects in welds: (a) Surface porosity [319] (b) misalignment, (c) excessive reinforcement, (d) undercutting and (e) solidification cracking.

2.7.2. Internal weld defects

Typical internal weld defects are lack of fusion, internal porosity, slag entrapment and hydrogen cracking. The latter one usually forms in the HAZ. Figure 2-18 shows the different forms of internal weld defects.

Similar to lack of penetration, lack of fusion happens when the WM fails to fuse on one side of the welded joint in the root or sidewall. This defect happens when a low heat input process is used

or the bevel angle is too small. In addition, insufficient cleaning of oily or scaled surfaces may result in lack of fusion in the WM. To have enough fusion in the root, it is necessary to use a small enough wire size to access the root [151]. Internal porosity is usually formed by freezing the gases, such as oxygen, nitrogen and hydrogen, in the weld during solidification [151,152]. Porosity may form due to weldment surface contamination and fast cooling of the weld, which does not allow gases to escape from the molten pool and, as such internal porosity is formed. Slag inclusions are usually associated with welding processes in which flux is used to shield the arc. The inclusions could occur when the arc force is not sufficient (arc force is a function of the arc current) and/or the weld travels quickly, which do not allow the flux to be removed and the flux is entrapped in the molten pool [153]. Hydrogen cracking occurs as a result of hydrogen diffusion from a humid electrode into the molten pool during welding. Also, steels with a higher fraction of hard phases, such as martensite, are more susceptible to the hydrogen cracking, which may form in the weld or in the HAZ [29,42].

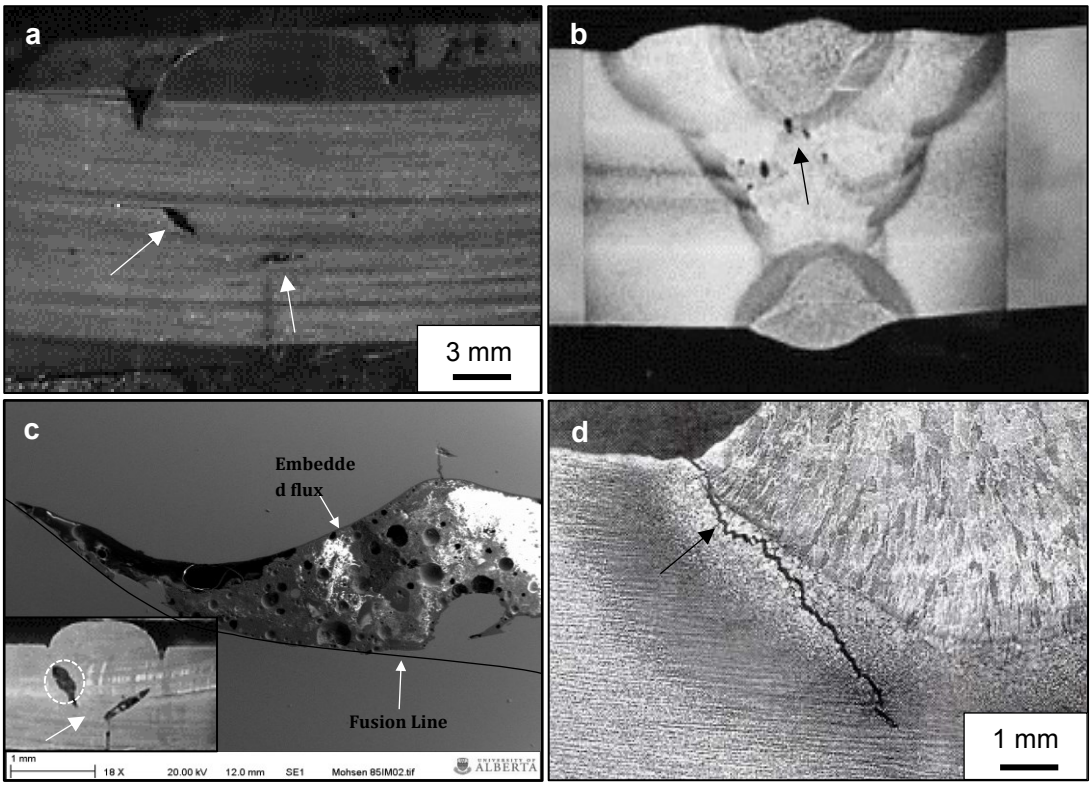

Figure 2-18 Macrographs of typical internal weld defects: (a) Lack of fusion, (b) internal porosity [319], (c) flux entrapment and (d) hydrogen cracking [151].

2.8. Toughness Design for Microalloyed Pipeline Steels

During the past several decades, the relationship between microstructure and mechanical properties of high strength microalloyed pipeline steels has been extensively studied in an effort to improve the fracture toughness and strength of this type of steel without appreciably increasing steel manufacturing and pipeline fabrication (welding) costs. Fueled by the demand for developing pipeline steels with high strength, toughness and low cost by the construction, energy and transportation industries, it is essential to improve the properties of microalloyed steels and their welds and HAZ.

Toughness is a measure of a material's resistance to fracture; the units are those of energy. A material exhibiting brittle fracture absorbs little energy, whereas a tough material requires a large expenditure of energy in the fracture process. In developing pipelines, fracture toughness, especially low-temperature toughness, and ductile to brittle transition temperature (DBTT) have been considered as two main fundamental aspects. However, toughness is essentially controlled by a number of microstructural factors [111,154,155]. DBTT, at which the steel loses its toughness and fails in brittle mode, is a crucial aspect for pipeline design when both strength and toughness are necessary at low temperatures [156,157]. From the Yoffee diagram [156] shown in Figure 2-19, there are two ways to suppress the ductile to brittle transition. One is to raise the brittle fracture stress (σ_B) and the other is to lower the steel yield stress (σ_Y). However, since the high yield strength is desirable for microalloyed steels, the preferred way is to increase σ_B. This can be achieved by refining the grain size (σ_B is also known as effective grain size) [156].

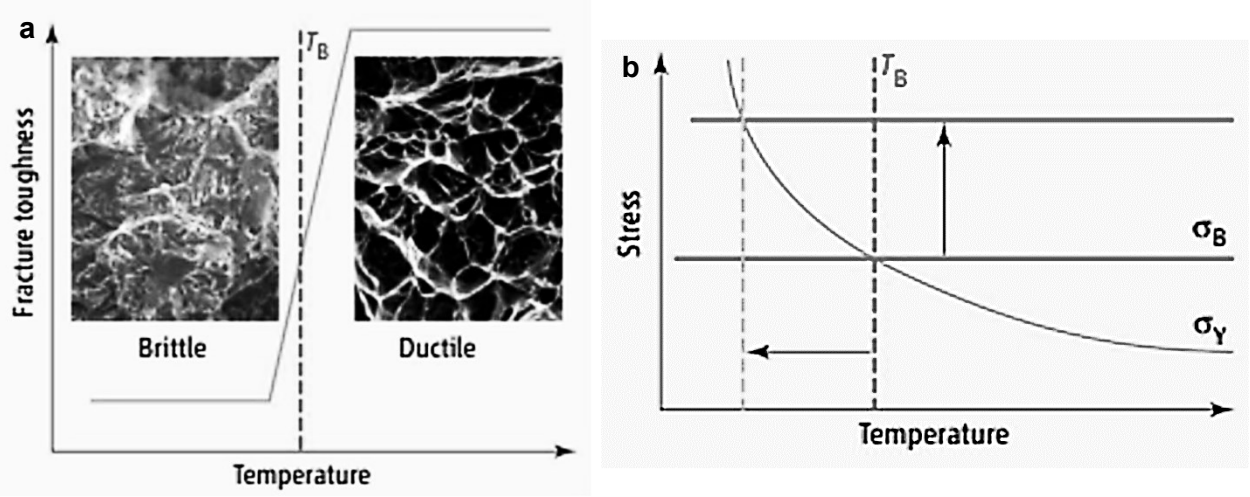

Figure 2-19 (a) Typical graph showing transition from ductile to brittle mode at DBTT. (b) Yoffee diagram indicating DBTT at the intersection of the σ_Y and σ_B [154].

The principle of the development of high strength low-carbon microalloyed steels has been based on achieving good strength and toughness by appropriate alloy design and TMCP technology. The final product possesses excellent mechanical properties due to the formation of a fine ferritc microstructure containing finely dispersed carbide, nitride and carbonitride type precipitates. However, the properties will deteriorate during the welding process. Welding is indispensable for pipeline fabrication. SAW, ERW and GMAW are the common processes used to fabricate pipes; the first two techniques are used in mill pipe manufacturing and the latter is widely used to join pipe sections in the field. The steel is inherently exposed to elevated temperatures during welding, which significantly alters the microstructure and consequently the mechanical properties. The region immediately adjacent to the fusion line, i.e., the CGHAZ, is characterized as a region with extreme grain coarsening (it is heated within the austenite region, 1100-1450°C) and a high fraction of elongated M-A constituents. Although many welding technical aspects, such as current, voltage, polarity, heat input and cooling rate, control the final microstructure in the HAZ, it is believed, from a metallurgical point of view, that the size of the primary formed austenite grains during heating governs the microstructure and, consequently, the properties of the HAZ. Several methods have been proposed by the researchers [158–162] to achieve high toughness in the HAZ of the welded microalloyed steels. These methods are briefly listed in the following:

- Refining prior austenite grain (PAG) size

  This can be achieved by controlled addition of Ti in a steel containing nitrogen or increasing the Al amount and lowering nitrogen. As such, fine TiN and AlN precipitates (which are stable in the temperature range of CGHAZ) prevent growth of austenite grains. However, in modern microalloyed steels containing appropriate amounts of alloying elements, another way to control the PAG size during welding is to reduce the heat input, since high heat input welding (which is widely used for pipeline manufacturing) increases the peak temperature and lowers the cooling rate, resulting in PAG growth. The technique of lowering effective welding heat input is fundamentally evaluated in the current thesis and will be discussed in Chapter 5.

- Nucleation of intra-granular ferrite

  Ferrite can nucleate intra-granularly on secondary phase particles or inclusions. This will result in the formation of finer ferrite grains. Inclusion include oxides, such as TiO, TiO_2, CaO, Al_2O_3 and rare earth metal oxides, which increase the number of ferrite nucleation sites within the austenite grains. The technique of addition of the oxides with high melting

points to the HSLA steel welds is widely used to improve weld toughness, which is discussed by Liu and Olson [163,164] and Feloseeva et al. [165].

- Refining the HAZ microstructural constituents

  As stated earlier, the M-A constituent is a major microstructural feature, which is formed in the CGHAZ, resulting in deterioration of the toughness. Although it is generally believed that a lower fraction of M-A constituents is beneficial to the HAZ toughness, Bhadeshia [139] has proposed that the fraction, shape, size, distribution and morphology of M-A constituents play a significant role in the effect of M-A islands on the properties. To modify the M-A constituents, there are several metallurgical methods, such as reducing the PAG size, reducing the M_s [166] and lowering the carbon equivalent of the steel. The former is achievable by controlling the welding heat input, which is comprehensively discussed in Chapter 4, however, latter has to be taken into account during steel processing.

- Increasing the toughness of the steel

  Some methods have been used to improve microalloyed steel toughness, such as addition of Ti, B and Al to reduce the quantity of free nitrogen and reducing carbon and nitrogen content. These methods are essentially developed to reduce the kinetics of austenite growth in the HAZ during welding.

As mentioned earlier, during welding, the mechanical properties of the welded steel (particularly its HAZ) often deviate strongly from the base material, which has excellent properties. Toughness deterioration in the CGHAZ and the ICRCGHAZ as a result of the formation of hard phases such as M-A constituents has always been a major concern [128,167–169]. A schematic of the microstructural constituents (i.e., packet boundaries and M-A constituents) affecting the performance of the HAZ in correlation with crack initiation and propagation is shown in Figure 2-20. Although cleavage cracking occurs, the crack is deflected by finely distributed fine M-A constituents within the PAGs and packet boundaries (fine microstructural features such as ferrite and bainitic ferrite). Accordingly, besides fine M-A regions, the formation of a fine structure with a high density of packet boundaries is desirable in improving crack propagation resistance. Cracks initiated at large elongated M-A constituents can connect and form a continuous long crack, resulting in a brittle cleavage fracture.

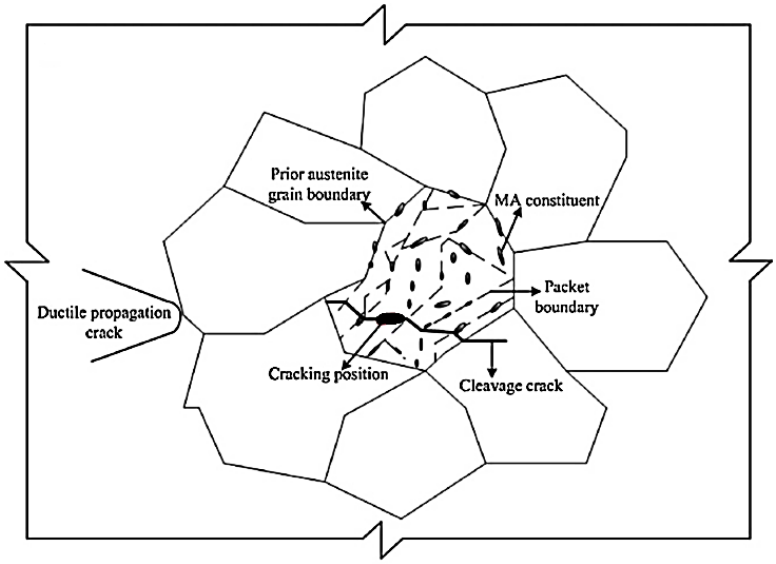

Figure 2-20 Schematic diagram showing crack deflection at M-A constituents and phase boundaries [170].

Due to the significant influence of M-A constituents on brittle fracture in the HAZ, the mechanism of M-A formation in the HAZ has recently generated interest [170–176]. In the study done by Long et al. [171], toughness deterioration was correlated with the retained austenite morphology for the microstructures with a constant fraction of M-A constituents. They found that elongated shaped M-A regions were detrimental to the fracture toughness. Li et al. [177] found that coarse PAGs promote large M-A regions along PAG boundaries and M-A regions become refined by PAG refinement. The presence of necklace-type M-A along the PAG boundaries is believed to noticeably increase the susceptibility to cleavage micro-crack nucleation. However, as stated by Bhadeshia [139], the size and morphology of M-A strongly influence the properties. A low fraction of finely distributed fine M-A constituents has been observed to act as crack arrestors for secondary cracks, which is beneficial to toughness [178].

2.9. Weld/HAZ Fracture Toughness Testing

Pipelines are sometimes subjected to large-scale bending and tensile deformation, which places the welds and their surroundings in tension. The weld and HAZ may contain small planar flaws, i.e., cracks, which makes it necessary to assess the resistance of the flaw to growth (toughness) under relevant stresses. Fracture toughness is an important property of materials used to describe the resistance of the material, especially at low temperatures, against fracture when a crack exists within the structure. The stress intensity factor, K, proposed by Irwin [179] is used for a crack in an elastic material. However, for a ductile crack, Rice [180] and Wells [181] proposed the J-integral

and the crack-tip opening displacement (CTOD) methods, respectively. The fracture toughness resistance curve (R-curve) of pipeline steels is a key tool to assess the resistance of the pipe to fracture. Accordingly, the R-curves are essential in the structural integrity assessment (SIA), engineering critical assessment (ECA) and strain-based design (SBD) of pipelines with respect to cracks [182]. The R-curve is generally represented by either the crack tip opening displacement (CTOD) resistance curve (CTOD-R curve) [183] or the J-integral resistance curve (J-R curve). It is worthwhile to note that the accuracy of the experimentally measured R-curve directly influences the accuracy of the design and assessment of pipelines.

Commonly fracture mechanics test methods, e.g., the compact tension (CT) test [184], the disc-shaped compact tension (DCT) test, the arc-shaped tension test [185] and the single edge notched bend (SENB) test [186], proposed in ASTM E1820 [187], BS 7448-1 [188] and ISO 12135 [189], are mainly used to address the measurement of fracture toughness in high crack-tip constraint conditions and high triaxiality conditions. This high constraint condition is due to the existence of a deep crack within the standard specimen, which does not necessarily represent the stress state around the defects in the real structures. SENB has been widely used for fracture toughness analysis of welded pipes, however, as stated earlier due to the deep crack, the value of the toughness is too conservative. In the most recent revision of ASTM E1820-13 [187], an appendix is added to support low-constraint shallow cracked SENB specimens, however, in general, bend specimens provide higher constraints than tension specimens at the same crack depth. With reference to pipeline fracture toughness, due to the thin wall thickness and large plasticity involved, it has become evident that fracture mechanics based on the ECA of pipelines using fracture toughness directly obtained from standard SENB specimen becomes too conservative. Accordingly, the single-edge notch tension (SENT) test has recently been developed to analyze the fracture toughness of pipelines in the low constraint crack-tip condition. A schematic of different fracture toughness techniques is depicted in Figure 2-21.

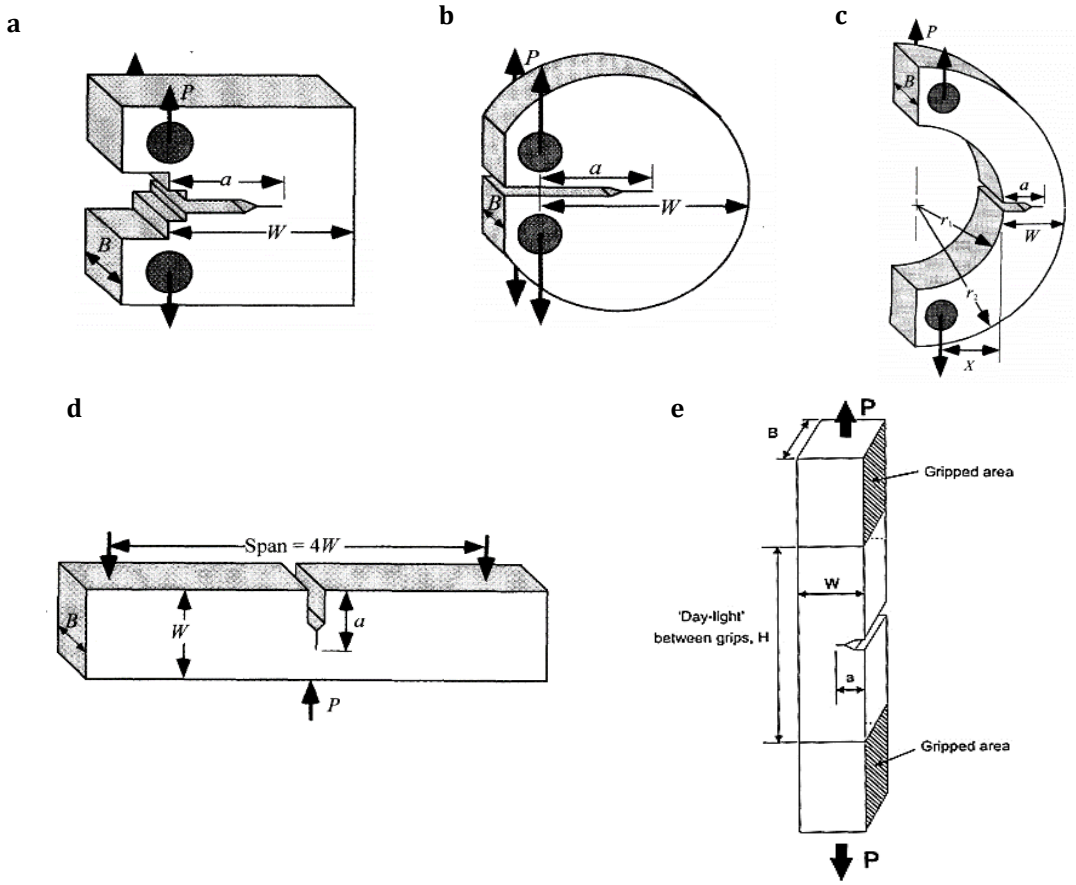

Figure 2-21 Conventional standardized fracture toughness test specimens: (a) CT specimen, (b) DCT specimen, (c) arc-shaped tension specimen and (d) SENB specimen in three-point bending. (e) developed SENT test specimen [183,200].

Several experimental methodologies have been proposed by DNV (Det Norske Veritas company) [190], Canmet Materials [191,192] and ExxonMobil [193]. There is still a lack of the standardization for the SENT test, however, a British standard (BS 8571) is currently being prepared based on the method described in DNV RP F108 [190] to determine fracture toughness using SENT specimens. There are also some advancements in the SENT test specimens proposed through some published research articles and reports [194–197]. The crack-tip constraint in a SENT specimen can be fine-tuned through the loading condition clamped and pin-leaded (shown in Figure 2-22), crack/width ratio (a_0/W) and the specimen length. The studies indicate that conducting SENT on a clamped specimen with a shallower crack results in lowering of the crack-tip constraint.

In the SENT test, there are two essential procedures, i.e., the multi-specimen technique and single-specimen method. The former method typically uses a set of seven specimens with the same initial crack size loaded to different load levels proposed by DNV RP F108. Subsequently, ductile

crack extension is determined after breaking the specimens in liquid nitrogen. However, these results are highly susceptible to scatter in the material data and require a significant amount of test material. Thus, currently the focus is on using the single-specimen technique. Accordingly, this technique uses either a single clip gauge or double clip gauges attached to the integral knife edge or mounted in a set of knife-edges, respectively, to estimate the crack-mouth opening displacement (CMOD) and CTOD. The CTOD can be estimated indirectly from the J-integral using the ASTM conversion procedure [187] and/or from the unloading compliance crack size equations proposed by DNV RP F108 [190] and Shen et al. [198] or directly from the original crack-tip position on the specimen by triangulation from the double clip gauges and then using the unloading compliance equations to predict the crack size. Direct-current potential-drop (DCPD) instrumentation can also be used for supplementary crack size measurement.

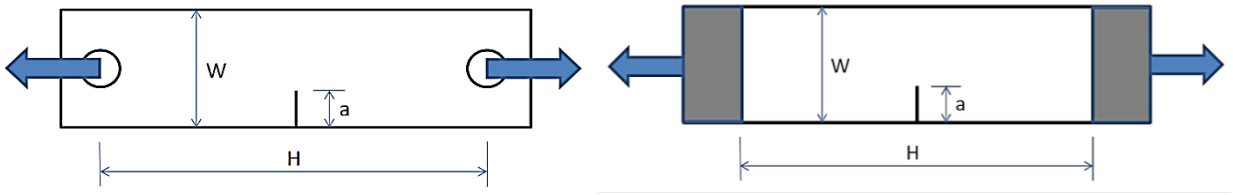

Figure 2-22 Schematic of SENT specimen in (a) pin-loaded condition, and (b) clamped condition [291].

Table 2-3 summarizes the details of the SENT test procedure carried out by several researchers. As stated earlier, the crack-tip constraint caused by thickness, size and configuration of fracture test specimens can have a strong effect on the measured values of fracture toughness. In general, high constraint results in higher crack-tip stresses with less crack-tip yielding and promotes a more brittle fracture or reduces the resistance curve toughness for ductile fracture. Low constraint results in lower crack-tip stresses with more crack-tip yielding and tends to reduce the possibility of brittle fracture and to raise the resistance curve toughness for ductile fracture. The specimen configuration, loading mode and crack depth can cause an effect on crack-tip constraint. For example, a deeply cracked bend dominated specimen will demonstrate higher constraint at the crack-tip than that shown by a shallow cracked tensile specimen. To reduce the effects of specimen configuration and thickness on the measured toughness results, a standard is required to specify the specimen's dimension with a fixed range of crack depth to width ratios, to set limits on remaining ligament to thickness ratios, to define the loading condition and, in many cases, to specify the side grooves along the crack ligament.

Table 2-3 Summary of previous work done on SENT testing method

	Specimen Side-grooved Each Side?	Notch location Orientation Pre-cracked?	a_0/W	Fracture toughness	Application	Welds	Validity	Loading
NIST, USA **Weeks et al.** [201]	BxB Yes 15%	Parent metal	0.4	J CTOD	UOE pipe	Parent metal	Based on E1820	Clamped
SGS **Kirk et al. 2014** [194]	BxB 15%	Parent or weld Surface OD Fatigue + EDM	0.3 - 0.4	J-R curve CTOD	Pipe	Weld HAZ	Based on ISO 12135:2002 criteria E2818 (ISO 15653): TWI criteria	Clamped
TWI **Draft BS 8571 2013** [200]	BxB or 2BxB 5% suggested	Parent or weld Surface or T-T Fatigue	0.3 - 0.5	J or CTOD Single point or R-curve M/S or U/C	General	Parent metal Weld metal HAZ PTM	Based on ISO 12135 and 15653	Clamped or pin loaded
Cravero Ruggieri 2007 [195]	Bx2B 10%	Parent metal	0.5	J R-curve U/C	Engineering structures under plastic regime	Parent metal only	No; tests to verify FEA	Clamped or pin loaded
Canmet **Shen et al., 2009** [198] **Park et al., 2015** [199]	BxB Yes 5, 10 and 15%	Parent metal	0.25 and 0.5	J R-curve U/C	Girth weld pipe	Parent metal Weld HAZ	Based on E1820	Clamped
ExxonMobil [193]	BxB 5%	Parent or weld Surface OD Fatigue or EDM	0.25 - 0.35	CTOD R-curve U/C or DCPD	Strain capacity of pipeline girth welds	Parent metal Weld metal HAZ PTM	Yes, range of validity limits	Clamped
DNV RP-F108 2006 [190]	2BxB (recommended) No	Parent or weld Surface OD Fatigue	0.2 - 0.5	J R-curve M/S	Installation of pipelines under high plastic strain	Weld notch Fusion line notch PTM	Not discussed; segment tests?	Clamped or pin loaded

2.10. Summary of the Literature

Any degradation in the properties of pipeline steels occurring during steel production, pipe manufacturing (welding and joining of pipelines) and in-service conditions may result in a severe failure at an unexpected time. Many pipeline failures and oil spills have been reported around the world. In the recent years, oil pipeline spills in North Battleford (Saskatchewan) and Refugio (California) in 2016, Red Deer River in 2012, Rainbow Lake (Alberta) in 2012, the Gulf of Mexico in 2010 and 2016 and Slave Lake (Alberta) in 2006 are some of the recent pipeline failures, resulting in contamination of the environment. In addition to the environmental issues, pipeline failures approximately cost the transmission pipeline industry 5.4 to 8.6 billion dollars annually. Pipeline failures have persuaded pipe fabricators to develop new precursor steels and manufacturing processes to improve the final product properties. From the view point of pipeline joining and welding, besides reducing the manufacturing cost, a major concern is to improve the quality of pipelines in terms of composition and welding process. During the past decades, submerged arc welding with more than one electrode, known as tandem submerged arc welding (TSAW), has been extensively utilized to produce oil and gas transportation pipelines with increased productivity. However, welding with more electrodes to improve welding productivity may cause an increase in the heat introduced to the weldment. Increasing welding heat input deteriorates the mechanical properties and microstructure of the weld metal (WM) and heat affected zone (HAZ) due to an increase in the peak temperature and a decrease in the cooling rate. High heat input promotes austenite grain coarsening and the formation of a higher fraction of large slender shaped martensite-austenite (M-A) constituents in the CGHAZ, which leads to property deterioration. As such, it is not always acceptable to increase the welding heat input to increase productivity. Cold wire tandem submerged arc welding (CWTSAW) has recently been developed to improve the overall productivity of pipeline manufacturing without an increase in the heat input of the welding process. In addition, cold wire influences the microstructure and mechanical properties of the welded steel, which will be discussed in this thesis. In fact, CWTSAW operates on the principle that an additional cold wire consumes and moderates the heat introduced to the weldment. The literature survey shows that most of the research work has been devoted to studying increased productivity for CWTSAW. In this research work, the aim is to study the microstructure and mechanical property alterations that occur when a cold wire is added to the conventional TSAW process.

Chapter 3

3. Influence of Cold Wire Tandem Submerged Arc Welding Parameters on Weld Geometry and Microhardness of Microalloyed Pipeline Steels

3.1. Introduction

Submerged arc welding (SAW) has been preferred over other welding processes in pipe production due to its inherent properties, such as high deposition rate, deep penetration and capability of welding thick sections [1]. SAW uses the intense energy of the electric arc to generate the heat necessary for fusion. In the SAW process, the arc is generated between a consumable electrode and a work piece, which is shielded along with the weld puddle by a solid flux [13,202]. To improve welding productivity in a global economy, many fabricators have resorted to tandem submerged arc welding (TSAW), which is SAW with two to five electrodes, to manufacture pipelines, pressure vessels and construction equipment [7,8,13]. However, in the TSAW process, heat input is increased as the number of electrodes increases because of the increase in the overall welding current and voltage for a higher deposition rate. Although TSAW provides higher productivity due to the high heat input, some adverse effects can be produced in terms of the microstructure, properties and geometry of the weld joint. The weld metal (WM) and heat-affected zone (HAZ) are particularly affected, since the weldment experiences higher peak temperatures and cools down more slowly after welding [8,14–16].

The addition of a cold wire to the one electrode SAW process was initially proposed by Mruczek et al. in 2005 [17]. In the current research, TSAW with an additional cold wire (CWTSAW) is developed to improve the productivity and the quality of the pipeline steel weld in terms of mechanical properties, weld geometry and dilution. The process involves two electrodes with arcs and one electrically cold electrode, which is fed at a lagging position close to the trail electrode. The authors have observed that the addition of a cold wire at the lagging position (close to the trail electrode) does not cause any reduction in the penetration depth compared with feeding a cold

wire at the forward position (close to the lead electrode) which does reduce penetration depth. A cold wire at the forward position is fed into the lead electrode's arc and consumes some of the heat of the lead electrode, resulting in slightly shallower penetration, whereas a cold wire at the lagging position is fed into the tandem weld pool and/or into the trail electrode's arc with no effect on the lead electrode's arc. The cold wire provides a higher deposition rate and better productivity for the welding process without increasing heat input compared with the TSAW process [17–19]. Furthermore, incorporating a cold wire in TSAW moderates the heat input by consuming the energy of the trail electrode as the wire melts into the weld puddle. Accordingly, better quality welds are expected with deep penetration at lower heat inputs per mass of deposited material and with a substantial reduction in arcing time causing the formation of a smaller and shorter weld pool (compared with TSAW without a cold wire). As such, CWTSAW technology is a promising technique for spiral welds commonly used in the pipeline industry.

From a welding process point of view, any change in the welding process parameters, such as heat input, voltage, travel speed, and polarity, and the addition of electrodes can cause considerable changes in the appearance of the weld, i.e., weld shape and geometry and HAZ geometry [20,21,23,149]. Since the microstructure and mechanical properties of the weld are significantly influenced by the composition of the WM, as well as the welding process and weld and HAZ shape and geometry [7,203], it is essential to optimize and control the CWTSAW process parameters. On the other hand, since the operator cannot observe the weld pool in submerged arc welding as the arcs are shielded by the consumable/nonconsumable granular flux, great reliance is placed on process parameter optimization [13]. The welding process optimization can be performed by the development of mathematical models through effective and strategic planning, design and execution of experiments. However, the selection of parameters and their values should be carefully done to ensure appropriate values of the process parameters. For this reason, in the current work, twenty initial welding trails were carried out prior to the designed experiments. Statistically designed experiments based on Taguchi methodology were then conducted. Accordingly, thirty-six welding runs were done and the amount of dilution, the geometry characteristics, i.e., aspect ratio (AR), semi-penetration ratio (SPR), CGHAZ area (CGHAZA) and reinforcement area (RA), and the microhardness of the WM and CGHAZ were measured. Three mathematical and statistical methods were employed to investigate and optimize the CWTSAW process parameters in terms of evaluating the significance of the parameters on weld and HAZ geometry, dilution and mechanical properties. The goal was to find suitable values for the welding parameters and to develop equations to predict the weld and HAZ geometry under different welding conditions. Also, the CWTSAW process was

compared with the conventional TSAW process in terms of microstructural alterations and mechanical properties. Optical microscopy, scanning electron microscopy (SEM) and microhardness measurements were utilized to correlate the microstructures with property changes in the CGHAZ.

3.2. Experimental Procedure

3.2.1. Microalloyed steel and CWTSAW procedure

Weld samples were prepared by CWTSAW of 13.4 mm thick plates of X70 microalloyed steel. A 90° V-shaped bevel with 5 mm depth was machined in the steel plates prior to welding. Direct current electrode positive (DCEP) and square wave alternating current (ACSQ) polarity were employed using constant current type power sources to operate the lead and trail electrodes, respectively. The cold wire composition was the same as that of the electrodes. The compositions of the microalloyed steel and the consumable electrodes are indicated in Table 3-1. The 4 mm diameter wires for the electrodes and cold wire were selected based on EN756/EN14295 (BA-S2Mo, Bavaria, Germany) and AWS A5.17/A5.23 (EA2). The consumable flux was chosen according to EN 760 (BF6.5, Bavaria, Germany).

Table 3-1 X70 microalloyed steel and electrode composition (wt.%)

X70 composition								
C	P	S	Mn	Si	N	V+Mo+Nb+Ti	Cu+Ni+Cr+Sn+Al+Ca	Fe
0.04	0.01	0.001	1.76	0.24	0.01	0.21	0.60	97.13

Electrode and cold wire composition									
Symbol	C	P	S	Mn	Si	Mo	Ni	Cr	Cu
BA-S2Mo	0.10	0.007	0.01	1.04	0.1	0.56	0.02	0.03	0.03

The CWTSAW process setup and the fixed welding parameters are illustrated in Figure 3-1. Eight welding parameters including five main welding parameters, i.e., heat-input and voltage of the lead and trail electrodes and travel speed, and the three main cold wire parameters, i.e., position, angle and feed speed, were varied through welding (Table 3-2). According to the eight welding parameters with mixed levels (a combination of two and three levels) considered in this work, an L36 orthogonal array, Taguchi methodology [204] was used and thirty-six welding runs were conducted to investigate the correlation of CWTSAW parameters with the weld and HAZ geometry, dilution and mechanical properties.

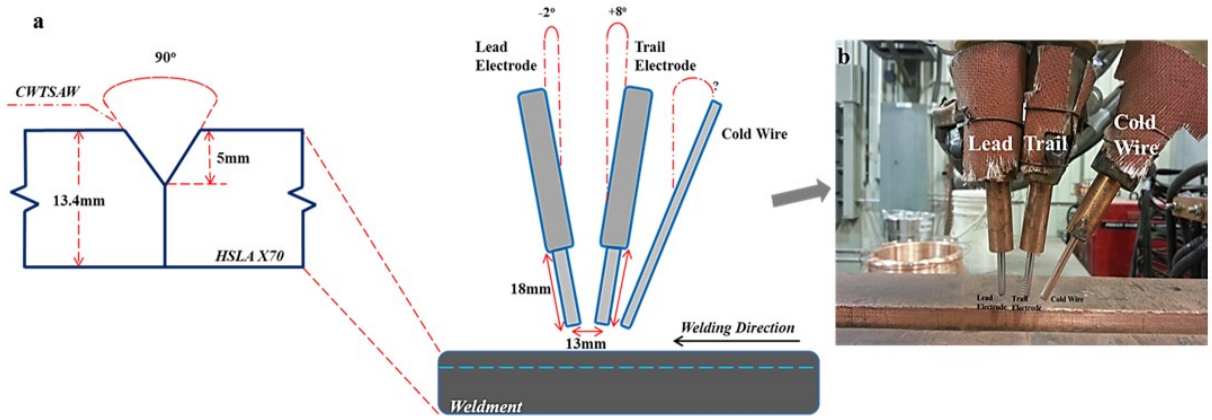

Figure 3-1 CWTSAW process setup. (a) Schematic view of fixed welding variables and weldment geometry. (b) Actual welding setup.

The geometry characteristics (i.e., SPR, AR, RA and CGHAZA), dilution and microhardness values were measured using a stereomicroscope (Fisher Scientific, Canada) and Vickers microhardness machine (Wilson VH3100, Buehler, Germany), respectively. Three measurements were carried out for each welding run to increase the accuracy of the final data for process analysis. Accordingly, 108 specimens were cut at the transverse direction relative to the welding direction and then mounted and polished according to ASTM E3-11 standard [205]. The weld samples were macro-etched with 4% Nital to reveal the WM, HAZ and their boundaries (Figure 3-2b).

3.2.2. Initial trials for welding parameter selection

In TSAW, the lead electrode is positioned to generate sufficient penetration of the weld and the trail electrode provides filling of the bevel, resulting in adequate joining of the metal pieces of interest. Accordingly, direct current electrode positive (DCEP) and alternating current square-wave (ACSQ) polarities were selected for the lead and trail electrode, respectively, as DCEP on the lead electrode causes deeper penetration and ACSQ on the trail electrode provides increased deposition rate relative to DCEP polarity [11]. Prior to starting the designed experiments, twenty welding trial runs were conducted to generate an overview of the CWTSAW process. During the early stages of setting up the CWTSAW process, the distance between the trail electrode and the cold wire was considered as a variable; however, through welding trials it was determined that the melting rate of the cold wire increased as the cold wire/trail electrode separation distance was decreased. In addition, the shape and size of weld bead changed when the cold wire position and angle were varied. Therefore, the position, angle and feed rate of the cold wire were used as the main cold wire parameters. Stick-out and electrode distance were set at 13 and 18 mm, respectively. The extreme values of the parameters, in particular those for the cold wire, were examined through welding trials by visual

inspection of the bead for visible defects, such as surface porosity, burn-through and undercutting. In many previous research studies, current has been selected as a welding variable; however, it was decided not to include current as a variable here. Since running a welding system at high current and low travel speed and vice versa is not a reasonable endeavor, in this research work heat input was considered as a major parameter and the current was set during welding according to the voltage and travel speed for welding in each run. The current is calculated according to Equation 3.1:

$$HI\left(\frac{kJ}{mm}\right) = \frac{\mu \cdot (V \cdot I)}{1000 \cdot TS} \qquad [3.1]$$

where μ is the arc efficiency, which depends on the welding process, and HI, V, I and TS are the heat input, voltage, current and travel speed (mm/s), respectively. The arc efficiency for submerged arc welding is 0.9-1.0.

Table 3-2 CWTSAW process parameters and levels

Symbol	***Process Parameter***	***Notation***	***Unit***	***Level 1***	***Level 2***	***Level 3***
A	Cold wire Position	CWP	….	Lagging	Side	….
B	Heat Input-Lead Electrode	HI-L	kJ/mm	1.10	1.20	….
C	Heat Input-Trail Electrode	HI-T	kJ/mm	0.95	1.08	….
D	Voltage-Lead Electrode	V-L	V	28	30	….
E	Voltage-Trail Electrode	V-T	V	30	34	….
F	Travel Speed	TS	mm/s	25.40	26.67	27.94
G	Cold wire Angle	CWA	degree	32	47	63
H	Cold wire Feed Speed	CWFS	mm/s	8.50	10.60	12.70

3.2.3. Developing the experimental design matrix

Since the results and conclusions that can be drawn from an experiment depend to a large extent on the manner in which the data are collected, a well-designed experiment is of major importance. Experimental design methods were originally developed by Fisher [206,207]. However, classical experimental design methods are too complex and are not easy to use. Furthermore, a large number of experiments have to be carried out as the number of the process parameters increases [208,209]. The Taguchi method developed by Genichi Taguchi employs a design of orthogonal arrays to study entire parameters with a small number of experiments relative to other experimental design methods. It was proposed that engineering optimization of a process or product should be carried out in a three-step approach: system design, parameter design and

tolerance design [204,210]. The objective of parameter design is to optimize the settings of the process parameter values for improving quality characteristics and to identify optimal process parameter values. In addition, it is expected that the optimal process parameter values obtained from parameter design will be insensitive to variation in environmental conditions and other noise factors. The quality engineering method of Taguchi methodology, i.e., employing designed experiments, provides an efficient and systematic way to optimize designs for performance, quality and cost. The use of Taguchi methodology simplifies the optimization procedure for determining optimal welding parameters in the SAW process. Dhas et al. [208], Tarng et al. [21,209] and Yang [211,212] have studied the optimization of SAW process parameters using Taguchi methodology.

According to the orthogonal arrays proposed by Taguchi, the design matrix for the welding process, including five parameters with two levels and three parameters with three levels, is an L36 orthogonal array which comprises 36 weld runs where the levels for each parameter are equally repeated through the design. The designed experiments based on the L36 orthogonal array are summarized in Table 3-4.

Table 3-3 Design matrix based on L36 orthogonal array

Run	A (CWP)	B (HIL)	C (HIT)	D (VL)	E (VT)	F (TS)	G (CWA)	H (CWFS)
1	1	1	1	1	1	1	1	1
2	1	1	1	1	1	2	2	2
3	1	1	1	1	1	3	3	3
4	1	1	1	1	1	1	1	1
5	1	1	1	1	1	2	2	2
6	1	1	1	1	1	3	3	3
7	1	1	2	2	2	1	1	2
8	1	1	2	2	2	2	2	3
9	1	1	2	2	2	3	3	1
10	1	2	1	2	2	1	1	3
11	1	2	1	2	2	2	2	1
12	1	2	1	2	2	3	3	2
13	1	2	2	1	2	1	2	3
14	1	2	2	1	2	2	3	1
15	1	2	2	1	2	3	1	2
16	1	2	2	2	1	1	2	3
17	1	2	2	2	1	2	3	1
18	1	2	2	2	1	3	1	2
19	2	1	2	2	1	1	2	1
20	2	1	2	2	1	2	3	2
21	2	1	2	2	1	3	1	3
22	2	1	2	1	2	1	2	2
23	2	1	2	1	2	2	3	3
24	2	1	2	1	2	3	1	1
25	2	1	1	2	2	1	3	2
26	2	1	1	2	2	2	1	3
27	2	1	1	2	2	3	2	1
28	2	2	2	1	1	1	3	2
29	2	2	2	1	1	2	1	3
30	2	2	2	1	1	3	2	1
31	2	2	1	2	1	1	3	3
32	2	2	1	2	1	2	1	1
33	2	2	1	2	1	3	2	2
34	2	2	1	1	2	1	3	1
35	2	2	1	1	2	2	1	2
36	2	2	1	1	2	3	2	3

3.3. Results and Discussion

The geometry characteristics, dilution and microhardness were measured to correlate the weld parameters with weld characteristics and properties. More details regarding the measured characteristics are provided in the Appendix (Table 3-A.1). SPR and AR are unitless characteristics defined by Equations 3.2 and 3.3, respectively.

$$AR = \frac{\text{Penetration Depth}}{\text{Bead Width}} \qquad [3.2]$$

$$SPR = \frac{\text{Weld Width at Half Penetration}}{\text{Bead Width}} \qquad [3.3]$$

Since the amount of dilution will influence the composition of the weld pool, and influence its metallurgical and mechanical properties, it is important to optimize the welding process based on the weld dilution. Dilution was calculated using the expression reported by Lancaster in Equation 3.4 [42]:

$$Dilution = \frac{\text{weight of parent metal melted}}{\text{total weight of fused metal}} = \frac{(\text{Penetration area} - \text{bevel area})}{(\text{penetration area} + \text{reinforcement area})} \qquad [3.4]$$

where penetration depth, bead width and weld width at half penetration are indicated in Figure 3-2b. As stated earlier, process optimization was carried out according to dilution and weld and HAZ geometry. Figure 3-2 depicts a macrograph of an X70 microalloyed steel welded by CWTSAW showing the weld geometry characteristics. A weld with large SPR and AR, and smaller dilution, CGHAZ area and reinforcement area, is desirable.

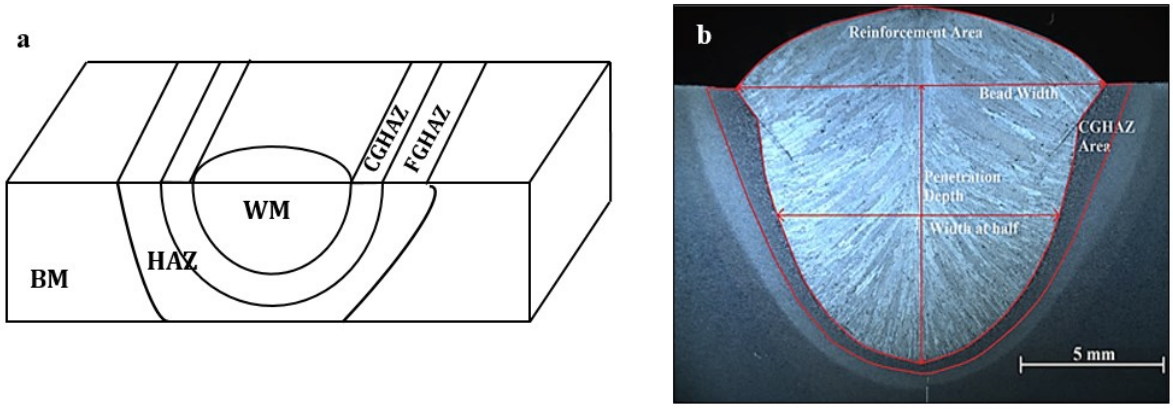

Figure 3-2 (a) Schematic of the welded steel indicating different weld zones. (b) Optical macrograph of X70 microalloyed steel welded by CWTSAW, indicating the geometry characteristics.

3.3.1. CWTSAW process parameters investigation

Three analysis steps were performed on the weld characteristic data to investigate and optimize the CWTSAW process parameters. The first step was to understand the significance of the welding parameters on the geometry characteristics and dilution; this was done by the analysis of variance (ANOVA) method. Taguchi methodology augmented the optimization procedure by evaluating the parameter levels resulting in the optimal effect on geometry characteristics and dilution. Since there is a need in welding related industries to be able to predict weld geometry for different

combinations of welding parameters, three-order multiple regression analysis (TOMRA) was employed to develop equations predicting geometry characteristics and dilution. Minitab software 17.0, a commercial statistical package, was utilized to perform the mathematical data analysis.

ANOVA was carried out on the data extracted from geometry, dilution and microhardness measurements. The purpose of ANOVA was to determine which welding process parameters significantly affected the parametric characteristics (i.e., geometry, dilution and microhardness) when all eight parameters were varied. The significance of the welding parameters on the parametric characteristics was mainly evaluated in terms of the F-test [213], P-value [20,208,211,212] and percentage contribution of each parameter. The detailed raw data extracted from ANOVA for the sum of the squares (adj SS), F-values and P-values of the welding variables are presented in the Appendix (Table 3-A.2). P-value is the probability of significance. A 90% confidence level was selected in the data analysis, which means that if the P-value for a factor is less than 0.1 then the welding parameter significantly influences the parametric characteristic. The F-test represents the systematic variance; if the independent variable (welding parameter) has an effect, then the dependent variable (parametric characteristic) should vary under different experimental conditions. Therefore, a higher F-value for a variable indicates that the parameter has a significant effect on the parametric characteristic [214]. As an example, the parameters which are highly significant for SPR are trail electrode voltage, travel speed and cold wire feed speed.

The percentage contribution of the parameters was calculated by measuring the sum of the squared deviations (deviations from the total mean value) and converting into contributions for each of the process parameters, according to Equation 3.5:

$$\text{Percentage contribution: } \rho\% = \frac{SS_i}{SS_{tot.}} \qquad [3.5]$$

where ρ is the contribution in percent of each parameter to the performance characteristic and SS_i and $SS_{tot.}$ are the sum of the squares for each parameter and the total sum of the squares, respectively. The percentage contribution for each of the process parameters in the total sum of the squared deviations can be used to evaluate the importance of the process parameter change on the performance characteristic. Based on Equation 3.5, the percentage contribution for each welding parameter was calculated and the values are shown in Figure 3-3. Accordingly, the maximum percentage contribution for the cold wire parameters (CWP, CWA and CWFS) on the geometry characteristics was 32.6% for AR. Also, the contribution for dilution variation was 35.7%. However, the other welding parameters (i.e., heat-input, voltage and TS) had a greater effect on the geometry characteristics and dilution of the weld compared with the cold wire parameters.

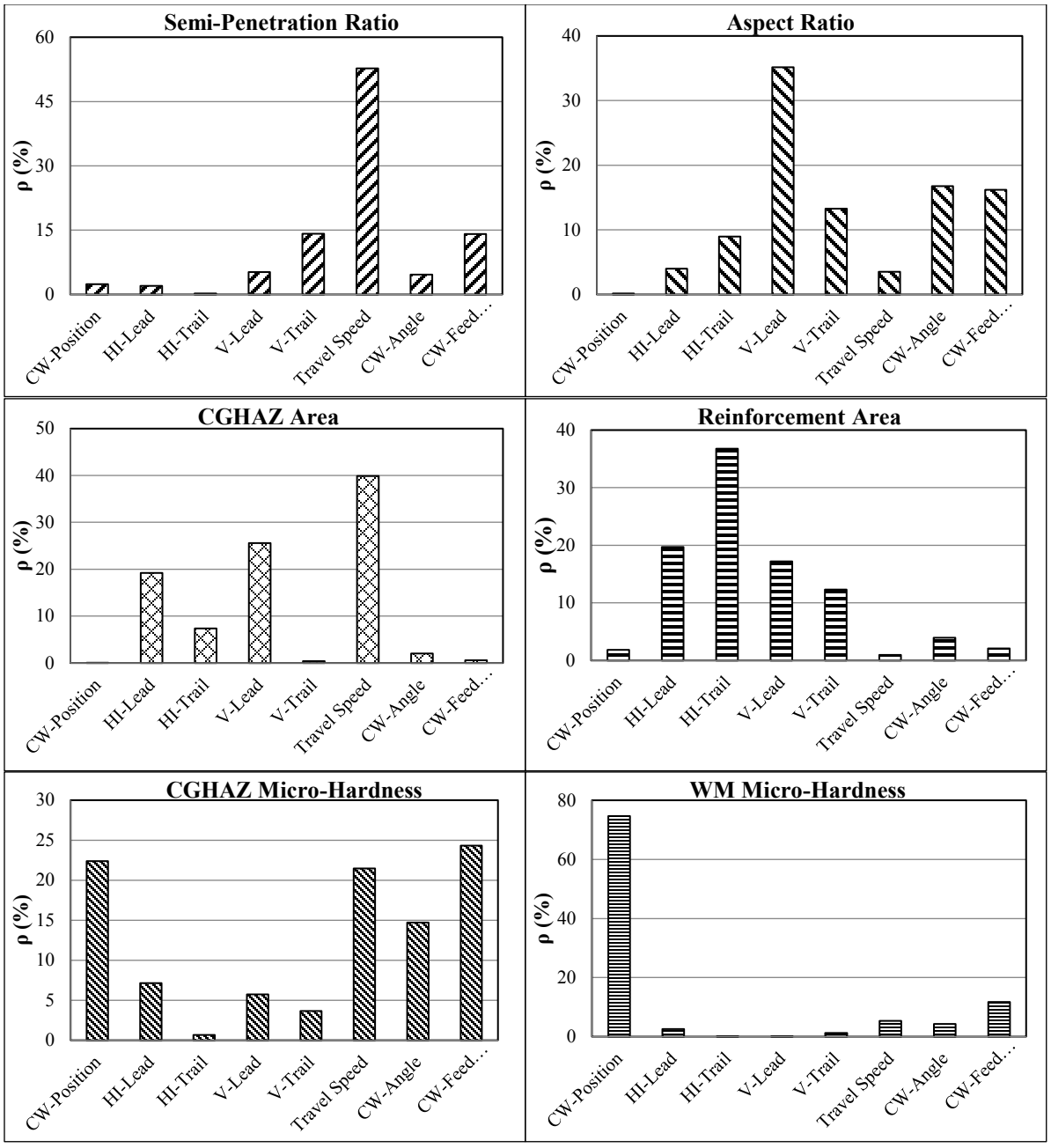
Semi-Penetration Ratio
ρ (%)
60
45
30
15
0
CW-Position
HI-Lead
HI-Trail
V-Lead
V-Trail
Travel Speed
CW-Angle
CW-Feed…
Aspect Ratio
ρ (%)
40
30
20
10
0
CW-Position
HI-Lead
HI-Trail
V-Lead
V-Trail
Travel Speed
CW-Angle
CW-Feed…
CGHAZ Area
ρ (%)
50
40
30
20
10
0
CW-Position
HI-Lead
HI-Trail
V-Lead
V-Trail
Travel Speed
CW-Angle
CW-Feed…
Reinforcement Area
ρ (%)
40
30
20
10
0
CW-Position
HI-Lead
HI-Trail
V-Lead
V-Trail
Travel Speed
CW-Angle
CW-Feed…
CGHAZ Micro-Hardness
ρ (%)
30
25
20
15
10
5
0
CW-Position
HI-Lead
HI-Trail
V-Lead
V-Trail
Travel Speed
CW-Angle
CW-Feed…
WM Micro-Hardness
ρ (%)
80
60
40
20
0
CW-Position
HI-Lead
HI-Trail
V-Lead
V-Trail
Travel Speed
CW-Angle
CW-Feed…

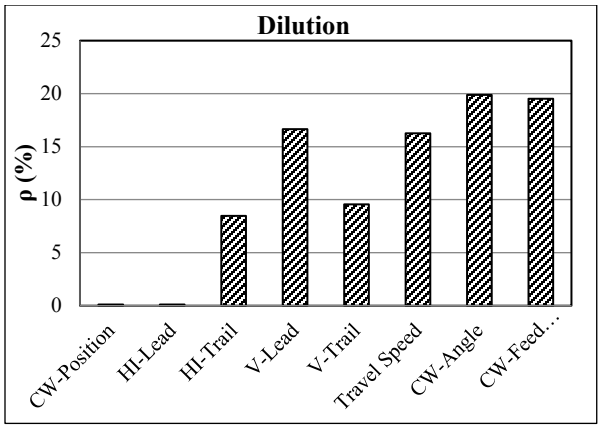

Figure 3-3 Significance of CWTSAW process parameters on geometry characteristics, dilution and microhardness of the WM and the CGHAZ.

Microhardness measurements of the thirty-six weld samples were done along the BM, HAZ and WM according to ASTM E384 [215] to investigate the significance of CWTSAW parameters on the mechanical properties of the WM and CGHAZ. A 500 g load was applied for a dwell time of 14 s per indentation. In total, 40 test points were examined per weld sample, with an average of 10-12 indents across each of the CGHAZ and WM. Figure 3-4 depicts the hardness measurement mapping for a typical welded sample using CWTSAW.

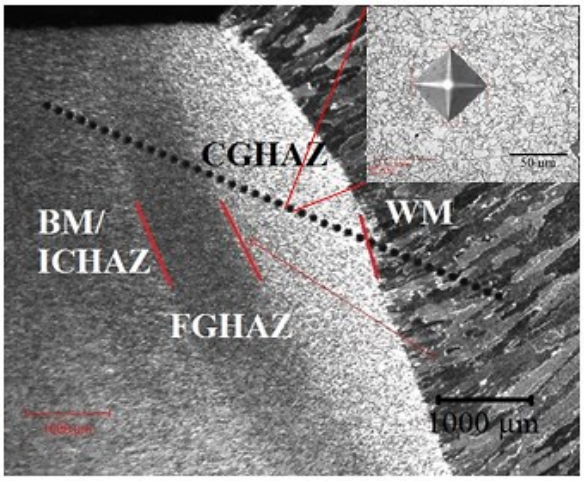

Figure 3-4 Microhardness mapping along the BM, HAZ and WM of a typical weld prepared by CWTSAW. The micrograph in the inset shows an indentation in the CGHAZ.

According to the ANOVA results for the hardness measurements, cold wire parameters i.e., position, angle and feed speed of the cold wire, show a significant effect on the hardness of the WM and CGHAZ. Other welding parameters, for the ranges studied, did not have a significant effect on the hardness for either the WM or CGHAZ. It should be noted that the parameter ranges were

selected based on initial welding trials. Microstructural analysis was carried out on two weld samples and is discussed in the next section. As stated earlier, the percentage contribution for each of the process parameters can also be used to evaluate the importance of a process parameter change on the performance characteristic. As shown in Figure 3-3, TS and the cold wire parameters, in particular variation in CWFS, show a significant contribution to the variation in hardness of the WM and CGHAZ compared with the other welding parameters. The CWFS effect is related to the heat introduced to the weldment and, consequently, the cooling rate within the WM and CGHAZ.

The control factors that may contribute to reducing variation (improving quality) can be quickly identified by looking at the amount of variation present as a response. The signal-to-noise ratio (S/N) was used to determine the deviation of the geometry characteristic and dilution from the desired value. Dilution, RA and CGHAZA belong to a "lower-the-better" quality characteristic. SPR and AR are "higher-the-better" quality characteristics. Since there is no general agreement to judge and determine whether lower or higher hardness leads to better overall mechanical properties, S/N ratio analysis was not performed on the microhardness values. The S/N ratio can be expressed as Equations 3.6 and 3.7 [204,210]:

$$\text{Lower-the-better: } (S/N)_{ratio} = -10\, log_{10}\left(\frac{1}{n}\sum_{i=1}^{n} {y_{ij}}^2\right) \qquad [3.6]$$

$$\text{Higher-the-better: } (S/N)_{ratio} = -10\, log_{10}\left(\frac{1}{n}\sum_{i=1}^{n} \frac{1}{{y_{ij}}^2}\right) \qquad [3.7]$$

where y_{ij} and n are the experimental values of the ith performance characteristic in the jth experiment and the number of trials, respectively. A level of input parameter with a higher average S/N ratio is considered as the best value of the parameter with an optimal effect on the geometry characteristics, i.e., SPR, AR, CGHAZA and RA, and dilution, since the largest S/N ratio indicates that the signal obtained from the considered parameters is much higher than the random effects of the noise factors [204,210]. The average S/N ratios for dilution and the geometry characteristics are provided in the Appendix (Table A.A-3). The higher S/N ratio for each parameter level shows an optimal effect on the parametric characteristics. Based on the calculated S/N ratio of the welding parameters, the suitable levels for the CWTSAW process parameters are indicated in Table 3-4. Overall, it can be concluded that the optimal parametric characteristics (i.e., weld and HAZ geometry and dilution) are achieved when the cold wire is fed at a lagging position (level 1) with a feed speed of 8.5 mm/s (level 1) and a high angle of 63° (level 3).

Table 3-4 Suitable levels of CWTSAW process parameters

SPR	CWP**1** HI-L**1** HI-T**1** V-L**1** V-T**1** T.S.**3** CWA**3** CWFS**1**
AR	CWP**1** HI-L**2** HI-T**1** V-L**1** V-T**1** T.S.**3** CWA**1** CWFS**1**
CGHAZA	CWP**2** HI-L**1** HI-T**1** V-L**2** V-T**2** T.S.**3** CWA**3** CWFS**2**
RA	CWP**1** HI-L**1** HI-T**1** V-L**2** V-T**2** T.S.**2** CWA**1** CWFS**1**
Dilution	CWP**1** HI-L**1** HI-T**2** V-L**2** V-T**1** T.S.**3** CWA**3** CWFS**1**

Multiple regression analysis, a statistical tool to ascertain the relationships among variables, was employed to predict the geometry characteristics of the welds prepared by the CWTSAW process. The developed empirical equations predict the weld geometry for different combinations of the CWTSAW parameters, which is important from an engineering and industrial perspective. The most frequently used method is that of linear equations. Three-order multiple regression analysis (TOMRA) considers the interaction of variables and their contributions to predicting the characteristics. TOMRA takes the form shown in Equation 3.8:

$$Y = \alpha_0 + \sum_{i=1}^{8}(\alpha_i \cdot x_i) + \sum_{i=1}^{8}(\alpha_{ii} \cdot x_i^2) + \sum_{i=1}^{8}\sum_{j>i}^{8}(\alpha_{ij} \cdot x_i \cdot x_j) + \sum_{i=1}^{8}(\alpha_{iii} \cdot x_i^3) + \sum_{i=1}^{8}\sum_{j>i}^{8}\sum_{k>j}^{8}(\alpha_{ijk} \cdot x_i \cdot x_j \cdot x_k) \qquad [3.8]$$

where Y is the dependent variable (geometry characteristics) which is to be predicted and x_i is the known variable (welding parameters) on which the predictions are made; α, α_i, α_{ii}, α_{ij}, α_{iii} and α_{ijk} are the coefficients. Multiple regression analysis of the CWTSAW process parameters is expressed in third-order equations, which are presented in the Appendix.

Table 3-5 CWTSAW samples used for confirmatory test of the developed equations

Weld id.	A(CWA)	B(HIL)	C(HIT)	D(VL)	E(VT)	F(TS)	G(CWA)	H(CWFS)
CT17	1	1.153	1.052	30	34	26.67	47	10.6
CT18	2	1.153	1.052	30	34	26.67	47	10.6
CT19	2	1.164	0.95	30	34	29.63	47	10.6
CT20	1	1.199	1.019	30	34	27.52	47	10.6

TOMRA employs the same analysis strategy as the ANOVA in which parameter interaction is accounted for as well. The welding parameters (including interactions), which result in higher sum of the squares (deviation from the mean value of a parametric characteristic), are considered to predict the parametric characteristic. As an example, only 19 variables from a total of 92 possible variables (including parameter interactions) are considered in the SPR equation, resulting in an equation which fits the observed values. Accordingly, the computed values for the geometry

characteristics were compared with the observed values from the experiments and showed good fitting. The validity of the equations was tested with four random combinations of weld and cold wire parameters (Table 3-5). The geometry characteristics of four welds with different CWTSAW parameter levels were measured and compared with the calculated values from the equations and showed good correlation with the actual values (Figure 3-5).

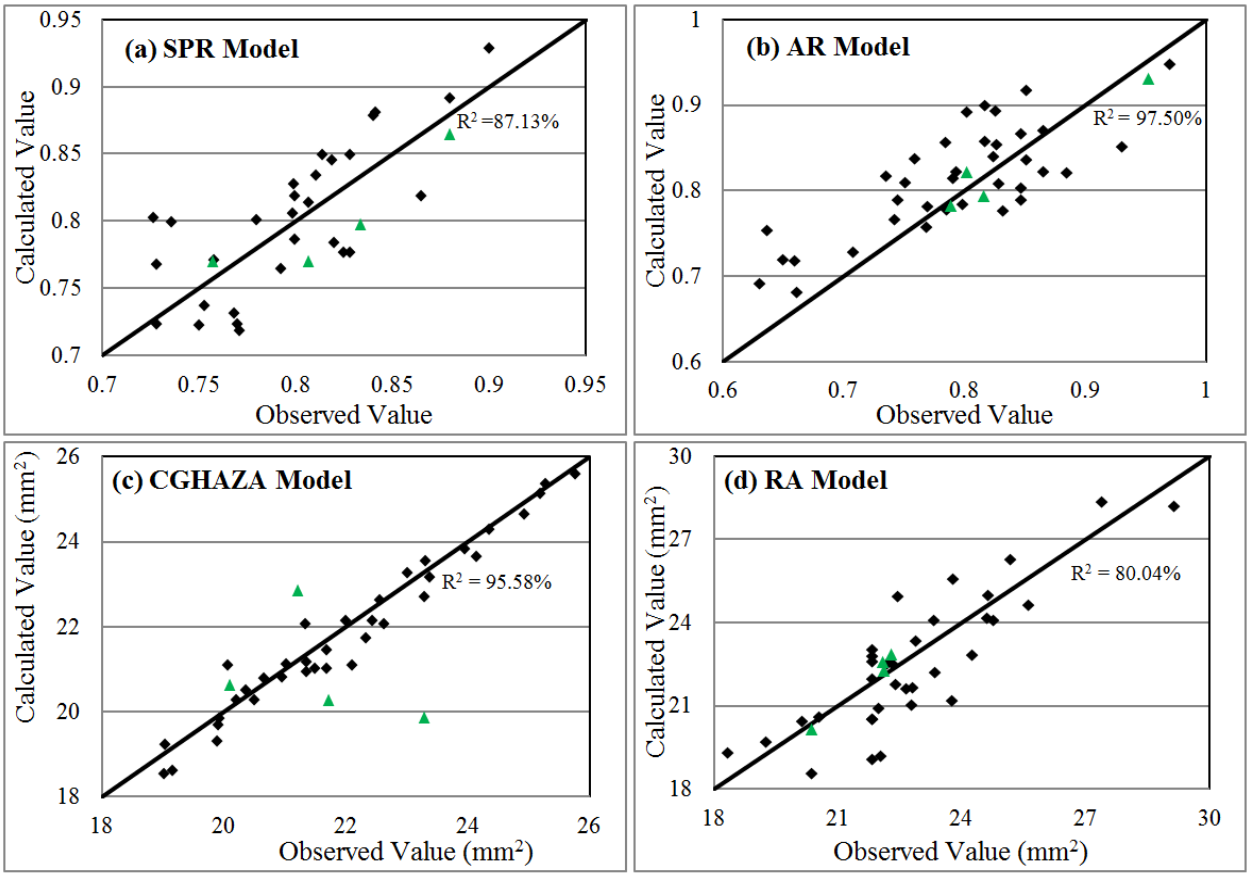

Figure 3-5 Comparison of calculated values and observed values for (a) SPR, (b) AR, (c) CGHAZA and (d) RA. The confirmatory test results are superimposed on the graphs (triangles). The straight line indicates the ideal condition in which the predicted values are equal to the observed values.

3.3.2. CWTSAW and TSAW comparison

Two weld samples, prepared by the CWTSAW and TSAW processes, were evaluated in terms of weld geometry, dilution and the CGHAZ microhardness. The welding conditions for preparation of the two weld samples are indicated in Table 3-6. Figure 3-6 depicts macrographs of the two weld samples, both with the same heat input of 2.15 kJ/mm. A comparison of the welds prepared by CWTSAW and conventional TSAW is given in Table 3-7. There is a significant reduction from 21.3 to 19.1 mm^2 and 0.65 to 0.56 in the CGHAZA and dilution, respectively. Also, the microhardness of the

CGHAZ was reduced by addition of a cold wire to the TSAW process. It is generally accepted that the part of the HAZ adjacent to the fusion line, which is characterized by the coarse grains associated with M-A constituents, localized brittle zones (LBZ), is the weakest region resulting in low toughness. The cold wire addition showed a reduction in the size of CGHAZ and a reduction in the CGHAZ microhardness, due to a reduction in the actual heat introduced to the weldment and the corresponding microstructural changes.

Table 3-6 Weld parameters used for CWTSAW and TSAW comparison

Weld type	HIL (kJ/mm)	HIT (kJ/mm)	VL (V)	VT (V)	TS (mm/sec)	CWP	CWA (degrees)	CWFS (mm/sec)
TSAW	1.15	1.00	30	33	25.4	NA	NA	NA
CWTSAW	1.15	1.00	30	33	25.4	Lagging	47	8.5

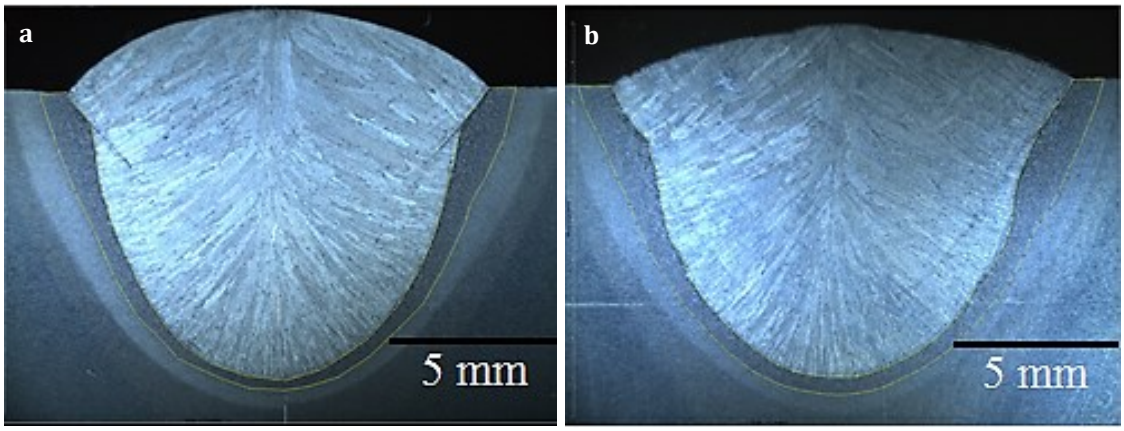

Figure 3-6 Macrographs of welds produced by: a) CWTSAW and b) TSAW. There is a reduction of ~10% in the CGHAZ area for the CWTSAW sample relative to the TSAW sample. The CGHAZ has been outlined in both images.

SEM and optical metallography of the CGHAZ of the steel samples, welded by both processes, indicate that the prior austenite grain (PAG) size decreased as the cold wire was added to the welding process. The PAG size of the CGHAZ (0-300 μm away from the fusion line) decreased from 56 to 45 μm on adding the cold wire. This phenomenon is attributed to a reduction in the actual heat introduced to the weldment, lowering of the peak temperature, reduction in the retention time in the austenitization temperature range (1100-1400°C) and an increase in the cooling rate by adding the cold wire. Eight SEM and optical micrographs were analyzed from the CGHAZ of each weld sample at the transverse direction relative to the welding direction. Figure 3-7 shows the microstructure of the CGHAZ for the CWTSAW and TSAW samples. The CGHAZ microstructure of

the TSAW sample (higher heat input) is comprised of large PAGs, polygonal ferrite and large elongated M-A constituents along the PAG boundaries. In contrast, the CGHAZ microstructure of the CWTSAW sample (lower heat input) has smaller PAGs and a region of polygonal ferrite associated with blocky shaped M-A constituents.

Table 3-7 Effect of cold wire addition on dilution, microhardness and geometry characteristics (three weld samples were analyzed for each welding condition)

Heat-input: 2.15 kJ/mm	**CWTSAW (CWFS: 8.5 mm/s)**	**TSAW**
CGHAZ area (mm^2)	19.10±0.81	21.30±0.63
Reinforcement area (mm^2)	24.90±1.82	18.60±1.50
Penetration area (mm^2)	86.50±0.50	97.30±1.04
Dilution	0.56±0.01	0.65±0.02
CGHAZ hardness (HV0.5)	222.93±6.46	236.11±7.02

The M-A constituents appear as a shiny white phase using LePera's etchant [140] (Figure 3-7d and Figure 3-7h). The M-A fraction in the CGHAZ of each weld sample was analyzed using ImageJ software (Figure 3-7j-n). Both optical and SEM micrographs were used for the M-A fraction analysis. The M-A fraction in the CGHAZ of the TSAW and CWTSAW samples, calculated from the SEM micrographs (Figure 3-7n and Figure 3-7m), was 7.6% and 5.4%, respectively, indicating a reduction in the fraction of M-A as a consequence of PAG size reduction [177,216–218] by cold wire addition. The M-A fraction in the CGHAZ, calculated from the optical micrographs (Figure 3-7j and Figure 3-7i), was 5.8% and 3.9% for the TSAW and CWTSAW samples, respectively. The trend is the same and the quantitative values are quite similar for both techniques, which confirm the validity of the M-A identification in the SEM images. The larger M-A constituents in the CGHAZ of the TSAW sample are due to the higher martensite start temperature (Ms) for samples with larger PAGs [177,217,219,220]. Bhadeshia et al. [139,217] found that as the PAG size decreases the Ms temperature also decreases, resulting in a lower volume fraction of martensite. The fraction of martensite is a function of the undercooling below the Ms temperature according to the classical Koistinen-Marburger (KM) equation [216] and the geometrical partitioning model by Fisher et al. [221]. According to the proposed models, the martensite volume fraction formed in the early stages of the transformation is proportional to the cube of the PAG size; hence, "the fraction of the transformation needed to detect Ms is reached at a smaller undercooling when the PAG size is larger" [217]. Therefore, a coarser PAG size increases the fraction and size of the M-A constituent. Li

et al. [177] and Yu et al. [218] showed that a coarse PAG size associated with a coarse M-A constituent is the dominant factor in promoting brittle fracture in the CGHAZ. Accordingly, there is a concurrent effect of both grain size refinement and M-A transformation, which plays a significant role in the strength, hardness and toughness of the HAZ. Due to the formation of the M-A constituent, there is a higher proportion of localized hardened zones in the CGHAZ of the TSAW sample compared with the CWTSAW sample. This shows up as higher microhardness values in the CGHAZ for the TSAW sample relative to the CWTSAW sample. Also, M-A constituents (LBZs) did not form along PAG boundaries in the HAZ of the CWTSAW sample, which should result in improved fracture toughness for the HAZ.

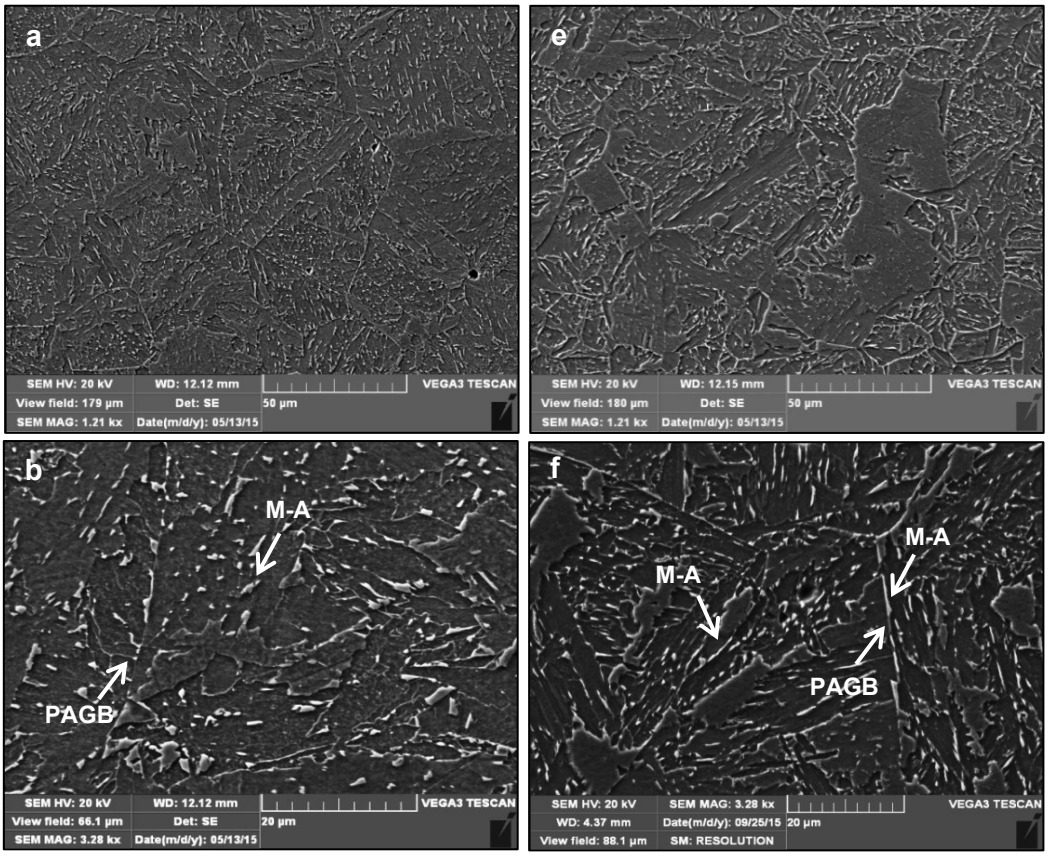

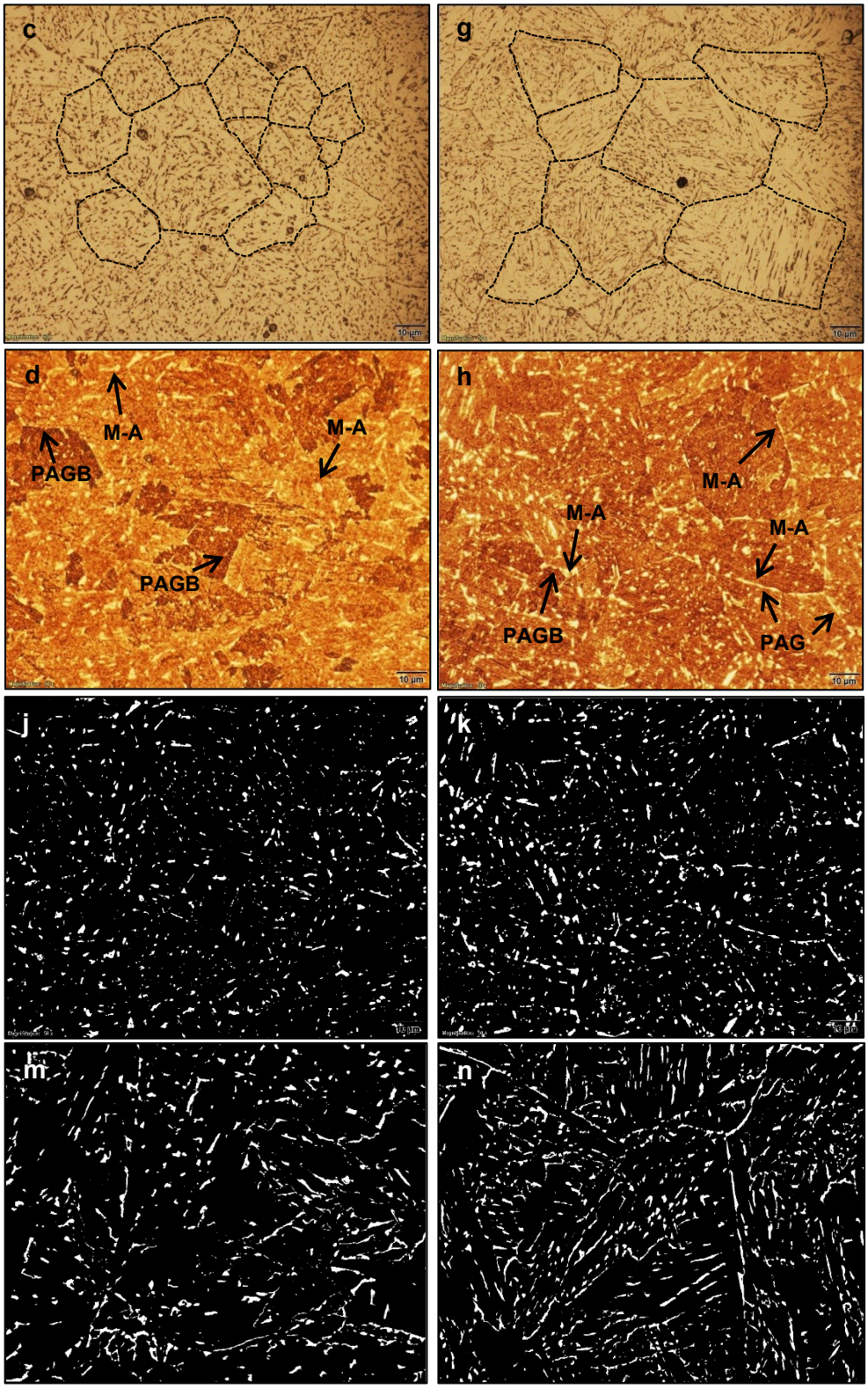

Figure 3-7 SEM SE images (a, b, e, f) and optical micrographs (c, d, g, h) of the CGHAZ of the steel welded using CWTSAW (a-d) and TSAW (e-h). M-A constituent analysis in the CGHAZ of the CWTSAW and TSAW sample (j, m) and the CGHAZ of the TSAW sample (k, n).

3.4. Conclusions

The influence of the cold wire tandem submerged arc welding (CWTSAW) process parameters on the geometry, dilution and microhardness of the weld and the HAZ was investigated and optimized for the first time in this research work. The following conclusions were drawn from the research work done on CWTSAW:

1) Variations in the cold wire parameters showed significant effects on the geometry characteristics, i.e., semi-penetration ratio (SPR) and aspect ratio (AR), dilution and the weld metal (WM) and coarse grain heat affected zone (CGHAZ) microhardness. The effects are a consequence of the considerable reduction in the total heat introduced to the weldment and the subsequent change in cooling rate when a cold wire is added to the molten pool during CWTSAW.
2) The maximum effect of cold wire parameter variation on geometry characteristics and dilution was 33.1% and 39.5%, respectively, compared with other parameters. The addition of cold wire at a lagging position with a feed speed of 8.5 mm/s at 63° resulted in an overall improvement in the weld geometry and properties.
3) There was a 14.0% and 10.3% reduction in dilution and CGHAZ area, respectively, for the CWTSAW process, because of a reduction in the overall heat introduced to the weldment.
4) Microstructural analysis, using both optical microscopy and scanning electron microscopy (SEM), indicated the formation of a finer prior austenite grains (PAG) and less M-A constituent within the CGHAZ of the CWTSAW samples, which is attributed to lower actual heat introduced to the weldment and faster cooling rates. These effects also led to lower microhardness values in the CGHAZ of the CWTSAW samples.

Appendix A

The measured values for SPR, AR, CGHAZA, RA, dilution, WM and CGHAZ microhardness are presented in Tables A.A-1 and A.A-2 in this section. The S/N ratios for the welding parameters for each parametric characteristic are indicated in Table A.A-3.

The developed empirical equations to predict the weld and HAZ geometry, performed by the TOMRA method, are presented below:

$$\mathbf{SPR} = 33.3 - 16.4 \cdot C - 0.56 \cdot D - 0.92 \cdot E - 0.18 \cdot F - 0.23 \cdot G - 0.8 \cdot H + 0.56 \cdot C \cdot E + 0.49 \cdot C \cdot G - 0.6 \cdot C \cdot H + 0.01 \cdot D \cdot E + 0.01 \cdot D \cdot F - 0.01 \cdot D \cdot G + 0.06 \cdot D \cdot H + 0.01 \cdot E \cdot G + 0.03 \cdot E \cdot H - 0.02 \cdot C \cdot E \cdot G + 0.01 \cdot C \cdot E \cdot H + 0.0003 \cdot D \cdot E \cdot G - 0.0017 \cdot D \cdot E \cdot H$$

$$\mathbf{AR} = 3199.7 - 110.4 \cdot A - 818 \cdot B - 543.3 \cdot C - 35.61 \cdot D - 17.95 \cdot E - 136.9 \cdot F + 11.12 \cdot G - 2.39 \cdot H + 32.82 \cdot A \cdot B + 2.26 \cdot A \cdot C + 3.13 \cdot A \cdot F + 0.07 \cdot A \cdot G + 1.81 \cdot A \cdot H + 0.67 \cdot B \cdot D + 32.22 \cdot B \cdot F - 2.09 \cdot B \cdot G + 3.23 \cdot B \cdot H + 23.55 \cdot C \cdot F - 1.87 \cdot C \cdot G + 1.55 \cdot D \cdot F - 0.13 \cdot D \cdot G - 0.03 \cdot D \cdot H + 0.79 \cdot E \cdot F - 0.07 \cdot E \cdot G - 0.01 \cdot F \cdot G - 0.006 \cdot G \cdot H - 0.28 \cdot A \cdot B \cdot G - 1.65 \cdot A \cdot B \cdot H$$

$$\mathbf{CGHAZA} = 154 + 2.36 \cdot D - 17.8 \cdot F - 43.7 \cdot A \cdot C + 7 \cdot B \cdot F + 0.25 \cdot D \cdot F + 0.08 \cdot D \cdot G - 67 \cdot A \cdot B^2 + 77.4 \cdot A \cdot B \cdot C + 2.27 \cdot A \cdot B \cdot D + 1.69 \cdot A \cdot B \cdot F - 1.91 \cdot A \cdot C \cdot D - 0.03 \cdot A \cdot D \cdot G - 0.01 \cdot A \cdot F^2 + 0.01 \cdot A \cdot G^2 - 0.01 \cdot A \cdot G \cdot H - 69.3 \cdot B^2 \cdot C + 57 \cdot B \cdot C^2 - 0.14 \cdot B \cdot D^2 - 0.01 \cdot B \cdot F \cdot G - 0.04 \cdot C \cdot G \cdot H - 0.002 \cdot D \cdot F \cdot G - 0.0004 \cdot E \cdot G^2 + 0.002 \cdot E \cdot G \cdot H + 0.001 \cdot F^2 \cdot G$$

$$\mathbf{RA} = 276 - 270 \cdot B - 159 \cdot C - 1.14 \cdot A \cdot H + 149 \cdot B \cdot C + 3.13 \cdot A \cdot B \cdot H + 0.79 \cdot A \cdot C \cdot H - 0.11 \cdot A \cdot D \cdot H + 1.34 \cdot B^2 \cdot D - 0.0003 \cdot D^2 \cdot E$$

Note that the parameters A, B, C, … correspond to the symbols given in the first column of Table A.A-2.

Table A.A.1 Measured weld characteristics- three specimens were characterized for each welding run

Weld no.	SPR	AR	CGHAZA (mm^2)	RA (mm^2)	Dilution	CGHAZ Hardness (HV0.5)	WM Hardness (HV0.5)
1	0.83±0.04	0.90±0.05	22.44±1.38	22.57±0.14	0.60±0.03	234.85±5.01	244.33±1.53
2	0.80±0.04	0.84±0.04	21.34±0.33	22.98±0.45	0.58±0.01	234.33±2.96	243.89±5.22
3	0.82±0.04	0.80±0.04	20.07±1.36	22.74±0.71	0.60±0.02	233.70±8.11	252.50±4.04
4	0.81±0.02	0.86±0.01	22.02±1.36	20.51±3.21	0.59±0.02	232.20±5.16	250.77±4.38
5	0.87±0.01	0.92±0.02	22.62±0.47	19.07±1.28	0.61±0.01	229.33±5.45	239.92±6.73
6	0.83±0.02	0.87±0.04	22.12±1.41	20.51±0.68	0.58±0.01	233.54±7.04	248.09±3.48
7	0.74±0.02	0.69±0.03	25.19±0.23	21.74±1.25	0.60±0.02	231.36±7.80	245.64±3.10
8	0.73±0.01	0.68±0.01	23.95±1.04	22.52±1.62	0.57±0.02	235.31±4.92	250.38±3.50
9	0.90±0.08	0.81±0.10	20.36±0.39	21.59±4.23	0.61±0.03	237.88±6.83	243.11±3.16
10	0.74±0.04	0.86±0.13	21.03±1.36	20.61±0.99	0.58±0.01	236.30±4.08	245.36±4.52
11	0.77±0.02	0.72±0.04	20.22±1.05	20.41±1.46	0.59±0.01	228.00±6.94	242.62±4.46
12	0.89±0.01	0.87±0.00	19.04±0.44	18.54±1.12	0.63±0.01	240.75±9.71	247.71±3.22
13	0.75±0.02	0.82±0.01	25.27±0.81	24.98±0.87	0.57±0.01	227.77±7.40	245.90±9.27
14	0.80±0.02	0.82±0.01	22.57±0.99	23.35±0.80	0.61±0.01	238.29±7.37	253.75±5.38
15	0.80±0.02	0.79±0.04	20.66±0.40	21.15±3.26	0.62±0.02	227.69±5.07	247.70±3.47
16	0.76±0.01	0.75±0.02	23.02±1.07	24.62±2.01	0.61±0.01	225.38±9.43	241.13±5.51
17	0.75±0.05	0.89±0.04	23.31±0.84	24.04±4.01	0.62±0.02	236.80±9.23	247.40±5.15
18	0.80±0.04	0.84±0.04	19.91±0.50	26.28±2.37	0.61±0.01	226.67±8.28	241.69±5.64
19	0.77±0.05	0.81±0.10	20.51±0.18	21.03±4.64	0.61±0.04	224.92±9.62	244.00±5.61
20	0.79±0.07	0.79±0.08	19.89±0.55	22.51±5.05	0.62±0.04	229.38±4.50	236.33±2.12
21	0.85±0.01	0.85±0.04	19.03±0.48	21.95±0.47	0.64±0.01	233.80±4.89	247.42±6.00
22	0.73±0.01	0.73±0.02	21.50±0.19	25.53±1.48	0.58±0.01	226.50±4.19	239.92±5.85
23	0.76±0.01	0.78±0.07	19.93±0.42	22.79±4.04	0.59±0.01	231.00±4.85	237.50±4.74
24	0.81±0.03	0.82±0.01	21.68±0.19	22.17±1.52	0.61±0.01	223.55±6.90	238.92±4.30
25	0.77±0.01	0.72±0.01	21.70±0.41	19.29±2.63	0.58±0.03	227.27±5.08	239.56±3.36
26	0.77±0.02	0.76±0.02	21.38±0.64	14.85±2.56	0.61±0.02	230.33±7.07	240.14±2.85
27	0.79±0.03	0.78±0.05	19.17±0.45	19.69±4.15	0.59±0.03	229.44±6.11	242.18±3.52
28	0.84±0.06	0.89±0.05	25.77±0.92	28.18±2.12	0.59±0.02	223.33±7.00	237.80±1.64
29	0.80±0.05	0.85±0.07	24.14±0.69	29.61±4.31	0.58±0.04	232.56±7.02	239.80±3.58
30	0.87±0.08	0.95±0.10	24.94±0.61	28.31±1.34	0.61±0.02	233.50±9.44	239.38±4.50
31	0.71±0.01	0.78±0.01	21.36±1.10	21.64±0.01	0.59±0.01	232.80±5.16	240.92±2.07
32	0.81±0.03	0.81±0.04	23.30±1.29	19.15±0.61	0.62±0.01	222.57±8.46	238.45±4.87
33	0.80±0.01	0.78±0.01	20.96±0.87	24.92±1.82	0.60±0.01	222.93±6.46	237.55±3.80
34	0.79±0.02	0.84±0.02	24.36±1.11	20.86±0.74	0.61±0.01	226.90±5.01	239.25±3.82
35	0.73±0.01	0.76±0.03	23.38±0.59	24.07±0.76	0.56±0.01	226.42±6.46	240.40±3.85
36	0.79±0.01	0.82±0.02	22.34±0.45	24.16±2.49	0.57±0.02	230.22±6.30	240.43±3.69

Table A.A.2 ANOVA results for seven parametric characteristics

Characteristi		CWP	HIL	HIT	VL	VT	TS	CWA	CWFS	Error
SPR	DF	1	1	1	1	1	2	2	2	3
	Adj SS	0.001	0.001	0.001	0.003	0.007	0.024	0.002	0.006	0.002
	F	0.77	0.65	0.07	1.69	4.57	8.49	0.74	2.27	
	P	0.39	0.43	0.79	0.21	0.04	0.00	0.49	0.10	
AR	DF	1	1	1	1	1	2	2	2	3
	Adj SS	0.001	0.012	0.027	0.105	0.040	0.011	0.050	0.049	0.006
	F	0.03	0.75	1.69	6.61	2.50	0.33	1.57	1.52	
	P	0.86	0.40	0.21	0.01	0.10	0.72	0.23	0.24	
CGHAZA	DF	1	1	1	1	1	2	2	2	3
	Adj SS	0.001	11.87	4.565	15.785	0.256	24.61	1.256	0.350	3.007
	F	0.00	4.57	1.76	6.08	0.10	4.74	0.24	0.07	
	P	0.98	0.04	0.20	0.02	0.76	0.02	0.79	0.94	
RA	DF	1	1	1	1	1	2	2	2	3
	Adj SS	4.338	46.33	86.476	40.443	29.00	2.324	9.253	4.885	12.275
	F	1.26	13.46	25.12	11.75	8.42	0.34	1.34	0.71	
	P	0.27	0.00	0.00	0.00	0.01	0.72	0.28	0.50	
CGHAZ Hardness	DF	1	1	1	1	1	2	2	2	3
	Adj SS	190.5	11.01	1.05	1.05	4.30	33.00	87.93	57.68	16.06
	F	11.69	0.68	0.06	0.06	0.26	1.01	2.70	1.77	
	P	0.01	0.42	0.80	0.80	0.61	0.38	0.08	0.19	
WM Hardness	DF	1	1	1	1	1	2	2	2	3
	Adj SS	355.0	9.50	0.65	2.68	2.90	5.01	14.88	50.86	38.31
	F	29.40	0.80	0.05	0.22	0.24	0.41	0.62	2.10	
	P	0.00	0.38	0.82	0.64	0.63	0.67	0.55	0.10	
Dilution	DF	1	1	1	1	1	2	2	2	3
	Adj SS	0.000	0.000	0.001	0.001	0.001	0.001	0.002	0.002	0.000
	F	0.03	0.00	2.06	4.04	2.32	1.97	2.41	2.37	
	P	0.88	0.97	0.16	0.05	0.14	0.12	0.10	0.10	

Table A.A.3 Mean S/N ratios for CWTSAW process parameters (S/N ratios with higher values are in bold)

Symbol	*Parameters*	*Level*	*SPR*	*AR*	*CGHAZA*	*RA*	*Dilution*
A	CWP	1	**-1.67**±0.54	**-1.09**±0.58	-26.80±0.70	**-26.86**±0.81	**-4.46**±0.24
		2	-2.11±0.45	-1.23±0.40	**-26.80**±0.77	-27.06±1.44	-4.48±0.28
B	HI-L	1	**-2.00**±0.49	-1.24±0.54	**-26.58**±0.63	**-26.53**±0.99	**-4.47**±0.24
		2	-2.11±0.50	**-1.07**±0.44	-27.02±0.76	-27.39±1.17	-4.48±0.28
C	HI-T	1	**-2.02**±0.49	**-1.09**±0.54	**-26.67**±0.57	**-26.35**±1.06	-4.53±0.25
		2	-2.08±0.51	-1.22±0.45	-26.93±0.85	-27.56±0.92	**-4.42**±0.26
D	V-L	1	**-1.96**±0.43	**-0.93**±0.38	-27.07±0.65	-27.37±1.04	-4.55±0.24
		2	-2.15±0.55	-1.39±0.50	**-26.54**±0.71	**-26.54**±1.13	**-4.40**±0.26
E	V-T	1	**-1.91**±0.45	**-1.00**±0.46	-26.84±0.72	-27.30±1.13	**-4.42**±0.22
		2	-2.19±0.51	-1.32±0.49	**-26.77**±0.75	**-26.62**±1.10	-4.53±0.28
F	TS	1	-2.30±0.46	-1.17±0.65	-27.15±0.68	-27.04±0.97	-4.55±0.19
		2	-2.18±0.43	-1.22±0.46	-26.90±0.59	**-26.78**±1.40	-4.50±0.28
		3	**-1.67**±0.37	**1.09**±0.38	**-26.36**±0.69	-27.05±1.05	**-4.37**±0.28
G	CWA	1	-2.07±0.43	**-1.02**±0.46	-26.83±0.67	**-26.76**±1.40	-4.43±0.30
		2	-2.13±0.48	-1.26±0.50	-26.88±0.70	-27.25±0.99	-4.59±0.22
		3	**-1.95**±0.59	-1.20±0.53	**-26.70**±0.76	-26.87±0.90	**-4.40**±0.23
H	CWFS	1	**-1.90**±0.42	**-1.09**±0.53	-26.85±0.66	**-26.79**±0.87	**-4.37**±0.17
		2	-2.02±0.55	-1.24±0.46	**-26.75**±0.77	-27.11±1.12	-4.48±0.28
		3	-2.23±0.48	-1.14±0.53	-26.81±0.71	-26.98±1.35	-4.57±0.29

Chapter 4

4. Characterization of HAZ of API X70 Microalloyed Steel Welded by Cold Wire Tandem Submerged Arc Welding

4.1. Introduction

Tandem submerged arc welding (TSAW), i.e., submerged arc welding with two to five electrodes [7,8,13], has been extensively utilized to fabricate high strength low alloy pipelines, pressure vessels, structures and wind turbine towers [222,223]. TSAW offers several advantages over other welding processes, such as high deposition rate, deep penetration, high quality welds and the ability to weld thick plates due to its high heat input [149,202]. The fracture toughness of the heat affected zone (HAZ), particularly the coarse grain heat affected zone (CGHAZ), of microalloyed steels tends to be weakened due to the high heat input and thermal cycles that the steel experiences during welding. The reduction in toughness in the CGHAZ is attributed to the formation of large prior austenite grains (PAGs) and martensite-austenite (M-A) constituents, which are characterized as localized brittle zones (LBZ), as a result of the high peak temperature and relatively fast cooling rate in the CGHAZ [129,177,218,224,225]. Davis et al. [128,226] and Reichert et al. [227] found that the formation of a network of enlarged M-A constituents along the PAG boundaries resulted in cleavage crack initiation in the HAZ. Moeinifar et al. [143] suggested that a reduced fraction of M-A constituents in the CGHAZ was beneficial to the impact toughness. However, the fraction and size of M-A constituents are essentially dependent on the PAG size. Yu et al. [218] and Li et al. [177] showed that the fraction and shape of M-A constituents were increased by coarsening the PAG size in the CGHAZ. They found that a coarse PAG size, associated with coarse M-A constituents, is the dominant factor in promoting brittle fracture in the CGHAZ. Gharibshahiyan et al. [228] have reported that the formation of coarser PAGs in the CGHAZ has a detrimental effect on the toughness of the HAZ. Yang and Bhadeshia [217] and Garcia-Junceda et al. [229] showed that the martensite start temperature (Ms) increases with an increase in the PAG size, which results in a higher volume fraction of martensite.

In the present work, cold wire TSAW (CWTSAW) is developed to improve the microstructure and the mechanical properties of the HAZ of an X70 microalloyed steel, while retaining appropriate weld geometry. The additional cold wire fed into the tandem weld pool essentially increases the deposition rate, resulting in better welding productivity for the welding process without increasing the heat input compared with the TSAW process [18,19,230]. The CWTSAW process parameters were correlated with the dilution, geometry characteristics and microhardness properties of the weld metal (WM) and HAZ in Chapter 3 (also presented in [231,232]). Incorporating a cold wire in TSAW moderates the heat input by consuming some of the excess energy of the trail electrode, which lowers the amount of heat introduced to the weldment [18,19,230]. Accordingly, better quality welds were achieved at lower heat inputs per mass of deposited material and with a substantial reduction in arcing time leading to the formation of a shorter weld pool (compared with TSAW without a cold wire) [231,232]. As such, CWTSAW technology is a promising technique for pipe seam welds commonly used in the pipeline industry. The present study characterizes the macrostructure, mechanical properties and microstructure alterations in the HAZ of a typical microalloyed steel and their evolution by varying the cold wire feeding rate in the CWTSAW process. Microstructural characterization is carried out using tint etching optical microscopy (TEOM) and scanning electron microscopy (SEM). Charpy-V-notch impact testing and microhardness testing are performed to investigate and correlate the properties changes with microstructure alterations in the HAZ of samples prepared by CWTSAW. The geometry characteristics are analyzed using stereomicroscopy.

4.2. Materials and Experimental Procedure

4.2.1. Materials and welding process

The microalloyed steel plates with a thickness of 13.4±0.3 mm, produced by Evraz Inc. NA through thermo-mechanical controlled processing (TMCP) [30], were V-shape beveled with an angle and depth of 80°±5° and 4 mm, respectively, prior to welding. Six welding runs at three different cold wire feed rates were carried out to prepare the weld samples. The weld samples were prepared using two 4 mm diameter EA2 electrodes (according to AWS-A5.23/ASME-SFA5.23) and one cold wire with the same diameter and composition as the electrodes. The flux was chosen according to EN 760 (BF6.5, Bavaria, Germany). The chemical compositions of the microalloyed steel and consumable electrodes are given in Table 4-1. According to Easterling [80], the welding crack susceptibility of steels is usually expressed in terms of a carbon equivalent that shows composition allowances to avoid cold cracking or hydrogen cracking. For low-carbon microalloyed steels, the

welding crack susceptibility index, Pcm, is calculated according to the Ito-Bessyo equation [81]. The compositions are given in wt.%.

$$\boldsymbol{P_{cm}} = \%C + \frac{\%Si}{30} + \frac{\%Mn + \%Cu + \%Cr}{20} + \frac{\%Mo}{15} + \frac{\%V}{10} + \frac{\%Ni}{60} + 5\%B \qquad [4.1]$$

The lead and trail electrodes were operated using direct current electrode positive (DCEP) and square wave alternating current (ACSQ) polarity, respectively, with constant current type power sources. The influence of CWTSAW process parameters on the geometry, dilution and microhardness of the weld and the HAZ was investigated and optimized in Chapter 3. The present CWTSAW process setup has been developed based on the optimized welding parameters. The welding conditions to fabricate the microalloyed steel joint are presented in Table 4-2. Visual inspection was performed on the prepared welds prior to any further investigation to ensure that the welds were free from macro-level defects, such as surface porosity, hot-cracking, undercutting and burn-through. The steel plate geometry and the CWTSAW process setup employed to fabricate the weld samples are depicted in Figure 4-1. The heat input of the welding processes was calculated according to the Equation 4.2 [25] and set at 22.2 kJ/cm.

$$HI\left(\frac{kJ}{cm}\right) = \frac{60 \cdot \mu}{1000 \cdot TS} \cdot [(V \cdot I)_{Lead} + (V \cdot I)_{Trail}] \qquad [4.2]$$

where μ is the arc efficiency, which depends on the welding process, and *HI*, *V*, *I* and *TS* are the heat input, voltage, current and travel speed (cm/s), respectively. The arc efficiency for submerged arc welding is 0.9-1.0.

Table 4-1 X70 microalloyed steel and electrode compositions (wt.%)

X70 composition								
C	P	S	Mn	Si	N	V+Mo+Nb+Ti	Cu+Ni+Cr+Sn+Al+Ca	Pcm
0.04	0.01	0.001	1.76	0.24	0.0098	0.21	0.60	0.175

Electrode and cold wire composition								
Symbol	C	P	S	Mn	Si	Mo	Ni	Cr	Cu
BA-S2Mo	0.10	0.007	0.01	1.04	0.1	0.56	0.02	0.03	0.03

All welding parameters were the same for the processes other than the additional cold wire. The weld samples prepared by CWTSAW at cold wire feed rates of 25.4 cm/min and 76.2 cm/min and by TSAW are henceforth referred to as CW1, CW3 and TS, respectively.

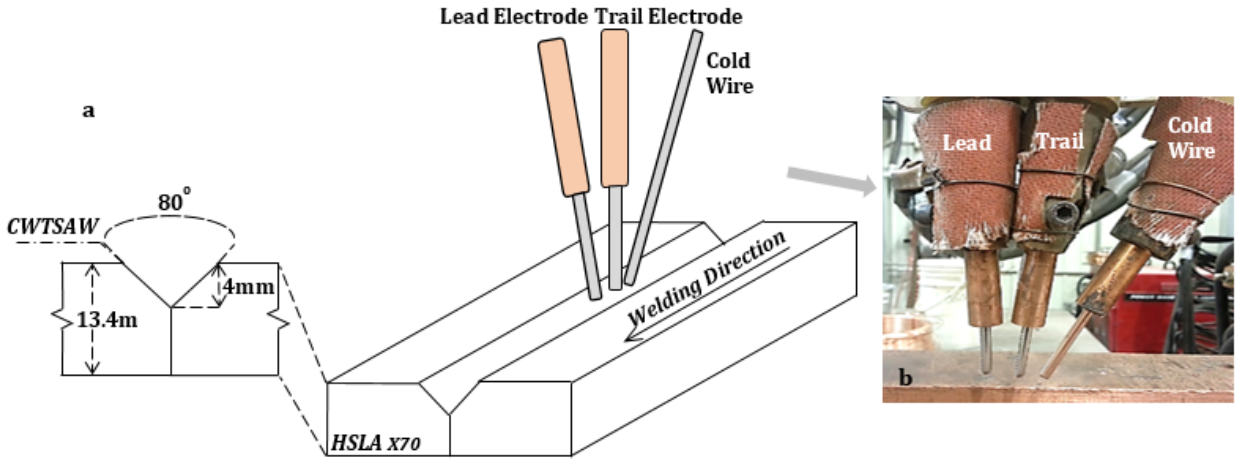

Figure 4-1 CWTSAW process setup. (a) Schematic view of joint configuration along with the positioning of the electrodes and cold wire and (b) welding setup designed at Evraz Inc. NA.

Microstructure and mechanical testing

Due to the bulbous shape of the weld metal and the HAZ and the relatively small size of the HAZ, it was not possible to fabricate full size Charpy specimens of the HAZ. As such, subsize Charpy-V-notch (CVN) specimens (5 mm x 10 mm x 55 mm) were machined along the transverse welding direction according to ASTM E23-12c [233]. These were extracted as close to the top metal surface as possible to ensure that half of the notch was located in the CGHAZ and half was located in the fine grain heat affected zone (FGHAZ). In order to position the V notch in the HAZ, the specimens were firstly macro-etched with 5% Nital to outline the HAZ boundaries. The Charpy impact tests were then performed at room temperature (RT), 243 K (-30°C) and 228 K (-45°C) and at least five specimens per weld condition and temperature were tested. Figure 4-2a illustrates the location of the notch for the toughness investigation. To analyze the microhardness variation along the weld samples (ASTM E384 [234]), two transverse samples from each weld were extracted according to ASTM E3-11 [205] to increase the number of data sets. A 500 g load was applied for a dwell time of 14 s per indentation, using a Wilson-VH3300 microhardness machine (Buehler, Germany). In total, forty test points were examined per weld, with an average of 14-18 indents across each of the FGHAZ and CGHAZ. Figure 4-2b depicts the hardness measurement mapping along a weld sample fabricated using CWTSAW.

Table 4-2 Welding process parameters

Process Parameter	Unit	Value		
Current- Lead Electrode	A	1040		
Current- Trail Electrode	A	830		
Voltage- Lead Electrode	V	30		
Voltage- Trail Electrode	V	34		
Welding Travel Speed	cm/min (in/min)	160 (63)		
		CW1	**CW3**	**TS**
Cold Wire Position	--	Lagging	Lagging	NA
Cold Wire Angle	degree	63	63	NA
Cold Wire Feed Speed	cm/min (in/min)	25.4 (10)	76.2 (30)	NA

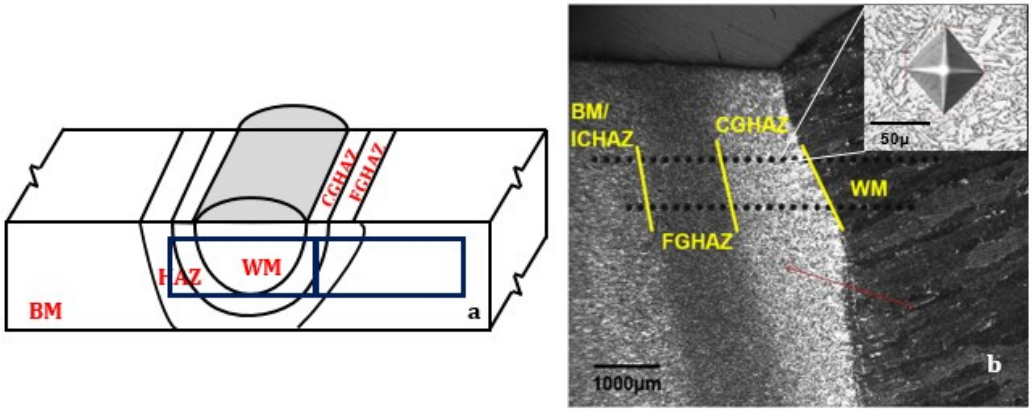

Figure 4-2 (a) Schematic view of the CVN specimen extraction from the weld sample. (b) Microhardness mapping along the BM, HAZ and WM of a typical weld prepared by CWTSAW. The micrograph in the inset shows an indentation in the CGHAZ.

Optical microscopy (Olympus BX61) and scanning electron microscopy (Tescan Vega-3 SEM) were utilized to analyze the microstructural alterations along the HAZ. The formation and fraction of M-A constituents is dependent on the cooling rate and the PAG size [129,177,220]. Revealing PAG boundaries and M-A constituents in microalloyed steels and their relevant welds can be difficult to achieve and depends very much on the etchant type and time, as well as the resolution limitations of the imaging method. As such, several etching procedures, using various etchants with different solution concentrations and etching times, were employed. After the etching trials, a chemical solution containing 4 g of picric acid in 96 ml ethanol along with a few drops of HCl acid was selected to reveal the PAG boundaries. The PAG size was analyzed using the mean linear intercept method according to ASTM E112 [235]. Freshly polished weld specimens were then tint etched through a separate process using modified LePera's etchant [140,141] for 30-50 s to reveal different

microstructural features. Microstructural analysis indicated a high sensitivity for phase identification to etchant composition and etching time. Quantitative analysis of the M-A constituent was done for both optical and SEM micrographs using ImageJ commercial image analysis software. The fraction of other microstructure features was examined according to ASTM E562 [236]. Fracture analysis of the CVN specimens was carried out by SEM.

4.3. Results

4.3.1. Charpy impact toughness

The specimens welded by CWTSAW and TSAW were tested by Charpy impact testing at three different temperatures. At least five specimens were tested per weld condition at each temperature. The average of the Charpy results and the minimum impact energy for each weld are presented in Figure 4-3. The minimum Charpy absorbed energy represents the lowest toughness that was measured and may be important from a practical perspective. According to Figure 4-3, the impact energy (both the average and minimum values) increased at the different testing temperatures when the cold wire was fed at 25.4 cm/min compared with the conventional TSAW process. However, the Charpy results showed no improvement when the cold wire was fed at 76.2 cm/min. Given the fact that fracture toughness of microalloyed steels is influenced by a number of microstructural factors, such as grain size, matrix microstructural features and the shape, size, distribution and fraction of M-A constituents, the microstructure of the HAZ is evaluated and discussed in detail below. The microstructural alterations in the HAZ, as a result of cold wire addition, are attributed to changes in the actual heat introduced to the weldment and the cooling rate in the CGHAZ, when cold wire is added to the TSAW process. The large error bars for the HAZ weld samples at 243 K (-30°C) are most likely related to the ductile-to-brittle transition temperature (DBTT) for this steel, which is close to 243 K (-30°C). In this regard, Graham [237] reported that the Charpy absorbed energy data for ferritic steels commonly exhibits large scatter in the DBTT region. However, the results show a consistent trend in CVN impact energy by cold wire addition at different test temperatures.

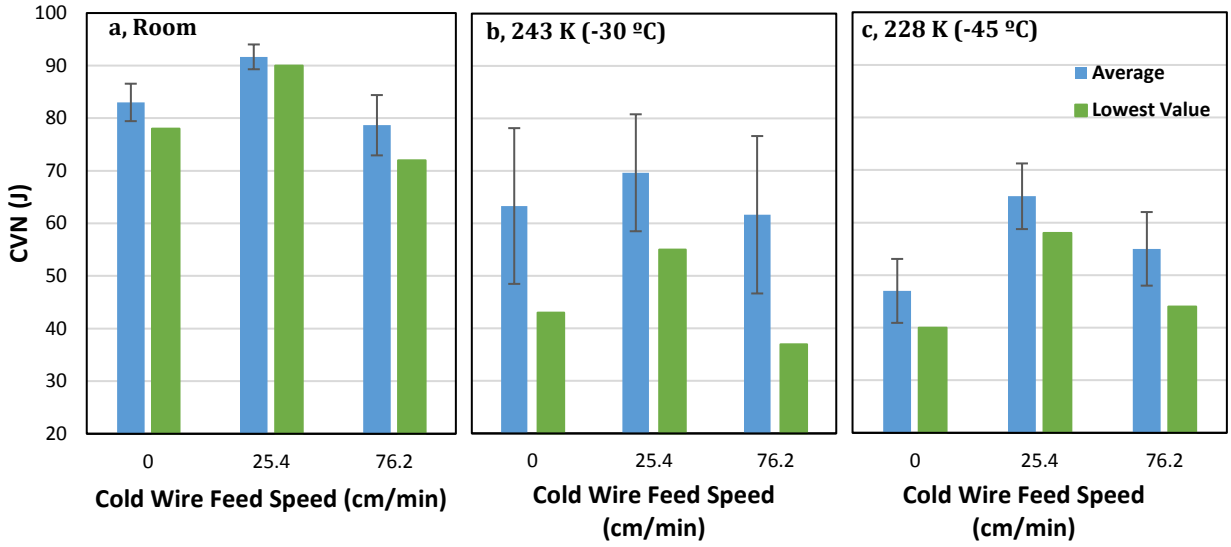

Figure 4-3 Charpy impact toughness of the HAZ for steel samples welded by TSAW (no cold wire) and CWTSAW (cold wire additions at 25.4 cm/min and 76.2 cm/min). (a), (b) and (c) represent Charpy results at room temperature (RT), 243 K and 228 K, respectively.

4.3.2. Microhardness and macrostructure

In addition to CVN testing, weld samples fabricated using the CWTSAW and TSAW processes were evaluated in terms of HAZ geometry and microhardness. The resultant CGHAZ area for the CWTSAW process was narrower than that for the TSAW process, due to lower actual heat introduced to the weldment by cold wire addition and the corresponding faster cooling rate. The reduction in the CGHAZ size was larger for the CW3 sample due to the higher cold wire feeding rate of 76.2 cm/min. Macrographs of three weld samples prepared via the CWTSAW and TSAW processes are shown in Figure 4-4. The results of four geometry measurements indicated a reduction in the CGHAZ area from 21.56±0.63 mm^2 for the TS weld to 20.30±0.50 mm^2 and 17.40±0.63 mm^2 for the CW1 and CW3 welds, respectively. The weld deposition rate was increased by 6% and 17% relative to the TSAW process, when the cold wire was fed at a rate of 25.4 cm/min (10 in/min) and 76.2 cm/min (30 in/min), respectively.

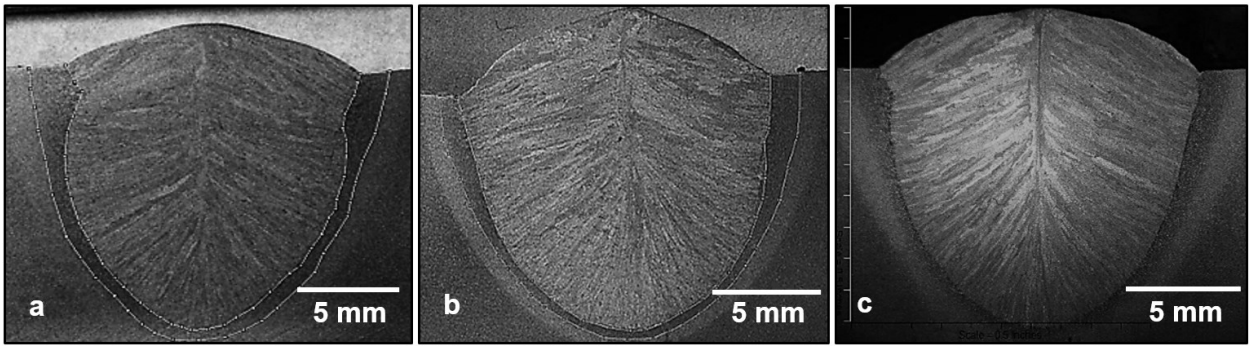

Figure 4-4 Macrographs of welded samples: (a) TS, (b) CW1 and (c) CW3.

Microhardness variations along the HAZ and the WM are depicted in Figure 4-5. The microhardness values of the as-received base metal (BM) were measured as 228±4 HV. As shown in Figure 4-5, the microhardness of the CGHAZ was reduced by the addition of a cold wire at 25.4 cm/min relative to the TSAW process. However, the average microhardness in the CGHAZ increased when the cold wire was fed at 76.2 cm/min. The different effects of cold wire addition on both microhardness and Charpy impact results is attributed to microstructural alterations taking place in the HAZ, due to changes in the actual welding heat input and consequent cooling rate, which are discussed later in this Chapter. The variation in the fraction, size, distribution and shape of M-A constituents (LBZ) formed within the HAZ of microalloyed steels plays a significant role in the variation in mechanical properties in the HAZ, particularly the CGHAZ, which has also been confirmed by Bhadeshia [139,238].

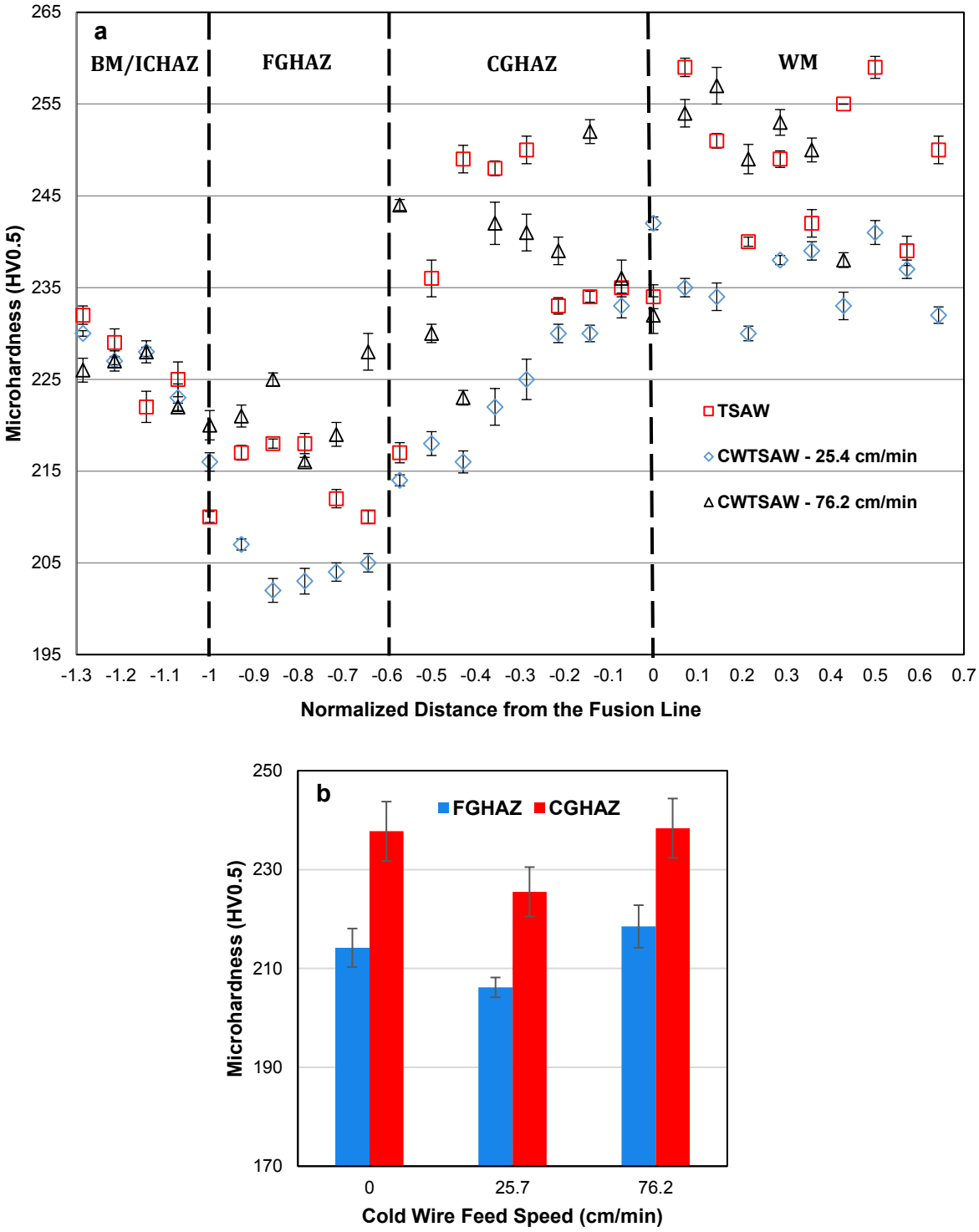

Figure 4-5 (a) Microhardness variation within the weld samples. (b) Average microhardness, with the standard deviation, for the FGHAZ and CGHAZ of steel samples welded by the CWTSAW and TSAW processes.

According to Cheng [239], the relationship between the hardness and the yield strength is empirically determined based on analysis of the dimensions of the indentations. As such, they found that the ratio of hardness to yield strength was related to the yield strength, Young's modulus, Poisson's ratio, work-hardening exponent and indenter half angle. In addition to this theoretical analysis, one empirical equation is widely used in literature [10–13], which approximates the relationship between the hardness HV and yield strength.

$$\sigma_Y = \frac{HV}{0.3} \qquad [4.3]$$

A relationship has been developed for welded C-Mn steels (ISO 15653) that can be used to estimate the yield strength (σ_Y) of the steel based on the Vickers hardness (HV) value in the range of 160 HV to 495 HV, as follows:

$$\boldsymbol{Parent\ Metal/HAZ}: \sigma_Y = 3.28HV - 221 \qquad [4.4]$$

$$\boldsymbol{Weld\ Metal}: \sigma_Y = 2.35HV + 62 \qquad [4.5]$$

Accordingly, the yield strength of the CGHAZ of the TS, CW1 and CW3 weld specimens is 559 MPa, 520 MPa and 560 MPa, respectively. As per Equation 4.5, the yield strengths in the WM of the TS, CW1 and CW3 welds are 620 MPa, 592 MPa and 622 MPa, respectively.

4.3.3. Microstructure

Figure 4-6 shows the microstructure of the X70 microalloyed steel used as the weldment in this study. The microstructure is comprised of 87% polygonal ferrite, 9% granular bainite, 3% bainitic ferrite and a fine distribution of M-A constituents (1%) with a PAG size of ~8 μm.

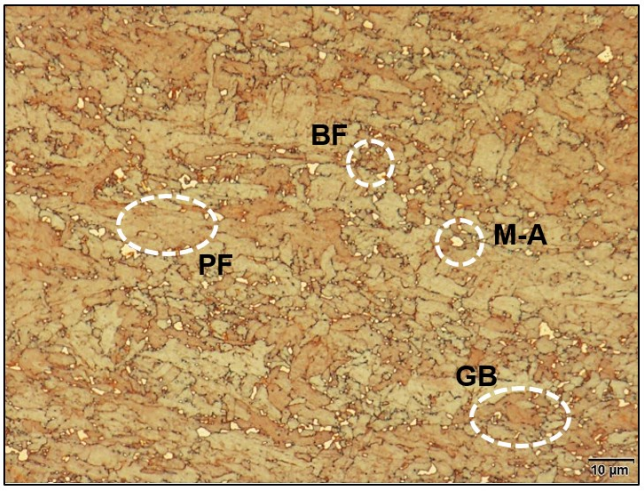

Figure 4-6 Optical micrograph illustrating the microstructure of X70 microalloyed steel used in this study.

The type and fraction of microstructural features along with the PAG formed in the region adjacent to the weld metal, i.e., the HAZ, are altered due to the heat input and thermal cycles during welding. The PAG size in the CGHAZ (Figure 4-7a-c) and the FGHAZ was decreased by the addition of the cold wire. The average PAG size in the CGHAZ (0-300 μm away from the fusion line) and FGHAZ (0-200 μm away from the CGHAZ/FGHAZ boundary) for the TS, CW1 and CW3 weld samples are indicated in Figure 4-8a. The reduction in the PAG size in the CGHAZ is attributed to a reduction in the actual heat introduced to the weldment, a reduction in the retention time in the austenite temperature range (1373-1673 K) and an increase in the cooling rate by adding the cold wire. The amount of M-A constituent, along with other microstructural features in the CGHAZ and FGHAZ of the three weld samples, is shown in Figure 4-7d-i. The M-A constituents are revealed as white regions using modified LePera's etchant [140,141]. SEM secondary electron (SE) micrographs of the CGHAZ of the weld samples are depicted in Figure 4-9a-c.

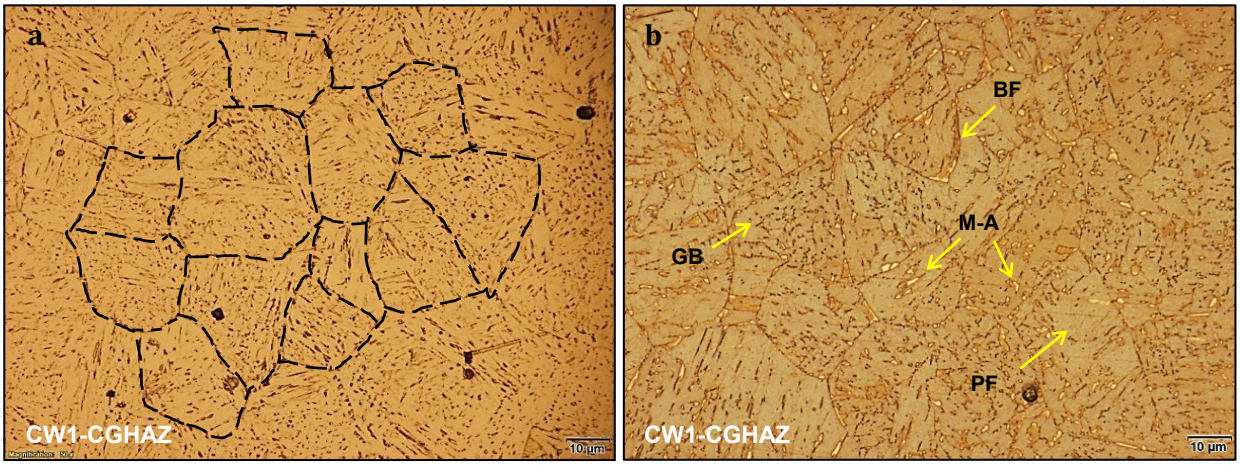

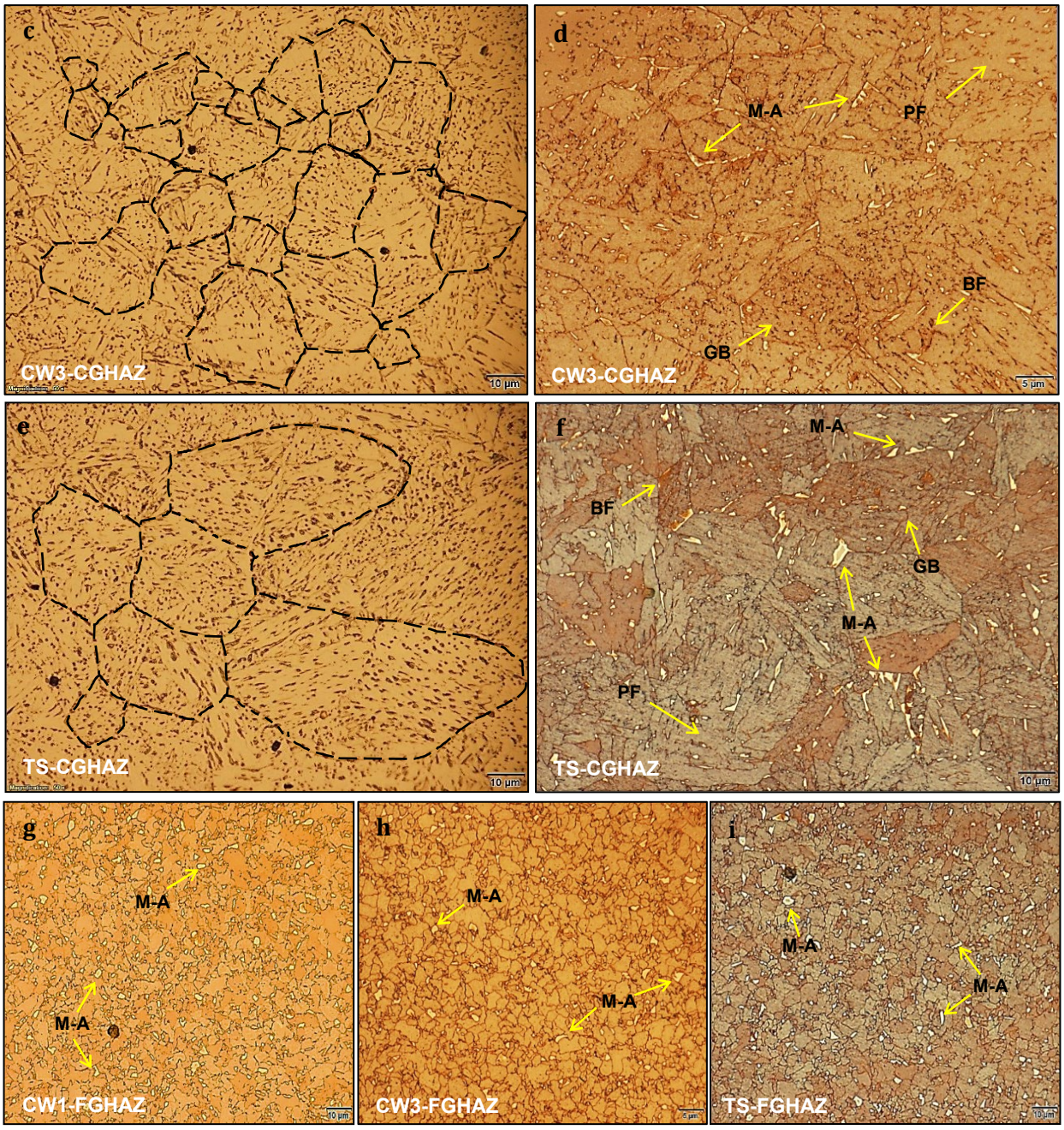

Figure 4-7 Optical micrographs of the CGHAZ and FGHAZ for the CW1 sample (a, b, g), the CW3 sample (c, d, h) and the TS sample (e, f, i). Images (a-f) and (g-i) are from the CGHAZ and FGHAZ, respectively.

4.4. Discussion

The PAG size influences the phase transformation temperature and kinetics during cooling [240,241]. Ying-Qiao et al. [224] and Shome [242] reported that the size of PAGs in the HAZ depends on the local thermal cycle and the PAG size increases by increasing the welding heat input.

Refining the PAG size influences the transformation products, particularly the M-A constituents, within the HAZ, which affect the toughness [129,177,220]. However, there has only been limited work done to correlate the PAG size and M-A constituents [129,177,220,243] In addition, Bhadeshia [139,238], Yan et al. [244] and Matsuda et al. [167] have suggested that, in addition to the PAG size, cooling rate affects the morphology of the M-A constituents, which also affect the toughness of the welded steel. Kim et al. [245] have reported that M-A islands are the main metallurgical factor, which contribute to local embrittlement of microstructures of welded microalloyed steels. They also stated that the Charpy impact toughness of the CGHAZ of high strength low-carbon steels is a function of the fraction, morphology, carbon content and distribution of the M-A islands. The work done by Lan et al. [172] indicated that the relatively fast cooling rate in the HAZ of a low-carbon steel led to the formation of slender M-A constituents with higher carbon levels and segregated silicon in the M-A islands, which resulted in an increase in the martensite hardness in the HAZ. As such, there is a concurrent effect of PAG size and cooling rate on the characteristics of the transformation products, in particular the M-A constituents, in the HAZ of microalloyed steels. Figure 4-7a-i depicts optical micrographs of the HAZ, revealing the PAGs and M-A constituents. The CGHAZ microstructure for the TS sample (with higher heat input) has large PAGs, polygonal ferrite (PF), granular bainite (GB), bainitic ferrite (BF) and a higher fraction of large M-A constituents, which are mostly formed along the PAG boundaries. In contrast with the TS sample, the CGHAZ microstructure of the CW1 sample is composed of finer PAGs, PF, GB and BF associated with fine, uniformly distributed M-A constituents. Due to the relatively faster cooling rate in the CGHAZ of the CW3 sample (with the fastest cold wire addition and the lowest actual heat input) compared with CW1 sample, smaller PAGs were formed in the CGHAZ of CW3, resulting in a lower fraction of elongated M-A constituents. However, longer M-A constituents are formed in the CGHAZ of the CW3 sample, which may be attributed to a greater reduction in the actual heat introduced to the weldment and the relatively fast cooling rate as a result of fast cold wire addition of 76.2 cm/min. The results indicate that the addition of the cold wire at 25.4 cm/min produced a favorable effect on the microstructure, which was beneficial to the toughness. The microstructure of the FGHAZ of the CW1 and CW3 samples is composed of PF and less GB and BF with smaller M-A constituents compared with that of the TS sample. However, fewer changes in the characteristics of the M-A constituents in the FGHAZ were observed by varying the cold wire addition. Phase fraction analysis of the transformation products in the CGHAZ and FGHAZ of the welded samples is indicated in Figure 4-8b.

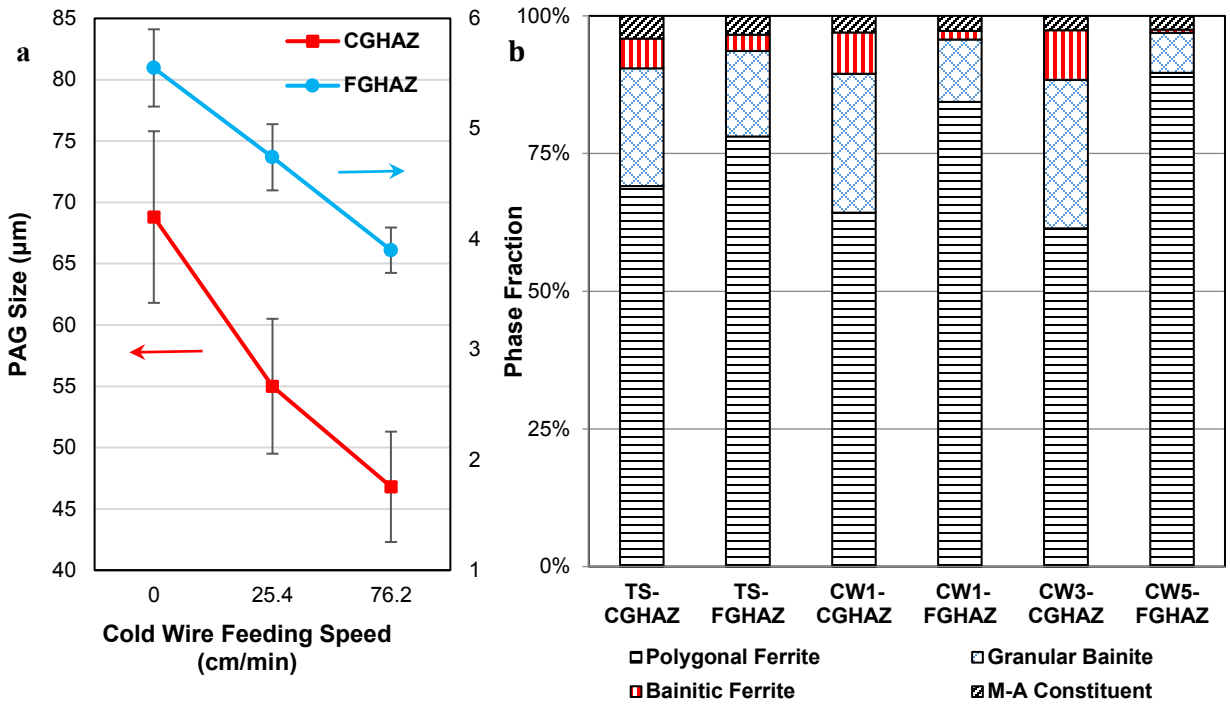

Figure 4-8 (a) PAG size in the CGHAZ and FGHAZ and (b) microstructural constituent analysis in the FGHAZ and CGHAZ for X-70 microalloyed steel welded by the CWTSAW (CW1 and CW3) and TSAW (TS) processes.

The M-A fraction in the CGHAZ, determined from the optical micrographs, was 4.1%, 3.0% and 2.7% for the TS, CW1 and CW3 samples, respectively, indicating a reduction in the fraction of M-A as a consequence of PAG size reduction [177,218] by cold wire addition. The M-A fraction in the CGHAZ of the TS, CW1 and CW3 samples, determined from the SEM micrographs, was 5.4%, 3.3% and 3.1%, respectively. These values are similar to those obtained using optical microscopy, which confirms the validity of M-A identification using optical images. The M-A fraction in the FGHAZ of the TS, CW1 and CW3 samples was 3.6%, 2.7% and 2.4%, respectively. Quantitative analysis of the M-A size distribution is shown in Figure 4-10. The sizes shown in Figure 4-10 are presented as an equivalent spherical diameter determined from the area of each particle analyzed. As shown in Figure 4-7b, d and f, the CGHAZ microstructure, particularly for the CW3 and TS samples, consists of more elongated shaped M-A constituents compared with the CW1 sample. A size distribution analysis was performed to evaluate the approximate size distribution of M-A constituents in the CGHAZ of the weld samples. In addition, image analysis carried out manually indicates that the fraction of M-A constituents in the CGHAZ, with sizes larger than 1.5 μm for TS, CW1 and CW3 samples, is 3.5%, 1.2% and 2.1%, respectively.

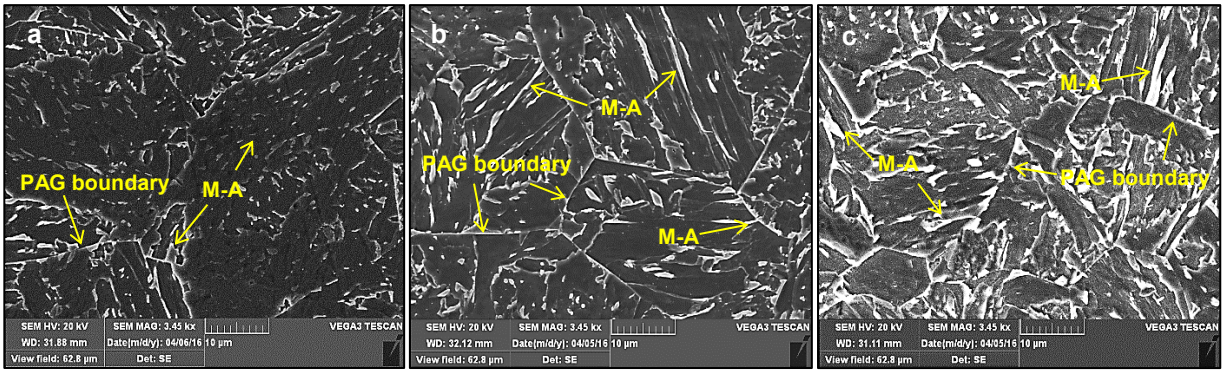

Figure 4-9 SEM SE images of the CGHAZ for the (a) CW1, (b) CW3 and (c) TS samples.

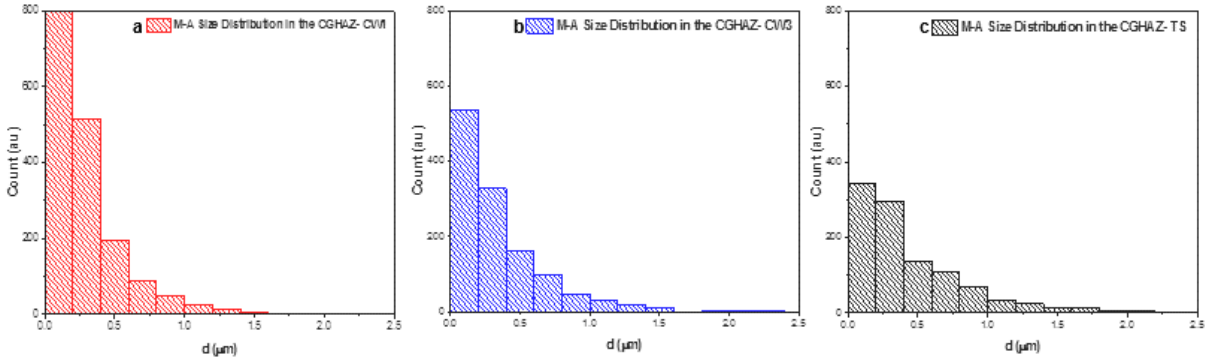

Figure 4-10 Size distribution analysis of M-A constituent in the CGHAZ for the (a) CW1 (b) CW3 and (c) TS samples.

The fracture toughness of the CGHAZ of welded microalloyed steels is highly influenced by the shape, size, distribution and fraction of M-A constituents in the CGHAZ [177,218,245]. The distribution of M-A constituents in the CGHAZ of the weld samples was analyzed using the mean inter-particle spacing equation developed by Somekawa et al. [246]. The equation takes into account the relative volume fraction, mean particle size and mean inter-particle spacing.

$$\boldsymbol{\lambda_p} = \frac{\pi d_p^2}{2\sqrt{3} f_p} - \frac{\sqrt{2} d_p}{\sqrt{3}} \qquad [4.6]$$

where, λ_p, d_p and f_p are the mean inter-particle spacing, the mean particle size and the volume fraction, respectively. To calculate the inter-particle spacing of M-A constituents in the CGHAZ, the measured M-A constituent volume fraction along with the mean M-A sizes of 0.48 μm, 0.3 μm and 0.38 μm for the TS, CW1 and CW3 welds, respectively, were used. The mean M-A constituent spacings in the CGHAZ of the TS, CW1 and CW3 welds were calculated from Equation 4.6 as 4.9 μm, 2.5 μm and 4.5 μm, respectively. Figure 4-11a and b indicates the variation in the Charpy impact toughness in the HAZ as a function of M-A size and inter-particle spacing. As the M-A size and inter-

particle spacing decrease in the CGHAZ of the CW1 sample, the fracture toughness increases. Accordingly, the formation of finely distributed M-A constituents in the CGHAZ of CW1 resulted in a beneficial effect on the fracture toughness.

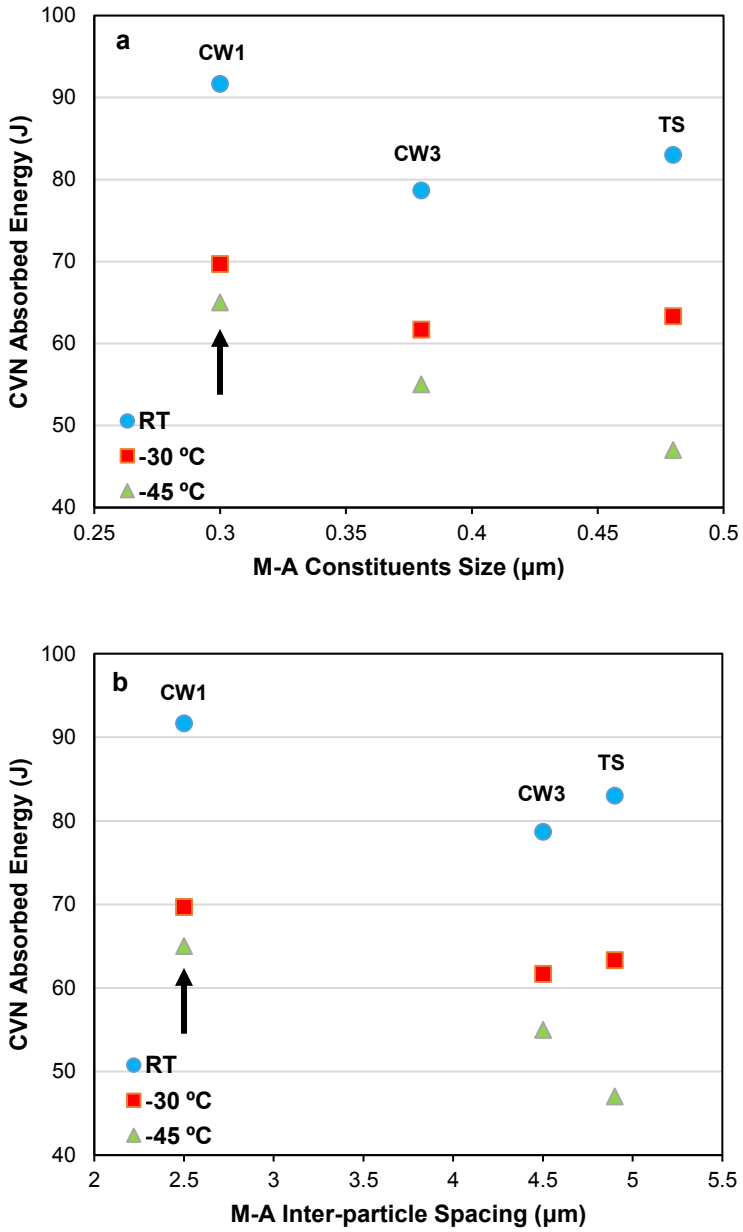

Figure 4-11 Variation in Charpy impact toughness as a function of (a) size and (b) inter-particle spacing of the M-A constituents in the CGHAZ of the CW1, CW3 and TS samples.

The larger M-A constituents in the CGHAZ of the TS sample are due to the higher martensite start temperature (Ms) for samples with larger PAGs [139,217,218,229]. Bhadeshia et al. [139,217], Heinze et al. [219] and Guimaraes [247] suggested that a decrease in Ms temperature corresponds

to a decrease in the PAG size, which results in a lower volume fraction of martensite. According to the classical Koistinen-Marburger (KM) equation [216] and the geometrical partitioning model by Fisher et al. [221], the fraction of martensite is a function of the amount of undercooling below the Ms temperature. Based on the proposed models, the martensite volume fraction formed in the early stages of the transformation is proportional to the PAG size cubed; hence, "the fraction of the transformation needed to detect Ms is reached at a smaller undercooling when the PAG size is larger" [217]. Therefore, a coarser PAG size increases the fraction and size of the M-A constituent. Yu et al. [218] and Li et al. [177] showed that a coarse PAG size, associated with a coarse M-A constituent, is the dominant factor in promoting brittle fracture in the CGHAZ. Accordingly, there is a concurrent effect of both grain size refinement and M-A transformation, which plays a significant role in the strength and toughness of the HAZ. Due to the formation of the M-A constituent, there is a higher proportion of LBZs in the CGHAZ of the TS sample compared with the CW1 and CW3 samples. This shows up as higher microhardness values in the CGHAZ for the TS sample relative to the CWTSAW samples. Also, a narrower distribution of fine M-A constituents (LBZs) inside the ferritic matrix in the CGHAZ of the CW1 sample resulted in a higher fracture toughness for the HAZ at the various test temperatures. Coarser PAGs with large M-A constituents, which are mostly formed along the PAG boundaries, led to relatively inferior toughness properties in the HAZ of the TS sample. This inferior toughness, due to the formation of M-A constituents along PAG boundaries, has been confirmed by the research work done by Davis et al. [128,226] and Reichert et al. [227]. They found that the combination of an elongated shape and the formation of a network of M-A constituents along the PAG boundaries is most detrimental to fracture properties. With reference to the CW3 sample, Yan et al. [244] and Bhadeshia [139,238] have proposed that, in addition to the PAG size, the shape, size and distribution of the M-A constituents, along with the martensite carbon content, are influenced by the cooling rate in the HAZ, which affects toughness of welded microalloyed steels [248]. Elongated M-A constituents, with large inter-particle spacing, are formed in the CGHAZ of the CW3 sample due to the relatively faster cooling rate in the CGHAZ as a result of fast cold wire addition relative to the CW1 sample. This leads to a slight decrease in toughness for the HAZ of the CW3 sample compared with the CW1 sample (Figure 4-11). This phenomenon has also been confirmed by the work done by Davis et al. [226], Kim et al.[245] and Lan et al. [172], who have suggested that the morphology of martensite changes and the carbon content of martensite increases in the M-A constituents as the cooling rate in the CGHAZ increases. As such, the relatively faster cooling rate in the CGHAZ of the CW3 sample compared with the CW1 sample led to the

formation of elongated M-A constituents with larger inter-particle spacing and higher carbon levels and segregated silicon to the M-A islands.

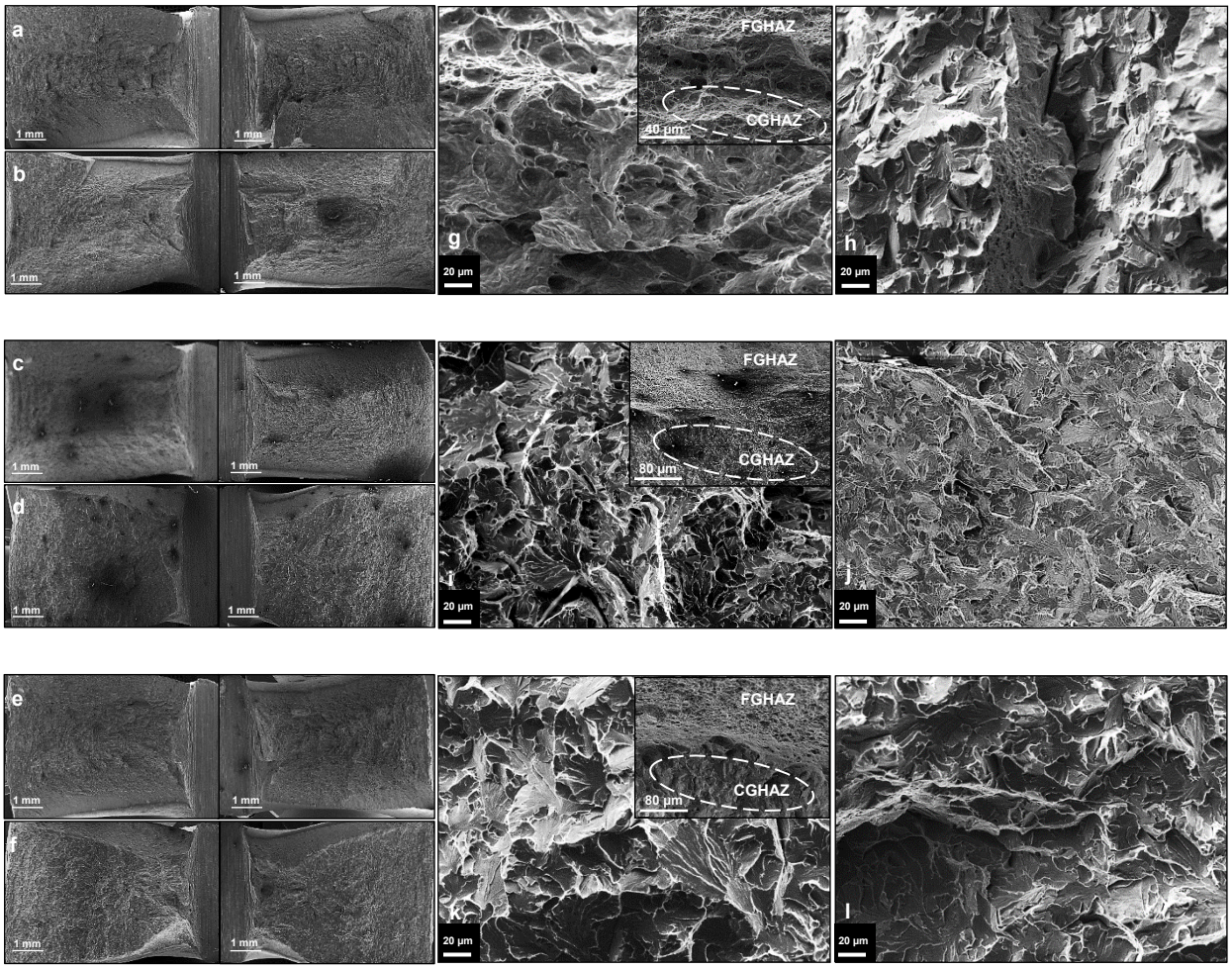

Figure 4-12 SEM SE fractographs for the (a, b) CW1, (c, d) CW3 and (e, f) TS specimens. SEM SE micrographs showing the fracture surfaces in the CGHAZ for the (g, h) CW1, (i, j) CW3 and (k, l) TS specimens. The insets in (g), (i) and (k) show the boundary between the FGHAZ and CGHAZ in the weld specimens. Micrographs (a, c, e, g, i, k) and (b, d, f, h, j, l) are from Charpy samples tested at RT and 243 K (-30 °C), respectively.

According to the impact toughness results shown in Figure 4-11, the toughness of the HAZ of the TS sample was lower compared with that of the CW1 sample, which is attributed to the formation of a high fraction of elongated and widely spaced M-A constituents inside and along the PAG boundaries due to the higher actual heat input. Lowering the actual heat introduced to the weldment, by addition of the cold wire at 25.4 cm/min, altered the size, shape, distribution and fraction of the M-A constituent, leading to an improvement in the HAZ toughness of the CW1 sample. The reduction in toughness by increasing welding heat input has been confirmed in the literature [102,143,242]. However, when the cold wire was fed at a faster rate of 76.2 cm/min, the

HAZ toughness was diminished due to the formation of large, widely spaced elongated M-A constituents inside and along PAG boundaries as a result of the faster cooling rate. The influence of the fast cooling rate on the fracture toughness of the HAZ of microalloyed steels has been well documented previously through the work done by Hutchinson et al. [162], Yan et al. [244] and Bhadeshia [139,238]. The faster the cooling rate, the greater the driving force for martensite transformation, which increases the fraction of martensite within the M-A constituents in the CGHAZ. At a relatively fast cooling rate in the CGHAZ, large M-A constituents with elongated shape are formed, leading to detrimental effects on the HAZ fracture toughness. Cracks initiated at large elongated M-A constituents can connect and form a long continuous long crack, resulting in brittle cleavage fracture. A low fraction of finely distributed fine M-A constituents can act as crack arrestors for secondary cracks, which is beneficial to toughness [178].

The fracture surface morphologies of the HAZ at RT and 243 K (-30°C) for the CW1, CW3 and TS Charpy samples are illustrated in Figure 4-12a, b, g and h, Figure 4-12c, d, i and j and Figure 4-12e, f, k and l, respectively. The boundary between the CGHAZ and FGHAZ on the fracture surface is shown in the inset micrographs in Figure Figure 4-12g, i and k. The fracture surface for the FGHAZ and CGHAZ of the CW1 weld sample at RT is fully ductile and the fracture mechanism involves microvoid coalescence (MVC). However, the fracture mechanism in the FGHAZ and CGHAZ for both the CW3 and TS samples at RT is different, i.e., MVC and quasi-cleavage, respectively, resulting in ductile and quasi-brittle fracture in the FGHAZ and CGHAZ at RT. Due to the large PAG size in the CGHAZ of the TS sample, large cleavage facets are present on the fracture surface. Moreover, the formation of large, elongated and widely spaced M-A constituents in the CGHAZ of the CW3 and TS samples contributed to lowering of the Charpy energy in the HAZ. A combination of MVC and quasi-cleavage fracture is seen on the CGHAZ fracture surface of the CW1 sample tested at 243 K (-30°C). However, the CGHAZ fracture surface of the TS sample consists of a mixture of cleavage and intergranular facets, resulting in brittle fracture in the CGHAZ of the TS sample tested at 243 K (-30°C) [249]. Similar to the TS sample, intergranular fracture along with cleavage is the dominant fracture mechanism of the CGHAZ of the CW3 sample, due to the formation of the elongated M-A constituents along the PAGs with large inter-particle spacing. Finer cleavage facets are evident on the CGHAZ fracture surface of the CW3 sample because of the formation of a finer PAG size in the CGHAZ of the CW3 sample due to the faster cooling rate (lower actual heat input by faster cold wire addition) in the CGHAZ compared with the other two weld samples.

The fracture mechanism at 228 K (-45°C) in the FGHAZ of the three weld samples was MVC, however, cleavage and intergranular fracture were observed to be the dominant mechanism in the

CGHAZ of the weld samples. Since the fracture mechanism of the three weld samples at 228 K (-45°C) was similar to the fracture mechanism for the CW3 and TS samples at 243 K (-30°C), the fractographs at 228 K (-45°C) are not shown here. The M-A constituent is significantly harder than the internal grain microstructure, so that cracks initiate easily along large M-A constituents. Aucott et al. [250] have suggested that the toughness of a welded X65 linepipe steel was reduced by the formation of coarse size particles with large inter-particle spacing. Moeinifar et al. [7] concluded from their microstructural study on multiple-wire TSAW samples that the size and shape of M-A constituents are significant factors affecting the Charpy impact properties of the CGHAZ and that microcrack nucleation may occur from M-A islands at the intersection of PAG boundaries. Moreover, Li et al. [178] found that an intercritically reheated CGHAZ demonstrated the lowest toughness, due to the presence of M-A constituents with high carbon content martensite. The large elongated shaped M-A constituents with large inter-particle spacing in the CGHAZ of the CW3 and TS samples of this work formed mostly along the PAG boundaries and can promote the formation of microcracks, resulting in brittle/quasi-brittle fracture in the HAZ.

4.5. Strengthening Mechanism in the HAZ of Low-Carbon Microalloyed Steels

Amongst the mechanical properties of welded high-strength, low-carbon microalloyed steels, fracture toughness in the HAZ is believed to be the most essential property. The region of the HAZ adjacent to the WM, i.e., the CGHAZ, is often the most critical region in terms of potential failures. However, strength variation also takes place within the HAZ and, as such, it is worthwhile to understand the microstructural alterations in the HAZ and correlate these changes with mechanical properties. An attempt is made to relate PAG coarsening, M-A constituent characteristics, ferrite/bainite grain size and strength together in the HAZ of an X70 microalloyed steel. The major strengthening mechanisms are briefly reviewed and their contributions to the strengthening of the CGHAZ is qualitatively and quantitatively studied.

With reference to microalloyed steels, the addition of microalloying elements (e.g., Ti, Nb and V) to the steels, combined with TMCP, can increase the strength, ductility and toughness of the steel. These improvements are essentially attributed to ferrite grain refinement, precipitation, solid-solution strengthening and dislocation strengthening [29,251]. The first three fundamentally contribute to strengthening (see, for example, Gladman [29]); however, dislocation strengthening is not taken into account as cold deformation is not commonly used in hot-rolled/normalized microalloyed steels. Cold deformation is not commonly used in Nb/Ti bearing microalloyed steels either and, hence, it is expected that dislocation strengthening will not contribute significantly to strengthening of microalloyed steels.

Grain refinement leads to an increase in the number of grain boundaries which inhibit dislocation movement, leading to pile-up of dislocations at the boundaries. This phenomenon results in stress intensification at the head of the pile-up. When this stress reaches a critical value, slip can be induced in the neighbouring grain. The intensity of the stress is a function of the number of dislocations at the pile-up, which in turn increases as the grain size increases. A reduction in the grain size increases the resistance to deformation [29]. The equation developed by Hall and Petch [252] in the early 1950's relates the yield strength with the grain size, i.e., there is an inverse dependence on the square root of the grain size.

Solid solution strengthening stems basically from elastic interaction of the strain fields of solute atoms with those of the dislocations. Substitutional atoms (e.g., Mn and Si) lead to a hydrostatic distortion in the lattice structure of iron and, consequently, interact solely with edge dislocations. Interstitial atoms (such as C and N) in the iron lattice structure give rise to asymmetrical distortions (with both hydrostatic and shear components), which interact with both edge and screw dislocations [29]. An empirical linear relationship considering the influence of various solutes in the yield strength of steel has been developed [29].

Precipitation strengthening is one of the most significant mechanisms contributing to strengthening of steel in different ways, such as coherency strengthening, precipitation dispersion hardening and interfacial area increase. However, according to Baker [253], the size, inter-spacing and volume fraction of precipitates are the main factors influencing the contribution of precipitates to strengthening. The equation developed by Ashby-Orowan is used to estimate the contribution of precipitation hardening (size, spacing and fraction of precipitates) to the yield strength of steel. Equation 4.7 represents the contribution of all the above mentioned mechanisms to the yield strength of steel.

$$\sigma_y(\text{MPa}) = \underbrace{\sigma_i + k_y d^{-\frac{1}{2}}}_{\textbf{Grain Refinement}} + \underbrace{\sum k_i C_i}_{\textbf{Solid Solution}} + \underbrace{\left(\frac{10.8 f_p^{1/2}}{d_p}\right) ln\left(\frac{d_p}{6.125 \times 10^{-4}}\right)}_{\textbf{Precipitation Hardening}} \qquad [4.7]$$

where σ_y is the yield stress, σ_i is the friction stress of iron, k_y is the strengthening coefficient for grain refinement, d is the grain size, k_i is the solute strengthening coefficient, C_i is the concentration of solute i, f_p is the volume fraction of the precipitates and d_p is the precipitate size (in microns).

Although these mechanisms are the key ones which contribute to strengthening of microalloyed steels, after welding, their influence on the strength in the CGHAZ is reduced (e.g., grain size strengthening) due to the thermal cycle that the steel experiences during welding. In contrast, the low-temperature transformation products, particularly M-A constituents, contribute to strengthening of the CGHAZ. In addition, depending on the cooling rate and the peak temperature in the CGHAZ, the ferrite/bainite grain size may influence the strength of the CGHAZ. It is believed that, in addition to the fraction of M-A constituents, the size, shape, distribution and carbon content of the M-A constituents play a significant role on the mechanical properties of the CGHAZ. In the CGHAZ (with a higher fraction of M-A constituents relative to the rest of steel), the contributions of M-A constituents to strengthening are similar to those considered for precipitation hardening. The contribution of M-A to strengthening of microalloyed steels can be considered as follows:

$$\sigma_{y,M-A}(MPa) = \left(\frac{10.8 f_{MA}^{1/2}}{d_{MA}}\right) ln\left(\frac{d_{MA}}{6.125 \times 10^{-4}}\right) \qquad [4.8]$$

where f_{M-A} and d_{M-A} are the volume fraction and size (in microns) of the M-A constituents, respectively. It is worthwhile to point out that the shape and carbon content of the M-A constituents are the other key factors that can also contribute to strengthening of the steel and its HAZ. However, these two factors are not taken into account in the Equation 4.8. The contribution of the M-A constituents to the yield strength in the base X70 microalloyed steel and the CGHAZ of the TS, CW1 and CW3 weld samples, calculated by Equation 4.8, is indicated in Table 4-3. As discussed earlier, as the PAG size increases, the hardenability increases due to an increase in the Ms temperature. Accordingly, a higher fraction of large M-A constituents is formed with large PAG size in the TS weld. However, from a precipitation strengthening point of view, both particle fraction and size affect the strength of the material of interest. As such, in spite of the lower fraction of M-A constituents in the CGHAZ of CW1 compared with the TS weld (based on Equation 4.8), a uniform distribution of fine M-A results in a higher contribution of M-A constituents to strengthening of the CGHAZ for the CW1 sample relative to the TS sample. On the other hand, although the M-A fraction in the CGHAZ of CW3 is less than that of TS, the relatively smaller size of M-A results in no reduction in strength due to M-A relative to the TS weld. However, it is worthwhile to note that, in addition to the fraction and size, the carbon content and fraction of martensite in the M-A constituents influence the strength of M-As. The relatively faster cooling rate in the CGHAZ of the CW3 weld compared with the other two welds results in a higher fraction of martensite in the M-A constituents. In addition, according to the work done by Lan et al. [172], the relatively faster cooling rate in the CGHAZ leads to higher carbon content and segregation of alloying elements, such as Si in

the M-A constituents. These two characteristics of the M-A constituents also contribute to the strengthening of the CGHAZ.

Table 4-3 Contribution of M-A constituents to the strengthening of the CGHAZ and X70 steel

Weld sample	TS	CW1	CW3	X70 steel
M-A contribution to strengthening (MPa)	30.4	38.6	30.0	29.6

To evaluate the ferrite/bainite grain size variation by cold wire addition, electron backscattered diffraction (EBSD) analysis was conducted on the CGHAZ of the weld samples. Figure 4-13 depicts EBSD maps of the CGHAZ of the weld samples. Individual grains were identified as having boundary angles larger than either 10° or 15°. The 10º-15º misorientation of two neighbor grains is known as the transition from low angle to high angle grain boundaries. The low angle boundaries (smaller than 10º-15º) are not effective obstacles for crack propagation and, consequently, they do not significantly contribute to the toughness, whereas, high angle grain boundaries (larger than 10º-15º) are more effective on properties [254–256]. Accordingly, the 10º and 15º thresholds were chosen as the criteria for grain size analysis. Although the ferrite/bainite grains in the CGHAZ are significantly coarser than those in the X70 microalloyed steel base metal, the results indicate that addition of a cold wire at a fast rate of 76.2 cm/min reduced the grain size (grains with boundary angles larger than 15°) in the CGHAZ from 17.6±5.5 μm (TS weld) to 11.5±4.5 μm (CW3 weld). However, no significant reduction in the ferrite/bainite grain size was observed when the cold wire was fed at 25.4 cm/min in the CW1 weld (15.3±5.0 μm) relative to the TS weld. According to the Hall-Petch equation (Equation 4.9) (k_y= 22 MPa $mm^{1/2}$ [119]), the grain size reduction in the CGHAZ of the CW3 weld relative to the TS weld should result in an increase in the strength from 166 MPa (TS weld) to 205 MPa (CW3 weld). Also, slight grain refinement in the CW1 weld relative to the TS weld caused an increase in the strength by 177 MPa. Grain refinement strengthening in the base metal of the X70 microalloyed steel was calculated at 347 MPa (the average grain size in the X70 microstructure was measured at 4 μm). The average grain size (considering boundary angles larger than 10° and 15°) in the CGHAZ of the weld samples is presented in Table 4-4.

$$\sigma_{y,grain}(MPa) = k_y d^{-1/2} \qquad [4.9]$$

Table 4-4 Average grain size in the CGHAZ of the weld samples

Weld Sample		**TS**	**CW1**	**CW3**
Average Grain Size (μm)	Angle >15°	17.6±5.5	15.3±5.0	11.5±5.0
	Angle >10°	15.7±4.5	14.5±5.0	10.6±4.5

In addition to the grain size and M-A constituent contribution to strengthening of the steel and its HAZ, precipitates also contribute to strengthening. Since precipitation leads to desirable mechanical properties in microalloyed steels, any conditions that affect re-precipitation and/or partial dissolution of these precipitates (e.g., welding) will change the proportion of precipitation strengthening. During welding, depending on the thermal cycle and peak temperature, precipitate dissolution, re-precipitation and coarsening may take place, which affect the strength in the HAZ [130]. Since different parts of the HAZ (e.g., the CGHAZ and FGHAZ) are exposed to different temperature profiles (different peak temperatures and cooling rates) throughout welding, precipitate fraction and size are not the same throughout the HAZ. In the FGHAZ, the peak temperature is too low for intermediate-size and small-size precipitates to dissolve, based on theoretical analysis performed by Poorhaydari et al. [119]. With reference to the CGHAZ, transmission electron microscopy (TEM) analysis [131] showed that intermediate-size and small-size NbC precipitates dissolved at a relatively low heat input (0.5 and 1.5 kJ/mm), whereas, at relatively higher heat inputs (2.5 kJ/mm) the precipitates became coarser than those in the BM and FGHAZ. In addition, a higher heat input leads to a higher fraction of precipitates that dissolve. Due to the high cooling rate at low heat inputs, re-precipitation is typically suppressed. However, re-precipitation occurs in high heat input welds due to the lower cooling rate and higher transformation temperature for austenite. Dissolution of precipitates enriches the matrix with microalloying elements, which influences austenite grain growth, phase transformation and, consequently, the mechanical properties of the weld. As such, precipitate behavior contributes to strengthening in the CGHAZ (in addition to the grain size and M-A constituent).

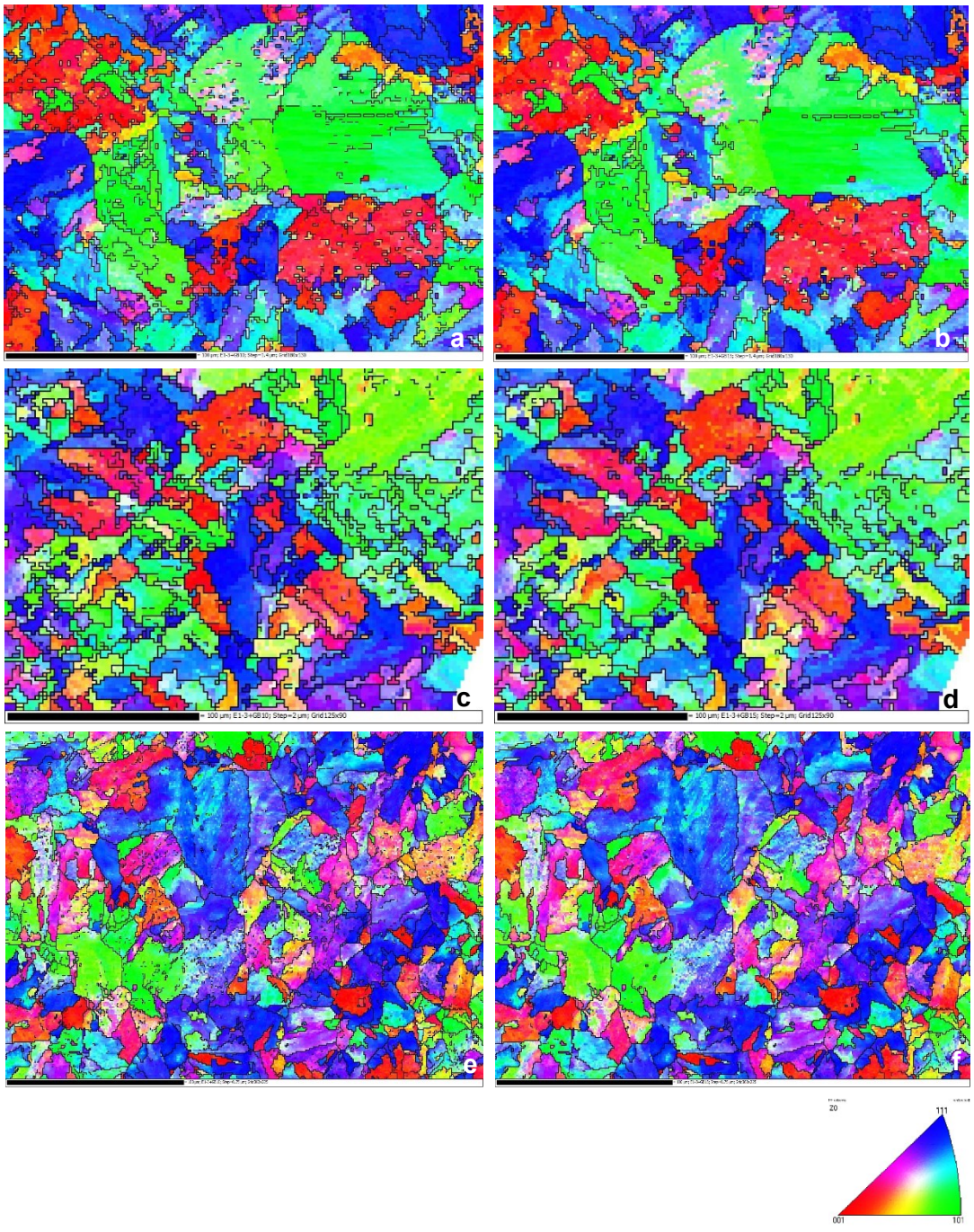

Figure 4-13 EBSD maps showing ferrite/bainite grains, based on boundaries with angles >10° (a, c, e) and >15° (b, d, f), of the CGHAZ of (a, b) TS, (c, d) CW1 and (e, f) CW3, respectively.

4.6. Conclusions

The influence of cold wire addition rate, in the recently developed cold wire tandem submerged arc welding (CWTSAW) process, on the microstructural characteristics and mechanical properties of the HAZ of a welded microalloyed steel has been studied for the first time. Cold wire addition resulted in a reduction in the prior austenite grain (PAG) size in the coarse grained heat affected zone (CGHAZ). Microstructural analysis indicated that the fraction of martensite-austenite (M-A) constituents in the CGHAZ was reduced and the distribution, size and shape were altered, when a cold wire was added to the TSAW process. The cold wire addition at a cold wire feed rate of 25.4 cm/min showed a reduction in the fraction of M-A constituents along with a uniform distribution of finer M-A constituents in the ferritic matrix, due to a reduction in the actual welding heat input and the PAG size. These effects resulted in an improvement in the fracture toughness of the HAZ. The changes to the fraction and characteristics of the M-A constituents in the HAZ of the cold wire sample (25.4 cm/min) relative to the sample with no cold wire are attributed to the lower actual heat introduced to the weldment and the resulting faster cooling rate, lower peak temperature and the formation of finer PAGs by cold wire addition. The PAG size was further reduced when the cold wire was fed at 76.2 cm/min (compared with the cold wire (25.4 cm/min) and TSAW weld samples), due to a faster cooling rate in the CGHAZ of the 76.2 cm/min cold wire sample; however, elongated shaped M-A constituents were formed. The relatively large elongated M-A constituents with large inter-particle spacing mostly formed along the PAG boundaries in the CGHAZ of the TSAW and cold wire (76.2 cm/min) samples. This morphology led to inferior toughness properties in the HAZ of the TSAW and cold wire (76.2 cm/min) samples, since the larger M-A constituents can stimulate the formation of microcracks leading to intergranular fracture.

Chapter 5

5. Evaluation of Cold Wire Addition Effect on Heat Input and Productivity of Tandem Submerged Arc Welding for Low-Carbon Microalloyed Steels

5.1. Introduction

Due to the inherent properties of submerged arc welding (SAW), such as high deposition rate, deep penetration and capability of welding thick sections, SAW has been preferred over other welding processes to manufacture pipelines and pressure vessels [101,224]. To improve welding productivity in a global economy, many fabricators have resorted to various techniques to increase the SAW deposition rate. The commonly used techniques to improve welding deposition rate are increasing electrode stick-out [5], twin-wire SAW [6], tandem SAW (TSAW) [7,8], applying a metal-cored wire [9,10], varying electrode polarity [11] and addition of a cold wire to a single electrode SAW [12] or in twin-wire SAW [13]. Some applications, such as pressure vessels, girth welds in pipes and spiral pipe mills, can benefit from the techniques employed to improve the deposition rate and, consequently, the productivity of the SAW process [257]. TSAW is a common process employed by industry to improve the welding deposition rate. However, in the TSAW process, heat input is increased as the number of electrodes increases because of the increase in the overall welding current and voltage to generate a higher deposition rate. Although TSAW provides higher productivity due to the high heat input, some adverse effects can be produced in terms of the microstructure, properties and geometry of the weld joint. The weld metal (WM) and particularly the heat-affected zone (HAZ) are affected by welding heat input as the weldment experiences higher peak temperatures and cools down more slowly after welding [8,14,15]. The addition of a cold wire to the one electrode SAW process was initially proposed by Mruczek et al. in 2005 [17]. It was found that the addition of a cold wire in one electrode SAW resulted in shallower weld penetration due to the consumption of the lead electrode heat by the additional cold wire.

In the current research work, tandem submerged arc welding with an additional cold wire (CWTSAW) has been developed to improve the productivity in terms of deposition rate and welding travel speed, while retaining adequate weld geometry and properties. Cold wire addition also improves the macrostructure, mechanical properties and microstructure of the HAZ [258]. These improvements, as a result of cold wire addition, are attributed to changes in the actual heat introduced to the weldment, the peak temperature and the cooling rate in the HAZ. The developed CWTSAW process involves two electrodes with arcs and one electrically cold electrode, which is fed at a lagging position close to the trail electrode. Since an appropriate understanding of the welding conditions is always essential in the development of a welding process to guarantee requisite weld geometry, appearance and mechanical properties, the CWTSAW process was initially optimized and investigated in terms of the welding parameters (i.e., heat input, voltage and travel speed and cold wire feed speed, position and angle) and this work has been presented in Chapter 3 [259]. The present CWTSAW process setup has been developed based on the optimized welding parameters. The cold wire provides a higher deposition rate and better productivity for the welding process, without increasing heat input, compared with the TSAW process [18,230]. Furthermore, incorporating a cold wire in TSAW moderates the heat input by consuming the energy of the trail electrode as the wire melts into the weld puddle. Accordingly, better quality welds are expected at lower heat inputs per mass of deposited material and with a substantial reduction in arcing time, causing the formation of a shorter weld pool (compared with TSAW without a cold wire) [18]. In addition to welding deposition rate, the effect of cold wire addition on welding travel speed is studied. The microstructure and toughness in the HAZ of a typical microalloyed steel, and their evolution by varying the cold wire feed rate and travel speed in the CWTSAW process, are also studied. Microstructural characterization is carried out using tint etching optical microscopy (TEOM) [231] and scanning electron microscopy (SEM). Charpy V-notch (CVN) impact testing and microhardness testing are performed to investigate the property changes in the HAZ of samples prepared by CWTSAW.

5.2. Materials and Welding Procedure

In TSAW, the lead electrode is positioned to generate sufficient penetration depth of the weld and the trail electrode(s) provide filling of the bevel, resulting in adequate joining of the metal pieces of interest [94]. Accordingly, in the CWTSAW process, DCEP (direct current electrode positive) and ACSQ (square wave alternating current) polarities were selected for the lead and trail electrodes, respectively, since DCEP on the lead electrode causes deeper penetration and ACSQ on the trail electrode provides increased deposition rate relative to DCEP polarity. The cold wire was fed at a

lagging position close to the trail electrode and consumed some of the heat of the trail electrode. The work presented in Chapter 3 indicated that the addition of a cold wire at a lagging position with an angle of 63° resulted in an overall improvement in the weld geometry, dilution and microhardness. In the current work, to assess the influence of cold wire addition on welding productivity and HAZ characteristics, the heat input and the cold wire feed speed were varied to investigate the properties, deposition rate and travel speed of welding. As such, seven weld samples were prepared by CWTSAW and TSAW of 13.4±0.1 mm thick plates sectioned from X70 microalloyed steel. The geometry of the V-shaped bevel machined in the steel plates, along with the CWTSAW process set-up, are illustrated in Figure 5-1. The compositions of the microalloyed steel and the consumable electrode are indicated in Table 5-1. According to Easterling [80], the welding crack susceptibility of steels is usually expressed in terms of a carbon equivalent that shows composition allowances to avoid cold cracking or hydrogen cracking. The Pcm (the welding crack susceptibility index) denoted in Table 5-1 is calculated based on the equation proposed by Ito-Bessyo [81] for low-carbon microalloyed steels. 4 mm diameter wires for the electrodes and cold wire were selected based on EN756/EN14295 (BA-S2Mo, Bavaria, Germany) and AWS A5.17/A5.23 (EA2). The consumable flux was chosen according to EN 760 (BF6.5, Bavaria, Germany).

Table 5-1 X70 microalloyed steel and electrode compositions (wt.%)

X70 composition								
C	**P**	**S**	**Mn**	**Si**	**N**	**V+Mo+Nb+Ti**	**Cu+Ni+Cr+Sn+Al+Ca**	**Pcm**
0.043	0.013	0.001	1.73	0.28	0.008	0.21	0.57	0.175

Electrode and cold wire composition								
Symbol	**C**	**P**	**S**	**Mn**	**Si**	**Mo**	**Ni**	**Cr**	**Cu**
BA-S2Mo	0.10	0.007	0.01	1.04	0.1	0.56	0.02	0.03	0.03

The welding conditions to fabricate the microalloyed steel joints are presented in Table 5-2. Sample T1 was welded by TSAW and then compared with welds fabricated by the CWTSAW process (i.e., samples C1-C6) in terms of productivity and properties. To determine the maximum travel speed that can be employed by cold wire addition, while maintaining adequate HAZ and weld geometry, appearance and properties, relatively high current, voltage and cold wire feed speed were employed. Visual inspection was conducted on the prepared welds prior to any further investigation to ensure that the welds were free from the macro-level defects, such as surface porosity, hot-cracking, undercutting and burn-through.

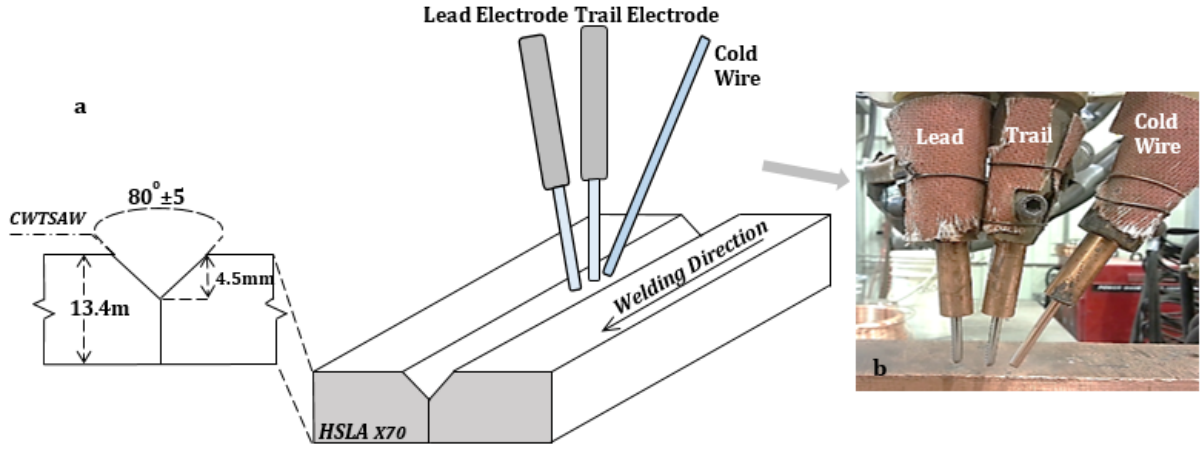

Figure 5-1 CWTSAW process setup: (a) Geometry of the steel plate along with the positioning of the electrodes and cold wire and (b) welding setup.

Table 5-2 Welding process parameters

Process Parameter		***Weld sample ID***						
	Unit	**T1**	**C1**	**C2**	**C3**	**C4**	**C5**	**C6**
Current-Lead Electrode	A	1040	1060	1070	1200	1250	1300	1350
Current-Trail Electrode	A	830	830	840	950	1000	1050	1050
Voltage-Lead Electrode	V	30	31	31	32	33	34	36
Voltage-Trail Electrode	V	34	34	34	36	37	38	39
Travel Speed	cm/min	160	167	177	190	203	216	229
Welding Heat Input	kJ/cm	22.2	22.1	20.5	23.0	23.2	23.5	23.6
Cold Wire Feed Speed	cm/min	NA	25.4	63.5	51	58	66	71

Due to the bulbous shape of the weld metal and the HAZ and the relatively small size of the HAZ, it was not possible to fabricate full size Charpy specimens of the HAZ. As such, subsize Charpy-V-notch (CVN) specimens (5 mm x 10 mm x 55 mm) were machined along the transverse welding direction according to ASTM E23-12c [260]. These were extracted as close as possible to the top metal surface to ensure that half of the notch was located in the CGHAZ and half was located in the fine grain heat affected zone (FGHAZ). In order to position the V notch in the HAZ, the specimens were firstly macro-etched with 5% Nital to outline the HAZ boundaries. Charpy impact tests were then performed at room temperature (RT), -30°C and -45°C, and at least five specimens per weld condition and temperature were tested. To analyze the microhardness variation along the weld samples (ASTM E384 [234]), a transverse sample from each weld was extracted according to ASTM E3-11 [205]. A 500 g load was applied for a dwell time of 14 s per indentation, using a Wilson-

VH3300 microhardness machine (Buehler, Germany). In total, forty test points were examined per weld, with an average of 14-18 indents across each of the FGHAZ and CGHAZ. Optical microscopy (Olympus BX61) and scanning electron microscopy (Tescan Vega-3 SEM) were utilized to analyze the microstructural alterations in the HAZ. Freshly polished weld specimens were then tint etched through a separate process using modified LePera's etchant [140,141] for 30-50 s to reveal different microstructural features. Microstructural analysis indicated a high sensitivity for phase identification to etchant composition and etching time. Quantitative analysis of the M-A constituent was done using ImageJ commercial image analysis software according to ASTM E562 [261].

5.3. Results and Discussion

5.3.1. Heat input assessment

Earlier studies done by Rigdal [262] and Mruczek [230] have reported that the addition of a cold wire produces a heat input which is less than the nominal heat input of a conventional SAW process, since the wire absorbs heat from the weld pool and/or electrode during its melting. Given the fact that the weld/HAZ microstructure and properties are directly influenced by welding heat input, a reduction in the heat input as a result of cold wire addition causes some alteration in the microstructure and mechanical properties in the HAZ [18,166]. Our studies (Chapter 4) have indicated that the microstructure in the HAZ of a typical microalloyed steel was altered by the additional cold wire in conventional TSAW, which led to an overall improvement in the HAZ toughness. However, since cold wire addition affects the welding heat input and consequently the cooling rate, the HAZ microstructure changes are affected by the cold wire feed rate. The term "effective heat input" [230,263] has been used to describe the reduced heat input, which is based on the relative volume of the electrode and cold wire melted to produce a heat input reduction factor. Mruczek et al. [230] used hardness readings and Charpy results to verify the heat input reduction. In the present study, Mruczek's approach is modified (Equation 5.1) according to the current CWTSAW process design. In our approach, it is assumed that the cold wire consumes the heat of the trail electrode since the cold wire is positioned adjacent to the trail electrode. Accordingly, the cold wire solely reduces the trail electrode energy (does not affect the lead electrode); therefore, the correction factor (Equation 5.2) only applies to the heat input produced by the trail electrode.

$$\boldsymbol{HI_{eff}}\left(\frac{kJ}{cm}\right) = HI_L + \eta . HI_T = \frac{60}{1000.TS}[(V_L . I_L) + \eta(V_T . I_T)] \qquad [5.1]$$

$$\boldsymbol{Correction\ factor}: \eta = \frac{Vol._T}{Vol_T + Vol_{CW}} = \frac{FS_T}{FS_T + FS_{CW}} \qquad [5.2]$$

where HI_{eff}, HI_L and HI_T are the effective welding heat input, lead heat input and trail heat input, respectively. Vol_T and Vol_{CW} are the volumes of the electrode and cold wire melted during welding. Since the electrode and cold wire have similar diameters and chemistry in this study, the feed speed of the trail electrode (FS_T) and the cold wire (FS_{CW}) can be used to calculate the correction factor (η). For the conventional TSAW process (without additional cold wire), η is equal to 1. The WM and CGHAZ microhardness values, CVN results and PAG size were analyzed to investigate the CWTSAW heat input. For this reason, two weld samples were prepared using CWTSAW (R1 and R3) and the correction factor was calculated for each weld and applied to the heat input equation to evaluate the effective heat input of the CWTSAW process. Subsequently, the calculated effective heat input was used to prepare two weld samples by conventional TSAW (R2 and R4). Various welding parameter configurations were employed to verify the correction factor in Equation 5.1, as shown in Table 5-3. The trail electrode feed speeds for the R1 and R3 welds were measured at 201 and 212 cm/min, respectively. Accordingly, the η values for the R1 and R3 samples were calculated as 0.80 and 0.73, respectively, which means 20% and 27% of the trail electrode heat was consumed by the cold wire. As such, the effective heat input employed to prepare the R2 and R4 samples (without a cold wire addition) were 20.0 and 20.7 kJ/cm, respectively.

Table 5-3 Welding runs performed to evaluate the effective heat input for the CWTSAW process

Process Parameter			***Weld Sample ID***			
	Notation	***Unit***	***R1***	***R2***	***R3***	***R4***
Current-Lead Electrode	I_L	A	1040	980	1085	1000
Current-Trail Electrode	I_T	A	830	810	900	850
Voltage-Lead Electrode	V_L	V	30	28	30	28
Voltage-Trail Electrode	V_T	V	34	32	34	32
Travel Speed	TS	cm/min	160	160	160	160
Cold Wire Feed Speed	FS_{CW}	cm/min	50.8	NA	76.2	NA

Table 5-4 shows the CVN results, average microhardness values and PAG size for weld specimens R1-R4. As indicated, the measured properties for R2 are similar to those for R1 and, likewise, the measured properties for R4 are similar to those for R3, respectively. These results confirm that the effective heat input of the CWTSAW process is as a function of the trail electrode and cold wire feed speed and can be accounted for by the correction factor η.

Table 5-4 Measured CVN, microhardness and PAG size for R1-R4 weld specimens

Weld Sample	*Welding Process*	*Heat Input (kJ/cm)*	*CVN (J)*		*PAG Size (μm)*		*Microhardness (HV0.5)*		
			RT	**-30°C**	**CGHAZ**	**FGHAZ**	**CGHAZ**	**FGHAZ**	**WM**
R1	CWTSAW	22.2	86±2.3	67±7.0	50.0±5.5	4.3±0.2	226±3.6	210±1.5	238±2.5
R2	TSAW	20.0	87±4.2	67±6.1	48.5±6.3	4.2±0.3	225±3.0	208±1.0	237±4.4
R3	CWTSAW	23.7	82±4.3	60±8.0	61.4±6.0	5.1±0.5	246±3.2	219±3.6	253±6.0
R4	TSAW	20.7	80±1.5	59±7.3	59.8±4.5	4.9±0.4	240±6.5	222±2.1	256±3.2

In addition to the electrode/cold wire relative volume method for effective heat input assessment, a heat balance analysis was also conducted to approximate the portion of the heat loss in the CWTSAW process as a result of the cold wire addition relative to the conventional TSAW process. Our experimental observations show that addition of a cold wire to the TSAW process has a two-fold effect on the reduction in the heat introduced to the weldment. When the cold wire is fed into the weld puddle/electrode arc, it consumes some portion of the weld heat in melting ($\Delta H_{Fusion-CW}$) (Equation 5.3). During welding runs, the current and voltage of electrodes were recorded every 0.5 s to ensure that the recorded values were equal to the nominal values, which were initially set. However, the data recorded during the welding runs indicates that the additional cold wire slightly influenced the arc stability of the electrodes, particularly the trail electrode. As such, the average values of recorded current and voltage for the electrodes were slightly reduced compared with the nominal values, resulting in an overall reduction in the welding heat input. No significant reduction in the current and voltage of the TSAW runs was observed. This reduction is calculated based on Equation 5.4 ($\Delta H_{Arc-instability}$). Our observations show that the amount of reduction in the electrode current and voltage increased as the cold wire feed speed increased. Equations 5.5 and 5.6 represent the heat input correction factor (η) and the effective heat input calculated from the heat balance analysis done for the CWTSAW process, respectively. In this method, the correction factor applies to the nominal heat input of both lead and trail electrodes.

$$\Delta \boldsymbol{H_{Fusion-CW}}\left(\frac{kJ}{cm}\right) = \frac{FS.A.\rho}{1000.TS}.\left\{\Delta H^{o}_{298} + \int_{25+273}^{1510+273} C^{s}_{p}.dT + \Delta H_{l} + \int_{1510+273}^{1900+273} C^{l}_{p}.dT\right\} \qquad [5.3]$$

$$\Delta \boldsymbol{H_{Arc-instability}}\left(\frac{kJ}{cm}\right) = \frac{60}{1000.TS}.\{[(V_L.I_L) + (V_T.I_T)]_{nominal} - [(V_L.I_L) + (V_T.I_T)]_{recorded}\} \quad [5.4]$$

$$\boldsymbol{Correction\ factor}: \eta = 1 - \frac{\Delta H_{Fusion-CW} + \Delta H_{Arc-instability}}{HI_{Welding}} \quad [5.5]$$

$$\boldsymbol{HI_{eff.}}\left(\frac{kJ}{cm}\right) = \eta . HI_{Welding} \quad [5.6]$$

where A, ρ and TS are the cold wire cross-section area and density and welding travel speed, respectively, and C_p^s and C_p^l are the specific heat capacities of the solid and molten wire. ΔH_l is the latent heat of fusion for the cold wire. The physical properties of the cold wire were assumed to be similar to those of a structural steel [264]. The recorded values of I and V represent the modified electrode current and voltage as a result of arc instability, due to the addition of a cold wire during CWTSAW. It is worth noting that the nominal current and voltage values and the average recorded values for both the lead and trail electrodes are very similar for the conventional TSAW process. $HI_{welding}$ is the nominal welding heat input calculated according to the initial set of current and voltage used to conduct the welding process. The variation in arc current and voltage, along with the electrode characteristics, are indicated in Table 5-5. According to Equation 5.5 and 5.6, the correction factor, η, for the R1 and R3 weld samples is calculated as 0.92 and 0.88, respectively, which means that the nominal welding heat input is reduced by 8% and 12% by the additional cold wire. Accordingly, the CWTSAW effective heat input for R1 and R3 weld samples is 20.4 and 21.0 kJ/cm, respectively.

Table 5-5 Physical characteristics of the electrodes and cold wire

Parameter	***Notation***	**R1**		**R3**	
		Set	*Recorded*	*Set*	*Recorded*
Current-Lead Electrode	I_L	1040	1039	1085	1083.5
Current-Trail Electrode	I_T	830	828.6	900	897.6
Voltage-Lead Electrode	V_L	30	29.2	30	28.6
Voltage-Trail Electrode	V_T	34	32.5	34	32
Cold wire feed speed	FS	50.8	50.8	76.2	76.2
	ρ (kg/cm^3)	ΔH_l(kJ/kg)	C_p^s (J/kg.K)		C_p^l (J/kg.K)
Cold wire/Electrode Characteristics	7.87*10^{-3}	270	$425 + 0.733T + 1.69 \times 10^{-4}T^2$ (**20<T<600**) $666 \times [13002/(T - 738)]$ (**600<T<735**) $545 - [17820/(T - 731)]$ (**735<T<900**) 650 (**900<T<1510**)		820

Table 5-6 indicates the η values and the effective heat input for the R1 and R3 weld samples calculated using both methods. As discussed earlier, the η value calculated from the relative volume method only applies to the trail electrode heat input, whereas the η value calculated from the heat balance analysis is employed for the entire nominal welding heat input. As such, both heat input analysis methods were in a good agreement, resulting in relatively similar heat input reduction by cold wire addition. The heat input analysis also confirms that cold wire addition lowers the welding heat input. However, the percentage of the heat input reduction in the CWTSAW process is a function of the cold wire feed rate. As the cold wire feed rate increases, more reduction in welding heat input will occur. Given the fact that microstructure and mechanical properties are directly influenced by the welding heat input, the effect of lowering the nominal welding heat input by an additional cold wire on the properties and microstructure of the HAZ is studied in the next sections. Moreover, cold wire addition leads to the formation of a narrower HAZ, particularly the coarse grain HAZ (CGHAZ - the high-temperature HAZ) [232].

To study any improvement in the HAZ toughness by cold wire addition, initially three weld samples, T1, C1 and C2 (presented in Table 5-2), were prepared (with an increase in the welding travel speed and productivity). According to the properties discussed in next section, the C1 sample showed an improvement in mechanical properties, whereas no improvement for the C2 sample (with additional cold wire) was observed relative to the T1 sample. The cold wire in the C1 sample had desirable effects on welding heat input and, consequently, cooling rate, which resulted in property improvement; however, the heat input was significantly decreased for the C2 sample, which resulted in a faster cooling rate and, therefore, no improvement in HAZ toughness. The microstructure and mechanical property changes are discussed in the next sub-sections. Accordingly, to study productivity and property changes relative to the T1 weld, C3-C6 weld samples were fabricated. The relative volume method was used to calculate the effective welding heat input and the heat input analysis results were employed to prepare the C3-C6 weld samples (Table 5-2) to investigate welding productivity improvement by cold wire addition to the conventional TSAW process (CWTSAW).

Table 5-6 Effective welding heat input calculated from the relative volume method and heat balance analysis method

Weld Sample	Heat Input Analysis Method	η	Effective Welding Heat Input (kJ/cm)
R1	Electrode/cold wire relative volume	0.80	20.0
	Heat balance analysis	0.92	20.4
R3	Electrode/cold wire relative volume	0.73	20.7
	Heat balance analysis	0.88	21.0

5.3.2. Mechanical properties

To evaluate the mechanical property changes in the HAZ when a cold wire was added to the TSAW process, weld specimens prepared by CWTSAW (C1-C6 – Table 5-2) were subjected to impact testing (CVN) at three different temperatures and microhardness analysis. The properties were compared with those for the TSAW sample (T1). Figure 5-2 depicts the CVN results for the HAZ of the weld samples. To increase the statistical accuracy of the results, at least four Charpy specimens for each weld at each temperature were tested and the average of the results is presented. The impact toughness of the C1 sample was increased when a cold wire was fed at 25.4 cm/min compared with the T1 sample at the same welding heat input. This improvement is attributed to the formation of a lower fraction of finely distributed martensite-austenite (M-A) constituents in the CGHAZ. However, the Charpy impact toughness value for the HAZ of the C2 weld was slightly reduced, relative to the T1 sample, when the cold wire was fed at 63.5 cm/min and the nominal welding heat input was reduced. This reduction in toughness is attributed to the formation of slender shaped M-A constituents, which formed mostly along the PAG boundaries as a result of the faster cooling rate in the CGHAZ of the C2 sample due to faster cold wire addition and lower nominal welding heat input. The microstructural alterations in the CGHAZ of the weld samples are discussed in detail in the next subsection. Given that the mechanical properties of microalloyed steels are directly influenced by the heat input of the welding process, the actual heat introduced to the C1 sample was calculated (according to the methods discussed in the subsection 5.3.1) and, accordingly, weld samples C3-C6 were prepared. By taking into account the heat input correction factor, η, for the C1 sample, the actual welding heat input of the C1 sample was calculated (using the relative volume method) as 20.62 kJ/cm. Since the actual welding heat input of the C1 sample (due to cold wire addition) resulted in a beneficial effect on the HAZ toughness compared with the T1 sample, the nominal welding heat input and the cold wire addition rate used to prepare the C3 to C6

weld samples were essentially selected to achieve the same actual welding heat input as for the C1 sample. Accordingly, the HAZ toughness of C3 and C4 weld samples (with higher nominal heat inputs and higher cold wire feed rates) was slightly increased relative to the T1 sample.

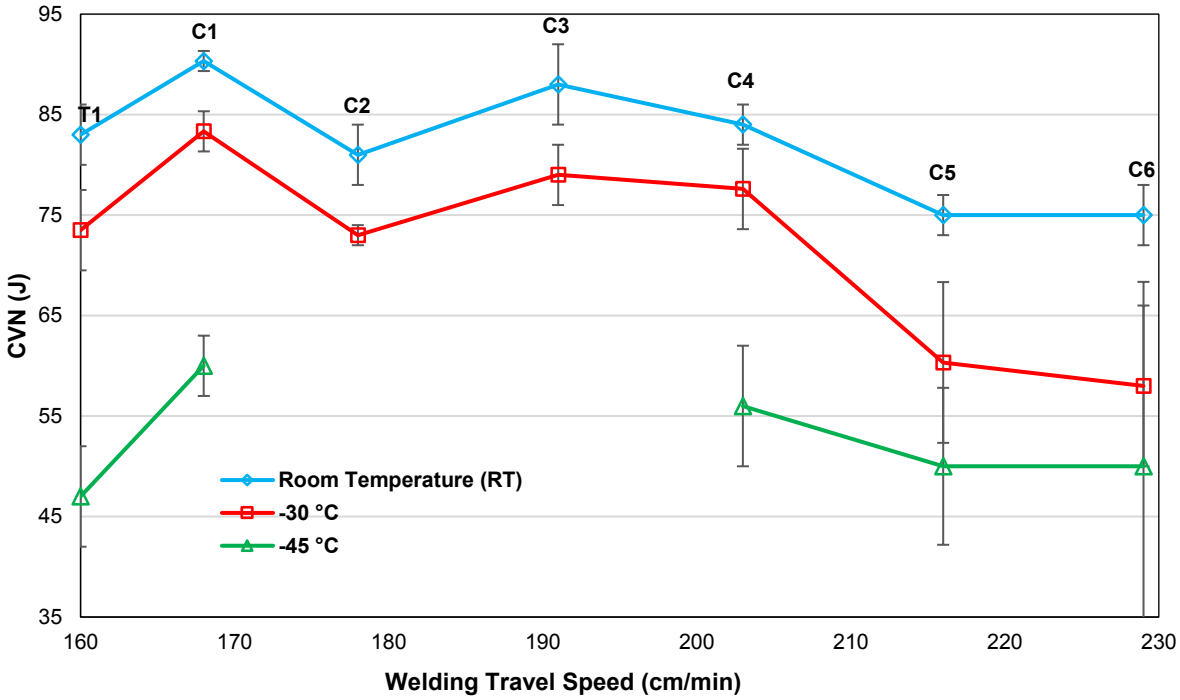

Figure 5-2 Charpy impact energy of the HAZ for steels welded at different travel speeds and cold wire feed rates.

Although the actual welding heat inputs for the C5 and C6 weld samples were the same as for the C1 sample, a significant reduction in the toughness of the C5 and C6 weld samples was observed. Macro and microstructural investigation indicated the formation of relatively large weld defects along the fusion line, which led to deviation of the crack during testing and a brittle response for the C5 and C6 welds. The granular flux used to shield the arcs during welding was entrapped in the weld metal along the fusion line. The phenomenon of flux entrapment in the weld metal is attributed to the arc force produced during welding. Rokhlin et al. [265] have found that the arc force is directly proportional to the arc current. This phenomenon is also confirmed through the work done by Adonyi et al. [266]. Electrical current flow generates magnetic fields that interact with current carriers and produce body Lorentz forces. Halmoy [267] formulated a simple approximate relation between arc force and current from the magnetohydrodynamic theory of an ideal conducting liquid with a homogeneous distribution of current across the arc. However, this model does not take into account the arc shape during welding. A welding arc force model was

developed by Converti [268] using a cone geometry, which is a better approximation to the real arc shape. The conical shape is caused by the constriction of the current at the cathode and arc expansion at the anode. The arc expansion is related to the welding current distribution and, therefore, to the arc force. According to his model, arc force has a quadratic dependence on the arc current. The relation between arc force (F_{arc}), current (I) and arc expansion (R_2/R_1) is given by Converti [269] as:

$$\boldsymbol{F_{arc}}: \frac{\mu_0 I^2}{8\pi}\left[1 + 2\ln\left(\frac{R_2}{R_1}\right)\right] \quad [5.7]$$

where R_2 and R_1 are the radius of the arc at the base plate and at the electrode, respectively, and μ_0 is the magnetic permeability in vacuum [269]. Although the current was significantly increased for the C5 and C6 welds to increase travel speed (i.e., productivity), the arc current was not sufficient to produce enough arc force to remove all the shielding flux while welding. However, our observations indicate that increasing the arc current resulted in a negative effect on the weld properties due to an increase in the overall welding heat input as well as some welding technical challenges such as arc blowing, arc sparking and burn-through. These welding challenges as a result of high welding current are also discussed elsewhere [203]. Figure 5-3 depicts the formation of weld defects and x-ray microanalysis of the defects. The defect composition is a combination of Al_2O_3, MgO, SiO_2 and CaF_2, which are the components present in the shielding flux [270]. Macroanalysis of the C5 and C6 samples showed consistent formation of these defects throughout the weld.

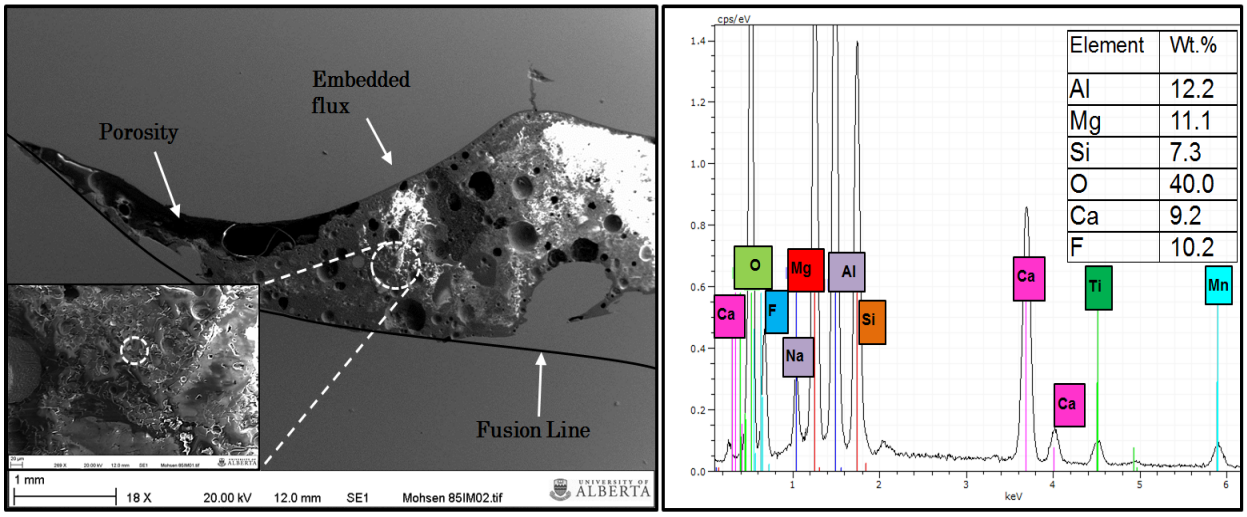

Figure 5-3 (a) SEM SE image representing defect formation in the weld region of the C5 and C6 weld samples. (b) Energy dispersive x-ray (EDX) spectrum from the defect at the region indicated in the inset.

The variation in the HAZ toughness of the T1 and C1-C4 weld samples is a result of microstructural alterations in the HAZ for the different welding conditions. The microstructural alterations in the HAZ, due to cold wire addition, are attributed to changes in the actual heat introduced to the weldment and, consequently, the cooling rate in the CGHAZ, when the cold wire is added to the TSAW process. Table 5-7 indicates the actual welding heat input calculated according to Equation 5.1. It is generally accepted that cooling rate is inversely proportional to the heat input of welding; therefore, the cooling rates in the C samples are higher than that of the T1 sample due to lower effective welding heat input of the C welds. Although the following equations developed by Easterling [80] and Poorhaydari [271] estimate the cooling rate (CR) of the weld, the equations, in this work, are employed to compare the approximate cooling times from 800 to 500°C ($\Delta t_{8\text{-}5}$) and the cooling rates for the fabricated welds according to their effective heat inputs.

$$\Delta t_{8-5}(sec) = \frac{HI_{eff.}}{2\pi\lambda} \times \left(\frac{1}{500 - T_0} - \frac{1}{800 - T_0}\right) \qquad [5.8]$$

$$CR\ \left(\frac{^{\circ}\mathrm{C}}{sec}\right) = \frac{300}{\Delta t_{8-5}} = \frac{2\pi\lambda(800 - T_0)(500 - T_0)}{HI_{eff.}} \qquad [5.9]$$

where T_0 and λ are the initial temperature (25°C) and thermal conductivity (41 J s^{-1} m^{-1} $°C^{-1}$), respectively. As stated earlier, as the heat input decreases, the cooling rate increases. As shown in Table 5-7, the cooling rate of the C1 sample was increased by 9.5% compared with the T1 sample. The cooling rates of the C3-C6 samples were fairly close to that of C1 sample. However, due to the lower effective heat input of the C2 weld, its cooling rate was substantially increased by 21%. The variation in the welding heat input and, consequently, the cooling rate by cold wire addition resulted in microstructural alterations and mechanical properties changes in the HAZ of the weld samples.

Table 5-7 Calculated actual welding heat input, CR and $\Delta t_{8\text{-}5}$, for the weld samples

Weld Sample	***Nominal Heat Input (kJ/cm)***	***Correction Factor (η)***	***Effective Heat Input (kJ/cm)***	***CR (ºC s^{-1})***	***$\Delta t_{8\text{-}5}$ (sec)***
T1	22.3	1.00	22.30	42.0	7.1
C1	22.1	0.87	20.62	46.0	6.5
C2	20.5	0.75	18.50	52.0	5.8
C3	23.0	0.79	20.65	46.0	6.5
C4	23.2	0.78	20.72	45.8	6.5
C5	23.5	0.77	20.81	45.6	6.6
C6	23.6	0.76	20.88	45.4	6.6

The results of our previous studies [166] indicated that the microstructure and mechanical properties of the HAZ are altered by a variation in the cold wire addition rate. Mruczek et al. [230] and Ramakrishnan et al. [18] have proposed that addition of a cold wire to SAW reduces the actual welding heat input, since the cold wire consumes the heat of the electrode. In addition, the HAZ cooling rate increases as the actual welding heat input decreases [242]. Accordingly, the addition of a cold wire in the conventional TSAW process affects the microstructure and mechanical properties of the HAZ due to reduction in the actual heat introduced to the weldment.

In addition to the Charpy impact testing, the weld samples were evaluated in terms of microhardness variation along the HAZ (Figure 5-4). The microhardness value of the as-received microalloyed steel plate was measured as 228±4 HV. The average microhardness in the HAZ of the C1 weld was reduced when a cold wire was fed at 25.4 cm/min compared with the T1 weld. However, an increase in the microhardness of the C2 sample was observed. This increase in microhardness of the C2 weld is due to the lower nominal welding heat input and faster cold wire addition in the welding process, which resulted in a decrease in the effective welding heat input and, consequently, a 21% increase in the cooling rate relative to the T1 weld (Table 5-7). However, by proper tuning of the nominal welding heat input and cold wire addition rate in the C3 and C4 welds, resulting in an effective welding heat input the same as the C1 weld, the average microhardness in the HAZ was close to that of the C1 sample. The variations in both microhardness and toughness of the weld samples are attributed to microstructural alterations taking place in the HAZ, due to the changes in the effective welding heat input and consequent cooling rate, which are discussed in a subsequent subsection.

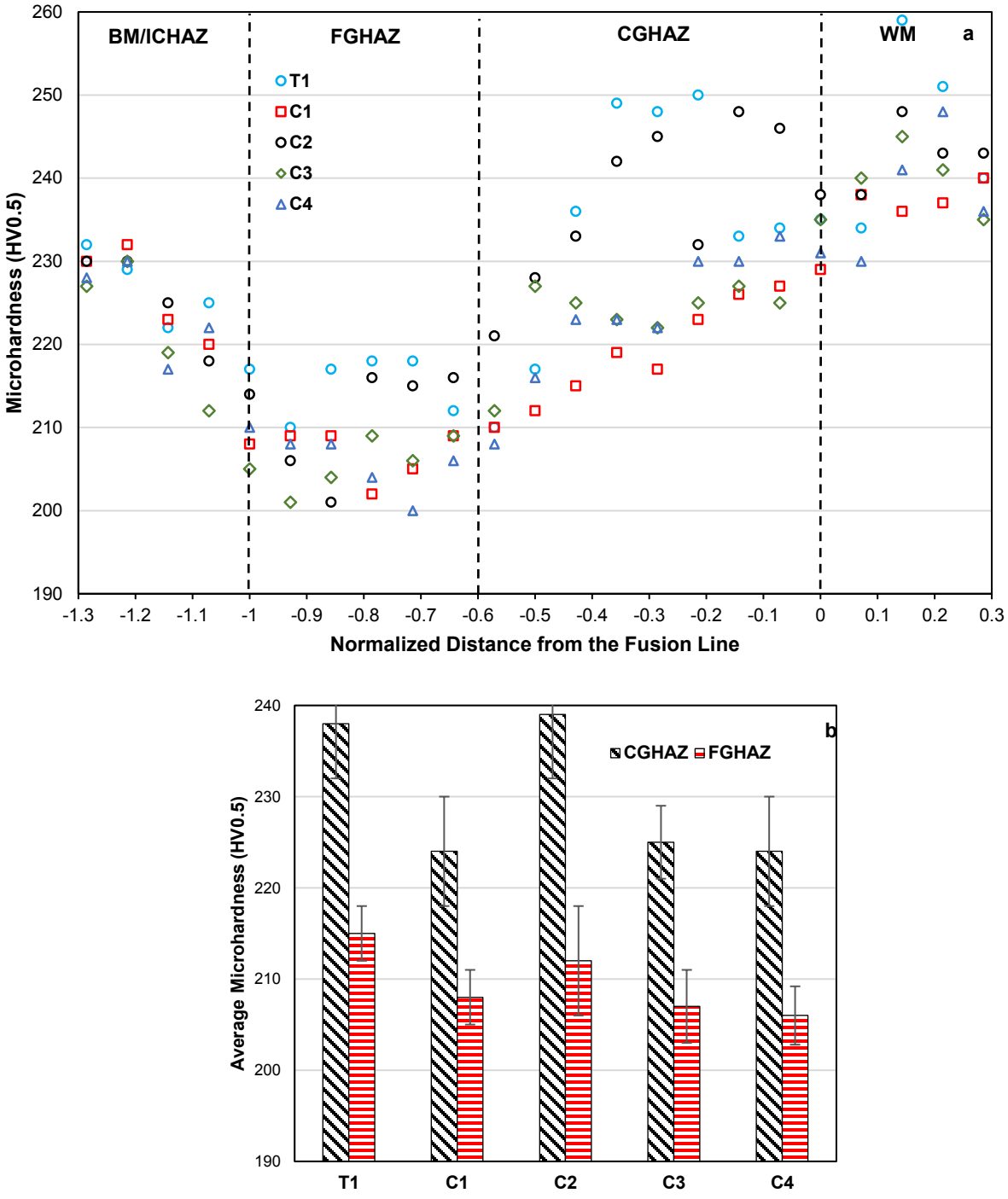

Figure 5-4 (a) Microhardness variation within the weld samples. (b) Average microhardness, with the standard deviation, for the FGHAZ and CGHAZ of steel samples welded by the CWTSAW and TSAW processes.

5.3.3. Welding productivity

The potential advantage of adding a cold wire in the conventional TSAW process is to increase the deposition rate to achieve a proper joint without increasing welding heat input [17,262]. Moreover, to join thick sections, fewer beads are needed for a given joint, thereby increasing productivity. Given the fact that cold wire addition increases the deposition rate, the possibility of the increasing welding travel speed using CWTSAW while retaining weld geometry, appearance and properties has been investigated. In this work, the T1 weld was prepared by conventional TSAW; however, a cold wire was fed during the process (i.e., welds C1-C6) to increase the deposition rate and travel speed without property deterioration and without the use of additional heat input. As discussed earlier, the travel speed was increased for the C1, C3 and C4 welds with no detrimental effect on the properties. Figure 5-5 depicts the increased travel speed and deposition rate by additional cold wire compared with the TSAW process.

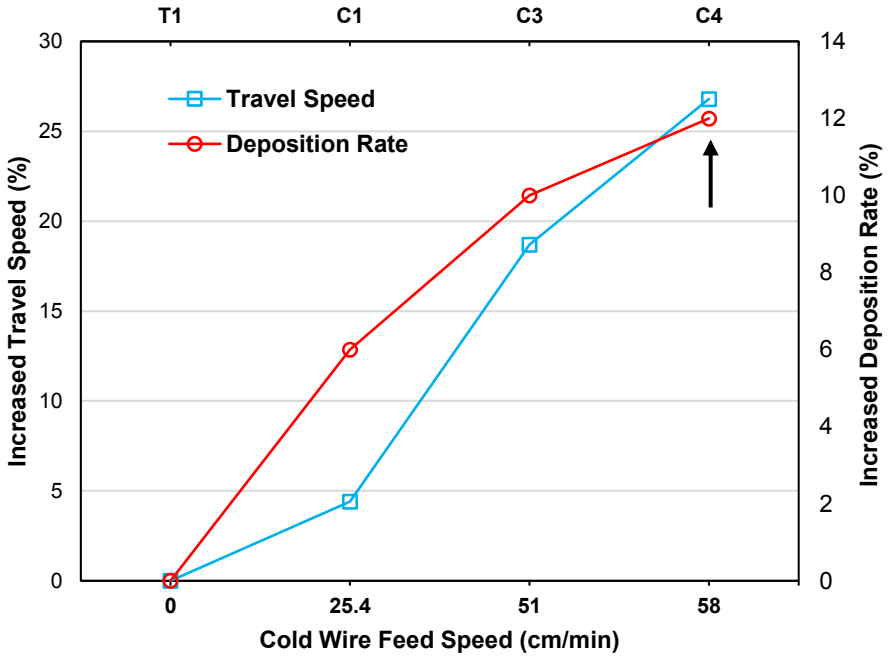

Figure 5-5 Percentage of increased travel speed and deposition rate as a function of the cold wire addition rate in TSAW.

5.3.4. Microstructure analysis

During welding, the region of the base metal affected by the heat of welding, the HAZ and the CGHAZ in particular, tends to weaken in terms of fracture toughness (relative to the base metal of the microalloyed steel) due to the high heat input and thermal cycles that the steel experiences

during welding. The deterioration in toughness of the CGHAZ is essentially attributed to the formation of large PAGs and martensite-austenite (M-A) constituents, which are characterized as localized brittle zones (LBZ), as a result of the high peak temperature and relatively fast cooling rate in the CGHAZ [100,129,177,218,224]. Davis et al. [226,272] and Reichert et al. [273] found that the formation of a network of enlarged M-A constituents resulted in cleavage crack initiation in the HAZ. Moeinifar et al. [274] suggested that a reduced fraction of M-A constituents in the CGHAZ was beneficial to the impact toughness. However, the fraction and size of M-A constituents are dependent on the PAG size. Yu et al. [218] and Li et al. [177] showed that the fraction and shape of M-A constituents were increased by coarsening the PAGs in the CGHAZ. They found that coarse PAGs, associated with coarse M-A constituents, are the dominant factor in promoting brittle fracture in the CGHAZ. Gharibshahiyan et al. [228] have reported that the formation of coarser PAGs in the CGHAZ has a detrimental effect on the toughness of the HAZ. Yang and Bhadeshia [217] and Garcia-Junceda et al. [229] showed that the martensite start temperature (Ms) increased with an increase in the PAG size, which resulted in a higher volume fraction of martensite. The work done by Lee et al. [275] led to a linear relation between the martensite temperature (Ms) and the ASTM gain size number (G) for low alloy steels.

$$M_s(°C) = 542.3 - 30.0 \times G \quad [5.10]$$

The PAG size in the CGHAZ of the C1-C4 welds were measured by the process explained in Chapter 4. Figure 5-6 indicates the variation in the Ms temperature as a function of the PAG size for T1 and C1-C4 welds. The PAG size reduction in the CGHAZ of the C welds relative to the T1 weld is due to a reduction in the effective welding heat input and, consequently, an increase in the cooling rate. According to Equation [10], as the PAG size increases (the ASTM number decreases), the Ms temperature increases. The coarser PAGs in the CGHAZ of the T1 weld compared with the other weld samples resulted in a higher fraction of martensite [139]. Furthermore, Bhadeshia [139,276], Yan et al. [244] and Matsuda et al. [277] have suggested that, in addition to the PAG size, cooling rate affects the morphology of the M-A constituents, which also affects the toughness of the welded steel. Kim et al. [245] have reported that M-A islands are the main metallurgical factor, which contribute to local embrittlement of microstructures of welded microalloyed steels. The Charpy impact toughness of the CGHAZ of high strength low-carbon steels is a function of the fraction, morphology, carbon content and distribution of the M-A islands. The work done by Lan et al. [278] indicated that the relatively fast cooling rate in the HAZ of a low-carbon steel led to the formation of slender M-A constituents with higher carbon levels and segregated alloying elements, such as silicon in the M-A islands, which resulted in an increase in the martensite hardness in the HAZ. As

such, there is a concurrent effect of PAG size and cooling rate on the characteristics of the transformation products, in particular the M-A constituents, in the HAZ of microalloyed steels.

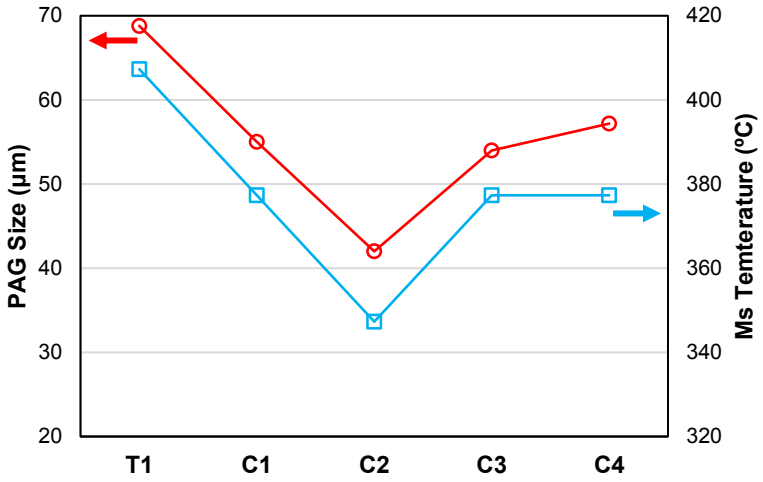

Figure 5-6 PAG size and Ms temperature of the CGHAZ of weld samples prepared by both CWTSAW and TSAW processes.

Optical micrographs of the CGHAZ of the weld samples analyzed using the TEOM method [140,141] are shown in Figure 5-7. The M-A constituents are revealed as white islands. The microstructure in the CGHAZ of the T1 weld (with higher heat input – Figure 5-7a) is comprised of polygonal ferrite (PF), granular bainite (GB), bainitic ferrite (BF) and a relatively high fraction of large M-A constituents along with large PAGs. In contrast with the T1 weld, the CGHAZ microstructure of the C1 sample is composed of finer PAGs, GB, PF and BF associated with fine, uniformly distributed M-A constituents (Figure 5-7b). The characteristics and fraction of the M-A constituents formed in the CGHAZ of the C3 and C4 welds (Figure 5-7d-e) are like those of the C1 weld, because of similar effective welding heat inputs and cooling rates. Due to the faster cooling rate in the CGHAZ of the C2 weld (with the lowest effective welding heat input), smaller PAGs were formed, resulting in a lower fraction of elongated M-A constituents in the CGHAZ of C2. Although a lower fraction of M-A was formed in the CGHAZ of C2 weld, there were more elongated M-A constituents formed along the boundaries. This may be attributed to a greater reduction in the actual heat introduced to the weldment and the relatively fast cooling rate of the C2 weld compared with the C1 and T1 welds.

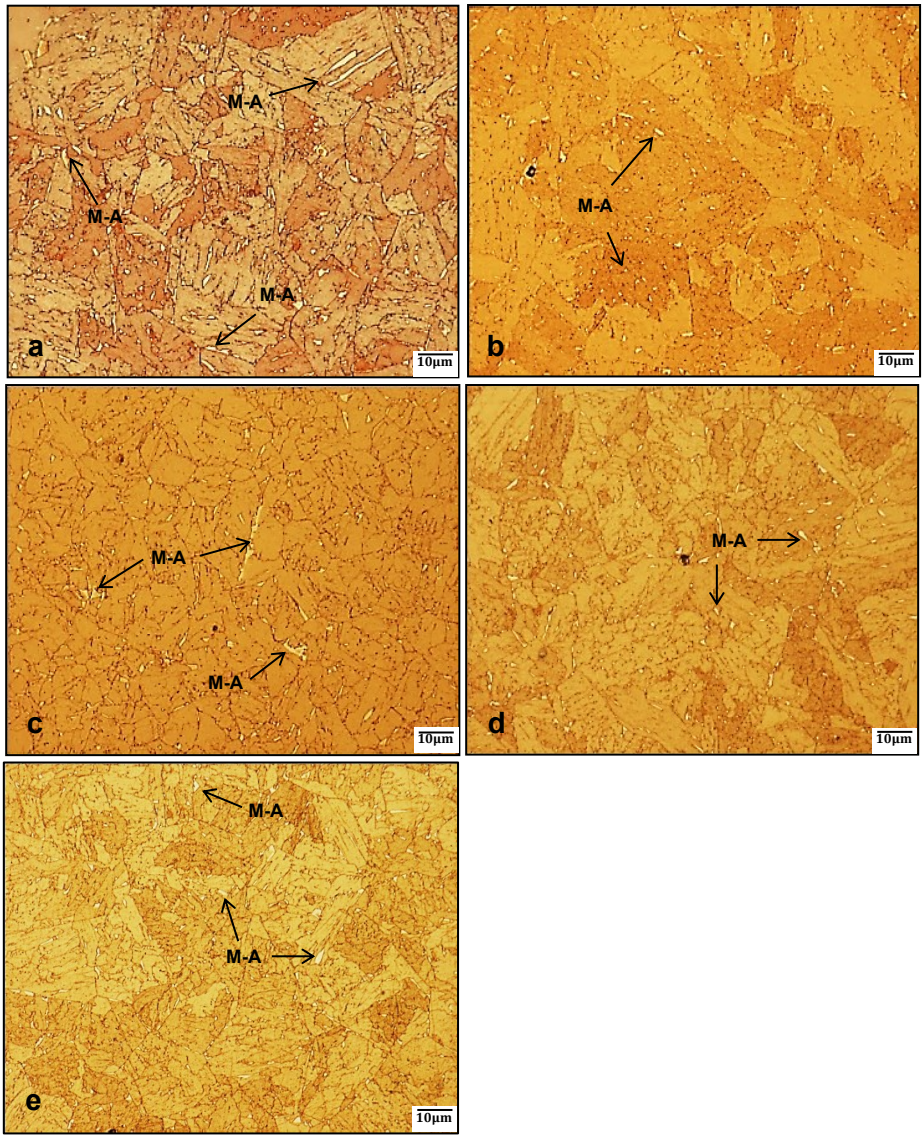

Figure 5-7 Optical micrographs of the CGHAZ of the (a) T1, (b) C1, (c) C2, (d) C3 and (e) C4 welds.

SEM secondary electron (SE) micrographs of the CGHAZ of the weld samples are depicted in Figure 5-8a-e. The fraction and characteristics of the M-A constituents, along with the PAGs formed in the CGHAZ, are altered due to the heat input, high peak temperature and thermal cycles during welding. The PAG size influences the phase transformation temperature and kinetics during cooling. Qiao et al. [224] and Shome [242] reported that the size of PAGs in the HAZ depends on the local thermal cycle and the PAG size increases when the welding heat input is increased. Refining the PAG size influences the transformation products, particularly the M-A constituents, within the HAZ, which affect the toughness. Studies by Bhadeshia [139,238] and Yan et al. [244] suggest that, in addition to PAG size, cooling rate affects the morphology of the M-A constituents, which also

affect the toughness of the welded steel. The Charpy impact toughness of the CGHAZ of high strength low-carbon steels is a function of the fraction, morphology and carbon content of the M-A islands [245]. Lan et al. [172] indicated that the relatively fast cooling rate in the HAZ of a low-carbon steel led to the formation of slender M-A constituents with higher carbon levels and segregated silicon in the M-A islands, which resulted in an increase in the martensite hardness in the HAZ. To evaluate the effect of M-A characteristics on the fracture toughness of the HAZ, mean size, inter-particle spacing and fraction of the M-A constituents in the CGHAZ for the T1 and C1-C4 welds were measured and are presented in Figure 5-9a-b. The distribution of M-A constituents in the CGHAZ of the weld samples was analyzed using the mean inter-particle spacing equation developed by Somekawa et al. [279] (Chapter 4). The equation correlates the inter-particle spacing with the relative volume fraction and the mean particle size.

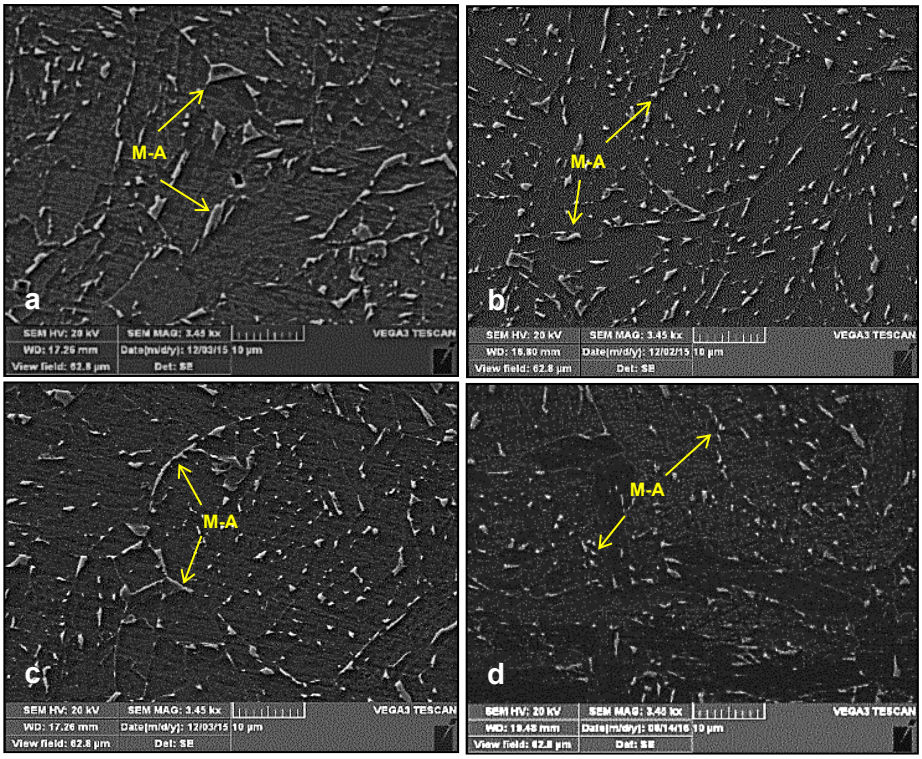

Figure 5-8 SEM SE images of the CGHAZ for the (a) T1, (b) C1, (c) C2 and (d) C3 samples.

The fracture toughness of the CGHAZ of welded microalloyed steels is highly influenced by the shape, size, distribution and fraction of M-A constituents in the CGHAZ [177,218,245]. As shown in Figure 5-9a, the M-A fraction in the CGHAZ was reduced from the T1 to the C1 and C2 samples, as a consequence of PAG size reduction due to the lower effective welding heat input [166,244]. However, the formation of slender shaped M-A constituents with large inter-particle spacing in the C2 sample, as a result of the relatively faster cooling rate, resulted in a reduction in the HAZ

toughness compared with the C1 weld sample. The characteristics and fraction of the M-A constituents in the CGHAZ of C3 and C4 welds were similar to those of the C1 sample. M-A was finely distributed within the PAGs with smaller inter-particle spacing relative to that of the T1 and C2 samples (Figure 5-9b). According to the Charpy results and the microstructural analysis, the fracture toughness of the HAZ of C1, C3 and C4 welds was increased due to a decrease in the M-A size and inter-particle spacing in the CGHAZ. Accordingly, the formation of finely distributed M-A constituents in the CGHAZ resulted in a beneficial effect on the fracture toughness.

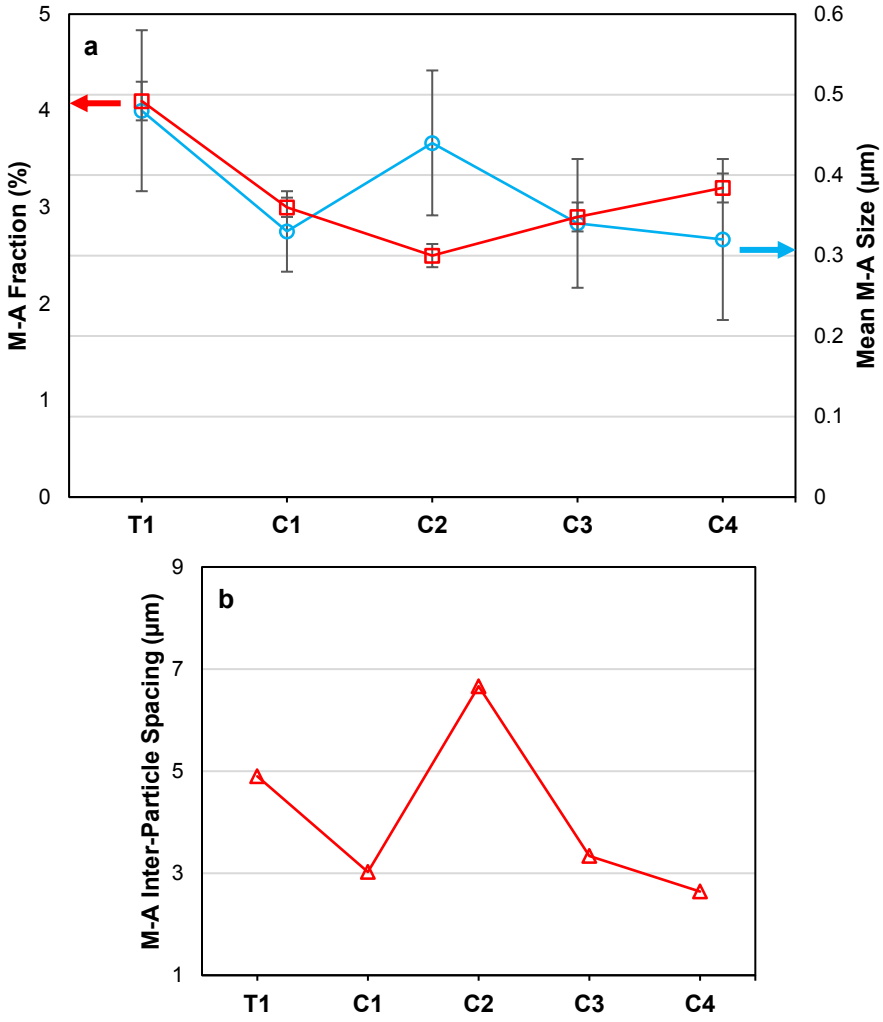

Figure 5-9 (a) Fraction and mean size of M-A constituent in the CGHAZ and (b) M-A inter-particle spacing in the CGHAZ for the weld samples.

Heinze et al. [219], Bhadeshia et al. [139,217] and Guimaraes [247] suggested that a decrease in the PAG size causes a decrease in Ms temperature, resulting in a lower fraction of martensite. According to the classical Koistinen-Marburger (KM) equation [216] and the geometrical

partitioning model by Fisher et al. [221], the fraction of martensite is a function of the amount of undercooling below the Ms temperature. Based on the proposed models, the martensite volume fraction formed in the early stages of the transformation is proportional to the PAG size cubed; hence, "the fraction of the transformation needed to detect Ms is reached at a smaller undercooling when the PAG size is larger" [217]. The higher Ms for samples with larger PAGs results in the formation of larger M-A constituents in the CGHAZ [139,217,218,229]. Therefore, a coarser PAG size increases the fraction and size of the M-A constituent. Yu et al. [218] and Li et al. [177] showed that a coarse PAG size, associated with a coarse M-A constituent, is the dominant factor in promoting brittle fracture in the CGHAZ. Accordingly, there are concurrent effects of both grain size refinement and M-A transformation, which play a significant role in the strength and toughness of the HAZ. Due to the formation of a higher proportion of the M-A constituent (LBZs) in the CGHAZ of the T1 sample compared with the C1-C4 samples, the microhardness values in the CGHAZ for the T1 sample were higher relative to the other welds (Figure 5-4). A relatively uniform distribution of fine M-A constituents inside the ferritic matrix in the CGHAZ of the C1, C3 and C4 samples resulted in a higher fracture toughness for the HAZ at the various testing temperatures. However, based on the work done by Davis et al. [128,226] and Reichert et al. [227], coarser PAGs with large M-A constituents led to inferior toughness properties in the HAZ of the T1 sample. They found that the combination of a slender shape and the formation of a network of M-A constituents along the boundaries is most detrimental to fracture properties. With reference to the C2 sample, Bhadeshia [139,238] and Yan et al. [244] have proposed that, in addition to the PAG size, the shape, size and distribution of the M-A constituents along with the martensite carbon content are influenced by the cooling rate in the HAZ, which affects toughness of welded microalloyed steels [248]. The formation of the slender shaped M-A constituents with large inter-particle spacing in the CGHAZ of the C2 sample, due to the relatively faster cooling rate in the CGHAZ as a result of the lower effective heat input compared with the C1 weld, led to a slight decrease in toughness for the HAZ of the C2 sample (Figure 5-10). This phenomenon has also been confirmed by the work of Davis et al. [226], Kim et al. [245] and Lan et al. [172], who have suggested that the morphology of martensite changes and the carbon content of martensite increases in the M-A constituents as the cooling rate in the CGHAZ increases. As such, the relatively faster cooling rate in the CGHAZ of the C2 sample compared with the C1, C3 and C4 welds resulted in the formation of slender M-A constituents with larger inter-particle spacing.

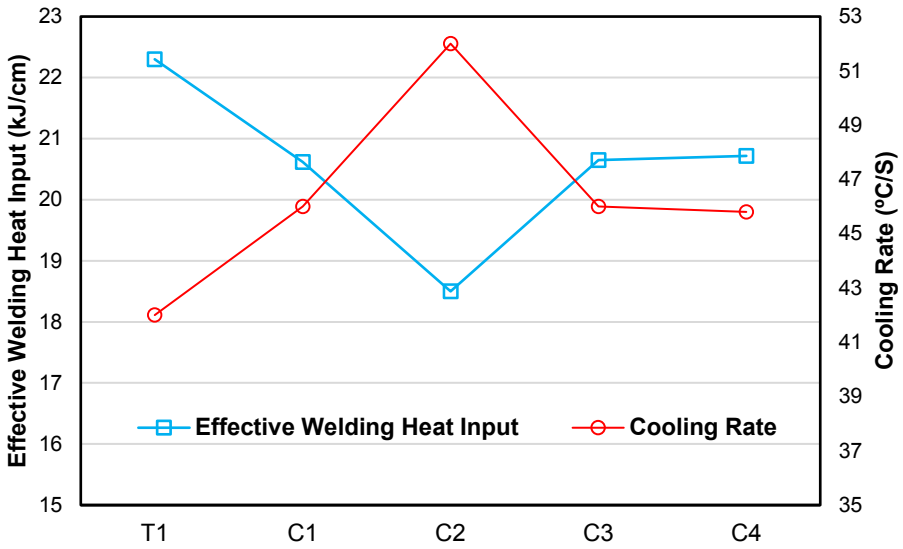

Figure 5-10 Effective welding heat input and cooling rate of different weld samples (as a function of the nominal welding heat input and cold wire feed speed).

5.4. Conclusions

The addition of a cold wire in conventional tandem submerged arc welding (TSAW), i.e., cold wire tandem submerged arc welding (CWTSAW), has a two-fold effect on the characteristics of the welded microalloyed steels; i.e., increased welding productivity and improved properties. The additional cold wire resulted in a higher deposition rate and travel speed for welding (increased productivity), while retaining adequate weld appearance and properties. In this work, a 12% and 26% increase in the deposition rate and travel speed, respectively, were achieved by addition of a cold wire at 58 cm/min in the TSAW process with a heat input of 23.2 kJ/cm. Moreover, cold wire addition resulted in an overall improvement in the fracture toughness of the HAZ; however, it should be noted that the improvement is greatly influenced by the cold wire addition rate and the consequent effective welding heat input. The cold wire moderates the heat input of welding by consuming some of the heat of the trail electrode. Accordingly, cold wire addition at 25.4 cm/min during TSAW with a heat input of 22.1 kJ/cm (C1 weld) showed an improvement in the fracture toughness of the HAZ due to a reduction in the prior austenite grain (PAG) size and the fraction of martensite-austenite (M-A) constituents, along with a uniform distribution of finer M-A constituents in the ferritic matrix. The microstructural alterations are attributed to the lower effective welding heat input (7.5% reduction compared with the TSAW (T1) sample). The C2 weld, prepared at a lower heat input of 20.5 kJ/cm and faster cold wire addition (63.5 cm/min) relative to the C1 weld, had a smaller PAG size compared with the C1 and T1 weld samples, due to the

relatively larger reduction in the effective welding heat input (17.1% reduction) and faster cooling rate in the CGHAZ of the C2 sample. However, elongated M-A constituents were formed. The relatively large elongated M-A constituents with large inter-particle spacing, which mostly formed along the boundaries in the CGHAZ, of the T1 and C2 welds compared with those of the other weld samples led to inferior toughness properties for the HAZ of the former samples, since larger M-A constituents can stimulate the formation of microcracks leading to intergranular fracture.

Chapter 6

6. Correlation between Microstructure and Toughness in the HAZ of the Welded X70 Microalloyed Steel Using Single-Edge Notch Tension (SENT) Testing

6.1. Introduction

Toughness is an important material property, where the resistance to fracture for a material containing a crack is assessed. In developing pipelines, fracture toughness, specifically low-temperature toughness, and the ductile-to-brittle transition temperature (DBTT) are considered as two main fundamental aspects. However, toughness is controlled by a number of microstructural factors, such as the type of phases and morphology of dispersed hard secondary phases (e.g., precipitates and M-A constituents) [111,154,155]. The DBTT, the temperature below which the steel loses its toughness and fails in a brittle mode, is a crucial consideration for pipeline design that needs to be addressed for any type of pipeline steel [156,157]. During the past several decades, the relationships between microstructure and mechanical properties of high strength microalloyed pipeline steels have been extensively studied in an effort to improve the fracture toughness and strength of this type of steel without appreciably increasing steel manufacturing and pipeline fabrication (welding) costs. Fueled by the demand for pipeline steels with high strength, toughness and low cost by the construction, energy and transportation industries, it is essential to improve the properties of microalloyed steels and their welds and HAZ.

The fracture toughness resistance curve, i.e., the J-integral resistance curve (J-R) and the crack tip opening displacement resistance (CTOD-R) curve, are broadly utilized in strain-based design of energy pipelines and engineering critical assessment (ECA) with respect to planar defects (cracks). According to fracture mechanics principles, an ECA is made to evaluate whether or not a given flaw within the material of interest is safe from brittle fracture, fatigue and creep under specific loading conditions. The fundamental concept in conventional elastic-plastic fracture mechanics is that the crack tip stress field can be defined by a single parameter, the J-integral (HRR (Hutchinson-Rice-

Rosengren) field) or the CTOD, and material fracture toughness, which is usually obtained from standard bending fracture mechanics testing specimens, can be transferred to an ECA of the structural components. However, there are many situations where the conventional single parameter approach becomes invalid and crack tip stress fields are influenced by a less severe crack tip constraint. In fact, the constraints can be understood as structural or material obstacles against plastic deformation, which is induced mainly by geometrical and physical boundary conditions [280]. There is, however, an emphasis in fracture mechanics to develop appropriate parameters to characterize the stress field at the crack tip. The crack tip stress field is essentially influenced by the specimen geometry, flaw depth (a) to specimen width (W) ratio (i.e., a/W), loading mode and the mismatch between different materials with different properties (for example, a crack formed at the interface of the weld metal and heat affected zone (HAZ)). In addition, the recent work by Eikrem et al. [281], Ren et al. [282] and Liu et al. [283] have shown that the pre-strain history which is induced in the material prior to service, such as stresses induced by pipe reeling and welding residual stresses, will result in additional crack tip constraints. All these situations have made the development of a fracture mechanics test method fulfilling all these conditions quite sophisticated. Zhu et al. [284,285] have presented a comprehensive technical review and standardized the fracture toughness test methods at the American Society for Testing and Materials (ASTM) in the USA. Amongst the standard fracture test methods, ASTM E399 [286] and ASTM 1820 [187] are two representatives which describe measuring the elastic plane strain fracture toughness (K_{IC}) for brittle materials and determining the elastic-plastic plane strain fracture toughness (J_{Ic} or δ_{Ic}), J-R curves and δ-R curves for ductile materials, respectively. In addition, there are numerous endeavors worldwide to standardize the fracture toughness test methods, such as the British Standard Institution (BSI 7448) [188] and the International Organization for Standardization (ISO 12135) [287] which corresponds to ASTM 1820.

6.2. Fracture Toughness Test Methods

How a metallic material behaves during a fracture toughness test can essentially be described by three aspects: the fracture behavior of the material, the strength and deformation behavior of the material and constraint effects associated with geometry. As such, understanding these aspects can help in performing successful fracture toughness tests. During the early stages of standardizing fracture toughness test methods, these three considerations tended to be confused. Thus, significant efforts have been made to distinguish their differences, so that proper fracture parameters and characterization procedures are used during fracture toughness testing for the

material of interest. Basically, the fracture behavior is related to the micro-mechanisms of fracture and is usually described as being either ductile or brittle. Brittle fracture behavior results in the development of rapid and unstable crack extension and can correspond to cleavage fracture. In brittle fracture, a test specimen macroscopically has a unique and well-defined point of crack initiation, corresponding to a sudden drop in load, and provides only a one data point for evaluating fracture toughness.

In ductile fracture behavior, slow and stable crack extension happens since a crack extends by microvoid growth and coalescence, which tends to absorb more energy. This macro-mode of fracture is a continuous process of ductile tearing rather than a point fracture, which requires a crack extension resistance curve (R-curve) to be measured for characterizing ductile fracture. The entire R-curve can be used to describe ductile fracture. However, many methods which use fracture toughness for ECA and structural integrity assessment (SIA) require a single point value of toughness. A typical point value of ductile fracture toughness is usually defined near the onset of stable crack tearing and deduced from the R-curve near the transition from initial crack blunting to crack tearing, which is usually characterized by a distinct change in slope of the R-curve. This result is referred to as fracture initiation toughness. A typical example is to estimate ductile fracture toughness as the toughness demonstrated by a deeply cracked bend type specimen at 0.2 mm of crack extension beyond initial crack tip blunting.

Pipelines are sometimes subjected to large-scale bending and tensile deformation, which places the welds and their surroundings in tension. The weld and HAZ may contain small planar flaws, i.e., cracks, which make it necessary to assess the resistance of the flaw to growth (toughness) under relevant stresses. The stress intensity factor, K, proposed by Irwin [179] is used for a crack in an elastic material. However, for a ductile crack, Rice [180] and Wells [181] proposed the J-integral and the CTOD methods, respectively. The fracture toughness resistance curve (R-curve) of pipeline steels is a key tool to assess the resistance of the pipe to fracture. Accordingly, R-curves are essential in SIA, ECA and strain-based design of pipelines with respect to cracks [182]. As stated earlier, the R-curve is generally represented by either the CTOD resistance curve (CTOD-R curve) [183] or the J-integral resistance curve (J-R curve). It is worthwhile to note that the accuracy of the experimentally measured R-curve directly influences the accuracy of the design and assessment of pipelines.

In order to assess the conservative fracture resistance, most fracture test standards involve deeply cracked specimens with more severe crack-tip constraint conditions. Fracture mechanics test methods, e.g., the compact tension (CT) test [184], the disc-shaped compact tension (DCT) test,

the arc-shaped tension test [185] and the single edge notched bend (SENB) test [186], which are proposed in ASTM E1820 [187], BS 7448-1 [188] and ISO 12135 [287], are mainly used to address the measurement of fracture toughness in severe crack-tip constraint conditions and high triaxiality conditions (Figure 2-21). Amongst these methods, CT and SENB are the two most often methods used for fracture toughness analysis. However, many experimental and theoretical works have shown that the crack-tip constraint level, which is basically due to the geometry of specimen, crack size and loading condition, has a strong effect on the fracture resistance in terms of J-R or CTOD-R curves. Generally speaking, a more severe constraint at the crack-tip results in a lower R-curve, while a less severe constraint specimen gives a higher R-curve. This high constraint condition is due to the existence of a deep crack within the standard specimen, which does not necessarily represent the stress state around defects in real structures. SENB has been widely used for fracture toughness analysis of welded pipes; however, as stated earlier, due to the deep crack, the value of the toughness is too conservative. In the most recent revision of ASTM E1820-13 [187], an appendix is added to support low-constraint shallow cracked SENB specimens; however, in general, bend specimens provide more severe constraints than tension specimens at the same crack depth. With reference to pipeline fracture toughness, due to the thin wall thickness and large amount of plasticity involved, it has become evident that fracture mechanics based on the ECA of pipelines using fracture toughness directly obtained from standard SENB specimen is too conservative. Accordingly, the single-edge notch tension (SENT) test has recently been developed to analyze the fracture toughness of pipelines in the less severe constraint crack-tip condition. A schematic of SENB and SENT fracture toughness techniques is depicted in Figure 6-1.

6.2.1. Single-edge notch tension (SENT) test

With reference to pipelines, Nyhus et al. [288] conducted a three-dimensional finite element analysis of surface semi-elliptical circumferential cracks and concluded that the level of crack-tip constraint is much closer to that of SENT specimens than SENB specimens. Their findings became the basis of the DNV guidelines for ECA of pipeline installation introducing plastic strains. Several experimental methodologies have been proposed by DNV [190], Canmet Materials [191,192] and Exxon Mobil [193]. There is still a lack of the standardization for the SENT test; however, a British standard (BS 8571 [200]) is currently being developed based on the method described in DNV RP F108 [190] to determine fracture toughness using SENT specimens. There are also some advancements in the SENT test specimens proposed through some published research articles and reports [194–197]. The crack-tip constraint in a SENT specimen can be fine-tuned through the loading condition (clamped and pin-leaded), crack/width ratio (a_0/W) and the specimen length

(shown in Figure 6-2). Cravero and Ruggieri [289] showed that pin-loaded SENT specimens with moderate and shallow cracks in plane strain conditions generate crack-tip constraint levels close to axial surface cracks in a pipe with identical crack sizes. Later, it was shown by Cravero et al. [195,290] that the clamped SENT condition results in crack-tip constraints similar to those for identical circumferential surface cracks in pipes. As such, both SENT conditions can be used to measure the fracture toughness for an axial or circumferential crack in a pipe. However, in general, the crack tip constraints of a SENT specimen can be increased by using pin-loading conditions, longer specimens and deeper cracks.

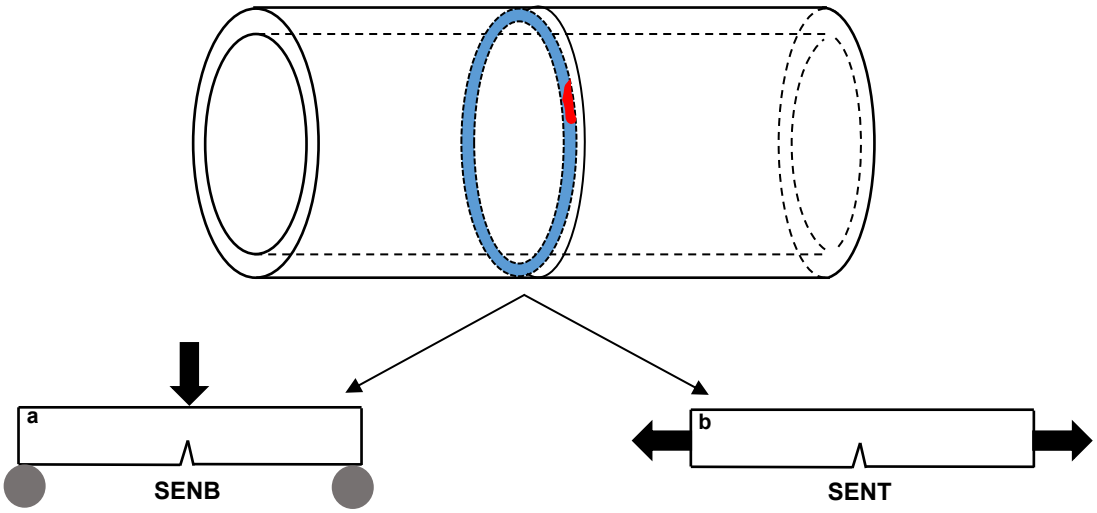

Figure 6-1 Fracture toughness testing specimens for pipeline applications: (a) single-edge notch bending (SENB) test and (b) single-edge notch tension (SENT) test.

Due to the less severe crack-tip constraint condition in an SENT specimen, it is often preferred over other test methods by pipeline industries to assess less conservatively the fracture toughness via low constraint SENT testing. In the SENT test, there are two essential procedures, i.e., the multi-specimen technique and single-specimen method. The former method typically uses a set of seven specimens with the same initial crack size loaded to different load levels proposed by DNV RP F108. Subsequently, ductile crack extension is determined after breaking the specimens in liquid nitrogen. However, these results are highly susceptible to scatter in the data and require a significant amount of test material. Thus, currently the focus is on using the single-specimen technique. Accordingly, this technique uses either a single clip gauge or double clip gauges attached to the integral knife edge or mounted in a set of knife-edges, respectively, to estimate the crack-mouth opening displacement (CMOD) and CTOD. The CTOD can be estimated indirectly from the J-integral using the ASTM conversion procedure [187] and/or from the unloading compliance crack

size equations proposed by DNV RP F108 [190] and Shen et al. [198]. The CTOD can also be directly determined from the original crack-tip position on the specimen by triangulation from the double clip gauges and then using the unloading compliance equations to predict the crack size. Direct-current potential-drop (DCPD) instrumentation can be used as well for supplementary crack size measurement.

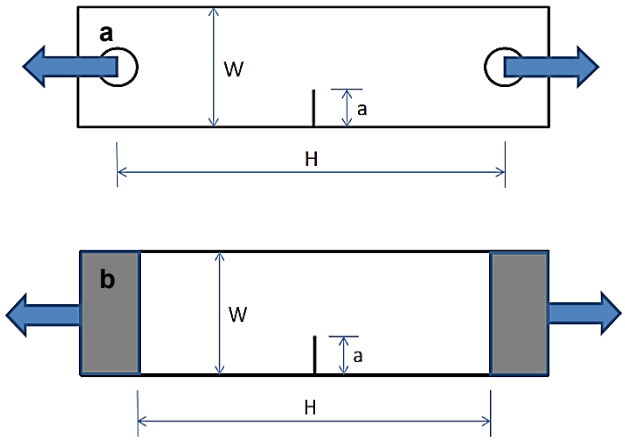

Figure 6-2 Schematic of (a) pin-loaded condition and (b) clamped condition to conduct an SENT test [291].

A detailed summary of the SENT test procedure carried out by several researchers is shown in Table 2-3 in Chapter 2. As stated earlier, the crack-tip constraints caused by the thickness, size and configuration of fracture test specimens can have a strong effect on the measured values of fracture toughness. In general, more severe constraint results in higher crack-tip stresses with less crack-tip yielding and promotes a more brittle fracture or reduces the resistance curve toughness for ductile fracture. Less severe constraint results in lower crack-tip stresses with more crack-tip yielding and tends to reduce the possibility of brittle fracture and to raise the resistance curve toughness for ductile fracture. The specimen configuration, loading mode and crack depth can cause an effect on crack-tip constraints. For example, a deeply cracked bend dominated specimen will demonstrate a more severe constraint at the crack-tip than that shown by a shallow cracked tensile specimen. To reduce the effects of specimen configuration and thickness on the measured toughness results, a standard is required to specify the specimen's dimension with a fixed range of crack depth to width ratios, to set limits on the remaining ligament to thickness ratios, to define the loading condition and, in many cases, to specify the side grooves along the crack ligament.

6.3. Fracture Mechanics

The fracture mechanics of ductile cracks and the methods of fracture toughness analysis are fundamentally presented in the ASTM, BSI and ISO standards. However, as stated earlier, most of the methods have severe constraints for the crack-tip, which depend on the geometry of the specimen and crack and the loading conditions. Here ASTM E1820-13 [187] standard and recently developed BS 8571-2014 [200] are described, based on the SENT fracture toughness test method developed. In addition, some SENT test procedures developed by companies are discussed.

6.3.1. ASTM E1820 standard fracture test methods

6.3.1.1. Basic method for J_{Ic} determination

In order to define a J fracture criterion, i.e., $J=J_{Ic}$, where J_{Ic} can be considered a material parameter, extensive experimental studies on the J-integral testing have been conducted to develop effective test methods for determining the critical value J_{Ic} for plane strain growing cracks. The early J-integral test methods were basically developed by considering the load vs. load-line displacement (LLD), standardized by ASTM [284]. ASTM E1152-87 was initially developed to generate J-R curves. According to the standard, the J-integral was separated into two elastic and plastic components to be determined separately.

$$J = J_{el} + J_{pl} \qquad [6.1]$$

where the elastic component, J_{el}, is directly calculated from the stress intensity factor, K, for a plain strain crack.

$$J_{el} = \frac{K^2}{E}(1-\nu^2) \qquad [6.2]$$

where E and ν are the Young's modulus and Poisson's ratio, respectively. J_{pl} for a stationary crack is determined from the following η-factor equation.

$$J_{pl} = \frac{\eta A_{pl}}{B_N b} \qquad [6.3]$$

where η is a plastic geometry factor (dependent on the crack depth to specimen width ratio (a/W) and specimen type) and b is the specimen ligament (b=W-a). B_N and A_{pl} are the thickness of the side-grooved specimen and plastic area under the load-LLD curve obtained from a fracture test, respectively. The above equations were initially adopted in ASTM E1152; however, these are used in the recent version of ASTM E1820 as the basic procedure of plane strain initiation toughness, J_{Ic}, evaluation where crack growth resistance is not needed. Accordingly, the determination of the plastic η factor has become essential in the experimental estimation of J-integral. The laboratory

work done by Sumpter et al. [292] showed comprehensively that J-based fracture toughness testing was feasible using the η-factor method.

The early approach to determine the plastic η factor was based on plastic limit analysis. For CT specimens with deep cracks, Clarke et al. [293] obtained an approximate fitted function of the η factor (Equation 6.4). In addition, for SENB specimens in pure bending, Sumpter [294] obtained the η factor for a complete range of crack sizes (Equation 6.5). However, many research works using finite element calculations [295,296] have been performed to determine more accurate values of the η factor.

$$\eta = 2 + 0.522\left(1 - \frac{a}{W}\right) \qquad [6.4]$$

$$\eta = \begin{cases} 2 & a/W > 0.282 \\ 0.32 + 12\left(\frac{a}{W}\right) - 49.5\left(\frac{a}{W}\right)^2 + 99.8\left(\frac{a}{W}\right)^3 & a/W \leq 0.282 \end{cases} \qquad [6.5]$$

Later, it was understood that CMOD is easier to measure and is more accurate compared with the LLD. As such, CMOD was used as a factor for SENB test to estimate the J value. Kirk and Dodds [295] proposed a CMOD-based J estimation equation (similar to Equation 6.3) using a CMOD-based plastic η factor.

$$J_{pl} = \frac{\eta_{CMOD} A^{pl}_{CMOD}}{B_N b} \qquad [6.6]$$

Equation 6.5 was adopted by ASTM E1820-13 as an alternative basic procedure to measure J_{Ic}. It is worthwhile to point out that this basic test procedure was originally developed for multi-specimen test methods (DNV); however, it is now applicable to single-specimen test methods with an appropriate crack growth correction.

6.3.1.2. Resistance curve test method for J-R curve testing

While the basic test method determines a point value of fracture toughness, the resistance curve test method determines toughness in a format of a resistance curve from a single-specimen test. Equations 3 and 6 for estimation of the J-integral are only valid for a stationary crack to obtain the critical J_{Ic} at ductile fracture initiation. However, for a growing crack, these equations need a crack growth correction for accurate J-R curve evaluation. In 1979, Hutchinson et al. [297] showed that the J-integral can be used to characterize the crack growth process, provided that the remaining ligament is large enough and the applied deformation is small enough so that a region of proportional strain field easily encompasses the local crack-tip non-proportional strain field [284]. This is the so-called J-controlled crack growth regime. To obtain a J-R curve from a single-specimen

test, Clarke et al. [298] proposed an elastic unloading compliance technique to determine the amount of crack extension present at a specific location on an experimental load-LLD record. In this procedure small elastic unloading cycles were applied periodically during the experimental test procedure and the change in compliance of these unloadings was used to estimate the crack extension. An early J–R curve was constructed by calculation of J using the η factor and the initial crack length. The results were accurate only for small amounts of crack growth; however, this approach provided a limited single-specimen J-R curve from which J_{Ic} could be evaluated. The basic procedure presented in the first J-based fracture toughness standard (ASTM E813-81) was the multi-specimen procedure and a rudimentary unloading compliance technique was introduced in its appendix. Later, the unloading compliance technique became the standard procedure for J-R analysis introduced in ASTM E813-88.

For more extensive crack growth, it was realized that additional crack growth corrections are necessary since the J-integral equations based on the η factor (Equation 6.3 and 6.6) are valid only for non-growing cracks. Accordingly, the early incremental unloading experimental techniques brought some motivation for researchers to develop incremental procedures to evaluate the J-integral for specimens with growing cracks. For a growing crack, accurate J-integral evaluation requires the use of the current crack size and the evaluation of a crack growth correction. Equations 6.3 and 6.6 were modified in different manners to consider the crack growth effect in a J–R curve evaluation.

Among the pioneers, in 1981, Ernst et al. [299] proposed an incremental approach to calculate the J-integral and develop a J-R curve. Since 1987, ASTM E1820 has adopted this incremental approach to determine the J-integral incrementally. At each loading step, the elastic component of J is calculated directly from the stress intensity factor using Equation 6.2 and the plastic component of J is determined using the Ernst incremental J-integral equation.

$$J_{pl,i} = \left(J_{pl,i-1} + \frac{\eta_{i-1}}{B_N b_{i-1}} A_{i-1,i}^{pl}\right)\left(1 - \frac{\gamma_{i-1}}{b_{i-1}}(a_i - a_{i-1})\right) \qquad [6.7]$$

where η and γ are two plastic geometry factors (η= 1.9 and γ= 0.9 [187]) and $A_{i-1,i}^{pl}$ denotes the incremental plastic area under the measured load-LLD curve, which is calculated from the following equation.

$$A_{i-1,i}^{pl} = \frac{1}{2}(P_i + P_{i-1})(\Delta_{pl,i} - \Delta_{pl,i-1}) \qquad [6.8]$$

where Δ_{pl} is the plastic component of LLD. The unloading compliance technique is recommended by ASTM E1820 for determining the instantaneous crack length through measurement of the

CMOD-based elastic unloading compliance in a single-specimen test. As such, the load (P), LLD (Δ) and CMOD records are required for J calculation in a J-R curve evaluation from a single-specimen test.

The above mentioned LLD-based resistance curve test method has been adopted in ASTM E1820 for more than thirty years. However, in 2008, Zhu et al. [300] developed a CMOD-based incremental J-integral equation in order to meet the long-time desire at ASTM for eliminating LLD measurement and for increasing the accuracy of J-R curve evaluation, o calculate the plastic component of J,

$$J_{pl,i} = \left(J_{pl,i-1} + \frac{\eta_{i-1}^{CMOD}}{B_N b_{i-1}}\left(A_i^{V_{pl}} - A_{i-1}^{V_{pl}}\right)\right)\left(1 - \frac{\gamma_{i-1}^{CMOD}}{b_{i-1}}(a_i - a_{i-1})\right) \qquad [6.9]$$

where η^{CMOD} and γ^{CMOD} are two CMOD-based plastic geometry factors and $A_i^{V_{pl}} - A_{i-1}^{V_{pl}} = A_{i-1,i}^{V_{pl}}$ denotes the incremental plastic area under the measured load-CMOD curve.

$$A_{i-1,i}^{V_{pl}} = \frac{1}{2}(P_i + P_{i-1})(V_{pl,i} - V_{pl,i-1}) \qquad [6.10]$$

$$\gamma_{i-1}^{CMOD} = \left[-1 + \eta_{i-1}^{CMOD} - \left(\frac{b_{i-1}}{W} \times \frac{\eta_{i-1}^{CMOD'}}{\eta_{i-1}^{CMOD}}\right)\right] \qquad [6.11]$$

$$\eta_{i-1}^{CMOD'} = W \left.\frac{\mathrm{d}\eta^{CMOD}}{\mathrm{d}a}\right|_{i-1} \qquad [6.12]$$

As stated earlier, the η factor is dependent on the geometry of the test specimen. Accordingly, Cravero et al. [301] and Hererra et al. [302] proposed an η factor, which is dependent on the a/W ratio, for both pin-loaded and clamped SENT specimens from CMOD using finite element analysis.

Pin-loaded Specimen: $\eta_{i-1}^{CMOD,P} = \left[0.9167 + 0.0837\left(\frac{a}{W}\right)\right]$ [6.13]

Clamped Specimen: $\eta_{i-1}^{CMOD,C} = \left[1.0398 - 0.6870\left(\frac{a}{W}\right)\right]$ [6.14]

By taking the derivative of the expressed η factors (Equations 6.13 and 6.14) based on Equation 6.12 and substituting into Equation 6.11, the crack growth correction in the J-integral method is readily done using the following Equations for the pin-loaded and clamped SENT specimens:

Pin-loaded Specimen: $\gamma_{i-1}^{CMOD,P} = \left[-0.0833 + 0.0837\left(\frac{a}{W}\right) + \frac{0.0837\left(\frac{a}{W}-1\right)}{0.9167+0.0837\left(\frac{a}{W}\right)}\right]$ [6.15]

Clamped Specimen: $\gamma_{i-1}^{CMOD,C} = \left[0.0398 - 0.6870\left(\frac{a}{W}\right) + \frac{0.6870\left(1-\frac{a}{W}\right)}{1.0398-0.6870\left(\frac{a}{W}\right)}\right]$ [6.16]

Note that Equation 6.9 only requires load and CMOD data to develop a J-R curve and, thus, ASTM E1820 in its 2008 and later versions altered Equation 6.7 with Equation 6.9 for a J-R curve evaluation. This new J-R curve test method is claimed by Zhu et al. [197] to be a reasonable method not only for standard specimens, but also for nonstandard specimens. The total J-integral and the elastic J_{el} at each load step (in the unloading compliance technique) are basically calculated from Equations 6.1 and 6.2, respectively. The γ_{CMOD} term in Equation 6.9 is used to correct J (described in Equation 6.6) to account for crack growth. In general, Equation 6.9 can be used for any specimen, provided the geometry factors η_{CMOD} and γ_{CMOD} are known a priori for that specimen. These geometry factors can be determined using the accurate finite element analysis.

6.3.1.3. J-Integral conversion method for CTOD testing

CTOD testing was initially proposed in ASTM E1290 [303] to determine the critical CTOD (δ_{Ic}) in order to quantify ductile crack initiation or cleavage instability. The earliest version of ASTM E1920 calculated δ_{Ic} according to the plastic hinge model[5] (also used by BS 7448-1 [188]). Due to the rotation radius dependency on the crack size and strain hardening, E1290 in 2002 discarded the plastic hinge model and changed to the J-integral conversion method to calculate δ_{Ic}. Accordingly, in 2005, ASTM E1820 utilized the J-integral conversion method to determine δ_{Ic} and δ-R curves. Equation 17 describes the conversion of δ_{Ic} from J_{Ic}.

$$CTOD = \delta = \frac{J}{m\sigma_Y} \qquad [6.17]$$

$$\sigma_Y = \frac{\sigma_{ys} + \sigma_{uts}}{2} \qquad [6.18]$$

where σ_{ys} and σ_{uts} are the yield stress and ultimate tensile stress, respectively. m is a function of a/W and σ_{ys}/σ_{uts}, which can be determined by finite element analysis [291].

6.3.2. DNV multiple specimen method for J-integral testing

Offshore pipelines installed by the reeling approach experience large plastic strains during installation. In addition, onshore pipelines either on ground or underground are exposed to plastic strains due to ground movement. These phenomena sometimes cause severe fracture in the girth weld and the HAZ of the pipe.

[5] In structural engineering, a beam theory term, plastic hinge, is used to express the deformation of a section of a beam where plastic bending happens. This model assumes that the specimen is a rigid-plastic body and rotates around a plastic hinge in the ligament. The CTOD concept was proposed by Wells in 1989 and first standardized in a British fracture test standard based on the plastic hinge model.

A fracture test method using a shallow cracked specimen was initially proposed by DNV in 2006 to measure low-constraint fracture toughness. The test was conducted in tension conditions, through a SENT test in clamped conditions (Figure 6-2b) and reported through DNV recommended practice DNV-RP-F108 [190]. This practice adopts the multiple specimen method for developing a J-R curve with SENT specimens in a pin-loaded or clamped condition. The specimen thickness was double its width (B=2W) and the distance between the two grips was H=10W. The pre-cracked length to specimen width ratio (a/W) was in the range of 0.2-0.5. However, side-grooves were not reported and the maximum crack extension was set as 3 mm.

The DNV fracture test method basically requires a minimum of six to ten valid results from SENT testing to generate a J-integral curve (the procedure is similar to the method mentioned in the early version of ASTM E1820). The total J-integral was separated into elastic and plastic parts (Equation 6.1) and these were calculated separately. The elastic J_{el} was calculated from the stress intensity factor K from Equation 6.2 and the plastic J_{pl} was calculated from the CMOD-based Equation 6.6. CMOD can be measured directly on the crack mouth of the specimen or estimated from double clip gauge measurements. Nevertheless, the multiple specimen method takes a relatively long time for testing and increases test material costs. As a result, a single-specimen method has been sought for SENT testing.

6.3.3. Canmet materials single-specimen SENT method for J-integral testing

A single-specimen SENT test method was developed by Canmet Materials Canada [191] in 2008 for clamped SENT specimens. According to the procedure, the specimen thickness and clamping distance are equal to its thickness (B=W) and ten times the specimen width (H=10W), respectively. The fatigue pre-crack size to width ratio (a/W) is in the range of 0.1-0.7 and side-grooves are applied to the specimens to a total depth of 15% of thickness. The Canmet Materials procedure is similar to the resistance curve method in ASTM E1820 for determining a J-R curve or CTOD-R curve. The unloading compliance technique is essentially utilized to measure the crack extension during testing. A single clip gauge is mounted at the crack mouth to measure the CMOD during the SENT test. The apparatus used for measuring load and CMOD are similar to that for SENB specimens described in E1820. However, due to the possibility of specimen rotation during SENT, a rotation correction factor is proposed by Park et al. in 2012 [304] from finite element analysis simulations. Most of the test details are similar to those specified in ASTM E1820 for standard SENB specimens. The CMOD-based incremental J-integral (Equation 6.9) is adopted in the SENT J-R curve evaluation. Park et al. [192,196,199] and Shen et al. [305] measured the fracture toughness for X100 pipeline steel and its welds according to the Canmet Materials procedure.

6.3.4. ExxonMobil single-specimen method for CTOD testing

In 2010, a SENT test procedure was proposed by ExxonMobil company [193,306] using two clip gauges mounted on a single-specimen. Accordingly, CMOD and CTOD are directly inferred from the clip gauges according to the following equations:

$$CMOD = V_1 - \frac{h_1}{h_2 - h_1}(V_2 - V_1) \qquad [6.19]$$

$$CTOD = V_1 - \frac{h_1 + a_0}{h_2 - h_1}(V_2 - V_1) \qquad [6.20]$$

where V_1 and V_2 are the crack opening displacements measured at heights of h_1 and h_2 above the specimen front knife-edge. Note that CTOD in Equation 20 is defined at the original crack tip. In the ExxonMobil method, the dimensions of clamped SENT specimens are B=W and H=10W and the initial crack length is between 0.25 and 0.35. A total side groove of 10% of the thickness is also recommended. The double clip gauge procedure is simple and convenient to use for measuring a δ-R curve with SENT specimens and, thus, it is of great practical importance. However, the allowed crack size is too small and the definition of CTOD is different from ASTM E1820.

6.3.5. British standard (BS 8571-2014) procedure for SENT testing

In 2010, Pisarski at The Welding Institute (TWI) in the U.K. [307] modified the SENT testing procedure previously described in the DNV-RP-F108 with respect to specimen preparation, testing procedure and analysis methods. Efforts were continued at TWI until December 2014 when the British Standard Institute published a standard test procedure, with a designation of BS 8571-2014, to determine the fracture toughness in metallic materials using SENT specimens [200]. The J-R curve test procedure proposed in the BS 8571 is applicable for both the multiple specimen method and the single-specimen method and the J estimation equations are the same as Equations 6.1, 6.2 and 6.6 without considering crack growth correction. However, this approach is different from the Canmet Materials procedure. A double clip gauge arrangement is utilized to measure the displacements at two different heights. The CMOD used to calculate J is inferred from the double clip gauge displacements using Equation 6.19 (CMOD is not directly measured on the specimen surface). The CTOD in a δ-R curve evaluation is calculated from the following equation:

$$CTOD = \frac{(1-\nu^2)K^2}{2\sigma_{ys}E} + \left(V_{pl,1} - \frac{z_2 + a_0}{z_2 - z_1}(V_{pl,1} - V_{pl,2})\right) \qquad [6.21]$$

where the first term determines the elastic CTOD and the second term determines the plastic CTOD with $V_{pl,1}$ and $V_{pl,2}$ being the plastic parts of the double clip gauge measured displacements at

heights z_1 and z_2. Note that the above equation is different from Equation 6.20, as the ExxonMobil uses the total CTOD without separation of elastic and plastic components. As such, BS 8571 is subject to extensive validation and evaluation.

6.4. Experimental Procedure

6.4.1. Weld sample fabrication

Microalloyed steel plates with a thickness of 13.4±0.3 mm, produced by Evraz Inc. NA through thermo-mechanical controlled processing (TMCP) [30], were used as the base metal. The weld samples were prepared by both cold wire tandem submerged arc welding (CWTSAW) and conventional tandem submerged arc welding (TSAW) using two 4 mm diameter EA2 electrodes (according to AWS-A5.23/ASME-SFA5.23) and one cold wire with the same diameter and composition as the electrodes. The flux was chosen according to EN 760 (BF6.5, Bavaria, Germany). The chemical compositions of the microalloyed steel and consumable electrodes are given in Table 6-1. Pcm, the welding crack susceptibility index, for low-carbon microalloyed steels is calculated according to the Ito-Bessyo equation [81].

Table 6-1 Chemical composition of X70 steel and electrode (key alloying elements)

X70 composition								
C	**P**	**S**	**Mn**	**Si**	**N**	**V+Mo+Nb+Ti**	**Cu+Ni+Cr+Sn+Al+Ca**	**Pcm**
0.046	0.01	0.001	1.76	0.24	0.0098	0.21	0.60	0.175

Electrode and cold wire composition									
BA-S2Mo	**C**	**P**	**S**	**Mn**	**Si**	**Mo**	**Ni**	**Cr**	**Cu**
	0.10	0.007	0.01	1.04	0.1	0.56	0.02	0.03	0.03

Two 85±5° V-shaped bevels, 4.0±0.2 mm and 2.5±0.2 mm in depth, were machined in the steel plates prior to welding. Two inner-diameter (ID) and outer-diameter (OD) weld runs were conducted for each welding process in order to ensure complete filling of the joint gap between the two pieces of steel sheets (Figure 6-3a). Otherwise, any gaps between the steel sheets would act as cracks during the SENT test and need to be avoided. The purpose of this study is to evaluate the effect of cold wire addition during the OD welding pass on the HAZ properties. Accordingly, the welding parameters for the ID weld run were similar for all prepared weld samples and only the OD welding parameters were varied. Direct current electrode positive (DCEP) and square wave alternating current (ACSQ) polarity were employed, using constant current type power sources to operate the lead and trail electrodes in the OD weld run, respectively. While, both the lead and trail electrodes in ID weld run were operated in ACSQ polarity. The ID welding parameters were

selected according to the procedure proposed by the industrial collaborator. The OD welding parameters and the CWTSAW process setup were developed based on the optimized welding parameters, which are presented in Chapter 3. The welding conditions to fabricate the microalloyed steel joint are presented in Table 6-2. The fabricated welds were visually inspected prior to any further investigation to ensure that the welds were free from the macro-level defects, such as surface porosity, hot-cracking, undercutting and burn-through. Figure 6-3 depicts the steel plate geometry and the CWTSAW process setup employed to fabricate weld samples. The heat input for both welding processes was constant and set at 22.2 kJ/cm. All welding parameters were the same for both processes other than the additional cold wire. The average microhardness values in the CGHAZ of the CWTSAW and TSAW weld specimens were 223.5 HV0.5 and 237.75 HV0.5, respectively. Accordingly, the yield and tensile strengths of the CGHAZ for both CWTSAW and TSAW welds were 619 MPa and 733 MPa, and 638 MPa and 757 MPa, respectively. The hardness to strength conversion method has been presented in Chapter 4.

Table 6-2 Welding process parameters

Process Parameter	Unit	ID-Weld TSAW	OD-Weld CWTSAW	OD-Weld TSAW
Current- Lead Electrode	A	880	1040	1040
Current- Trail Electrode	A	770	830	830
Voltage- Lead Electrode	V	28	30	30
Voltage- Trail Electrode	V	30	34	34
Welding Travel Speed	mm/s (in/min)	26.67 (63)	26.67 (63)	26.67 (63)
Cold Wire Position	--	NA	Lagging	NA
Cold Wire Angle	°	NA	63	NA
Cold Wire Feed Speed	mm/s (in/min)	NA	4.23 (10)	NA

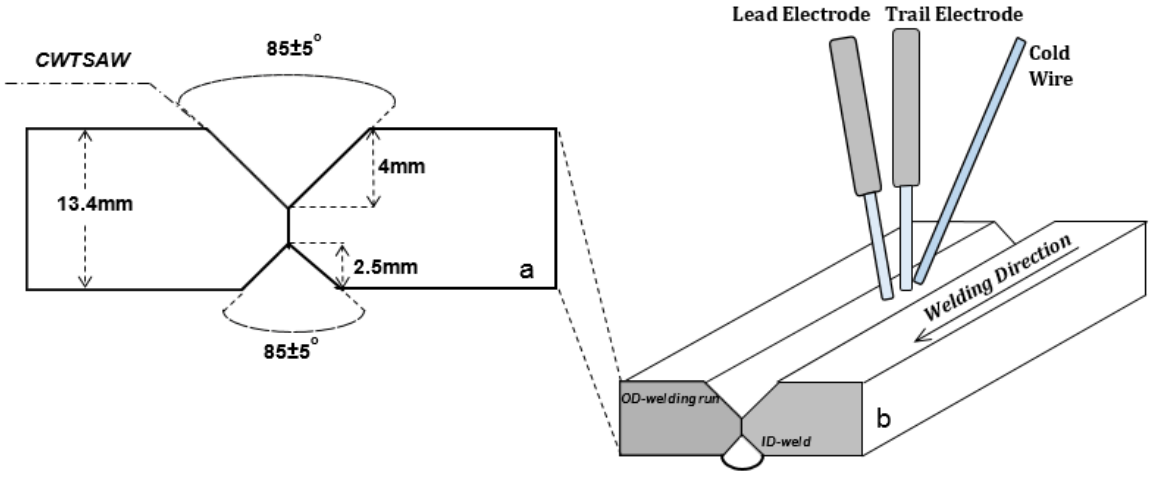

Figure 6-3 (a) X70 steel joint geometry indicating both ID and OD bevels. (b) Schematic view of CWTSAW process with positioning of the electrodes and cold wire.

6.4.2. SENT specimen preparation

From two batches of welds produced by the TSAW and CWTSAW processes, eight weld coupons were cut in the transverse direction relative to the weld direction for SENT testing. Prior to machining, the SENT specimen blanks were straightened through a bend flattening procedure in order to compensate for weld distortion and preserve as much specimen thickness as possible. The flattening to ±0.3mm was conducted in accordance with the bending method described in Part 2 of the BS 7448 standard, with bending rollers applied at least 2B (twice the specimen thickness) away from the weld fusion line. Afterwards, the specimens were machined to the final thickness (B) and width (W) of 11.8±0.05 mm (BxB) as proposed by Shen et al. [198]. The specimen length (H) was ~118 mm (H=10W). There was additional length to accommodate gripping of the ends with hydraulic wedges. The specimens were surface notched by electrical discharge machining (EDM) from the OD surface and then fatigue pre-cracked in the sample target microstructure of the coarse grain heat affected zone (CGHAZ). The target fatigue pre-crack depth was a_0=0.3W (W=B). To mitigate against excessive pre-crack curvature, fatigue pre-cracking was conducted in accordance to ISO 12135:2002/ISO 15653:2010 criteria (up to 16% higher pre-cracking loads relative to the ASTM E1820-15a limits). An initial trial of fatigue pre-cracking was conducted according to the ASTM E1820 limits; however, the specimen was rejected due to excessively poor straightness. A typical weld specimen (with ID and OD welds) and notch locations is shown in Figure 6-4a. The fatigue pre-cracking setup is shown in Figure 6-4b. An average of 170,000 cycles with a maximum load of 5 kN and a stress ratio of -0.08 were used for pre-cracking.

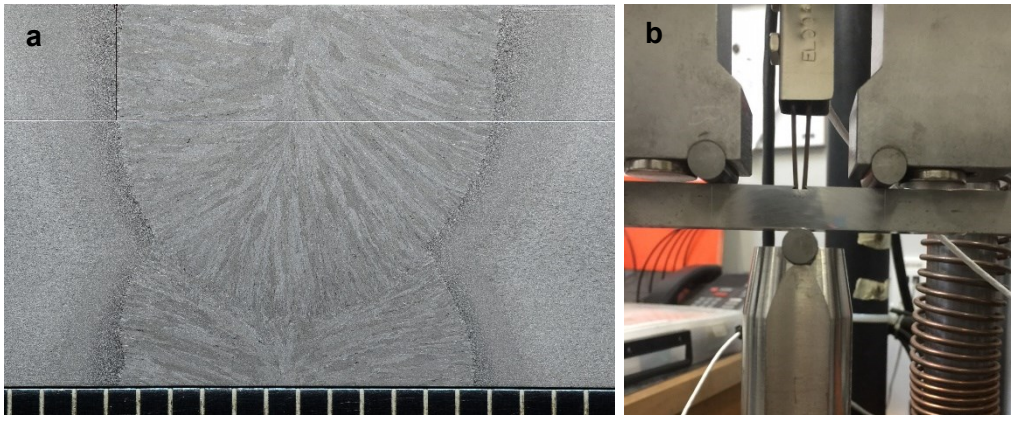

Figure 6-4 (a) Typical weld profile and HAZ surface notch location. (b) Setup for fatigue pre-cracking.

Due to the difference in constraints at mid-thickness (towards plane strain) and at the sides (plane stress) of the specimen, crack tunneling is expected [308]. This tunneling results in a deteriorated accuracy in crack growth measurements [309]. Accordingly, following fatigue pre-cracking, SENT specimens for J-R curve development were side grooved to a depth of approximately 0.8 mm on each side (for a total reduction of up to 15% of the thickness) with a groove radius of approximately 0.25±0.05 mm and an angle of 45°. As such, the net thickness, B_N, was equal to 0.85B. Side grooving was conducted to minimize final crack curvature by generating relatively uniform constraints across the crack tip. Figure 6-5 depicts the SENT specimen geometry.

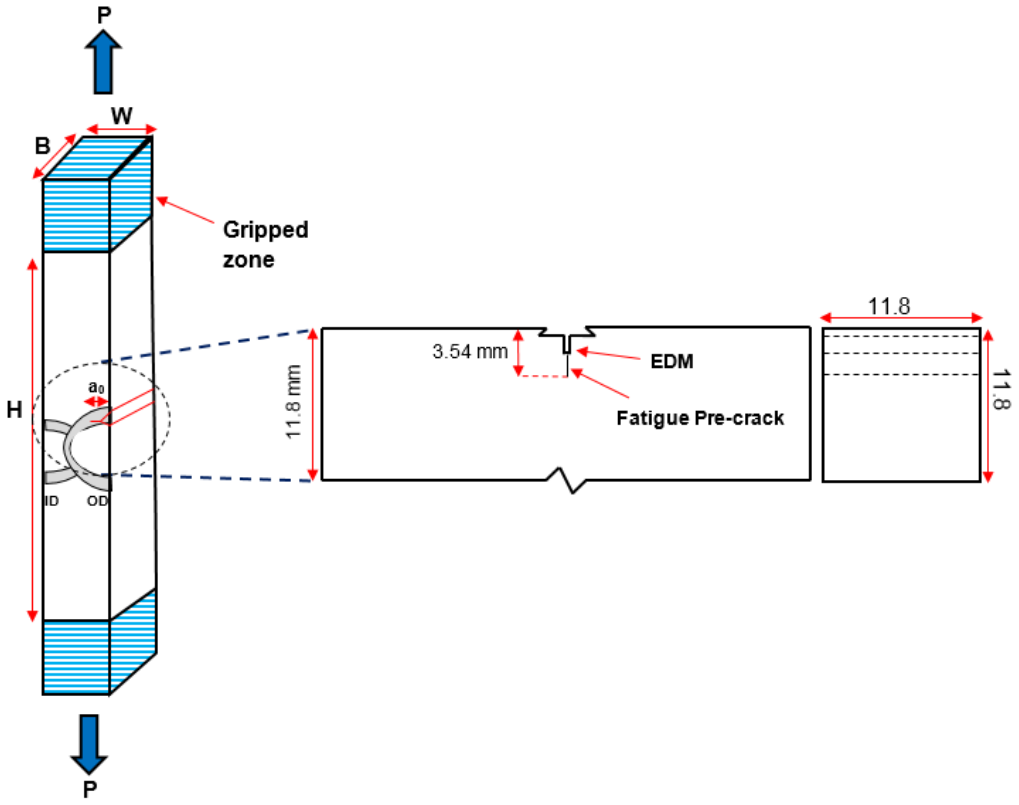

Figure 6-5 A schematic of SENT specimen geometry with a notch placed at HAZ for the 12.4 mm thick pipe.

6.4.3. SENT test procedure

Recently, analytical efforts to support the development of laboratory measurements of J-R data have focused essentially on the unloading compliance method based on testing of a single-specimen. The J-R determination method essentially stems from measuring the instantaneous value of the specimen compliance at partial unloading during the measurement of the load vs. displacement curve as illustrated in Figure 6-6. The specimen response is defined in terms of load-LLD or load-CMOD. The technique then enables accurate estimations of J and Δa at several locations on the load-CMOD records from which the J-R curve can be developed. The equations and

parameters needed to determine the crack growth resistance curves for the SENT specimens, are discussed earlier in this Chapter; however, the essential equations will again be briefly presented here.

The SENT tests conducted in this study were performed in the CGHAZ of the weld specimens at three temperatures, i.e., room-temperature (RT), -5ºC and -30ºC. For the colder temperatures, the specimens were cooled by circulating ethanol through a small chamber within the specimen length (length of 10W) between the grip faces. The instantaneous temperature at the vicinity of the crack tip was measured using a thermocouple. A test temperature as low as -30°C was maintained within ±3°C (the E1820 variation limit) within a distance of at least ±2B from the specimen notch. The specimens were clamped using hydraulic grips, restricting all rotational degrees of freedom. The SENT specimen was then loaded under displacement control with a displacement rate of 0.01 mm/sec, representing quasi-static conditions. The specimens were partially unloaded and reloaded during the tests to allow for evaluation of the compliances during the test. The design of these loading-unloading cycles has been adopted from the recommended practice provided by Canmet Materials [191].

During the initial elastic portion of the Load-CMOD test record, several unloading/reloading sequences were performed to calculate the initial crack size and that value was compared with the measured initial crack size, a_0. A load range between $0.25P_Y$ and $0.5P_Y$ was used for the initial unload/reload cycles.

Six unloading cycles were then performed in the elastic regime with the applied force, P_Y, equal to:

$$P_Y = \frac{\sigma_{ys} + \sigma_{uts}}{2}(W - a)B_e \qquad [6.22]$$

where σ_{ys} and σ_{uts} are the yield strength and ultimate tensile strength of the specimen, respectively. W and a are the specimen width and the current crack length of the SENT specimen, respectively.

The effective specimen width, B_e, is calculated from the following equation:

$$B_e = B - \frac{(B - B_N)^2}{B} \qquad [6.23]$$

The amount of unloading equals $P_Y/4$.

Following the elastic unloading cycles, subsequent unloading cycles were performed at fixed intervals of the crack mouth opening displacement (CMOD). For all cycles the amount of unloading was load controlled and was also equal to $0.25P_Y$. For the first five plastic unloading cycles, the CMOD intervals were equal to 0.02 mm and subsequent intervals of 0.04 mm were used.

The unloading compliance method essentially assumes a monotonically increasing relation between crack depth and compliance. To evaluate the specimen's compliance during the test, the specimen is partially unloaded and reloaded at predefined intervals of CMOD, as described above. The slope of a linear regression line through the unloading data is then defined as the compliance. The required tensile force is obtained from the load cell of the test rig and the CMOD is obtained from the clip gauge reading.

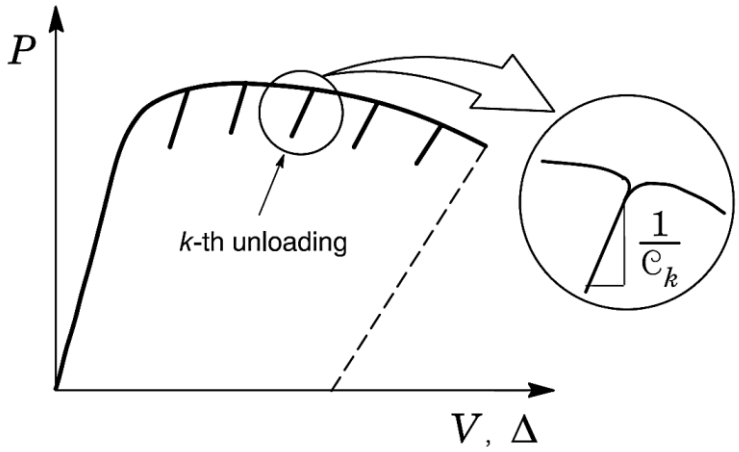

Figure 6-6 An illustration of typical loading-unloading. Partial unloading during evolution of the load with displacement is shown, indicating the compliance (C_k) [195].

6.4.4. Analytical procedure

Since the basics of the J-integral analysis were defined in Section 6.3, the sequence of J-integral calculation is briefly described here. The same formulation for J-integral as given in Equation 6.1 is also used for SENT specimens.

$$J = J_{el,i} + J_{pl,i} \qquad [6.24]$$

where i is the index of a specific unload/reload cycle. The elastic component of J is given by:

$$J_{el} = \frac{K_i^2(1-\nu^2)}{E} \qquad [6.25]$$

K_i, the stress-intensity factor, is given by:

$$K_i = \left(\frac{P_i\sqrt{\pi a_i}}{\sqrt{BB_N}W}\right) \times G\left(\frac{a_i}{W}\right) \qquad [6.26]$$

where E is plane stress Young's modulus and ν is Poisson's ratio at the test temperature. a_i is the current crack size and P_i is the load at the beginning of the unload/reload cycle. $G(a_i/W)$ is a function which is expressed as follows:

$$G\left(\frac{a_i}{W}\right) = \sum_{i=1}^{12} t_i \left(\frac{a_i}{W}\right)^{i-1} \qquad [6.27]$$

Table 6-3 indicates the coefficients of the polynomial regression (t_i) based on finite element analyses performed by Shen et al. [310].

Table 6-3 Coefficient ti in Equation 6.27 for 0.05≤a/W≤0.95 and H/W=10

i	1	2	3	4	5	6	7	8	9	10	11	12
t_i	1.20	-2.13	23.89	-69.05	100.46	-41.40	-36.14	51.21	-6.61	-52.32	18.57	19.47

The plastic component of the J-integral in Equation 6.24 is expressed as:

$$J_{pl,i} = \left(J_{pl,i-1} + \frac{\eta_{i-1}^{CMOD}}{B_N b_{i-1}}\left(A_i^{V_{pl}} - A_{i-1}^{V_{pl}}\right)\right)\left(1 - \frac{\gamma_{i-1}^{LLD}}{b_{i-1}}(a_i - a_{i-1})\right) \qquad [6.28]$$

where, $b_i=(W-a_i)$ and $A_{pl,i}$ are the ligament size and the plastic area under the load-CMOD curve, respectively (shown in Figure 6-7).

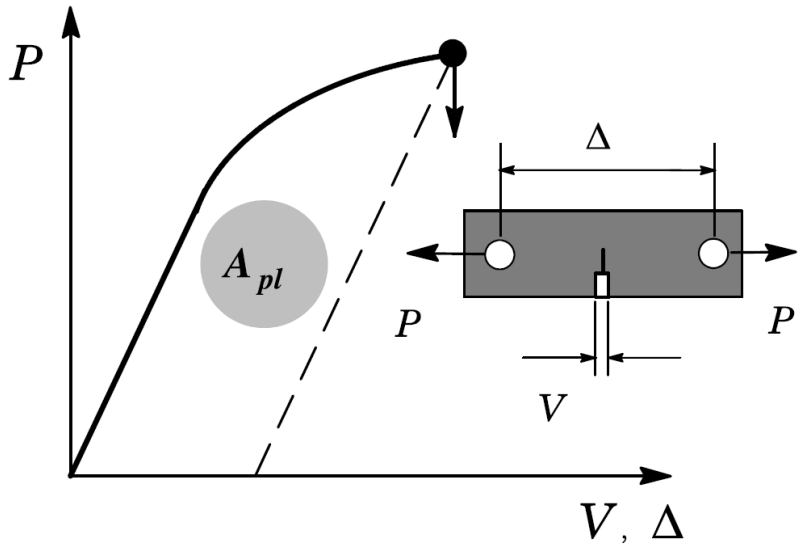

Figure 6-7 Definition of plastic area under the load-CMOD curve [195,301].

The parameters $\eta_{CMOD,i}$ and $\gamma_{LLD,i}$ have been developed via finite element analysis under a two-dimensional (2-D) plane strain assumption [311], and are expressed in Equations 6.29 and 6.30.

$$\eta_{CMOD} = \sum_{i=1}^{11} \phi_i \left(\frac{a_i}{W}\right)^i \qquad [6.29]$$

$$\gamma_{LLD} = \eta_{LLD} - 1 - \left(1 - \frac{a_i}{W}\right)\left(\frac{\eta'_{LLD}}{\eta_{LLD}}\right) \qquad [6.30]$$

where, $\eta_{LLD} = \sum_{i=1}^{11} \psi_k \left(\frac{a_i}{W}\right)^k$ [6.31]

The coefficients ϕ_i and ψ_k are given in Table 6-4 and Table 6-5, respectively. In Equation 6.30, the first derivative of η_{LLD}, i.e., η'_{LLD}, is defined as:

$$\eta'_{LLD} = \sum_{i=1}^{11} k\psi_k \left(\frac{a_i}{W}\right)^{k-1} \qquad [6.32]$$

Table 6-4 Coefficients ϕ_i in Equation 29 used to calculate ηCMOD

i	1	2	3	4	5	6	7	8	9	10	11
$\boldsymbol{\phi_i}$	1	-1.089	9.519	-48.572	109.225	-73.116	-77.984	38.487	101.401	43.306	-110.77

The equation used for determination of crack size based on CMOD elastic compliance (C_i) measurements developed from finite element analysis, valid for 0.05<a/W<0.95, is:

$$\frac{a_i}{W} = \sum_{i=1}^{10} r_i U_i \qquad [6.33]$$

where

$$U_i = \frac{1}{\sqrt{B_e C_i E} + 1} \qquad [6.34]$$

r_i is the coefficient of a polynomial least-square fitting function, which is shown in Table 6-6 [287]. It is interesting to note that changes in CMOD compliance (expressed as B_eC_iE in Equation 6.34) as a function of a/W for clamped SENT specimens are significantly larger than for SENB specimens, according to the formulas prescribed by ASTM E1820-11 (Figure 6-8) [187,310].

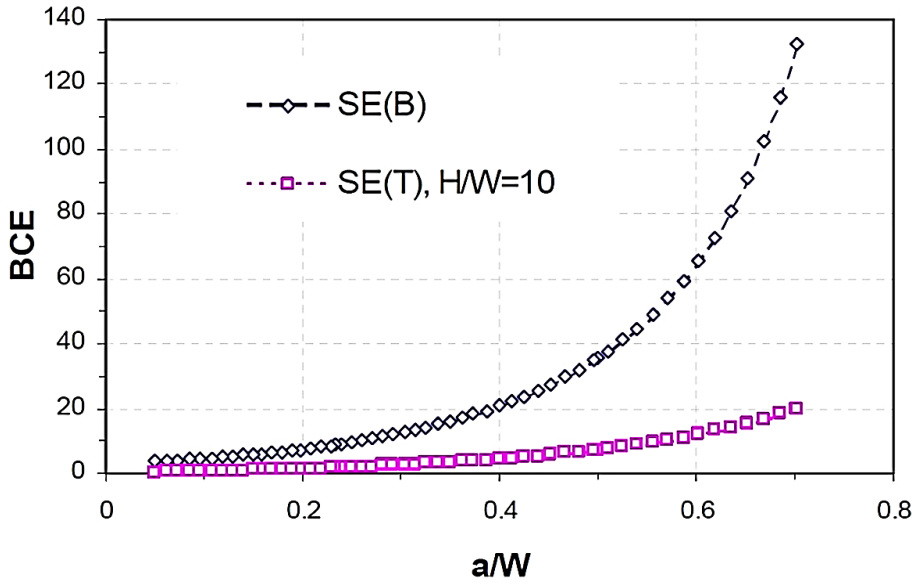

Figure 6-8 Relationship between BeCiE and a/W for SENB and clamped SENT specimens (here H is the specimen daylight length, i.e., the distance between the grips - Figure 7-3) [62].

Table 6-5 Coefficients ψ_i in Equation 6.31 used to calculate η'CMOD

i	1	2	3	4	5	6	7	8	9	10	11
$\boldsymbol{\psi_i}$	-0.88	15.19	-35.44	18.64	18.40	-1.27	-12.76	-12.20	-4.45	5.40	14.19

The value of elastic compliance to be used in Equation 6.34 must be corrected for specimen rotation as the center of the remaining ligament moves toward the load line. Accordingly, the compliance is corrected according to the following equation [195,312]:

$$C_{c,i} = \frac{C_i}{F_{r,i}} \qquad [6.35]$$

where,] $C_{c,i}$ and $F_{r,i}$ are the rotation-corrected compliance and rotation correction factor, respectively. $F_{r,i}$ has been established by means of 2-D plane-strain finite element analysis for clamped SENT specimens with H/W=10 and a_0/W between 0.2 and 0.5 as:

$$F_{r,i} = 1 - 0.165\frac{a_0}{W}\left(\frac{P_i}{P_Y}\right) \qquad [6.36]$$

where P_i and P_Y are the load at the beginning of the unload/load cycle and the load limit for the SENT test, respectively.

Table 6-6 Coefficients r_i in Equation 6.33 for H/W=10

i	1	2	3	4	5	6	7	8	9	10
$\mathbf{r_i}$	2.04	-15.73	73.24	-182.90	175.65	60.93	-113.99	-113.03	8.55	142.84

6.5. Results and Discussion

6.5.1. SENT testing

Figure 6-9 shows the SENT setup for testing the CGHAZ of a weld specimen instrumented with a single clip gauge at RT and lower temperatures.

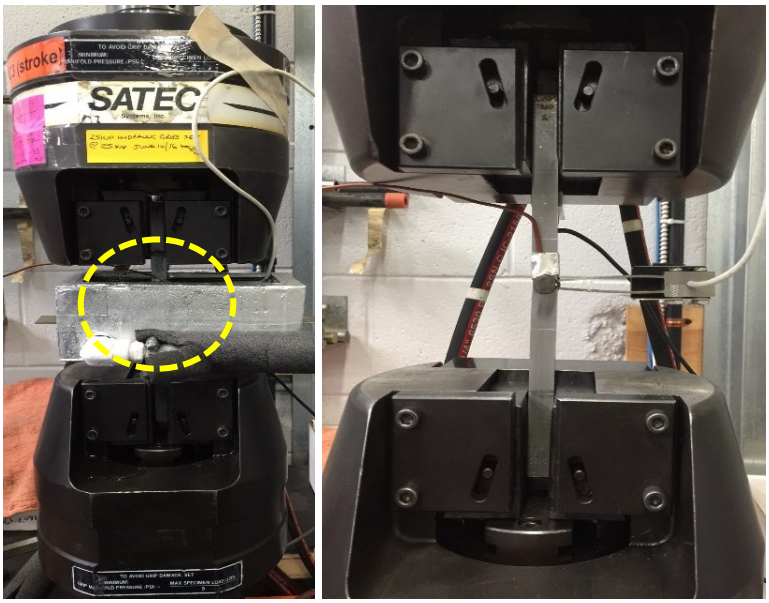

Figure 6-9 Illustration of SENT specimen under loading.

Typical load-displacement records for a fully ductile specimen (e.g., RT test specimen) and a specimen with brittle instability, known as pop-in, (e.g., -30°C test specimen) are shown Figure 6-10. Load-displacement data were regressed to J-R curves using crack mouth opening displacement (CMOD) compliance relationships from the Canmet Materials method for SENT specimen [196,199,313].

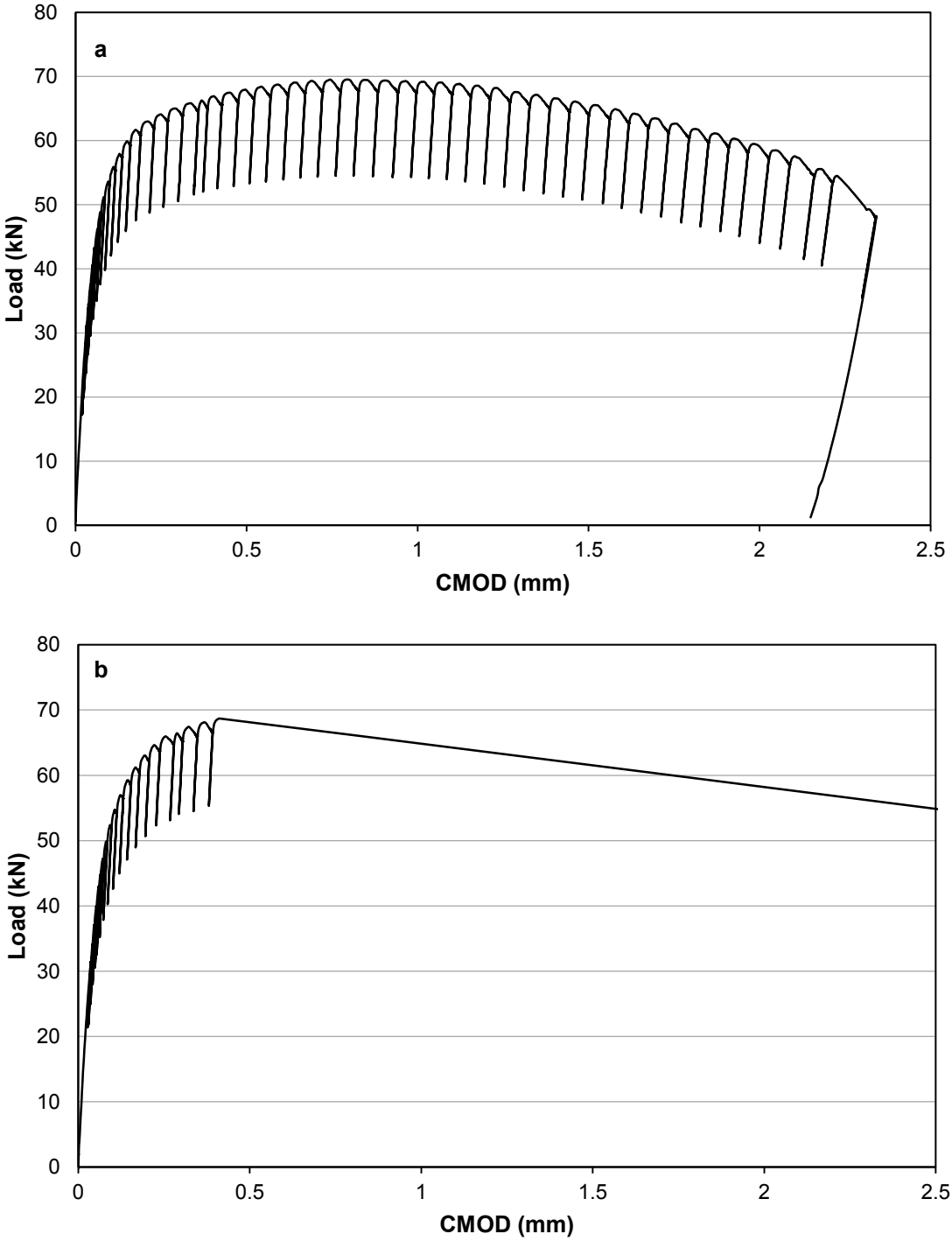

Figure 6-10 Typical load vs. CMOD for (a) a ductile SENT specimen and (b) a brittle SENT specimen showing pop-in.

J-R curves for weld samples tested in the CGHAZ at RT, -5°C and -30°C are shown in Figure 6-11. A typical J-R curve indicating the methodology of measuring the J-integral values from the J-R curve

is shown in Figure 6-12. The J_q[6] and J_m[7] or J_{qc}[8] values for SENT testing in the CGHAZ of the weld specimens are presented in Table 7-7. According to the J-integral results, there is an increase in the J value at the three different test temperatures through the addition of a cold wire to the conventional TSAW process, with a corresponding reduction in the actual heat introduced to the weldment. The trend in the J-integral values for the CGHAZ of the CWTSAW weld samples relative to the TSAW weld samples correlates with the Charpy impact testing results, which were presented in Chapter 4. Since the CGHAZ fracture toughness is influenced by a number of microstructural factors, such as grain size, matrix microstructure and the shape, size and distribution of M-A constituents, microstructural alterations within the HAZ are briefly evaluated and discussed below. A comprehensive study of the microstructural alterations was presented in Chapter 4.

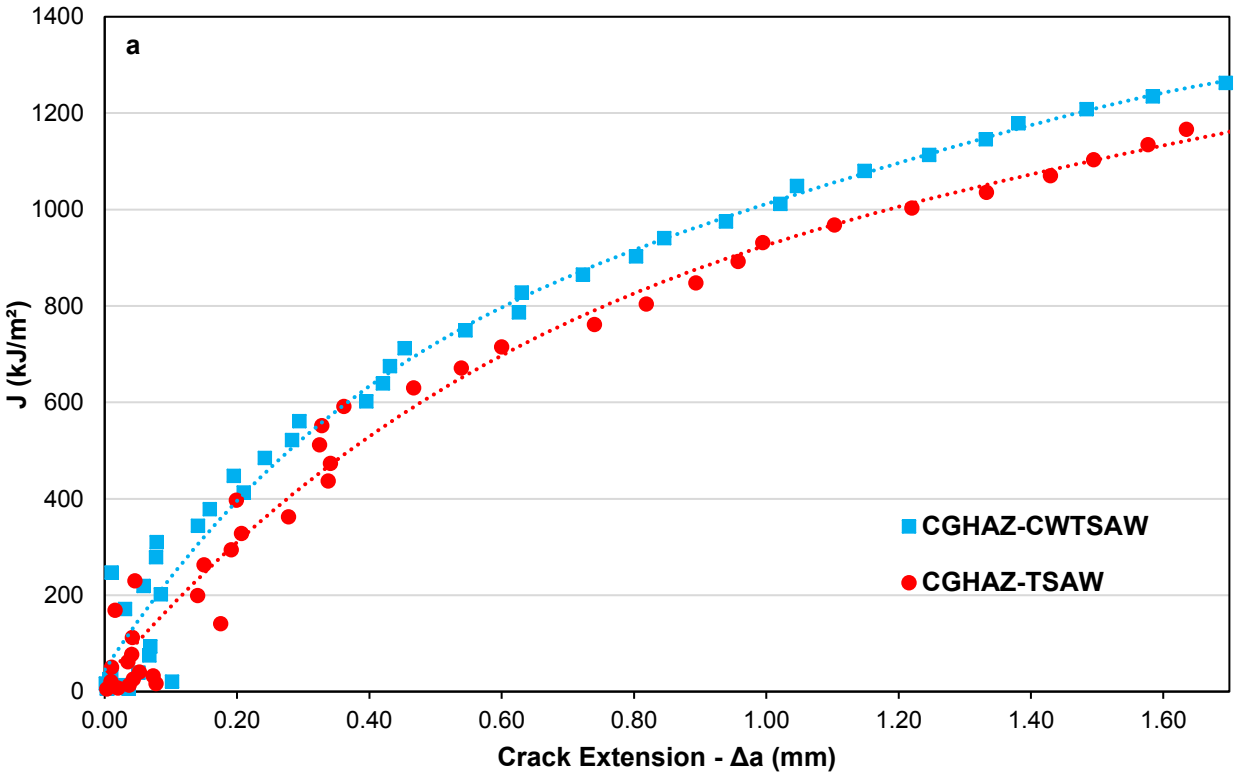

[6] J_q is the J-integral at the onset of ductile tearing (0.2 mm offset) according to ASTM E1820-11 Annex A9.
[7] J_m is the J-integral at the maximum load.
[8] J_{qc} is the J-integral at pop-in with less than 0.2 mm of prior ductile tearing.

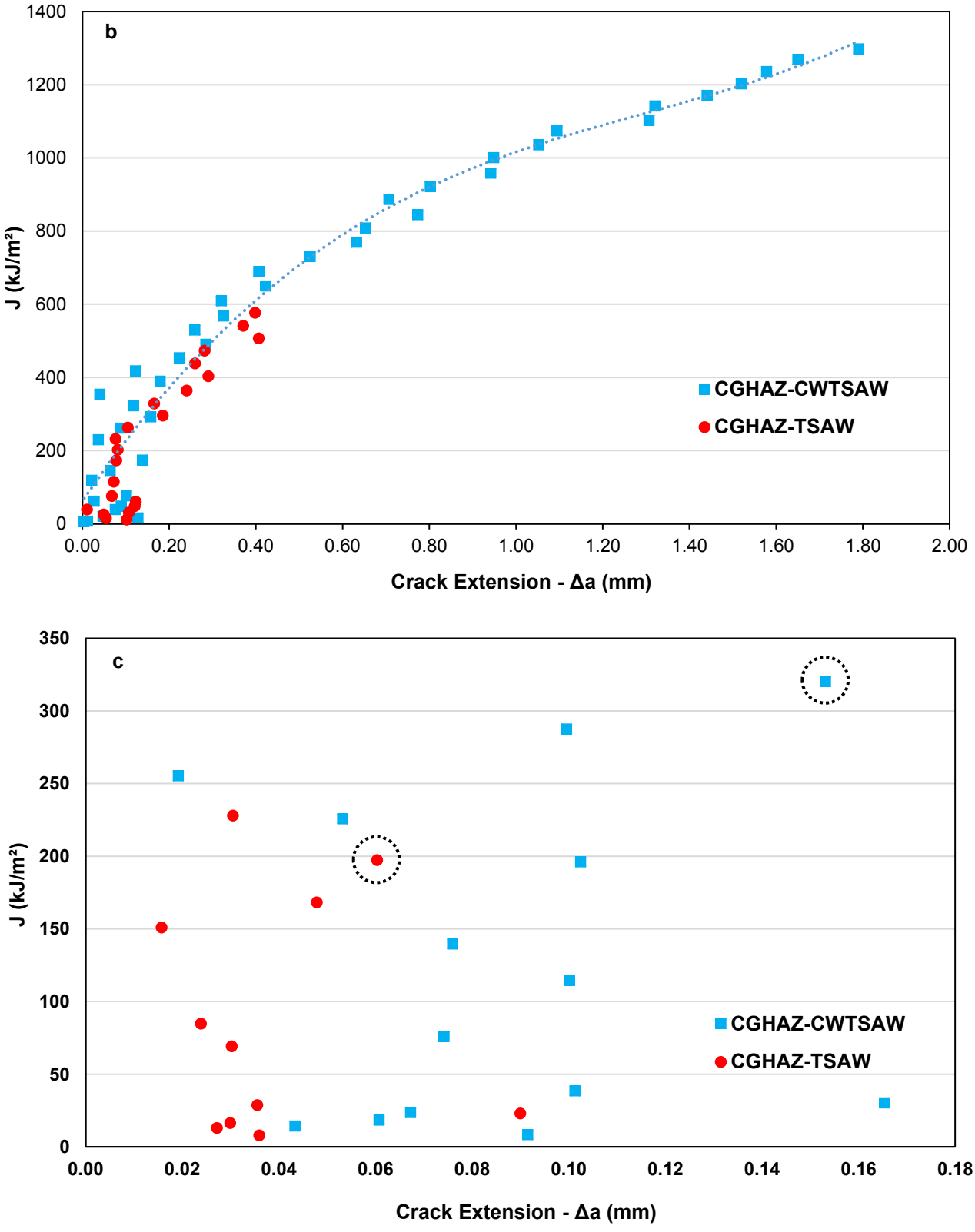

Figure 6-11 J-R curves for the CGHAZ of CWTSAW and TSAW weld specimens at (a) RT, (b) -5°C and (c) -30°C.

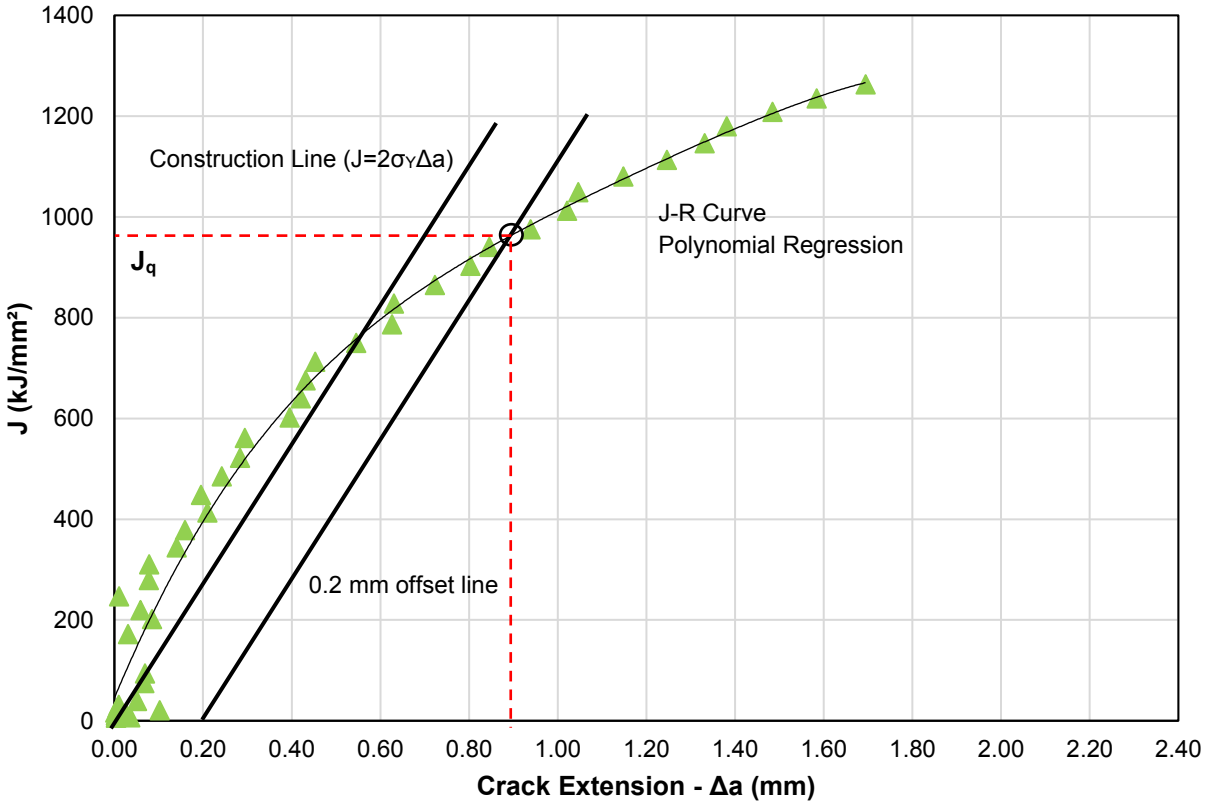

Figure 6-12 Typical J-R curve indicating the methodology of measuring the J_q value from the J-R curve.

As stated earlier, the J_q value was measured from the J-R curves of the specimens showing ductile fracture (i.e., samples tested at RT and the CWTSAW sample tested at -5°C). However, for specimens with brittle fracture behavior without ductile tearing, it was not possible to measure the J_q value. There were not sufficient J-R data points for power law regression (curve fitting) to satisfy ASTM E1820-15a Clause A9.6.6.6. Specifically, insufficient data values at large crack extension were due to early pop-ins. Accordingly, no valid J_q initiation toughness results can be calculated for the samples tested at -30°C and the TSAW sample tested at -5°C. J values for these samples were measured at the onset of the brittle pop-in (J_{qc}), which occurred prior to achieving sufficient ductile crack extension to estimate J_q. Optical microscopy measurements of crack extension prior to pop-in were used to determine J_{qc}.

Table 6-7 J-integral values for the CGHAZ of the weld specimens tested with the SENT method

Notch Position	Welding Process	Test Temperature (°C)	Initiation Toughness, J (kJ/m²)	Toughness Qualification	J_m (kJ/m²)
CGHAZ	CWTSAW	RT	970	J_q	561
		-5	950	J_q	530
		-30	320	J_{qc}	320
	TSAW	RT	815	J_q	474
		-5	576	J_{qc}	576
		-30	228	J_{qc}	228

In addition to the calculation of J-R curves from the load-CMOD data and determination of the J-integral, the straightness of initial and final cracks during SENT testing is essential for a sufficient estimation of material toughness. To measure the crack size, after SENT testing, the specimens were heat tinted and then force-fractured at cryogenic temperatures to facilitate fracture surface examination and crack length measurements. Assessments of initial (pre-crack) and final (ductile tear) crack front straightness were conducted according to ASTM E1820-11 and ASTM E2818-11 procedures. E1820-11 evaluates crack straightness based on the maximum difference of all nine physical crack measurements from the average measurement and considers the straightness valid when the maximum difference is less than or equal to 0.05B (E1820-11, Section 9.1.4). E2818-11, with reference to ISO 15653 and ISO 12135 [287], evaluates crack straightness based on the maximum difference of the inner seven physical crack measurements from the average measurement. ISO 12135 (intended for homogeneous material testing) considers the straightness valid when the maximum difference is less than or equal to $0.10a_0$ or $0.10(a_0+\Delta a)$, while ISO 15653 (intended for weld testing) considers $0.20a_0$ or $0.20(a_0+\Delta a)$ as the requirements. The crack straightness assessments are summarized in Table 6-8. Here, the assessment has been made according to that described in ASTM E1820-11, because ISO 15653 standard, which is for weld samples testing, has higher threshold value of acceptance for the crack straightness evaluation than ASTM 1820-11. For example, in this case, the specimen thickness (B= W) and a_0/W are 11.8 mm and 0.3, respectively. As such, ISO 15653 provides the threshold of straightness acceptance at 0.708 mm, while ASTM 1820-11 provides 0.55 mm. Accordingly, since the crack straightness is an important factor in fracture toughness testing, the ASTM 1820-11 is used to ensure that the lower threshold of crack straightness acceptance is employed for testing. Macrographs of the fracture surfaces of the SENT specimens after testing are shown in Figure A.B-1.

Table 6-8 Initial and final crack straightness assessment*

Notch Position	Welding Process	Test Temperature (°C)	Measurement Difference, mm (%B)	Straightness Validity	Measurement Difference, mm (%B)	Straightness Validity
CGHAZ	CWTSAW	-30	0.14 (1.2)	Valid	0.13 (1.1)	Valid
		-5	0.21 (1.8)	Valid	0.11 (0.9)	Valid
		RT	0.21 (1.7)	Valid	0.57 (4.7)	Valid
	TSAW	-30	0.11 (1.0)	Valid	0.13 (1.1)	Valid
		-5	0.11 (0.9)	Valid	0.13 (1.1)	Valid
		RT	0.36(3.0)	Valid	0.47 (3.9)	Valid

* ASTM E1820-15 assesses crack straightness based on the maximum difference of all nine physical crack measurements from the average measurement and considers the straightness valid when the maximum difference is less than or equal to 0.05B.

6.5.2. Microstructural analysis

Variation in the fracture toughness of the CGHAZ of welded microalloyed steels relative to the rest of the welded steel is essentially influenced by the heat input and thermal cycle that the steel experiences during welding [242]. The property changes in the CGHAZ are attributed to the PAG size and the fraction and morphology of the microstructural features. Refining the PAG size influences the transformation products, particularly the M-A constituents, within the HAZ, which results in beneficial effects on toughness [129,177,220]. Optical micrographs of the HAZ, revealing the PAGs and M-A constituents (using modified LePera's etchant [140,141]) are shown in Figure 6-13a-d. The PAG size in the CGHAZ was decreased by addition of the cold wire. The PAG size in the CGHAZ for CWTSAW and TSAW weld samples was measured as 55 μm and 68 μm, respectively. The reduction in the PAG size in the CGHAZ is attributed to a reduction in the actual heat introduced to the weldment, lowering of the peak temperature, reduction in the retention time in the austenitization temperature range (1100-1400°C) and an increase in the cooling rate by adding the cold wire. The heat input analysis, based on the method discussed in Chapter 5, indicated that the heat input of the CWTSAW process was reduced by 8% relative to TSAW. Accordingly, the cooling rate was reduced by 9%. SEM micrographs of the CGHAZ of the weld samples are depicted in Figure 6-14a and b. The CGHAZ microstructure of the TSAW sample (with higher heat input) has large PAGs, polygonal ferrite (PF), granular bainite (GB), bainitic ferrite (BF) and large M-A constituents, which are mostly formed along the PAG boundaries. In contrast, the CGHAZ microstructure of the

CWTSAW sample (with lower heat input) is composed of finer PAGs, PF, GB and BF associated with fine, blocky shaped M-A constituents. Less M-A is formed within the CGHAZ of the CWTSAW weld sample compared with the TSAW sample. The microstructure of the FGHAZ of the CWTSAW sample is composed of PF and less GB and BF with smaller M-A constituents compared with the FGHAZ of the TSAW sample. The fraction, size and distribution of M-A constituents in the CGHAZ of the weld samples are indicated in Table 6-9.

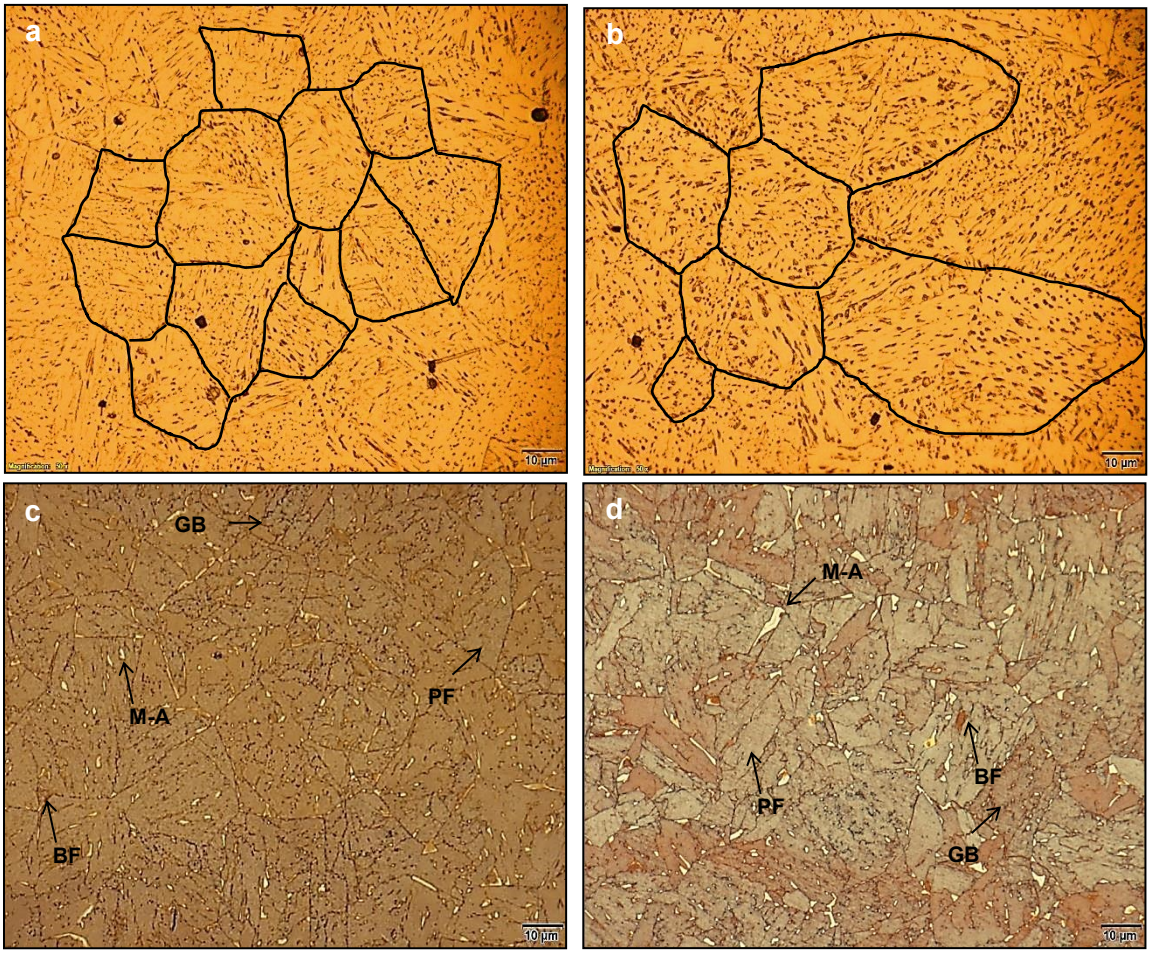

Figure 6-13 Optical micrographs of the CGHAZ for the CWTSAW sample (a, c) and the TSAW sample (b, d).

The M-A fraction in the CGHAZ, determined from the optical micrographs, was 4.1% and 3.0% for the TSAW and CWTSAW samples, respectively, indicating a reduction in the fraction of M-A as a consequence of PAG size reduction [177,218] by cold wire addition. Quantitative analysis of the M-A regions indicates that the fraction of M-A constituents in the CGHAZ with sizes larger than 1.5 µm for TSAW and CWTSAW samples is 3.5% and 0.9%, respectively. The low toughness in the CGHAZ of welded microalloyed steels is highly influenced by the shape, size, distribution and fraction of M-A

constituents in the CGHAZ [177,218,258]. The larger M-A constituents in the CGHAZ of the TSAW sample are due to the higher martensite start temperature (Ms) for samples with larger PAGs [71,229]. Bhadeshia [139], Heinze et al. [219] and Guimaraes [247] suggested that a decrease in Ms temperature happens with a decrease in the PAG size, which results in a lower volume fraction of martensite. According to the classical Koistinen-Marburger (KM) equation [216] and the geometrical partitioning model by Fisher et al. [221], the fraction of martensite is a function of the amount of undercooling below the Ms temperature. Based on the proposed models, the martensite volume fraction formed in the early stages of the transformation is proportional to the PAG size cubed. A such, "the fraction of the transformation needed to detect Ms is reached at a smaller undercooling when the PAG size is larger" [71]. Therefore, a coarser PAG size increases the fraction and size of the M-A constituent. Li et al. [177] and Yu et al. [218] showed that a coarse PAG size, associated with a coarse M-A constituent, is the dominant factor in promoting brittle fracture in the CGHAZ. Accordingly, there is a concurrent effect of both grain size refinement and M-A transformation, which plays a significant role in the toughness of the HAZ. Due to the formation of the M-A constituent, there is a higher proportion of localized brittle zones (LBZs) in the CGHAZ of the TSAW sample compared with the CGHAZ of the CWTSAW sample. This shows up as higher microhardness values in the CGHAZ for the TSAW sample relative to the CWTSAW sample. Also, a narrower distribution of fine M-A constituents (LBZs) inside the ferritic matrix in the CGHAZ of the CWTSAW sample resulted in higher J-integral values for the CGHAZ at different test temperatures. Coarser PAGs with large M-A constituents, which are mostly formed along the PAG boundaries, led to inferior toughness properties in the HAZ of the TSAW sample. This inferior toughness, due to formation of M-A constituents along PAG boundaries, was confirmed by the work done by Davis et al. [128] and Reichert et al. [314]. They found that the combination of the slender shape and the formation of a network of M-A constituents along the PAG boundaries is most detrimental to fracture properties. The improved microstructural alterations and consequent mechanical property changes in the HAZ of the CWTSAW sample are attributed to the lower actual heat introduced to the steel and the relatively faster cooling rate within the HAZ by the addition of the cold wire during welding.

Table 6-9 Characteristics of the M-A constituents in the CGHAZ of different welds

Weld Sample	**Fraction (vol.%)**	**Mean Size (μm)**	**Inter-Spacing (μm)**
CWTSAW	3.0	0.3	2.5
TSAW	4.1	0.48	4.9

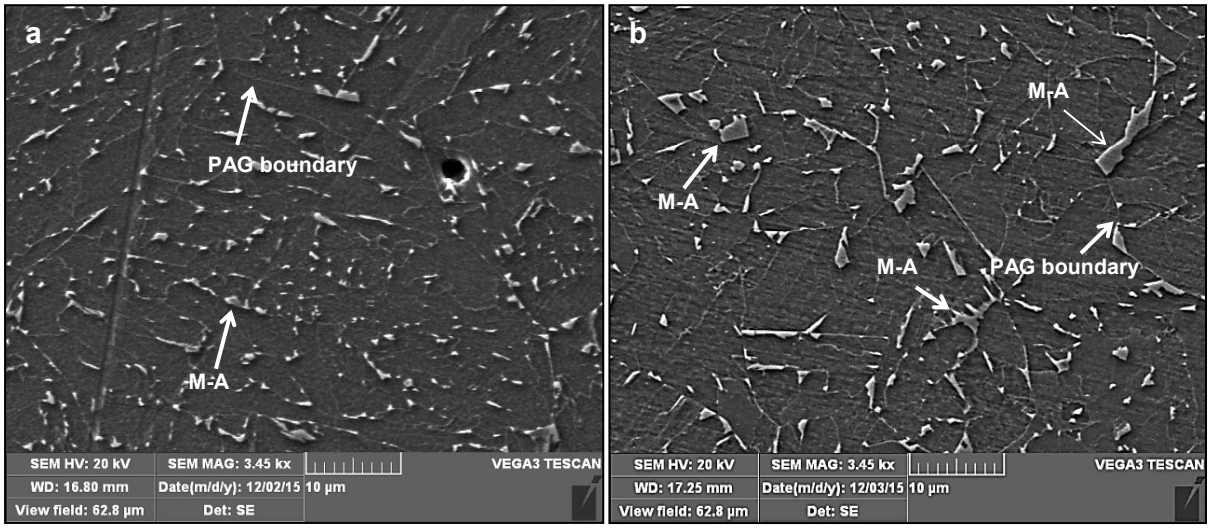

Figure 6-14 SEM secondary electron (SE) images of the CGHAZ of (a) the CWTSAW and (b) the TSAW samples.

6.6. Conclusions

Fracture mechanics testing of the known brittle region, i.e., the coarse grain heat affected zone (CGHAZ), within an X70 low-carbon microalloyed steel weld was carried out at three different test temperatures of room temperature, -5°C and -30°C for two different weld conditions. The single-edge notch tension (SENT) test was used for determination of fracture toughness of the welded microalloyed steels. The addition of a cold wire to the conventional tandem submerged arc welding (TSAW) process, which is widely used for pipeline manufacturing, resulted in an overall improvement in the fracture toughness of the CGHAZ at different temperatures. The improvement in the toughness of the CGHAZ was attributed to the reduction in the prior austenite grain (PAG) size and consequent formation of a lower fraction of finely distributed fine martensite-austenite (M-A) constituents in the CGHAZ. The alterations are principally due to lowering the actual heat introduced to the weldment and increasing the cooling rate by cold wire addition. The relatively large elongated M-A constituents which mostly formed along the PAG boundaries, along with the relatively large PAGs, of the TSAW samples (compared with those of the CWTSAW) led to inferior toughness properties in the CGHAZ of the TSAW sample, since the larger M-A constituents can stimulate the formation of microcracks leading to intergranular fracture. From a procedure/ standards point of view, SENT testing appears to be robust and mature enough to be considered for incorporation into future revisions of fracture toughness standards, such as ASTM E1820 and ISO 12135. However, additional work is needed to establish and qualify the specimen measuring capacity (J_{max}) and the crack extension limit (Δa_{max}) for the SENT specimen geometry.

Appendix B

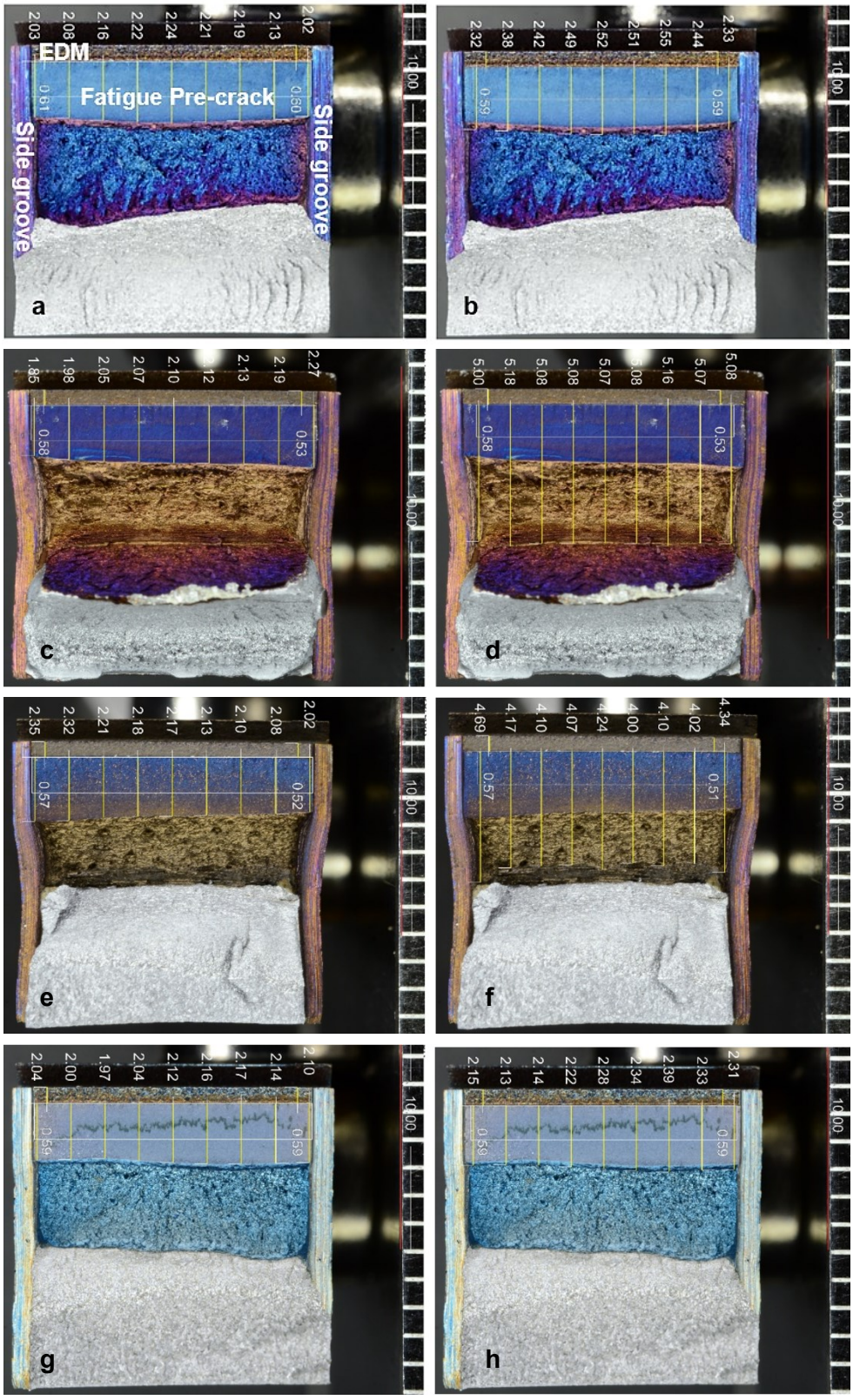

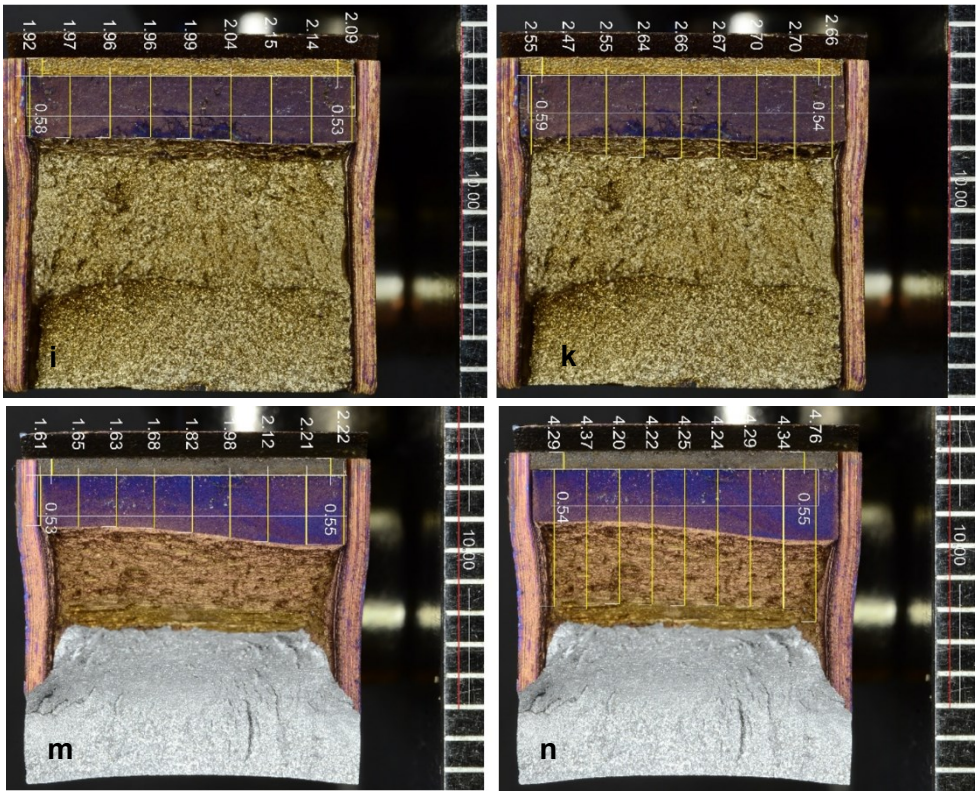

Figure A.B-1 Optical macrographs of the fracture surfaces of SENT specimens after testing at (a, b) -30°C, (c, d) -5°C and (e, f) RT for CWTSAW weld samples and at (g, h) -30°C, (i, k) -5°C and (m, n) RT for TSAW weld samples. The left column represents the initial crack (fatigue pre-crack) size measurements and the right column represents the final crack length measurements. The small region on top of each specimen represents the EDM notch, which was machined prior to pre-cracking of the specimens. Small grooves along both sides of each specimen are the side grooves machined on the specimens after pre-cracking and prior to SENT testing.

Appendix C

Tint Etching Optical Microscopy (TEOM)

A.1 Introduction

Recent developments in the automotive industry have been essentially focused on the design of high strength steels with appropriate weldability. The challenge is to reduce car body weight and CO_2 emissions while increasing passenger safety. This has led to the demand for stronger and more ductile materials like HSLA (high-strength low-Aalloy) steels. Furthermore, with reference to pipeline engineering, high operating pressures and/or pipes with thinner wall are a means to reduce transmission costs. In addition to transportation costs, steels utilized for manufacturing oil and gas transportation pipelines must have sufficient strength and toughness (particularly low-temperature fracture toughness) according to engineering critical assessment (ECA). However, conventional steels typically lack sufficient strength and toughness.

HSLA steels are known as multi-phase steels comprised of hard phases, such as martensite-retained austenite, i.e., martensite-austenite (M-A) constituents, and bainite embedded within a soft matrix of ferrite. Due to the low carbon and alloying element content and, consequently, low hardenability, HSLA steels possess excellent weldability. To have a better understanding of the mechanical properties (e.g., strength and toughness) in the base steel and its weld zones, knowledge about the microstructure is vital. Techniques like optical microscopy (OM) or scanning electron microscopy (SEM) are widely utilized to visualize the microstructure. Besides its lower cost, the advantage of OM over SEM is the capability of visualizing and identifying various features through colors (i.e., tint etching optical microscopy or TEOM). As such, it is possible to use OM for not only grain boundary etching, but also color etching and a combination of different etching techniques for microstructure visualization.

To reveal specific microstructural characteristics, several etching techniques have been developed. Among these, chemical etching is undoubtedly the most facile and feasible and the most widely used. This technique employs a controlled corrosion process driven by electrochemical potential differences between surfaces with chemical or physical heterogeneities [315]. Etching induces the selective dissolution or preferential staining of the phases present. Amongst the general etching solutions for steels, Nital (a solution of nitric acid in ethanol) is the most common etchant for revealing ferrite and ferrite/cementite grain boundaries. However, examination of Nital etched HSLA steels by optical microscopy is generally not very satisfactory. These steels contain a very fine

dispersion of martensite islands embedded in a ferritic matrix, which are not well revealed with Nital etching. Accordingly, this has led to the development of new, more suitable tint etchants [4], which reveal different phases by coloring them [315,316].

To observe microstructural features with SEM using secondary electron (SE) contrast, topographic contrast through etching of the different phases is necessary. Nital is well suited as it preferentially etches ferrite while leaving austenite and cementite intact. Ferritic phases, such as polygonal ferrite, bainitic ferrite (or acicular ferrite), allotromorphic and idiomorphic ferrite (usually observed in the steel weld zone) and pearlitic ferrite are dissolved and exhibit a typical morphology that generally allows for their recognition. However, the situation becomes more complex when a microstructure simultaneously consists of austenite and martensite as second phases, known as M-A constituents. In this case, common Nital etching is not selective enough to reveal M-A islands. This limitation is critical, since the M-A constituents are considered to be a significant microstructure. Herein, existing tint etching techniques that can be applied and adapted to low-carbon microalloyed steels to reveal the microstructure within base steel and different regions of heat affected zone (HAZ) and weld metal (WM) by optical microscopy (TEOM), are discussed.

A.2 Materials and TEOM Procedure

An X70 microalloyed steel produced via thermo-mechanical controlled processing (TMCP) was welded by tandem submerged arc welding (TSAW). The steel composition and the welding procedure are shown in Chapter 4 (Table 4-1). Metallographic specimens were cut in the transverse direction relative to the welding direction (longitudinal to the rolling direction). Microstructural characterization was carried out in different regions of the base metal, HAZ and WM using optical microscopy (Olympus BX61) and scanning electron microscopy (Tescan Vega-3 SEM). With respect to the microstructure, the size, fraction and morphology of microstructural features, particularly M-A constituents and prior austenite grains (PAGs) formed in the HAZ and WM, are greatly dependent on the thermal cycle (peak temperature and cooling rate) that steel experiences during welding [129,177,220]. Revealing PAG boundaries and M-A constituents in low-carbon microalloyed steels and their relevant welds can be difficult to achieve and depends very much on the etchant type and time of etching. As such, several etching procedures, using various etchants with different solution concentrations and etching times, were employed, and are shown in Table A.C-1.

Table A.C-1 List of etchants used for revealing microalloyed steel microstructure

#	Etchant	Concentration	Time	Temperature (°C)	Etching Principle	Application
1	Nital	- 2 ml nitric acid in 100 ml ethanol - 4 ml nitric acid in 100 ml ethanol	10-20 s	RT	Grain boundary etching	General microstructure Unknown beforehand Ferrite grains
2	LePera	(a) 1 g $Na_2S_2O_5$ in aqueous dilution, (b) 4 g picric acid in ethanol →A mixture of part **a** and **b** in equal portion (1:1 Vol.)	60-90 s	RT	Anodic surface layer etching	Tint etching of ferrite, bainite and M-A constituents (M-A is revealed as white)
3	Modified Picral Etchant	4 g picric acid in 96 ml distilled water + few drops of HCl	30-60 s	RT and 60	Anodic surface layer etching	PAG boundaries
4	Modified LePera	LePera + few drops of HCl	30-50 s	RT and 60	Anodic surface layer etching	Accelerated tint etching of polygonal ferrite, bainitic ferrite, granular bainite and M-A constituents (M-A ia revealed as shiny white)
5	10% $Na_2S_2O_5$	10 g $Na_2S_2O_5$ in 100 ml distilled water	7-12 s	RT	Anodic surface layer etching	Tint etching of microstructural features
6	Liang's Etchant	10 gr CrO_3 + 1.5 g picric acid + 50 g NaOH in 100 ml distilled water	15-30-60-90-120-180 min	60-180	Cathodic surface layer etching	PAG boundaries
7	Nital+$Na_2S_2O_5$	Preetching with Nital 4%, wet etching with $Na_2S_2O_5$ 10% in aqueous dilution	10 s + 7 s (up to 15 s)	RT	Grain boundary and anodic surface layer etching	High contrast of the grain boundaries due to a combination of grain boundary etching with anodic surface layer etching
8	Nital+LePera	Preetching with Nital 4%, wet etching with modified LePera	10 s + 20 s (up to 40 s)	RT	Grain boundary and anodic surface layer etching	High contrast of grain boundaries and M-A identification
9	Marshall's reagent	(a) 5 ml sulphuric acid + 8 g oxalic acid in 100 ml water (b) 30% solution hydrogen peroxide A mixture of **a** and **b** in equal quantities	20-180 s	RT	Cathodic surface layer etching	PAG boundaries

After the etching trials, it was concluded that etchants 3 and 4 in Table A.C-1 showed the best and the most stable results in terms of revealing features of interest (relative to the other etchants). It is worthwhile to note that etchant 5 had poorer etching response relative to modified LePera's etchant; however, etchant 6 did not work at all for revealing the microstructural features. Accordingly, a chemical solution containing 4 g of picric acid in 96 ml ethanol, along with a few drops of HCl acid was selected to reveal the PAG boundaries. The PAG size was analyzed using the mean linear intercept method according to ASTM E112 [235]. Freshly polished weld specimens were then tint etched at RT through a separate process using modified LePera's etchant [140,141] for 30-50 s to reveal different microstructural features in different colors. Microstructural analysis indicated a high sensitivity for phase identification to etchant composition and etching time. Quantitative analysis of the M-A constituent was done using ImageJ image analysis software. The fraction of other microstructure features was examined according to ASTM E562 [236]. The PAGs in the fine grain HAZ (FGHAZ) and coarse grain HAZ (CGHAZ) are shown in Figure A.C-1a and A.C-1b, respectively. Optical and SEM micrographs revealing M-A constituents, along with other features using the TEOM technique, are shown in Figure A.C-2 and A.C-3, respectively.

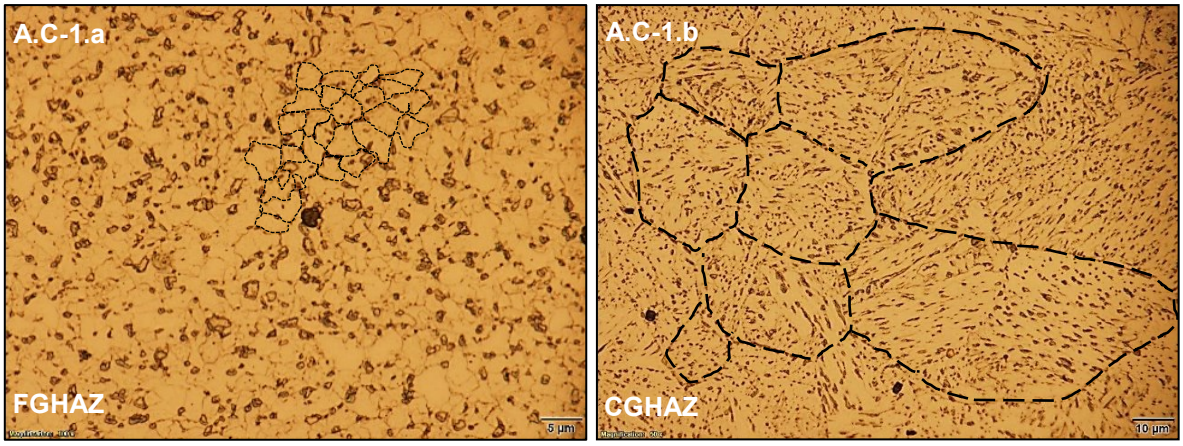

Figure A.C-1 Optical micrographs indicating PAG boundaries in the (a) FGHAZ and (b) CGHAZ.

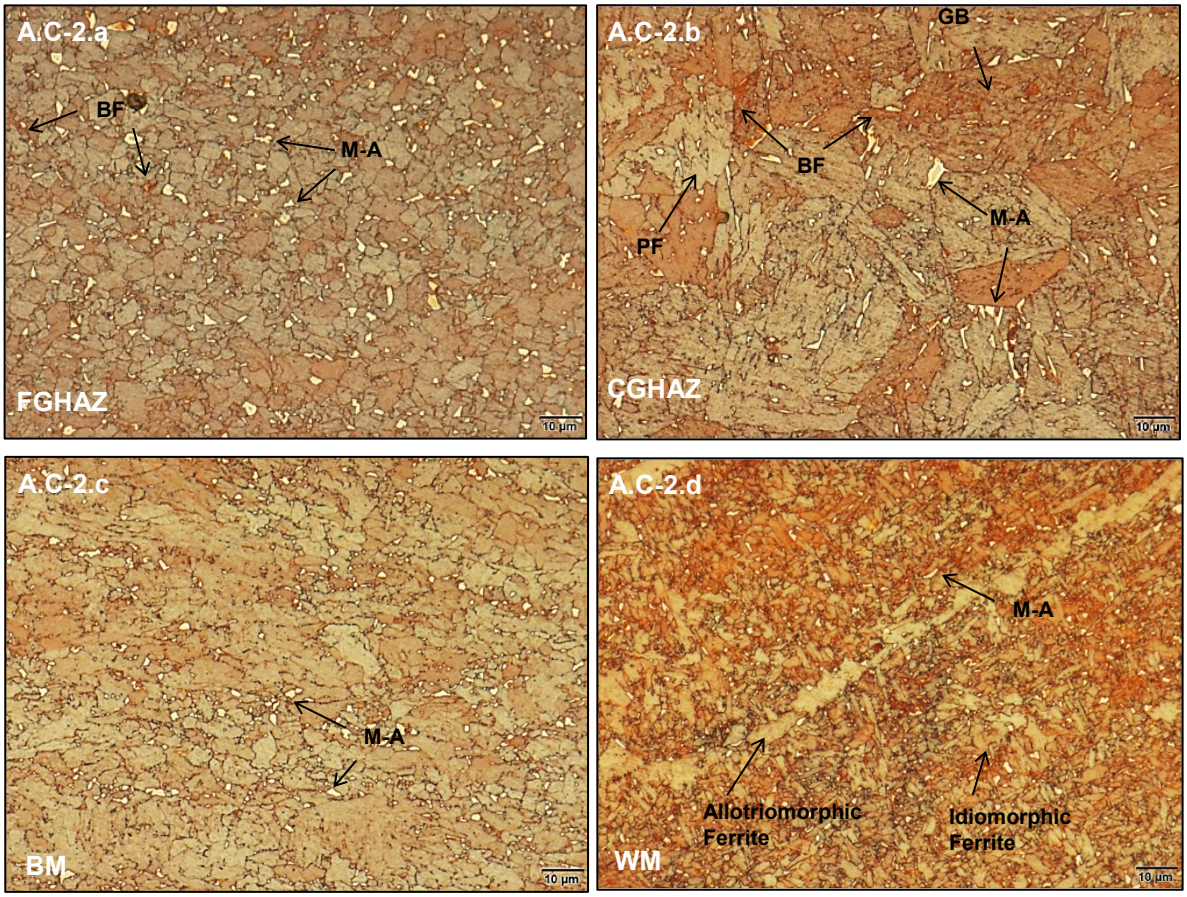

Figure A.C-2 Tint etching optical micrographs of the (a) FGHAZ, (b) CGHAZ, (c) base metal (BM) and (d) WM. M-A constituents are revealed as white regions.

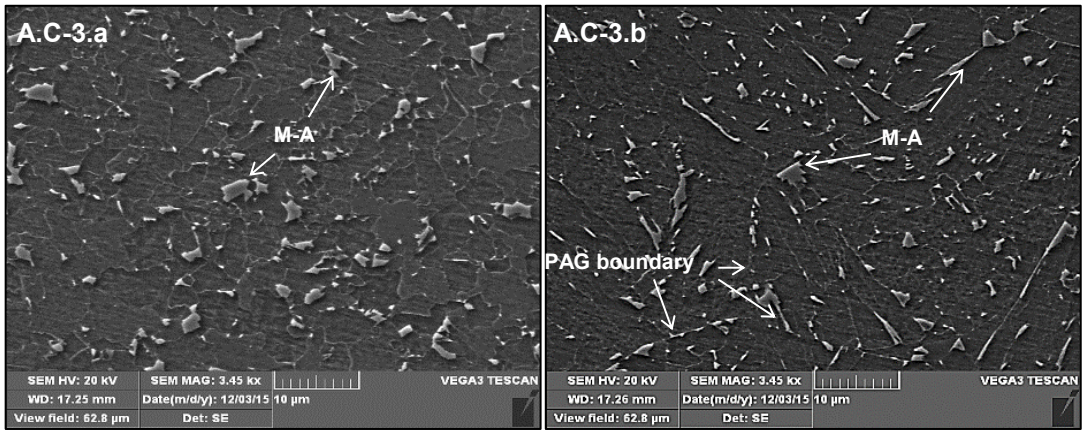

Figure A.C-3 SEM secondary electron (SE) images of the (a) FGHAZ and (b) CGHAZ using tint etching technique.

As shown in Figure A.C-4 and A.C-5, characterization and quantification of Nital-etched microalloyed steel and its HAZs is extremely challenging. As such, TEOM is a powerful method for microstructural characterization of microalloyed steels and their weld regions. Since mechanical property changes are related to microstructural alterations, it is essential to characterize and quantify microstructural features. Polygonal ferrite (PF), granular bainite (GB) and bainitic ferrite (BF) are revealed as yellow, light brown and dark brown, respectively, using TEOM. The PAG size in the FGHAZ and CGHAZ was 5.5±0.4 and 68±7 μm, respectively. The fraction of PF, GB, BF and M-A constituents in the CGHAZ and FGHAZ, using the TEOM etchant, was 69.1%, 21.5%, 5.4% and 4.0%, and 78.1%, 15.3%, 3.0% and 3.6%, respectively. The M-A fraction in the CGHAZ and FGHAZ, calculated from the SEM micrographs (Figure A.C-3a and A.C-3b), was 5.4 % and 4.9%, respectively. The results indicate that similar results are attainable for both SEM and OM techniques (and both tint etching methods), which confirm the validity of the M-A identification using TEOM techniques.

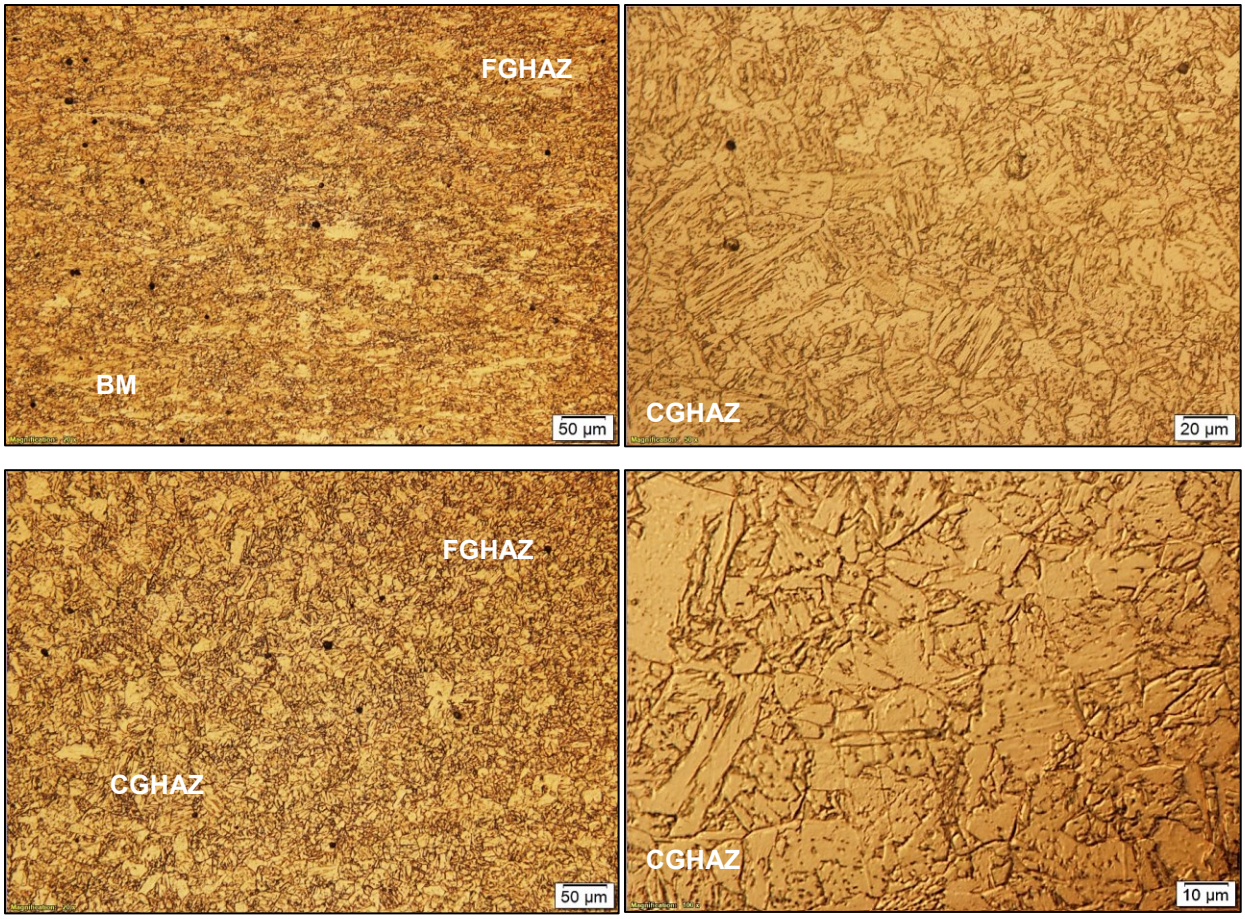

Figure A.C-4 Optical micrographs showing overall microstructure in various regions of the X70 steel and its HAZ etched with 4% Nital. It is difficult to identify and quantify different phases compared with TEOM.

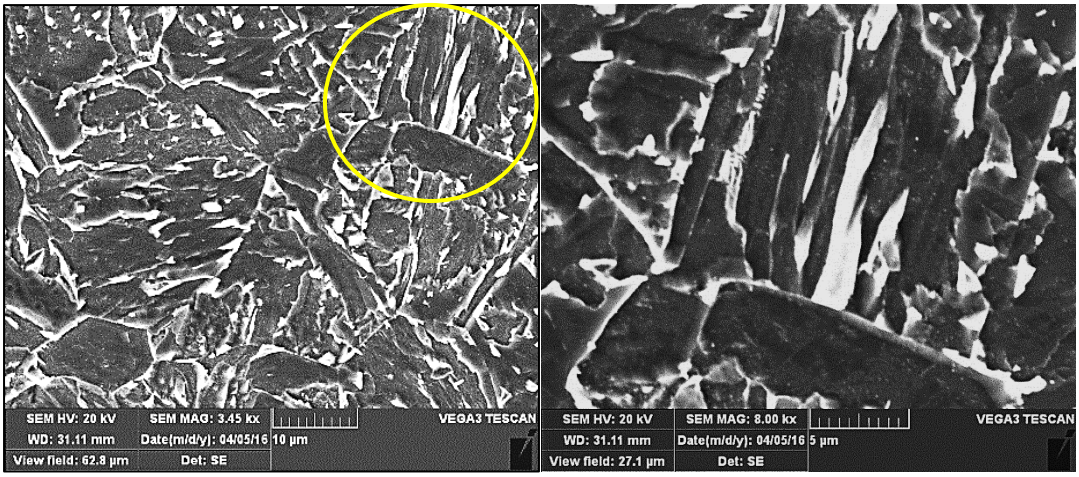

Figure A.C-5 SEM SE images of the CGHAZ using 4% Nital etchant: (a) lower and (b) higher magnification.

Chapter 7

7. General Conclusions and Recommendations

7.1. Summary and Conclusions

During processing of low-carbon microalloyed steels, a good combination of strength and toughness is obtained by appropriate alloying design and thermo-mechanical controlled processing (TMCP) [1,2]. However, this strength and toughness combination can be deteriorated by the heat input and the thermal cycles that the steel experiences during welding. Since welding is an unavoidable stage in pipe manufacturing, it is essential to produce welded pipe with as low a heat input as possible while retaining adequate joint geometry and properties. During the past decades, submerged arc welding (SAW) has been extensively utilized to produce oil and gas transportation pipelines, due to its inherent properties, such as deep penetration, high deposition rate and capability of welding thick sections. To improve welding productivity in a global economy, many fabricators have resorted to tandem submerged arc welding (TSAW), which is SAW with two to five electrodes. However, welding heat input in the TSAW process is increased, due to the increase in the overall welding current and voltage needed for a higher deposition rate, which results in some adverse effects on the microstructure and toughness of the weld joint. It is generally accepted that the portion of the base metal which is affected by the heat of welding, the heat affected zone (HAZ), and particularly the zone adjacent to the fusion line, the coarse grain heat affected zone (CGHAZ), has lower toughness relative to the rest of the steel. The deterioration in toughness in the CGHAZ is attributed to the formation of large prior austenite grains (PAGs) and martensite-austenite (M-A) constituents, which are localized brittle zones (LBZ), as a result of the high peak temperature and relatively fast cooling rate in the CGHAZ. High heat input promotes PAG coarsening and the formation of a higher fraction of large slender shaped M-A constituents in the CGHAZ, which leads to property deterioration. As such, it is not always acceptable to increase the welding heat input to increase productivity.

In this thesis, cold wire tandem submerged arc welding (CWTSAW) was developed to improve the overall productivity of pipeline manufacturing in terms of deposition rate and travel speed

without an increase in the heat input of the welding process. In addition to increasing the productivity, cold wire addition influenced the macrostructure (geometry), microstructure and mechanical properties of the welded steel. In fact, CWTSAW operates on the principle that an additional cold wire consumes and moderates the heat introduced to the weldment. Accordingly, the research work in this thesis was designed in four main steps as follows:

1. Design and development of the CWTSAW process:

To have an appropriate understanding of the welding process to guarantee requisite weld geometry, appearance and properties, the process was initially designed using Taguchi methodology. The CWTSAW parameters, such as heat input, voltage and travel speed of both electrodes along with three main cold wire parameters (position, angle and feed speed) were investigated and correlated with the geometry of the weld and HAZ, i.e., aspect ratio (AR), semi-penetration ratio (SPR), reinforcement area (RA) and CGHAZ area, dilution and the microhardness of the weld metal (WM) and CGHAZ.

Variations in the cold wire parameters showed significant effects on the WM and CGHAZ microhardness, and the geometry characteristics, i.e., increases in SPR and AR and a reduction in dilution. The effects are a consequence of the considerable reduction in the total heat introduced to the weldment and the subsequent change in cooling rate when a cold wire is added to the molten pool during CWTSAW. The maximum contribution of cold wire parameters on the variation of geometry characteristics and dilution was 33.1% and 39.5%, respectively, compared with other parameters. The addition of cold wire at a lagging position with a feed speed of 8.5 mm/s at 63° resulted in an overall improvement in the weld geometry and properties.

There was a 14.0% and 10.3% reduction in dilution and the CGHAZ area, respectively, for the CWTSAW process, because of a reduction in the overall heat introduced to the weldment. Microstructural analysis, using both optical microscopy and scanning electron microscopy (SEM), indicated the formation of finer PAGs and less M-A constituent within the CGHAZ of the CWTSAW samples, which is attributed to lower actual heat introduced to the weldment and faster cooling rates. These effects also led to lower microhardness values in the CGHAZ of the CWTSAW samples.

2. Influence of the cold wire addition on the microstructural characteristics and mechanical properties of the HAZ:

To evaluate the microstructural evolutions in the HAZ, tint etching optical microscopy (TEOM) technique was utilized. TEOM was used to quantify the phase transformations in the HAZ, particularly CGHAZ. The technique was coupled with SEM to analyze the microstructural features. Cold wire addition resulted in a reduction in the PAG size in the CGHAZ. Microstructural analysis

indicated that the fraction of M-A constituents in the CGHAZ was reduced and the distribution, size and shape were altered, when a cold wire was added to the TSAW process. Cold wire addition at a cold wire feed rate of 25.4 cm/min showed a reduction in the fraction of M-A constituents along with a uniform distribution of finer M-A constituents in the ferritic matrix, due to a reduction in the actual welding heat input and the PAG size. These effects resulted in an improvement in the fracture toughness of the HAZ. The changes to the fraction and characteristics of the M-A constituents in the HAZ of the cold wire sample (25.4 cm/min) relative to the sample with no cold wire are attributed to the lower actual heat introduced to the weldment and the resulting faster cooling rate, lower peak temperature and the formation of finer PAGs by cold wire addition. The PAG size was further reduced when the cold wire was fed at 76.2 cm/min (compared with the cold wire (25.4 cm/min) and TSAW weld samples), due to a faster cooling rate in the CGHAZ of the 76.2 cm/min cold wire sample; however, elongated shaped M-A constituents were formed. The relatively large elongated M-A constituents with large inter-particle spacing formed primarily along the PAG boundaries in the CGHAZ of the TSAW and cold wire (76.2 cm/min) samples. This morphology led to inferior toughness properties in the HAZ of the TSAW and cold wire (76.2 cm/min) samples, since the large M-A constituents can stimulate the formation of microcracks leading to intergranular fracture.

3. Heat input, properties and productivity correlation in both developed CWTSAW and conventional TSAW:

The addition of a cold wire in conventional TSAW had a two-fold effect on the characteristics of the welded microalloyed steels; i.e., increased welding productivity and improved properties. A 12% and 26% increase in the deposition rate and travel speed, respectively, were achieved by addition of a cold wire at 58 cm/min in the TSAW process with a heat input of 23.2 kJ/cm. Cold wire addition resulted in an overall improvement in the fracture toughness of the HAZ; however, it should be noted that the improvement was greatly influenced by the cold wire addition rate and the consequent effective welding heat input. Accordingly, cold wire addition at 25.4 cm/min during TSAW with a heat input of 22.1 kJ/cm showed an improvement in the fracture toughness of the HAZ due to a reduction in the PAG size and the fraction of M-A constituents, along with a uniform distribution of finer M-A constituents in the ferritic matrix. The microstructural alterations were attributed to the lower effective welding heat input (7.5% reduction compared with the TSAW (T1) sample). The lower heat input of 20.5 kJ/cm and faster cold wire addition (63.5 cm/min) resulted in a smaller PAG size compared with the other studied weld samples, due to the relatively larger reduction in the effective welding heat input (17.1% reduction) and faster cooling rate in the CGHAZ. However, the formation of relatively large elongated M-A constituents with large inter-

particle spacing led to inferior toughness properties for the HAZ of the former samples, since larger M-A constituents can stimulate the formation of microcracks leading to intergranular fracture.

4. Fracture toughness analysis in the HAZ of the welded X70 microalloyed steel using single-edge notch tension (SENT) testing:

The SENT test method has been recently designed and developed to investigate the toughness of pipeline steels and their welds. The advantage of the SENT test over other test procedure is that the test conditions in the SENT test, such as the tensile loading condition (clamped and pin-loaded), crack/width ratio (a_0/W) and specimen length, result in less severe constraints at the tip of the crack. As such, less conservative toughness results can be achieved. Accordingly, the fracture toughness of the known brittle region, i.e., CGHAZ, within an X70 low-carbon microalloyed steel weld was carried out using SENT testing at three different temperatures (i.e., room temperature, -5°C and -30°C) for two different weld conditions. The addition of a cold wire to the conventional TSAW process resulted in an overall improvement in the fracture toughness of the CGHAZ at different temperatures. The SENT results showed similar trends to those achieved from Charpy impact testing, i.e., overall higher fracture toughness in the HAZ was achieved when a cold wire was fed in the conventional TSAW process. As stated earlier, the improvement in the toughness was attributed to the reduction in the PAG size and consequent formation of a lower fraction of finely distributed fine M-A constituents in the CGHAZ. The alterations were principally due to lowering of the actual heat introduced to the weldment (~8%) and increasing the cooling rate (~10%) by cold wire addition. The relatively large elongated M-A constituents which mostly formed along the PAG boundaries, along with the relatively large PAGs, of the TSAW samples (compared with those of the CWTSAW) led to inferior toughness properties in the CGHAZ of the TSAW sample, since the larger M-A constituents can stimulate the formation of microcracks leading to intergranular fracture. From a procedure/standards point of view, SENT testing appears to be robust and mature enough to be considered for incorporation into future revisions of fracture toughness standards, such as ASTM E1820 and ISO 12135. However, since the test procedure is under development, additional work is needed to establish and qualify the specimen measuring capacity (J_{max}) and the crack extension limit (Δa_{max}) for the SENT specimen geometry.

7.2. Recommendations for the Future Work

This study was aimed at designing and developing CWTSAW process parameters in such a way that the microstructure, fracture toughness and macrostructure (geometry) of the weld and HAZ were improved. The effect of cold wire addition on the toughness of the CGHAZ (with poor toughness) was studied. During manufacturing, the steel pipe is exposed to two inner-diameter and outer-

diameter weld passes, so it is worthwhile to study the influence of the cold wire addition on the microstructure and properties of the inter-critically reheated CGHAZ. This region is believed to show the lowest toughness relative to the rest of the steel, which is very sensitive to welding heat input.

Welding is a complex process, with many unknown technical factors which directly influence the properties of the final product. During welding, both technical and metallurgical aspects are involved making it necessary to carefully consider and correlate both welding process and metallurgical factors simultaneously for final process development. Accordingly, a full quantification of the microstructural alterations when the process parameters vary is always necessary. Quantification of precipitate alterations in the HAZ by variation of the heat input as a result of cold wire addition needs to be done.

Carbon content and segregated alloying elements affect the M-A constituents and, as such affect the properties of the CGHAZ. A quantity study examining the effect of segregation of alloying elements on the M-A constituent is worth pursuing.

The developed CWTSAW process is a promising technique for spiral welds commonly used for the pipe manufacturing, since a smaller weld pool is expected to form due to the reduction in the overall heat introduced to the weldment. Although this study was conducted on a laboratory scale (at AMPL at the University of Alberta and at Evraz Inc. NA), the process needs to be scaled up to a real pipeline manufacturing process, e.g., spiral pipe manufacturing process.

References

[1] G.Y. Qiao, F.R. Xiao, X.B. Zhang, Y. Bin Cao, B. Liao, Effects of contents of Nb and C on hot deformation behaviors of high Nb X80 pipeline steels, Trans. Nonferrous Met. Soc. China (English Ed. 19 (2009) 1395–1399. doi:10.1016/S1003-6326(09)60039-X.

[2] W. Wang, Y. Shan, K. Yang, Study of high strength pipeline steels with different microstructures, Mater. Sci. Eng. A. 502 (2009) 38–44. doi:10.1016/j.msea.2008.10.042.

[3] W. Yuhui, L. Bo, L. Ligang, L. Xianfeng, S. Hang, Y. Caifu, W. Qingfeng, Effects of N and B on continuous cooling transformation diagrams of Mo–V–Ti micro-alloyed steels, Phase Transitions. 85 (2012) 419–426. doi:10.1080/01411594.2011.611401.

[4] R. Li, X. Zuo, Y. Hu, Z. Wang, D. Hu, Microstructure and properties of pipeline steel with a ferrite/martensite dual-phase microstructure, Mater. Charact. 62 (2011) 801–806. doi:10.1016/j.matchar.2011.05.013.

[5] J.T. Pepin, Effects of submerged arc weld (SAW) parameters on bead geometry and notch-toughness for X70 and X80 linepipe steels, Master Thesis, University of Alberta, 2009.

[6] T. Fabricator, Improving productivity with submerged arc welding, Fabr. Manuf. Assoc. Intl. (2010) 1–4.

[7] S. Moeinifar, A.H. Kokabi, H.R.M. Hosseini, Role of tandem submerged arc welding thermal cycles on properties of the heat affected zone in X80 microalloyed pipe line steel, J. Mater. Process. Technol. 211 (2011) 368–375. doi:10.1016/j.jmatprotec.2010.10.011.

[8] D. V. Kiran, S.A. Alam, A. De, Development of process maps in two-wire tandem submerged arc welding process of HSLA steel, J. Mater. Eng. Perform. 22 (2013) 988–994. doi:10.1007/s11665-012-0381-2.

[9] P.D. Thomas, L.A. Craig, Automatic submerged arc welding with metal powder additions to increase productivity and maintain quality, Newport News Shipbuilding, Washington, VA, 1986.

[10] Fabricator, Improving productivity with submerged arc welding, Fabr. Manuf. Assoc. Intl. (2010) 1–4.

[11] J. Pepin, C. Penniston, H. Henein, D.G. Ivey, L. Collins, D. Boyd, Using semipenetration ratio to characterise effects of waveform variables on bead profile and heat affected zone with single electrode submerged arc welding, Can. Metall. Q. 51 (2012) 284–293. doi:10.1179/1879139512Y.0000000018.

[12] M.F. Mruczek, P.J. Konkol, Cold wire feed submerged arc welding: Technical Report, PA,

2006.

[13] ESAB, Submerged arc welding (Technical Handbook), TX, 2013.

[14] B. Beidokhti, A.H. Kokabi, A. Dolati, A comprehensive study on the microstructure of high strength low alloy pipeline welds, J. Alloys Compd. 597 (2014) 142–147. doi:10.1016/j.jallcom.2014.01.212.

[15] H. Farhat, Effects of multiple wires and welding speed on the microstructures and properties of submerged arc welded X80 steel, PhD Diss. Univ. Saskatchewan. (2007).

[16] N. Murugan, V. Gunaraj, Prediction and control of weld bead geometry and shape relationships in submerged arc welding of pipes, J. Mater. Process. Technol. 168 (2005) 478–487. doi:10.1016/j.jmatprotec.2005.03.001.

[17] M.F. Mruczek, P.J. Konkol, Twin-arc and cold-wire-feed submerged-arc welding of HSLA-100 steel, in: 5th Sess. Am. Weld. Soc., 2005.

[18] M. Ramakrishnan, V. Muthupandi, Application of submerged arc welding technology with cold wire addition for drum shell long seam butt welds of pressure vessel components, Int. J. Adv. Manuf. Technol. (2012) 1–12. doi:10.1007/s00170-012-4230-0.

[19] M. Ramakrishnan, K. Padmanaban, V. Muthupandi, Studies on fracture toughness of cold wire addition in narrow groove submerged arc welding process, Int. J. Adv. Manuf. Technol. 68 (2013) 293–316. doi:10.1007/s00170-013-4729-z.

[20] K.Y. Benyounis, A.G. Olabi, Optimization of different welding processes using statistical and numerical approaches - A reference guide, Adv. Eng. Softw. 39 (2008) 483–496. doi:10.1016/j.advengsoft.2007.03.012.

[21] Y.S. Tarng, W.H. Yang, Application of the Taguchi method to the optimization of the submerged arc welding process, Mater. Manuf. Process. 13 (1998) 455–467. doi:10.1080/10426919808935262.

[22] V. Gunaraj, N. Murugan, Application of response surface methodology for predicting weld bead quality in submerged arc welding welding of pipes, Mater. Process. Technol. 88 (1999) 266–275.

[23] N. Akkas, D. Karayel, S.S. Ozkan, A. Oğur, B. Topal, Modeling and analysis of the weld bead geometry in submerged arc welding by using adaptive neurofuzzy inference system, Math. Probl. Eng. 2013 (2013). doi:10.1155/2013/473495.

[24] S. Moeinifar, A.H. Kokabi, H.R.M. Hosseini, Effect of tandem submerged arc welding process and parameters of Gleeble simulator thermal cycles on properties of the intercritically reheated heat affected zone, Mater. Des. 32 (2011) 869–876.

doi:10.1016/j.matdes.2010.07.005.

[25] L.P. Connor, R.L. O'Brien, Welding Handbook: Welding technology, American Welding Society, Miami, 1987.

[26] P.T. Hould Croft, Submerged arc welding, 2nd ed., Abington Publishing, Cambridge, England, 1989.

[27] H. Okamoto, The C-Fe (carbon-iron) system, J. Phase Equilibria. 13 (1992) 543–565. doi:10.1007/BF02665767.

[28] D. Yapp, S.A. Blackman, Recent developments in high productivity pipeline welding, J. Brazilian Soc. Mech. Sci. Eng. 26 (2004) 89–97. doi:http://dx.doi.org/10.1590/S1678-58782004000100015.

[29] T. Gladman, Physical metallurgy of microalloyed steels, The Institute of Materials, London, 1997.

[30] N. Shikanai, S. Mitao, S. Endo, Recent Development in microstructural control technologies through the thermo-mechanical control process (TMCP) with JFE steel's high-performance: JFE Technical Report No. 18 Plates, JFE Steel, Tokyo, 2007.

[31] A.A. Gorni, J.H. Dolabela da Silveira, Accelerated cooling of steel plates: The time has come, J. ASTM Int. 5 (2008) 1–7. doi:DOI: 10.1520/JAI101777.

[32] D. Bai, M.A. Cooke, J. Asante, J. Dorricott, Process for making high strength micro-alloy steel, 2004.

[33] T. Hickel, B. Grabowski, F. Körmann, J. Neugebauer, Advancing density functional theory to finite temperatures: methods and applications in steel design, J. Phys. Condens. Matter. 24 (2012) 53202. doi:10.1088/0953-8984/24/5/053202.

[34] M.J. Gaudet, The tensile properties and toughness of microstructures relevant to the HAZ of X80 linepipe steel girth welds, PhD Thesis, University of Britich Columbia, 2015.

[35] K. Venkatesan, R. Sivasankari, V. Balusamy, A. Saxena, P. Jha, R. Datta, Hydrogen-induced cracking in GMA welds of vanadium-titanium microalloyed high strength steel, Mater. Manuf. Process. 25 (2010) 175–179. doi:10.1080/10426910903206766.

[36] R.K. Dayal, N. Parvathavarthini, Hydrogen embrittlement in power plant steels, Sadhana. 28 (2003) 431–451. doi:10.1007/BF02706442.

[37] T. Handeland, E. Erkkila, J. Gjonnes, A combined electron microscope and optical metallographic study of microstructures in high-strength , low-alloy (HSLA) steels after welding, J. Microsc. 144 (1986) 251–259.

[38] R.E. Dolby, Advances in welding metallurgy of steel, Met. Technol. 10 (1983) 349–362.

doi:10.1179/030716983803291172.

[39] S.D. Bhole, A.G. Fox, Influence of GTA welding thermal cycles on hsla-100 steel plate, Can. Metall. Q. 35 (1996) 151–158. doi:http://dx.doi.org/10.1016/0008-4433(95)00047-X.

[40] J. Malina, I. Samardzic, V. Gliha, Susceptibility to hydrogen-induced cracking of weld beads on high-strength structural steel, Mater. Sci. 41 (2005) 253–258. doi:10.1007/s11003-005-0158-y.

[41] P. Deb, K.D. Challenger, D.R. Clark, Transmission electron microscopy characterizations of preheated and non-preheated shielded metal arc weldments of HY-80 steel, Mater. Sci. Eng. 77 (1986) 155–167. doi:10.1016/0025-5416(86)90364-2.

[42] S. Kou, Welding metallurgy, Second Ed., John Wiley & Sons, New Jersey, 2003. doi:10.1016/j.theochem.2007.07.017.

[43] R.E. Dolby, Joining issues for new constructional steels, Sci. Technol. Weld. Join. 5 (2000) 341–346. doi:10.1179/136217100101538407.

[44] T. Taira, K. Matsumoto, Y. Kobayashi, K. Takeshige, I. Kozasu, Development of super tough acicular ferrite steel for linepipe-optimization of carbon and niobium content in low-carbon steel, in: HSLA Steels Technol. Appl. ASM Int., 1984: pp. 723–731.

[45] K. Sampath, An understanding of HSLA-65 plate steels, J. Mater. Eng. Perform. 15 (2006) 32–40. doi:10.1361/105994906X83439.

[46] J. Davis, High-strength structural and high strength aow-alloy steels., 2nd ed., ASM International, 1990.

[47] H. Kimura, N. Yokota, TomoyukiIshikawa, S. Kakihara, J. Kondo, T. Yokota, Development of grade X80 high charpy energy linepipe by MA formation control, in: 11th Int. Pipeline Conf., American Society for Mechanical Engineers, 2016: pp. 1–6.

[48] M. Hudson, Welding of X100 linepipe, PhD Thesis, Cranfield University, 2004.

[49] H.G. Hillenbrand, C. Kalwa, High strength line pipe for project cost reduction, World Pipelines. 2 (2002) 1–10. http://scholar.google.com/scholar?hl=en&btnG=Search&q=intitle:High+strength+line+pipe+for+project+cost+reduction#1.

[50] T. Gladman, I. Mclver, F.B. Pickering, Some aspects of the structure-property relationships in high-carbon ferrite-pearlite steels, J. Iron Steel Inst. 210 (1972) 916–930.

[51] F.B. Pickering, T. Gladman, An investigation into some factors which control th estrength of carbon steels, in: Br. Iron Steel Res. Assoc. Harrogate Conf., 1963.

[52] Y. Smith, A. Coldren, R. Cryderman, Towaard improved ductility and toughness, Climax

Molybdenum C. Ltd., Tokyo, Japan, 1972.

[53] G. Krauss, S.W. Thompson, Ferritic microstructure in continuously cooled low- and ultralow-carbon steels, ISIJ Int. 35 (1995) 937–945.

[54] B. Bramfitt, J. Speer, A perspective on the morphology of bainite, Metall. Mater. Trans. A. 21 (1990) 817–829.

[55] N. Ishikawa, M. Okatsu, J. Shimamura, S. Endo, N. Shikanai, J. Kondo, R. Muraoka, Development and production of ultra-high strength linepipes with dual-phase microstructure for high strain application, in: 26th Int. Conf. Offshore Mech. Arct. Eng., San Diego, California, USA, n.d.: pp. 1–7. doi:10.1115/OMAE2007-29561.

[56] W.W. Bose-Filho, A.L.M. Carvalho, M. Strangwood, Effects of alloying elements on the microstructure and inclusion formation in HSLA multipass welds, Mater. Charact. 58 (2007) 29–39. doi:http://dx.doi.org/10.1016/j.matchar.2006.03.004.

[57] V.B. Da Trindade, J.D.C. Payão, L.F.G. Souza, R.D.R. Paranhos, The role of addition of Ni on the microstructure and mechanical behaviour of C-Mn weld metals, Exacta. 5 (2007) 177–183. doi:10.5585/exacta.v5i1.1037.

[58] B. Beidokhti, A.H. Koukabi, A. Dolati, Effect of titanium addition on the microstructure and inclusion formation in submerged arc welded HSLA pipeline steel, J. Mater. Process. Technol. 209 (2009) 4027–4035. doi:http://dx.doi.org/10.1016/j.jmatprotec.2008.09.021.

[59] G.M. Evans, Microstructure and properties of ferritic steel welds containing Ti and B, Weld. J. 75 (1996) 251s–260s.

[60] M.G. Akben, B. Bacroix, J.J. Jonas, Effect of vanadium and molybdenum addition on high temperature recovery, recrystallization and precipitation behavior of niobium-based microalloyed steels, Acta Metall. 31 (1983) 161–174. doi:http://dx.doi.org/10.1016/0001-6160(83)90076-7.

[61] R. Lagneborg, T. Siwecki, S. Zajac, B. Hutchinson, The role of vanadium in microalloyed steels, Scandanavian J. Metall. (1999) 1–85.

[62] S.S. Hansen, Microalloyed plate and bar products: Production technology, in: Fundam. Microalloying Forg. Steels Proc. an Int. Symp., The Metallurgical Society of AIME, Colorado, 1987: pp. 155–174.

[63] W. Huang, Thermodynamic properties of the Fe-Mn-V-C system, Metall. Trans. A. 22 (1991) 1911–1920. doi:10.1007/BF02669859.

[64] R.A. Ricks, P.R. Howell, G.S. Barritte, The nature of acicular ferrite in HSLA steel weld metals, J. Mater. Sci. 17 (1982) 732–740. doi:10.1007/BF00540369.

[65] R.A. Farrar, P.L. Harrison, Acicular ferrite in carbon-manganese weld metals: An overview, J. Mater. Sci. 22 (1987) 3812–3820. doi:10.1007/BF01133327.

[66] S.S. Tuliani, T. Boniszewski, N.F. Eaton, Notch toughness of commercial submerged-arc weld metal, Weld. Met. Fabr. 37 (1969) 327–339.

[67] Z. Tang, W. Stumpf, The role of molybdenum additions and prior deformation on acicular ferrite formation in microalloyed Nb-Ti low-carbon line-pipe steels, Mater. Charact. 59 (2008) 717–728. doi:10.1016/j.matchar.2007.06.001.

[68] F. Xiao, B. Liao, D. Ren, Y. Shan, K. Yang, Acicular ferritic microstructure of a low-carbon Mn–Mo–Nb microalloyed pipeline steel, Mater. Charact. 54 (2005) 305–314. doi:10.1016/j.matchar.2004.12.011.

[69] W.B. Lee, S.G. Hong, C.G. Park, K.H. Kim, S.H. Park, Influence of Mo on precipitation hardening in hot rolled HSLA steels containing Nb, Scr. Mater. 43 (2000) 319–324. doi:http://dx.doi.org/10.1016/S1359-6462(00)00411-5.

[70] R. Uemori, R. Chijiiwa, H. Tamehiro, H. Morikawa, AP-FIM study on the effect of Mo addition on microstructure in Ti-Nb steel, Appl. Surf. Sci. 76 (1994) 255–260. doi:http://dx.doi.org/10.1016/0169-4332(94)90351-4.

[71] H.-W. Yen, C.-Y. Huang, J.-R. Yang, Characterization of interphase-precipitated nanometer-sized carbides in a Ti–Mo-bearing steel, Scr. Mater. 61 (2009) 616–619. doi:http://dx.doi.org/10.1016/j.scriptamat.2009.05.036.

[72] E.P. McDonald, Factors influencing the microstructure and mechanical properties of ultra low carbon bainitic 100 tungsten inert gas multipass weldments, PhD Thesis, University of Utah, 1992.

[73] M. Kutz, Handbook of Materials Selection, John Wiley & Sons, Now York, USA, 2002.

[74] D.D. Crockett, J.A. Rhone, R.F. Young, D.C. Noernberg, Design considerations for submerged arc consumables intended for the manufacture of line pipe, Pipeline Eng. 1 (1995) 151–162.

[75] E. Surian, J. Trotti, A. Cassanelli, L. De Vedia, Influence of chromium on the mechanical properties and microstructure of weld metal from a high strength SMA electrode, Weld. J. 73 (1994) 45–s–53–s.

[76] M.H. Avazkonandeh-Gharavol, M. Haddad-Sabzevar, A. Haerian, Effect of chromium content on the microstructure and mechanical properties of multipass MMA, low alloy steel weld metal, J. Mater. Sci. 44 (2009) 186–197. doi:10.1007/s10853-008-3103-2.

[77] B. Beidokhti, A. Dolati, A.H. Koukabi, Effects of alloying elements and microstructure on the susceptibility of the welded HSLA steel to hydrogen-induced cracking and sulfide stress

cracking, Mater. Sci. Eng. A. 507 (2009) 167–173. doi:http://dx.doi.org/10.1016/j.msea.2008.11.064.

[78] J. Amanie, Effect of submerged arc welding parameters on the microstructure of SA516 and A709 steel welds, PhD Thesis, University of Saskatchewan, Saskatoon, Canada, 2011.

[79] H.K.D.H. Bhadeshia, Some phase transformations in steels, Mater. Sci. Technol. 15 (1999) 22–29. doi:10.1179/026708399773002773.

[80] K.E. Easterling, Introduction to the physical metallurgy of welding, Butterworth-Heinemann Ltd, Oxford, 1992.

[81] B. De Meester, The weldability modern structural TMCP steels, ISIJ Int. 37 (1997) 537–551.

[82] M.D. Herynk, S. Kyriakides, A. Onoufriou, H.D. Yun, Effects of the UOE/UOC pipe manufacturing processes on pipe collapse pressure, Int. J. Mech. Sci. 49 (2007) 533–553. doi:http://dx.doi.org/10.1016/j.ijmecsci.2006.10.001.

[83] M. Fraldi, F. Guarracino, Towards an accurate assessment of UOE pipes under external pressure: Effects of geometric imperfection and material inhomogeneity, Thin-Walled Struct. 63 (2013) 147–162. doi:http://dx.doi.org/10.1016/j.tws.2012.10.007.

[84] Europipe, UOE manufacturing diagram, http://www.europipe.com/102-1-UOE-Process.html, 2014.

[85] J.Y. Koo, M.J. Luton, N.V. Bangaru, R.A. Petkovic, D.P. Fairchild, C.W. Petersen, H. Asahi, T. Hara, Y. Terada, M. Sugiyama, H. Tamehiro, Y. Komizo, S. Okaguchi, M. Hamada, A. Yamamoto, I. Takeuchi, Metallurgical design of ultra high-strength steels for gas pipelines, Int. J. Offshore Polar Eng. 14 (2004) 2–10.

[86] C.L. Jenney, A. O'Brien, Welding handbook, 1991.

[87] K.-H. Brensing, B. Sommer, Steel tube and pipe manufacturing processes, Salzgitter GroBrohre GmbH, n.d.

[88] D.-W. Cho, W.-H. Song, M.-H. Cho, S.-J. Na, Analysis of submerged arc welding process by three-dimensional computational fluid dynamics simulations, J. Mater. Process. Technol. 213 (2013) 2278–2291. doi:10.1016/j.jmatprotec.2013.06.017.

[89] B.Y.R.S. Chandel, Mathematical modeling of melting rates for submerged arc welding, Weld. Res. Suppliment. (1987) 135s–140s.

[90] D.V. Kiran, S.-J. Na, Experimental studies on submerged arc welding process, J. Korean Weld. Join. Soc. 32 (2014) 1–10. doi:10.5781/JWJ.2014.32.3.1.

[91] B.G. Renwick, B.M. Patchett, Operating characteristics of the submerged arc process, Weld. Journal, Res. Suppl. 55 (1976).

[92] Lincoln-Electric, The Procedure Handbook of Arc Welding, Lincoln Electric Company, Ohio, 1995.

[93] D.W. Nugent, R.M., Dybas, R.J., Hunt, J.F., Meyer, Submerged arc welding. AWS Welding Handbook, 8th Ed., American Welding Society, Miami, 2009.

[94] J.T. Pepin, Effects of submerged arc weld (SAW) parameters on bead geometry and notch-toughness for X70 and X80 linepipe steels, MSc Thesis, University of Alberta, 2009.

[95] S. Massey, Increasing productivity with submerged arc welding, Edison Welding Institute, Columbus, 2012.

[96] T. Tsuyama, K. Nakai, T. Tsuji, Development of submerged arc welding method using hot wire, Weld. World. 58 (2014) 713–718. doi:10.1007/s40194-014-0153-8.

[97] S. Kenny, University of Alberta welding projects: Review and path forward, 2013.

[98] S. Nand, P.K. Singh, Effect of addition of metal powder on deposition rate, mechanical properties and metallographic property of weld joints during submerged arc welding process, J. Mach. Form. Technol. 6 (2014) 159–168.

[99] L. Devillers, D. Kaplan, C. Donaldille, P.V. Riboud, Advances in welding science and technology, in: Int. Conf. Trends Weld. Res., Americal Society of Metals, Tennessee, USA, 1986: pp. 609–613.

[100] Z.H. Xia, X.L. Wan, X.L. Tao, K.M. Wu, Effect of heat input on toughness of coarse-grained heat-affected zone of an ultra low carbon acicular ferrite steel, Adv. Mater. Res. 538–541 (2012) 2003–2008. doi:10.4028/www.scientific.net/AMR.538-541.2003.

[101] D.M. Viano, N.U. Ahmed, G.O. Schumann, D.M. Viano, N.U. Ahmed, G.O. Schumann, Influence of heat input and travel speed on microstructure and mechanical properties of double tandem submerged arc high strength low alloy steel weldments, 5 (2013) 26–34. doi:10.1179/stw.2000.5.1.26.

[102] G.-L. Liang, S.-W. Yang, H.-B. Wu, Microstructure and mechanical performances of CGHAZ for oil tank steel during high heat input welding, Rare Met. 32 (2013) 129–133. doi:10.1007/s12598-013-0036-y.

[103] C.B. Dallam, S. Liu, D.L. Olson, Flux Composition dependence Of microstructure and toughness of submerged arc HSLA weldments, Weld. J. 64(5) (1985) 140–s–151–s.

[104] H.S. Randhawa, P.. K. Ghosh, S.R. Gupta, Geometrical characteristics of pulsed current positional GMA weld, ISIJ Int. 38 (1998) 276–284.

[105] M.F. Ashby, K.E. Easterling, A first report on diagrams for grain growth in welds, Acta Metall. 30 (1982) 1969–1978.

[106] L.E. Collins, M.J. Godden, J.D. Boyd, Microstructures of linepipe steels, Can. Metall. Q. 22 (1983) 169–179. doi:10.1179/cmq.1983.22.2.169.

[107] O. Grong, D.K. Matlock, Microstructural development in mild and low-alloy steel weld metals, Int. Met. Rev. 31 (1986) 27–48. doi:10.1179/imtr.1986.31.1.27.

[108] D.J. Abson, R.J. Pargeter, Factors influencing as-deposited strength, microstructure, and toughness of manual metal arc welds suitable for C-Mn steel fabrications, Int. Met. Rev. 31 (1986) 141–196. doi:10.1179/imtr.1986.31.1.141.

[109] J.R. Yang, Development of microstructure in high strength weld deposits, PhD Thesis, Trinity College, Cambridge, United Kingdom, 1987.

[110] N.A. Fleck, G.R. Grong, G.R. Edwards, D.K. Matlock, The role of filler metal wire and flux composition in submerged arc weld metal transformation kinetics, Weld. J. 65 (1986) 113s–121s.

[111] R.W.K. Honeycombe, H.K.D.H. Bhadeshia, Steels: Microstructure and paroperties, Metallurgy and Materials Science Series, Edward Arnold, London, Great Britain, 1996.

[112] H.K.D.H. Bhadeshia, L.E. Svensson, Modelling the evolution of microstructure in steel weld metal, Math. Model. Weld Phenomena, Eds Cerjak, H., Easterling E.K., Inst. Mater. London. (1993) 109–182.

[113] J.E. Indacochea, M. Blander, S. Shah, Submerged arc welding: Evidence for electrochemical effects on the weld pool, Weld. J. 68 (1989) 77s–83s.

[114] H.K.D.H. Bhadeshia, Steels: Microstructure and properties, 3rd ed., Butterworth-Heinemann Ltd, Cambridge, England, 2006.

[115] H.K.D.H. Bhadeshia, Control of weld metal microstructure and properties, in: INT'L Conf. Metall. Weld. Qualif. Microalloyed Steel Weldments, American Welding Society, Houston, Texas, USA, 1990: pp. 34–69.

[116] A.E. Amer, M.Y. Koo, K.H. Lee, S.H. Kim, S.H. Hong, Effect of welding heat input on microstructure and mechanical properties of simulated HAZ in Cu containing microalloyed steel, J. Mater. Sci. 45 (2010) 1248–1254. doi:10.1007/s10853-009-4074-7.

[117] Z. Zhu, J. Han, H. Li, Influence of heat input on microstructure and toughness properties in simulated CGHAZ of X80 steel manufactured using high-temperature processing, Metall. Mater. Trans. A. 46 (2015) 5467–5475. doi:10.1007/s11661-015-3122-y.

[118] C. Thaulow, A.J. Paauw, K. Guttormsen, The heat-affected zone toughness of low-carbon microalloyed steels, Weld. Res. Suppl. (1987) 266s–279s.

[119] K. Poorhaydari-Anaraki, Microstructure and property examination of the weld HAZ in grade

100 microalloyed steel, PhD Thesis, University of Alberta, Edmonton, Canada, 2005.

[120] S. Moeinifar, Microstructure and toughness properties of subcritically, intercritically and supercritically heat affected zones in X80 microalloyed pipeline steel, Adv. Mater. Res. 383–390 (2011) 5886–5893. doi:10.4028/www.scientific.net/AMR.383-390.5886.

[121] N. Ishikawa, T. Shinmiya, S. Igi, J. Kondo, Toughness evaluation on seam weld HAZ of high strength UOE linepipe, in: 6th Int. Pipeline Conf., American Society for Mechanical Engineers, Calgary, AB, Canada, n.d.: pp. 223–230.

[122] Z. Zhu, L. Kuzmikova, H. Li, F. Barbaro, Effect of inter-critically reheating temperature on microstructure and properties of simulated inter-critically reheated coarse grained heat affected zone in X70 steel, Mater. Sci. Eng. A. 605 (2014) 8–13. doi:http://dx.doi.org/10.1016/j.msea.2014.03.034.

[123] Z. Zhu, L. Kuzmikova, H. Li, F. Barbaro, The effect of chemical composition on microstructure and properties of intercritically reheated coarse-grained heat-affected zone in X70 steels, Metall. Mater. Trans. B. 45 (2014) 229–235. doi:10.1007/s11663-013-0008-5.

[124] H.I. McHenry, J.M. Potter, Fatigue and fracture testing of weldments, ASM International, Philadelphia, USA, 1990.

[125] T. Haze, Metallurgical factors controlling HAZ toughness in HT50 steels, International Institute of Welding, Tokyo, Japan, 1986.

[126] B. Silwal, L. Li, A. Deceuster, B. Griffiths, Effect of postweld heat treatment on the toughness of heat-affected zone for grade 91 steel, Weld. Res. 92 (2013) 80s–87s.

[127] J.-B. Ju, W. Kim, J. Jang, Variations in DBTT and CTOD within weld heat-affected zone of API X65 pipeline steel, Mater. Sci. Eng. A. 546 (2012) 258–262. doi:http://dx.doi.org/10.1016/j.msea.2012.03.062.

[128] C.L. Davis, J.E. King, Cleavage initiation in the intercritically reheated coarse-grained heat-affected zone : Part I . Fractographic evidence, Metall. Mater. Trans. A. 25 (1994) 563–573. doi:10.1007/BF02651598.

[129] X. Li, Y. Fan, X. Ma, S.V. Subramanian, C. Shang, Influence of martensite-austenite constituents formed at different intercritical temperatures on toughness, Mater. Des. 67 (2015) 457–463. doi:10.1016/j.matdes.2014.10.028.

[130] T. Taira, K. Matsumoto, Y. Kobayashi, K. Takeshige, I. Kozasu, Development of super-tough acicular ferrite steel for line pipe--optimization of carbon and niobium content in low-carbon steel, in: HSLA Steels, Technol. Appl., American Society for Metals, 1984: pp. 723–731.

[131] K. Poorhaydari, B.M. Patchett, D.G. Ivey, TEM Microstructure examination of weld HAZ in

microalloyed steels, in: Microacopy Microanal., Microscopy Society of America, 2002: pp. 1252–1253. doi:10.1017.S1431927602104697.

[132] E.T. Turkdogan, Fundamental of steelmaking, The Institute of Materials, London, England, 1996.

[133] C. Wagner, Thermodynamics of alloys, Addison-Wesley Co., Readings, Mass, 1952.

[134] G. Krauss, S.W. Thompson, Ferritic microstructures in continuously cooled low- and ultralow-carbon steels, ISIJ Int. 35 (1995) 937–945. doi:10.2355/isijinternational.35.937.

[135] Z.G. Yang, H.S. Fang, An overview on bainite formation in steels, Curr. Opin. Solid State Mater. Sci. 9 (2005) 277–286. doi:http://dx.doi.org/10.1016/j.cossms.2006.06.005.

[136] L.E. Collins, D. Bai, F. Hamad, C. Xiande, High strength spiral linepipe for strain-based pipeline designs, in: 17th Int. Offshore Polar Eng. Conf., International Society of Offshore and Polar Engineers, Lisbon, Portugal, 2007: pp. 2969–2975.

[137] K.W. Andrews, Empirical formulas for the calculation of some transformation temperatures, J. Iron Steel Inst. 203 (1965) 721–727.

[138] J. Trzaska, Calculation of critical temperatures by empirical formulae, Arch. Metall. Mater. 61 (2016) 981–986. doi:10.1515/amm-2016-0167.

[139] H.K.D.H. Bhadeshia, About calculating the characteristics of the martensite-austenite constituent, in: Int. Semin. Weld. High Strength Pipeline Steels, CBMM and The Minerals, Metals and Materials Society, The Minerals, Metals and Materials Society (TMS), USA, 2013: pp. 99–106.

[140] F.S. LePera, Improved etching technique for the determination of percent martensite in high-strength dual-phase steels, Metallography. 12 (1979) 263–268. doi:10.1016/0026-0800(79)90041-7.

[141] M. Mohammadijoo, H. Henein, D.G. Ivey, Microstructural characterization of the HAZ in welded microalloyed steels, in: Microsc. Soc. Canada 43rd Annu. Meet., Edmonton, AB, 2016: pp. 68–69.

[142] E. Curiel-Reyna, A. Herrera, V. Castaño, M.E. Rodríguez, Influences of the precooling treatment in the heat affected zone of the welding in a used hadfield-type steel, Mater. Manuf. Process. 21 (2006) 573–578. doi:10.1080/10426910600599380.

[143] S. Moeinifar, A.H. Kokabi, H.R. Madaah Hosseini, Influence of peak temperature during simulation and real thermal cycles on microstructure and fracture properties of the reheated zones, Mater. Des. 31 (2010) 2948–2955. doi:10.1016/j.matdes.2009.12.023.

[144] R.S. Chandel, S.R. Bala, Cooling time and features of submerged arc weld beads, Weld. Res.

Suppl. (1985) 201s–208s.

[145] A.K. Das, The present and the future of line pipe steels for petroleum industry, Mater. Manuf. Process. 25 (2010) 14–19. doi:10.1080/10426910903202427.

[146] F.R. Xiao, B. Liao, Y.Y. Shan, G.Y. Qiao, Y. Zhong, C. Zhang, K. Yang, Challenge of mechanical properties of an acicular ferrite pipeline steel, Mater. Sci. Eng. A. 431 (2006) 41–52. doi:http://dx.doi.org/10.1016/j.msea.2006.05.029.

[147] V. Gliha, T. Vuherer, B. Ule, J. Vojvodic-Tuma, Fracture resistance of simulated heat affected zone areas in HSLA structural steel, Sci. Technol. Weld. Join. 9 (2004) 399–406. doi:10.1179/136217104225021698.

[148] S. Moeinifar, Influence of thermal simulated and real tandem submerged arc welding process on the microstructure and mechanical properties of the coarse-grained heat-affected zone, Mater. Manuf. Process. 26 (2011) 1423–1429. doi:10.1080/10426914.2010.544827.

[149] S. Shen, I.N.A. Oguocha, S. Yannacopoulos, Effect of heat input on weld bead geometry of submerged arc welded ASTM A709 Grade 50 steel joints, J. Mater. Process. Technol. 212 (2012) 286–294. doi:10.1016/j.jmatprotec.2011.09.013.

[150] German-Welding-Society, European Welding Engineer Education Course, DVS-EWF1173, 2001.

[151] The-Welding-Institute, Job Knowledge for Welders: Submerged Arc Welding, 2004.

[152] J. Lancaster, Metallurgy of welding, Allen&Unwin Publishing, London, UK, 1987.

[153] IIS, Welding Engineering Qualification Course, Chapter 3-5, 2003.

[154] J.Y. Koo, M.J. Luton, N.V. Bangaru, R.A. Petkovic, Metallurgical design of ultra-high strength steels for gas pipelines, in: 13th Int. Offshore Polar Eng. Conf., Honolulu, Hawaii, USA, n.d.: pp. 10–18.

[155] H. Tamehiro, H. Asahi, T. Hara, Y. Terada, M.J. Luton, J. Koo, Ultra-high strength, weldable steels with excellent ultra-low temperature toughness, 2001.

[156] J.W. Morris, Stronger, tougher steels, Science (80-.). 320 (2008) 1022.

[157] O. Onal, B. Bal, S.M. Toker, M. Mirzajanzadeh, D. Canadinc, H.J. Maier, Microstructure-based modeling of the impact response of a biomedical niobium–zirconium alloy, J. Mater. Res. 29 (2014) 1123–1134. doi:10.1557/jmr.2014.105.

[158] G.S. Rohrer, Introduction to grains, phases, and interfaces—an interpretation of microstructure, Trans. AIME, 1948, vol. 175, pp. 15–51, by C.S. Smith, Metall. Mater. Trans. A. 41 (2010) 1063–1100. doi:10.1007/s11661-010-0215-5.

[159] C.S. Smith, Grains, phases, and interfaces: An interpretation of microstructure, Met. Technol.

(Reprinted Metall. Mater. Trans. B 2010). 15 (1948) 1–37.

[160] Y.T. Pan, J.L. Lee, Development of TiOx-bearing steels with superior heat-affected zone toughness, Mater. Des. 15 (1994) 331–338. doi:http://dx.doi.org/10.1016/0261-3069(94)90027-2.

[161] S. Kumar, S.K. Nath, V. Kumar, Continuous cooling transformation behavior in the weld coarse grained heat affected zone and mechanical properties of Nb-microalloyed and HY85 steels, Mater. Des. 90 (2016) 177–184. doi:http://dx.doi.org/10.1016/j.matdes.2015.10.071.

[162] B. Hutchinson, J. Komenda, G.S. Rohrer, H. Beladi, Heat affected zone microstructures and their influence on toughness in two microalloyed HSLA steels, Acta Mater. 97 (2015) 380–391. doi:doi:10.1016/j.actamat.2015.05.055.

[163] S. Liu, D.L. Olson, The influence of inclusion chemical composition on weld metal microstructure, J. Mater. Eng. 9 (1987) 237–251. doi:10.1007/BF02834144.

[164] S. Liu, D.L. Olson, The role of inclusions in controlling HSLA steel weld microstructures, Weld. J. Res. Suppl. (1986) 139s–149s.

[165] E.M. Fedoseeva, V.M. Yazovskikh, Properties and structure formation in welded joints when welding steel X65 by different technologies, Metallurgist. 60 (2016) 69–75. doi:10.1007/s11015-016-0253-3.

[166] M. Mohammadijoo, S. Kenny, L. Collins, H. Henein, D.G. Ivey, Effect of cold-wire addition in the TSAW process on microstructure and mechanical properties of the HAZ of X70 microalloyed pipeline steel, Am. Soc. Mech. Eng. 3 (2016) 1–9. doi:10.1115/IPC2016-64549.

[167] F. Matsuda, K. Ikeuchi, Y. Fukada, Y. Horii, H. Okada, T. Shiwaku, C. Shiga, S. Suzuki, Review of mechanical and metallurgical investigations of M-A constituents in welded joint in Japan, Transcations JWRI. 24 (1995) 1–24.

[168] E. Bonnevie, G. Ferrière, A. Ikhlef, D. Kaplan, J.M. Orain, Morphological aspects of martensite–austenite constituents in intercritical and coarse grain heat affected zones of structural steels, Mater. Sci. Eng. A. 385 (2004) 352–358. doi:http://dx.doi.org/10.1016/j.msea.2004.06.033.

[169] J.H. Chen, Y. Kikuta, T. Araki, M. Yoneda, Y. Matsuda, Micro-fracture behaviour induced by M-A constituent (Island Martensite) in simulated welding heat affected zone of HT80 high strength low alloyed steel, Acta Metall. 32 (1984) 1779–1788. doi:http://dx.doi.org/10.1016/0001-6160(84)90234-7.

[170] L. Lan, C. Qiu, D. Zhao, X. Gao, L. Du, Microstructural characteristics and toughness of the simulated coarse grained heat affected zone of high strength low carbon bainitic steel, Mater.

Sci. Eng. A. 529 (2011) 192–200. doi:http://dx.doi.org/10.1016/j.msea.2011.09.017.

[171] X.Y. Long, J. Kang, B. Lv, F.C. Zhang, Carbide-free bainite in medium carbon steel, Mater. Des. 64 (2014) 237–245. doi:http://dx.doi.org/10.1016/j.matdes.2014.07.055.

[172] L. Lan, C. Qiu, D. Zhao, Analysis of martensite-austenite constituent and its effect on toughness in submerged arc welded joint of low carbon bainitic steel, J. Mater. Sci. 47 (2012) 4732–4742. doi:10.1007/s10853-012-6346-x.

[173] X. Zhang, H. Gao, X. Zhang, Y. Yang, Effect of volume fraction of bainite on microstructure and mechanical properties of X80 pipeline steel with excellent deformability, Mater. Sci. Eng. A. 531 (2012) 84–90. doi:http://dx.doi.org/10.1016/j.msea.2011.10.035.

[174] K. Nakai, T. Sakamoto, R. Asakura, Y. Kotani, N. Isomura, S. Kobayashi, M. Hamada, Y.I. Komizo, Nucleation of bainite at small angle dislocation network in austenite and its effects on mechanical properties in steels, ISIJ Int. 51 (2011) 274–279. doi:10.2355/isijinternational.51.274.

[175] P. Mohseni, J.K. Solberg, M. Karlsen, O.M. Akselsen, E. Østby, Cleavage Fracture initiation at M–A constituents in intercritically coarse-grained heat-affected zone of a HSLA steel, Metall. Mater. Trans. A. 45 (2014) 384–394. doi:10.1007/s11661-013-2110-3.

[176] K. Ohya, J. Kim, K. Yokoyama, M. Nagumo, Microstructures relevant to brittle fracture initiation at the heat-affected zone of weldment of a low carbon steel, Metall. Mater. Trans. A. 27 (1996) 2574–2582. doi:10.1007/BF02652351.

[177] X. Li, X. Ma, S.V. Subramanian, C. Shang, R.D.K. Misra, Influence of prior austenite grain size on martensite-austenite constituent and toughness in the heat affected zone of 700MPa high strength linepipe steel, Mater. Sci. Eng. A. 616 (2014) 141–147. doi:10.1016/j.msea.2014.07.100.

[178] Y. Li, T.N. Baker, Effect of morphology of martensite-austenite phase on fracture of weld heat affected zone in vanadium and niobium microalloyed steels, Mater. Sci. Technol. 26 (2010) 1029–1040. doi:10.1179/026708309X12512744154360.

[179] G.R. Irwin, Analysis of stresses and strains near the end of a crack traversing a plate, J. Appl. Mech. 27 (1957) 361–364.

[180] J.R. Rice, A path independent integral and the approximate analysis of strain concentrations by notches and cracks, J. Appl. Mech. 35 (1968) 379–386.

[181] A.A. Wells, Application of fracture mechanics at and beyond general yielding, Weld. J. 10 (1963) 563–570.

[182] D.P. Fairchild, S.A. Kibey, H. Tang, V.R. Krishnan, X. Wang, M.L. Macia, W. Cheng, Continued

advancements regarding capacity predicition of strain-based pipelines, in: 9th Int. Pipeline Conf., American Society for Mechanical Engineers, Calgary, Alberta, Canada, 2012: pp. 24–28.

[183] T.L. Anderson, Fracture mechanics- fundamentals and applications, Taylor & Francis, Boca Raton, 2005.

[184] D.E. McCabe, Evaluation of the compact tension specimen for determining plane-strain fracture toughness of high strength materials, J. Mater. Sci. 7 (1972) 449–542.

[185] J.H. Underwood, D.P. Kendall, Cooperative plane strain fracture toughness tests with C-shaped specimens, J. Test. Eval. 6 (1978) 296–300.

[186] R.H. Heyer, D.E. McCabe, Evaluation of a test method for plane-strain fracture toughness using a bend specimen. In: Review of developments in plane-strain fracture toughness. ASTM STP 463 testing, Am. Soc. Test. Mater. (1970) 22–41.

[187] ASTM, ASTM E1820-13: Standard test method for measurement of fracture toughness, ASTM International, Conshohocken, PA, USA, 2013.

[188] British-Standard, BS 7448-1: Fracture mechanics toughness tests - Part 1: Method for determination of KIc, critical CTOD and critical J values of metallic materials, British Standard Institute (BSI), 1991.

[189] ISO, ISO-12735: Metallic Materials - Determination of plane-strain fracture toughness, International Organization for Standardization, 2010.

[190] Det-Norske-Veritas, Control for pipeline installation methods introducing cyclic plastic strain, 2006.

[191] Canmet-Materials, Recommended practice: Fracture toughness testing using SE(T) samples with fixed-grip loading, 2010.

[192] D.-Y. Park, J.-P. Gravel, M. Arafin, J. Liang, C. Hari Manoj Simha, Evaluation of two low-constraint toughness test methods in a single specimen, J. Eng. Mater. Technol. 137 (2014) 11003. http://dx.doi.org/10.1115/1.4028728.

[193] ExxonMobil, Measurement of crack tip opening displacement (CTOD) - Fracture resistance curves using single-edge notched tension (SENT) specimens, 2010.

[194] P.B.S. Kirk, V. Chum, Practical application of low constraint SENT fracture toughness testing for pipeline girth welds, in: 10th Int. Pipeline Conf., 2014: pp. 1–11.

[195] S. Cravero, C. Ruggieri, Estimation procedure of J-resistance curves for SE(T) fracture specimens using unloading compliance, Eng. Fract. Mech. 74 (2007) 2735–2757. doi:10.1016/j.engfracmech.2007.01.012.

[196] D.-Y. Park, J.-P. Gravel, C. Hari Manoj Simha, J. Liang, D.-M. Duan, Low-constraint toughness

testing of two single-edge notched tension methods in a single specimen, J. Press. Vessel Technol. 138 (2016) 51401. doi:10.1115/1.4032998.

[197] X. -k. Zhu, Review of fracture toughness test methods for ductile materials in low-constraint conditions, Int. J. Press. Vessel. Pip. 139–140 (2016) 173–183.

[198] G. Shen, J.A. Gianetto, W.R. Tyson, Measurement of J-R curves using single-specimen technique on clamped SE(T) specimens, in: 19th Int. Offshore Polar Eng. Conf., Osaka, Japan, 2009.

[199] D.-Y. Park, J.P. Gravel, M. Arafin, J. Liang, C. Hari Manoj Simha, Evaluation of two low-constraint toughness test methods in a single specimen, J. Eng. Mater. Technol. 137 (2015) 11003-1-11003–9. doi:10.1115/1.4028728.

[200] H. Pisarski, P. Moore, E. Hutchison, Development of a British standard single edge notch tension (SENT) test method (BS8571), in: 6th Int. Pipeline Technol. Conf., Ostend, Belgium, n.d.

[201] T.S. Weeks, E. Lucon, Direct comparison of single-specimen clamped SE(T) test methods on X100 line pipe steel, in: 10th Int. Pipeline Conf., American Society for Mechanical Engineers, Calgary, Alberta, Canada, n.d.: pp. 1–16.

[202] D.W. Nugent, R.M., Dybas, R.J., Hunt, J.F., Meyer, Submerged arc welding. AWS Welding Handbook, 8th Ed., American Welding Society, Miami, 2009.

[203] L.P. Connor, R.L. O'Brien, Welding Handbook: Welding Technology, American Welding Society, Miami, 1987.

[204] G. Taguchi, A.J. Rafanelli, Taguchi on robust technology development: Bringing quality engineering upstream, J. Electron. Packag. 116 (1994) 161. doi:10.1115/1.2905506.

[205] ASTM, E3-11: Standard guide for preparation of metallographic specimens, ASTM International, PA, 2011. doi:10.1520/E0003-11.2.

[206] R.A. Fisher, Statistical methods for research workers., Q. J. R. Meteorol. Soc. 82 (1956) 119–119. doi:10.1002/qj.49708235130.

[207] D.C. Montgomery, Design and analysis of experiments, 7th Edition, 2009.

[208] J.E.R. Dhas, S. Kumanan, Optimization of parameters of submerged arc weld using non conventional techniques, Appl. Soft Comput. J. 11 (2011) 5198–5204. doi:10.1016/j.asoc.2011.05.041.

[209] Y.S.S. Tarng, S.C.C. Juang, C.H.H. Chang, The use of grey-based Taguchi methods to determine submerged arc welding process parameters in hardfacing, J. Mater. Process. Technol. 128 (2002) 1–6. doi:10.1016/S0924-0136(01)01261-4.

[210] R. Roy, A primer on the taguchi method, Van Norstrand Reinhold, New York, 1990.

[211] L.J. Yang, R.S. Chandel, M.J. Bibby, An analysis of curvilinear regression equations for modeling the submerged-arc welding process, J. Mater. Process. Tech. 37 (1993) 601–611. doi:10.1016/0924-0136(93)90121-L.

[212] L.J. Yang, R.S. Chandel, M.J. Bibby, The effects of process variables on the bead width of submerged-arc weld deposits, J. Mater. Process. Tech. 29 (1992) 133–144. doi:10.1016/0924-0136(92)90430-Z.

[213] S.R.A. Fisher, The design of experiments, Hafner Publ. Co. (1971) 1–27.

[214] S.F. Arnold, Design of experiments with MINITAB, 2006. doi:10.1198/tas.2006.s46.

[215] ASTM, E384-11: Standard test method for knoop and vickers hardness of materials, ASTM International, PA, 2012. doi:10.1520/E0384-11E01.2.

[216] D.P. Koistinen, R.E. Marburger, A general equation prescribing the extent of the austenite-martensite transformation in pure iron-carbon alloys and plain carbon steels, Acta Metall. 7 (1959) 59–60. doi:10.1016/0001-6160(59)90170-1.

[217] H.S. Yang, H.K.D.H. Bhadeshia, Austenite grain size and the martensite-start temperature, Scr. Mater. 60 (2009) 493–495. doi:10.1016/j.scriptamat.2008.11.043.

[218] L. Yu, H.H. Wang, T.P. Hou, X.L. Wang, X.L. Wan, K.M. Wu, Characteristic of martensite-austenite constituents in coarse grained heat affected zone of HSLA steel with varying Al contents, Sci. Technol. Weld. Join. 19 (2014) 708–714. doi:10.1179/1362171814Y.0000000246.

[219] C. Heinze, A. Pittner, M. Rethmeier, S.S. Babu, Dependency of martensite start temperature on prior austenite grain size and its influence on welding-induced residual stresses, Comput. Mater. Sci. 69 (2013) 251–260. doi:10.1016/j.commatsci.2012.11.058.

[220] Y. Prawoto, N. Jasmawati, K. Sumeru, Effect of prior austenite grain size on the morphology and mechanical properties of martensite in medium carbon steel, J. Mater. Sci. Technol. 28 (2012) 461–466. doi:10.1016/S1005-0302(12)60083-8.

[221] J.C. Fisher, J.H. Hollomon, D. Turnbull, Kinetics of the austenite-martensite transformation, Trans. Am. Inst. Min. Metall. Eng. 185 (1949) 691–700.

[222] D.M. Viano, N.U. Ahmed, G.O. Schumann, D.M. Viano, N.U. Ahmed, G.O. Schumann, Influence of heat input and travel speed on microstructure and mechanical properties of double tandem submerged arc high strength low alloy steel weldments, Sci. Technol. Weld. Join. 5 (2000) 26–34. doi:10.1179/stw.2000.5.1.26.

[223] Y. Watanabe, K. Yoshii, Y. Yoshida, Development of 590N/mm2 steel with good weldability

for building structures, Technichal Report No. 90, 2004.

[224] Y.Q. Zhang, H.Q. Zhang, J.F. Li, W.M. Liu, Effect of heat input on microstructure and toughness of coarse grain heat affected zone in Nb microalloyed HSLA steels, J. Iron Steel Res. Int. 16 (2009) 73–80. doi:10.1016/S1006-706X(10)60014-3.

[225] Z.H. Xia, X.L. Wan, X.L. Tao, K.M. Wu, Effect of heat input on toughness of coarse-grained heat-affected zone of an ultra low carbon acicular ferrite steel, Adv. Mater. Res. 538–541 (2012) 2003–2008. doi:10.4028/www.scientific.net/AMR.538-541.2003.

[226] C.L. Davis, J.E. King, Effect of cooling rate on intercritically reheated microstructure and toughness in high strength low alloy steel, Mater. Sci. Technol. 9 (1993) 8–15.

[227] J.M. Reichert, T. Garcin, M. Militzer, W.J. Poole, A new approach using EBSD to quantitatively distinguish complex transformation products along the HAZ in X80 linepipe steel, in: 9th Int. Pipeline Conf., American Society of Mechanical Engineering, Calgary, AB, 2014.

[228] E. Gharibshahiyan, A. Honarbakhsh, N. Parvin, M. Rahimian, The effect of microstructure on hardness and toughness of low carbon welded steel using inert gas welding, Mater. Des. 32 (2011) 2042–2048. doi:10.1016/j.matdes.2010.11.056.

[229] A. Garcia-Junceda, C. Capdevila, F.G. Caballero, C. Garcia, D. Andre, Dependence of martensite start temperature on fine austenite grain size, Scr. Mater. 58 (2008) 134–137. doi:10.1016/j.scriptamat.2007.09.017.

[230] M.F. Mruczek, P.J. Konkol, Cold wire feed submerged arc welding: Technical Report, Advanced Technology Institute (ATI), Johnstown, PA, 2006.

[231] M. Mohammadijoo, S. Kenny, J.B. Wiskel, D.G. Ivey, H. Henein, Cold-wire tandem submerged arc welding: A novel technique for pipeline manufacturing, in: 54th Anuual Conf. Metall., Canadian Institute of Mining, Metallurgy and Petroleum, Toronto, ON, 2015: pp. 1–13.

[232] M. Mohammadijoo, S. Kenny, L. Collins, H. Henein, D.G. Ivey, Influence of cold-wire tandem submerged arc welding parameters on weld geometry and microhardness of microalloyed pipeline steels, Int. J. Adv. Manuf. Technol. (2016). doi:10.1007/s00170-016-8910-z.

[233] ASTM, ASTM E23-12C: Standard test methods for notched bar impact testing of metallic materials, ASTM International, PA, 2012.

[234] ASTM, E384: Standard test method for knoop and vickers hardness of materials, ASTM International, PA, 2012. doi:10.1520/E0384-11E01.2.

[235] ASTM, E112-12: Standard test methods for determining average grain size, ASTM International, PA, 2012. doi:10.1520/E0112-12.1.4.

[236] ASTM, ASTM E562-11: Standard test method for determining volume fraction by systematic

manual point count, ASTM International, PA, 2011. doi:10.1520/E0562-11.2.

[237] S.M. Graham, Evaluation of welds exhibiting large scatter in charpy toughness using the reference temperature, J. Test. Eval. 33 (2005).

[238] H.K.D.H. Bhadeshia, Local brittle zones and the role of niobium, Mater. Sci. Forum. 783–786 (2014) 2129–2135. doi:10.4028/www.scientific.net/MSF.783-786.2129.

[239] Y.T. Cheng, C.M. Cheng, Scaling, dimensional analysis, and indentation measurements, Mater. Sci. Eng. R Reports. 44 (2004) 91–149. doi:http://dx.doi.org/10.1016/j.mser.2004.05.001.

[240] M. Shome, O.P. Gupta, O.N. Mohanty, Effect of simulated thermal cycles on the microstructure of the heat-affected zone in HSLA-80 and HSLA-100 steel plates, Metall. Mater. Trans. A. 35A (2004) 985–996.

[241] G. Spanos, R.W. Fonda, R.A. Vandermeer, A. Matuszeski, Microstructural changes in HSLA-100 steel thermally cycled to simulate the heat-affected zone during welding, Metall. Mater. Trans. A. 26A (1995) 3277–3293.

[242] M. Shome, Effect of heat-input on austenite grain size in the heat-affected zone of HSLA-100 steel, Mater. Sci. Eng. A. 445–446 (2007) 454–460. doi:10.1016/j.msea.2006.09.085.

[243] R. Cao, J. Li, D.S. Liu, J.Y. Ma, J.H. Chen, Micromechanism of decrease of impact toughness in coarse-grain heat-affected zone of HSLA steel with increasing welding heat input, Metall. Mater. Trans. A. 46A (2015) 2999–3014. doi:10.1007/s11661-015-2916-2.

[244] P. Yan, H.K.D.H. Bhadeshia, The austenite-ferrite transformation in enhanced-niobium, low-carbon steel, Mater. Sci. Technol. 31 (2015) 1066–1076. doi:DOI 10.1179/1743284714Y.0000000673.

[245] B.C. Kim, S. Lee, N.J. Kim, D.Y. Lee, Microstructure and local brittle zone phenomena in high-strength low-alloy steel welds, Metall. Mater. Trans. A. 22 (1991) 139–149.

[246] H. Somekawa, T. Mukai, Fracture toughness in an extruded ZK60 magnesium alloy, Mater. Trans. 47 (2006) 995–998.

[247] J.R.C. Guimaraes, P.R. Rios, Martensite start temperature and the austenite grain-size, J. Mater. Sci. 45 (2010) 1074–1077. doi:10.1007/s10853-009-4044-0.

[248] C.R. Brooks, Principles of the heat treatment of plain carbon and low-alloy steel, ASM International, Ohio, 1996.

[249] M. Shome, O.P. Gupta, O.N. Mohanty, Effect of simulated thermal cycles on the microstructure of the heat-affected zone in HSLA-80 and HSLA-100 steel plates, Metall. Mater. Trans. A. 35A (2004) 985–996.

[250] L. Aucott, S.W. Wen, H. Dong, The role of Ti carbonitride precipitates on fusion zone strength-

toughness in submerged arc welded linepipe joints, Mater. Sci. Eng. A. 622 (2015) 194–203.

[251] D. Bai, M.A. Cooke, J. Asante, J. Dorricott, High-strength micro-alloy steel and process for making same: Patent U.S. 6682, 2004.

[252] N.J. Petch, The cleavage strength of polycrystals, J. Iron Steel Inst. 174 (1953) 25–28.

[253] T.N. Baker, Determination of the friction stress from microstructural measurements, in: Yield, Flow Fract. Polycrystals Appl. Sci. Publ., 1982: pp. 235–273.

[254] H.M. Flower, T.C. Lindley, Electron backscattering diffraction study of acicular ferrite, bainite, and martensite steel microstructures, Mater. Sci. Technol. 16 (2000) 26–40. doi:10.1179/026708300773002636.

[255] J.M. Rodriguez-Ibabe, The role of microstructure in toughness behaviour of microalloyed steels, Mater. Sci. Forum. 284–286 (1998) 51–62. doi:10.4028/www.scientific.net/MSF.284-286.51.

[256] F.G. Caballero, C. Capdevila, J. Chao, The microstructure of continuously cooled tough bainitic steels, in: 2nd Int. Conf. Super-High Strength Steels, 2010.

[257] S. Massey, Increasing productivity with submerged arc welding, Columbus, 2012.

[258] M. Mohammadijoo, S. Kenny, L. Collins, H. Henein, D.G. Ivey, Effect of cold-wire addition in the TSAW process on microstructure and mechanical properties of the HAZ of X70 microalloyed pipeline steel, Am. Soc. Mech. Eng. 3 (2016) 1–9. doi:10.1115/IPC2016-64549.

[259] M. Mohammadijoo, S. Kenny, L. Collins, H. Henein, D.G. Ivey, Influence of cold-wire tandem submerged arc welding parameters on weld geometry and microhardness of microalloyed pipeline steels, Int. J. Adv. Manuf. Technol. (2016). doi:10.1007/s00170-016-8910-z.

[260] ASTM, E23-12C: Standard test methods for notched bar impact testing of metallic materials, ASTM International, PA, 2012.

[261] ASTM, E562-11: Standard test method for determining volume fraction by systematic manual point count, ASTM International, PA, 2011. doi:10.1520/E0562-11.2.

[262] S. Rigdal, L. Karlsson, L. Östgren, Synergic cold wire (SCW™) submerged arc welding, ESAB Weld. Cut. J. 57 (2002) 26–31. doi:10.1007/978-3-319-26324-3.

[263] S. Rigdal, L. Karlsson, L. Östgren, Synergic cold wire (SCW™) submerged arc welding, ESAB Weld. Cut. J. 57 (2002) 26–31. doi:10.1007/978-3-319-26324-3.

[264] V. Adarsh Narang, Heat transfer analysis in steel structures, Master Thesis, Worcester Polytechnic Institute, 2005.

[265] S.I. Rokhlin, A.C. Guu, A study of arc force , pool depression , and weld penetration during gas tungsten arc welding, Weld. Res. Suppl. (1993) 381s–390s.

[266] Y. Adonyi, W. Richardson, W.A. Baeslack, Investigation of arc force effects in subsurface GTA welding, Weld. Res. Suppl. (1992) 321s–330s.

[267] E. Halmoy, The pressure of the arc acting on the weld pool. Arc Physics and Weld Pool Behavior, The Welding Institute, Cambridge, 1979.

[268] J. Converti, Plasma-jets in arc welding, PhD Thesis, Massachusetts Institute of Technology, 1981.

[269] J. Converti, Plasma-jets in arc welding, PhD Thesis, Massachusetts Institute of Technology, 1981.

[270] Bavaria, Agglomerated Welding Flux BF6.5, Bavaria Schweisstechnik, Germany.

[271] K. Poorhaydari, B.M. Patchett, D.G. Ivey, Estimation of cooling rate in the welding of plates with intermediate thickness, Weld. Res. (2005) 149s–155s.

[272] C.L. Davis, J.E. King, Cleavage initiation in the intercritically reheated coarse-grained heat-affected zone : Part I. fractographic evidence, Metall. Mater. Trans. A. 25 (1994) 563–573. doi:10.1007/BF02651598.

[273] J.M. Reichert, T. Garcin, M. Militzer, W.J. Poole, A new approach using EBSD to quantitatively distinguish complex transformation products along the HAZ in X80 linepipe steel, in: 9th Int. Pipeline Conf., American Society of Mechanical Engineering, Calgary, AB, 2014.

[274] S. Moeinifar, A.H. Kokabi, H.R. Madaah Hosseini, Influence of peak temperature during simulation and real thermal cycles on microstructure and fracture properties of the reheated zones, Mater. Des. 31 (2010) 2948–2955. doi:10.1016/j.matdes.2009.12.023.

[275] S.-J. Lee, Y.-K. Lee, Effect of austenite grain size on martensitic transformation of a low alloy steel, Mater. Sci. Forum. 475–479 (2005) 3169–3172.

[276] H.K.D.H. Bhadeshia, Local brittle zones and the role of niobium, Mater. Sci. Forum. 783–786 (2014) 2129–2135. doi:10.4028/www.scientific.net/MSF.783-786.2129.

[277] F. Matsuda, K. Ikeuchi, Y. Fukada, Y. Horii, H. Okada, T. Shiwaku, C. Shiga, S. Suzuki, Review of mechanical and metallurgical investigations of M-A constituents in welded joint in Japan.pdf, Transcations JWRI. 24 (1995) 1–24.

[278] L. Lan, C. Qiu, D. Zhao, Analysis of martensite – austenite constituent and its effect on toughness in submerged arc welded joint of low carbon bainitic steel, J. Mater. Sci. 47 (2012) 4732–4742. doi:10.1007/s10853-012-6346-x.

[279] H. Somekawa, T. Mukai, Fracture toughness in an extruded ZK60 magnesium alloy, Mater. Trans. 47 (2006) 995–998.

[280] H. Yuan, W. Brocks, Quantification of constraint effects in elastic-plastic crack front fields, J.

Mech. Phys. Solids. 46 (1998) 219–241. doi:10.1016/S0022-5096(97)00068-9.

[281] P.A. Eikrem, Z.L. Zhang, B. Nyhus, Effect of plastic prestrain on the crack tip constraint of pipeline steels, Int. J. Press. Vessel. Pip. 84 (2007) 708–715. doi:http://dx.doi.org/10.1016/j.ijpvp.2007.08.007.

[282] X.B. Ren, Z.L. Zhang, B. Nyhus, Effect of residual stresses on ductile crack growth resistance, Eng. Fract. Mech. 77 (2010) 1325–1337. doi:http://dx.doi.org/10.1016/j.engfracmech.2010.03.007.

[283] J. Liu, Z.L. Zhang, B. Nyhus, Residual stress induced crack tip constraint, Eng. Fract. Mech. 75 (2008) 4151–4166. doi:http://dx.doi.org/10.1016/j.engfracmech.2008.03.010.

[284] X.K. Zhu, J.A. Joyce, Review of fracture toughness (G, K, J, CTOD, CTOA) testing and standardization, Eng. Fract. Mech. 85 (2012) 1–46. doi:http://dx.doi.org/10.1016/j.engfracmech.2012.02.001.

[285] X.K. Zhu, Fracture toughness (K, J) testing, evaluation, and standardization, J. Pipeline Eng. 12 (2013) 145–155.

[286] ASTM, E-399-12e3: Standard test method for linear-elastic plain strain fracture toughness KIC of metallic materials, ASTM Int. (2013).

[287] ISO, 12135: Metallic materials - Unified method of test for the determination of quasistatic fracture toughness, Int. Organ. Stand. (2014).

[288] B. Nyhus, M.L. Polanco, O. Orjasether, SENT specimen and alternative to SENB specimens for fracture mechanics testing of pipelines, in: Int. Conf. OMAE, Cancun, Mexico, n.d.

[289] S. Cravero, C. Ruggieri, Correlation of fracture behavior in high pressure pipelines with axial flaws using constraint designed test specimens––Part I: Plane-strain analyses, Eng. Fract. Mech. 72 (2005) 1344–1360. doi:http://dx.doi.org/10.1016/j.engfracmech.2004.10.010.

[290] S. Cravero, R.E. Bravo, H.A. Ernst, Constraint evaluation and effects on J-R curves for pipes under combined load conditions, in: ECF-17, Brno, Czech, 2008.

[291] X.-K. Zhu, Advances in fracture toughness test methods for ductile materials in low-constraint conditions, Procedia Eng. 130 (2015) 784–802. doi:10.1016/j.proeng.2015.12.195.

[292] J.D.G. Sumpter, C.E. Turner, Method for laboratory determination of JC (contour integral for fracture analysis), in: Cracks Fract. ASTM STP 601. Am. Soc. Test. Mater., 1976.

[293] G.A. Clarke, J. Landes, Evaluation of the J integral for the compact specimen BT - Evaluation of the J integral for the compact specimen, J. Test. Eval. 7 (1979) 264–269.

[294] J.D.G. Sumpter, Jc determination for shallow notch welded bend specimens, Fatigue Fract.

Eng. Mater. Struct. 10 (1987) 479–493. doi:10.1111/j.1460-2695.1987.tb00498.x.

[295] M. Kirk, R. Dodds, J and CTOD estimation equations for shallow cracks in single edge notch bend specimens BT, J. Test. Eval. 21 (1993) 228–238.

[296] M. Nevalainen, R.H. Dodds, Numerical investigation of 3-D constraint effects on brittle fracture in SE(B) and C(T) specimens, Int. J. Fract. 74 (1996) 131–161. doi:10.1007/BF00036262.

[297] J.W. Hutchinson, P.C. Paris, Stability analysis of J-controlled crack growth. In: Elastic-plastic fracture, ASTM STP 668. Am. Soc. Test. Mater. (1979) 37–64.

[298] G.A. Clarke, W.R. Andrews, P.C. Paris, D.W. Schmidt, Single specimen tests for JIC determination, Mech. Crack Growth. ASTM STP 590. Am. Soc. Test. Mater. (1976) 27–42.

[299] H.A. Ernst, P.C. Paris, J.D. Landes, Estimation on J-integral and testing modulus T from a single specimen tets record, in: 13th Fract. Mech. Conf., 1981: pp. 476–502.

[300] X. Zhu, B. Leis, J. Joyce, Experimental estimation of J-R curves from load-CMOD record for SE(B) specimens, J. ASTM Int. 5 (2008) 1–15.

[301] S. Cravero, C. Ruggieri, Further developments in J evaluation procedure for growing cracks based on LLD and CMOD data, Int. J. Fract. 148 (2007) 387–400. doi:10.1007/s10704-008-9211-9.

[302] R. Herrera, J.D. Landes, Direct J–R curve analysis of fracture toughness test, J. Test. Eval. 16 (1988) 427–449.

[303] ASTM, E1290: Standard test method for crack-tip opening displacement (CTOD) fracture toghness measurement (withdrawn in 2013), ASTM International, 2012.

[304] D.-Y. Park, W.R. Tyson, J.A. Gianetto, R.S. Eagleson, Fracture toughness of X100 pipe welds using SE(T) and SE(B) tests, in: 9th Int. Pipeline Conf., Calgary, AB, Canada, 2012.

[305] G. Shen, W.R. Tyson, Evaluation of CTOD from J-integral for SE(T) specimens, in: Pipeline Technol. Conf., Ostend, Belgium, 2009.

[306] H. Tang, M. Macia, K. Minaar, P. Gioielli, S. Kibey, D.P. Fairchild, Development of the SENT test for strain-based design of welded pipelines, in: 8th Int. Pipeline Conf., Calgary, AB, Canada, 2010.

[307] H.G. Pisarski, Determination of pipe girth weld fracture toughness using SENT, in: 8th Int. Pipeline Conf., Calgary, AB, Canada, 2010.

[308] W. Lan, X. Deng, M.A. Sutton, Investigation of crack tunneling in ductile materials, Eng. Fract. Mech. 77 (2010) 2800–2812. doi:http://dx.doi.org/10.1016/j.engfracmech.2010.06.010.

[309] F. Riemelmoser, R. Pippan, H. Weinhandl, O. Kolednik, The influence of irregularities in the

crack shape on the crack extension measurement by means of the direct-current-potential-drop method, J. Test. Eval. 27 (1999) 42–46.

[310] G. Shen, J.A. Gianetto, W.R. Tyson, Development of procedure for low-constraint toughness testing using a single-specimen technique: MTL Report No. 2008-18(TR), CanmetMaterials, Ottawa, Canada, 2008.

[311] G. Shen, W.R. Tyson, Crack size evaluation using unloading compliance in single-specimen single-edge notched tension fracture toughness testing, J. Test. Eval. 37 (2009) No. 4, JTE102368.

[312] J.A. Joyce, R.E. Link, Effect of constraint on upper shelf fracture toughness, in: Fract. Mech. ASTM STP 1256, ASTM Int. Philadelphia, 1995: pp. 142–177.

[313] E. Lucon, T.S. Weeks, J.A. Gianetto, W.R. Tyson, D.-Y. Park, Fracture toughness characterization of high-pressure pipe girth welds using single-edge notched tension [SE(T)] specimens, Mater. Perform. Charact. 4 (2015) 20130098. doi:10.1520/MPC20130098.

[314] J.M. Reichert, T. Garcin, M. Militzer, W.J. Poole, Formation of martemsite/austenite (M/A) in X80 linepipe steel, in: 9th Int. Pipeline Conf., Calgary, AB, Canada, 2012.

[315] G.F. Vander Voort, Metallography: Principles and Practice, McGraw-Hill, New York, 1984.

[316] A. Ray, S.K. Dhua, Microstructural manifestations in color: some applications for steels, Mater. Charact. 37 (1996) 1–8.

[317] J.M.B. Losz, K.D. Challenger, HAZ microstructures in HSLA steel weldments, in: First United States--Japan Symp. Adv. Weld. Metall., American Welding Society, Miami, 1990: pp. 323–357.

[318] G. Weimer, R. Cagganello, Electric resistance welding at a glance: Process, power and weld roll basics, J. Tube Pipe. (2002).

[319] The-Welding-Institute, Defects/imperfections in welds, Job Knowledge 42, 2016. http://www.twi-global.com/technical-knowledge/job-knowledge/defects-imperfections-in-welds-porosity-042/.